# Microwave-driven Rabi Magnetometry Implemented in Hot Atomic Vapor

by

**Christopher Hamilton Kiehl**

B.A., Lawrence University, 2017

A thesis submitted to the

Faculty of the Graduate School of the

University of Colorado in partial fulfillment

of the requirements for the degree of

Doctor of Philosophy

Department of Physics

2024

Committee Members:

Cindy A. Regal, Chair

Svenja Knappe

James K. Thompson

Murray J. Holland

Robert A. Marshall

Kiehl, Christopher Hamilton (Ph.D., Physics)

Microwave-driven Rabi Magnetometry Implemented in Hot Atomic Vapor

Thesis directed by Prof. Cindy A. Regal

In this thesis, I describe the development of a novel approach to atomic vector magnetometry that utilizes the directional information contained in microwave-driven Rabi oscillations between the hyperfine manifolds of $^{87}$Rb. These measurements take place in a heated microfabricated vapor cell embedded within a microwave cavity with a single optical axis. By utilizing a complete model for the atom-microwave coupling and collisional decoherence, I show how nontrivial spin dynamics during Rabi oscillations from spin-exchange collisions in the strong-driving limit characterizes basic properties of the atomic vapor. Additionally, I illustrate how this theoretical framework enables the in-situ correction of heading errors in free induction decay (FID) signals, operating under realistic conditions of imperfect pumping and high buffer gas pressures that often hinder other methods of heading error-free measurements. Finally, I demonstrate vector magnetometry by referencing Rabi measurements from multiple hyperfine transitions against calibrated microwave polarization ellipses (MPEs). I further show how to accurately reference an intrinsic magnetometer frame to the attitude of a probe beam from the magnetic field orientation where the Rabi oscillation signal zeroes. This Rabi Amplitude Nulling to determine Beam Attitude (RANBA) technique could be applied to calibrate a vector gradiometer and to monitor overall drifts in the intrinsic magnetometer frame. While state-of-the-art vector magnetometers calibrate systematic errors arising from drifts through sensor or bias field rotations, this research lays the groundwork towards achieving practical vector calibration by only leveraging electromagnetic field manipulations; thereby circumventing the need for intricate mechanical rotations or the application of large bias fields.

## Dedication

To my high school teachers Peter Bergman and Hella Willis who helped foster and support my curiosity in physics within and outside the classroom. To John Brandenberger who pulled me into the field of AMO and was one of my most influential mentors. To my parents Greg and Karen, my sister Maddie, my grandparents Don, Nancy, Art, and Mary, and to Mar Cols Margenet for their love and unconditional support in my life.

## Acknowledgements

After two years of working with single ultracold atoms, my advisor Cindy inquired if I was interested in a 'quick' hot vapor cell magnetometry experiment, which ultimately culminated in the research presented in this thesis several years later. My deep appreciation goes to Cindy for her unwavering support and mentorship, and for the opportunity to be part of her lab.

This thesis also owes a great deal to Tobias Thiele, who not only co-developed this experiment with me in its initial year but also served as a significant mentor. The late-night work sessions and engaging discussions with him have been instrumental in my growth as a physicist. In addition, my gratitude extends to Yolanda Duerst for programming the Labview code that operated our experiment, and to Svenja Knappe for her invaluable collaboration, providing us with microfabricated vapor cells and a magnetic shield, alongside her expertise in hot vapor cell magnetometry. A special thanks also goes out to Yuan-Yu Jau, Christoph Affolderbach, and Georg Bison for their insightful discussions on Rabi oscillation coherence, frequency fitting, and heading errors.

I am immensely thankful for working alongside my lab mate Thanmay Menon, who not only assisted in relocating our experiment to the B236 lab but also significantly contributed to the development of the experimental apparatus. I am also grateful for discussions and colloboration with Dawson Hewatt, Michaela Ellmeier, Juniper Pollock, and Newton Rai. It has also been a pleasure to get to know other graduate students in Cindy's lab over the years including Ting-Wei Hsu, Ting-you, Zhenpu, Willa, Stephen, Matteo, Mark, and Yinheng

Finally, I am profoundly grateful for the support from my family and the many friends I've made along this journey, who have made my PhD experience so much more enjoyable.

# Contents

# Tables

**Table**

# Figures

**Figure**

# Chapter 1

# Introduction

## 1.1 Optically pumped magnetometry context

The development of the first optically-pumped atomic magnetometers (OPMs) dates back to the early 1960s, following the pioneering work in spin-polarized optical pumping first concieved by A. Kastler [92] in 1950, and experimentally demonstrated by Brossel et al. [36] in 1952 and W. B. Hawkins and R. H. Dicke in 1953 [75]. The first spin precession and magnetic resonance signals from optically pumped atomic vapors were demonstrated by Dehmelt in 1957 [52] and W. E. Bell and A. L. Bloom in 1957 [24] respectively, leading to the unveiling of the first optically-pumped magnetometers soon after [25, 136, 165]. OPMs provided several advantages compared to earlier magnetometer technologies such as fluxgates and proton precessional magnetometers. In comparison to fluxgates, OPMs demonstrated no saturation effects and provided higher accuracy and precision [136]. Relative to proton magnetometers, OPMs featured a greater bandwidth, could be designed more compactly, and had lower power consumption [40]. The development of OPMs over recent decades has progressed to achieving record magnetic sensitivites reaching below 1 fT/$\sqrt{\text{Hz}}$ [41, 50, 101, 164]. This advancement has opened the door to new magnetometer applications ranging from the precise detection of biological signals [30, 35, 190], to aiding in searches for the permanent neutron electric dipole moment [17, 138] and dark matter [3, 141].

The core principle of atomic magnetometers is based on measuring the Zeeman splitting that occurs among the magnetic sublevels in the hyperfine structure of atoms. Zeeman splitting is directly proportional to the magnitude of the magnetic field, represented as $|\vec{B}_{\mathrm{DC}}|$, and is quantified by the Larmor precession frequency, given by the equation

$$f_L = \gamma |\vec{B}_{\rm DC}| \tag{1.1}$$

where $\gamma$ is the gyromagnetic ratio associated with the atomic spin. OPMs typically employ alkali atoms, where, for example, $\gamma \approx 7$ kHz/$\mu$T is the gyromagnetic ratio of the isotope $^{87}$Rb. This gyromagnetic ratio corresponds to the total atomic spin $\vec{F}$, which is formed by adding the nuclear spin $\vec{I}$ and the outer electron spin $\vec{S}$, that is expressed as $\vec{F} = \vec{I} + \vec{S}$. A fundamental magnetometry technique to detect these Zeeman shifts, with origins in nuclear magnetic resonance (NMR) [82], is the concept of free induction decay (FID) [see Fig. 1.1] that involves the direct observation of the Larmor spin-precession of the atomic spin ensemble [86]. Many other approaches have been developed [57] to detect the Zeeman shifts such as Bell-Bloom [25], $M_z$ [10, 31, 157], $M_x$ [31, 67], nonlinear magneto-optical resonance (NMOR) [38, 39], and coherent population trapping [130, 167].

Regardless of the technique, the precision $\delta B$ of atomic magnetometers after a measurement time $t$ is limited by the number of atoms $N$ being probed and the coherence time $T_2$ of the Zeeman transitions given by [41]

$$\delta B = \frac{1}{\gamma\sqrt{N T_2 t}}. \tag{1.2}$$

Decoherence in vapor cells stems from various factors, including spin-exchange, buffer gas and wall collisions, light scattering, and spatial variations of the magnetic field across the vapor cell. In the most sensitive OPMs, which utilize high atomic densities, spin-exchange collisions typically emerge as the predominant source of decoherence. A notable discovery in the 1970s [71, 72] revealed that, under conditions of low magnetic fields and high atomic densities, spin relaxation effects of spin-exchange collisions diminish, a phenomenon now known as the spin-exchange relaxation free (SERF) regime [12]. This discovery was the essential ingredient to reaching sub-fT sensitivities without requiring enormous vapor cell volumes $V \gg 1$ cm$^3$ [101]. The ultimate sensitivity that atomic magnetometers can reach is limited by atomic spin projection noise fundamentally set by the Heisenberg uncertianty relation [57]

$$\Delta F_y \Delta F_z \geq \frac{\langle F_x \rangle}{2} \tag{1.3}$$

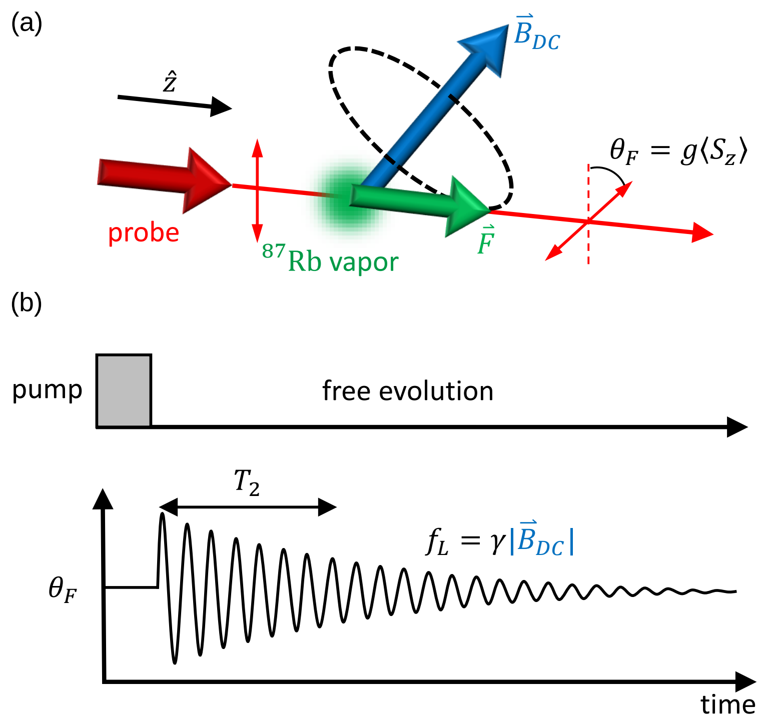


Figure 1.1: Operational schematic of an OPM utilizing free induction decay (FID). (a) Following the initialization of the macroscopic spin angular momentum $\vec{F}$ along the $\hat{z}$ axis using optical pumping, the precession of $\vec{F}$ about the magnetic field $\vec{B}_{\mathrm{DC}}$ is detected by a probe beam. Often the OPM is configured to detect the Faraday rotation angle $\theta_F$ of the probe's linear polarization. This angle is directly proportional to the z-component $(S_z)$ of the electron spin. (b) FID pump and measurement timing diagram. The precessional Larmor frequency $(f_{\mathrm{L}})$ is proportional to the magnetic field strength $(|\vec{B}_{\mathrm{DC}}|)$. The decay of the FID signal is characterized by the coherence time $T_2$. For $^{87}$Rb the gyromagnetic ratio is given by $\gamma \approx 7$ kHz/$\mu$T.

where $\Delta F_j$ denotes the uncertainty in the macroscopic spin component $F_j$, for $j = x, y, z$. Consequently, atomic magnetometers utilizing spin-squeezing techniques to surpass this limit are a focus of ongoing research [104, 161, 172, 173, 186].

In certain applications of OPMs, factors such as spatial resolution and compact sensor size are just as critical as sensitivity. A significant advancement in this regard was the development of microfabricated vapor cells using silicon micromachining in the early 2000s [113], and is likely to be essential for reducing OPM production costs and facilitating mass production. Microfabricated vapor cells [185], with volumes as small as 1 mm$^3$, have enabled the spatial mapping of magnetic fields with millimeter resolution. These developments have applications in medical fields like magnetoencephalography [7] and magnetocardiography [30], as well as in remote NMR detection [105]. Additionally, the compact size of these cells is beneficial for space satellite integration, offering reduced size and weight [98, 154]. In these MEMS cells, buffer gases like $N_2$ are crucial for increasing diffusion length and mitigating wall collisions, thereby enhancing the coherence time $T_2$. The ongoing quest to miniaturize vapor cells further to micrometer scales and beyond is an active area of research [19, 49, 116, 139].

### 1.1.1 Operational challenges of atomic magnetometers

Practical use of OPMs in geomagnetic fields such as navigation [42, 146], geophysics [61, 169], space [27, 55, 103], and unexploded ordinance detection [28, 144] requires addressing systematic errors that depend on the orientation of the sensor with respect to the magnetic field known as **heading errors**. For the most common OPMs made of alkali atoms the dominant heading error at geomagnetic fields is on the order of 10 nT [107]. This systematic error manifests from unknown strengths of unresolved frequency components in the magnetometer signal arising from nonlinear Zeeman (NLZ) shifts from each of the ground state hyperfine manifolds [8, 107]. If unaccounted for, these heading errors can appear as additional noise such as in magnetic navigation where the magnetometer orientation is generally not fixed. Furthermore, heading errors can degrade the positioning accuracy in magnetic navigation, which often require scalar accuracies at the 1 nT level or better to reach $\sim$100 m positioning accuracy [42, 43]. Additional details on known research to mitigate heading errors in OPMs, and the associated challenges are discussed in Ch. 4.

Another notable challenge in the operation of atomic magnetometers in geomagnetic fields is the degradation of the magnetometer signal for certain orientations of the magnetic field known as **deadzones**. This is exemplified in the FID sensing configuration where no spin precession occurs when the magnetic field is parallel to the pumping axis. To eliminate deadzones, various methods have been implemented, which, while effective, result in increased sensor complexity. These methods include multiple probe beams or vapor cells [44, 45], mechanical rotations of components [69], unpolarized light combined with varying microwave field configurations [6], and switching between

$M_x$ and $M_z$ magnetometer configurations [182]. In addition, using coherent population trapping resonances [26, 140] have been show to have no deadzones. Although CPT magnetometers achieve sensitivities near 50 pT/$\sqrt{\text{Hz}}$, they do not reach the same level of sensitivity as state-of-the-art OPMs.

Accurate mapping of the magnetic field vector is another challenge for OPMs because they **lack an inherent 3D reference**. In contrast to a variety of magnetometers, such as fluxgates [16, 99], magneto-resistive sensors [192], hall sensors [91, 131], and superconducting quantum interference devices (SQUIDs) [46, 51], that directly detect a component of the magnetic field, OPMs are total-field sensors detecting only the magnetic field strength $|\vec{B}_{\text{DC}}|$. For the directional magnetometers just listed full magnetic field mapping involves mounting three of these sensors in near-orthogonal orientations [16, 51]. In high-accuracy applications such as magnetic anomaly detection [144, 196], navigation [42, 145], space exploration [27, 55, 103], and geophysics [108], these directional magnetometers alone are often insufficient due to lack of absolute measurements and environmental drift. An OPM is often included as a scalar reference to help mitigate these inaccuracies. Even so, the act of vectorizing an OPM removes the necessity for multiple sensors, and can lead to improvements in overall accuracy and sensitivity [11, 66].

Many OPMs achieve vector operation through various atom-light interactions including electromagnetically induced transparency (EIT) [120, 193], nonlinear magneto-optical rotation [121, 147], double resonance atomic alignment [87, 187], the Voigt effect [148], vector light shifts from modulated light fields [137], and methods that detect spin projections on multiple laser beams [29, 58, 199]. These approaches reference the atomic quantization axis, determined by the magnetic field direction, against known characteristics of an applied electromagnetic field such as a laser beam's polarization structure or propagation direction. Because these techniques utilize amplitude-based detection, and require precise modeling of the atom-light coupling, achieving vector accuracies beyond 1 degree (17 mrad) through robust sensor calibration is a complex task. For this reason, several frequency-based techniques using scalar detection ($|\vec{B}_{\text{DC}}|$) are routinely utilized, including a directional varying reference field [9, 11], low-frequency coil modulations [13, 66], and fast rotating fields [184]. Because scalar measurements are directly extracted from the atomic signal without complex modeling, these measurements are highly accurate.

In particular, coil modulation is a well-established approach that has been implemented with a $^4$He OPM in the European Space Agency SWARM mission [109]. This mission consisted of three satelites, each equipped with a $^4$He vector OPM, to accurately map spatial and temporal variations of the geomagnetic field. High-accuracy applications often employ $^4$He because it lacks nuclear spin, thereby eliminating heading errors from nonlinear Zeeman effects that are common in alkali OPMs. That sensor reached 10 $\mu$rad accuracy (1 part in $10^5$) after a scalar calibration involving multiple sensor rotations [66]. If calibrations were not employed drifts in the coil factors would have degraded the $^4$He OPM vector accuracy to about 0.02° (350 $\mu$rad) [109].

A drawback of modulation techniques, however, is that the vector sensitivity degrades with increased magnetic field strength for the same modulation depth. Moreover, in many cases weak modulation fields are necessary due to power requirements, prevention of coupling to external objects, and slew-rate limitations of coil feedback electronics [198]. For instance, by employing modulation depths exceeding 15 $\mu$T, vector component sensitivities of down to 6 pT/$\sqrt{\text{Hz}}$ have been achieved, as reported in [184]. Conversely, in the SWARM mission, vector component sensitivities are restricted to 1 nT/$\sqrt{\text{Hz}}$, a limitation attributed to the more modest modulation depths of 50 nT, as detailed in [109]. In addition, modulation techniques offer limited insight from atomic measurements for monitoring environmental drifts in the vector reference. As a result, achieving high accuracy can entail performing iterative calibrations without prior knowledge. This process often requires rotations of either the sensor or a large bias field, which can lead to intervals of sensor downtime.

Vector magnetometers are often utilized in applications requiring magnetic field mapping, as demonstrated by the SWARM mission, or for referencing to magnetic field maps. One practical example is their use in magnetic navigation. While scalar measurements are commonly preferred for their orientation insensitivity and high accuracy [42, 43], accurate vector measurements could significantly enhance navigation precision due to the additional information from vector components [129].

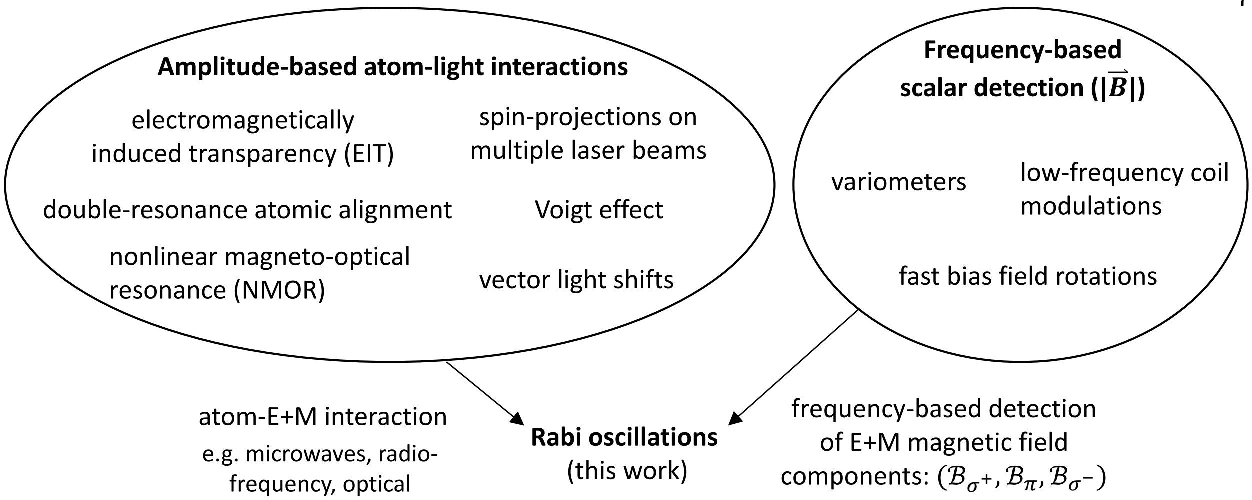


Figure 1.2: A schematic of vector OPM techniques categorized as either amplitude-based atom-light interactions or as scalar detection often employing frequency-based measurements. A vector OPM utilizing microwave-driven Rabi oscillations, the subject of this thesis, contains aspects of both of these categories. While this thesis focuses on microwave-driven Rabi oscillations between hyperfine manifolds, examples of possible generalizations of this technique are using other types of electromagnetic driving fields, such as radio-frequency or optical field, or different types of atomic transitions, such as Zeeman sublevels within a hyperfine manifold.

To counteract time-dependent environmental magnetic field distortions, tensor measurements using four vector magnetometers have been suggested [84, 106, 129]. Theoretical exploration has shown that underwater vehicles could achieve attitude determination with an accuracy of about 0.3° using magnetic anomaly maps, assuming vector magnetometer precision and accuracy below 10 nT [84]. For tensor measurements, vector sensitivity is crucial for discerning magnetic gradients over distances, based on vehicle speed, and influences the minimal size of the magnetometer. For instance, a magnetic anomaly map from a dipole with $10^8$ A/m$^2$ strength, which diminishes as $1/r^3$, could produce a magnetic field gradient of around 100 nT/m at a distance of 100 m. In such scenarios, tensor measurements with vector magnetometers spaced merely a centimeter apart would require a resolution of 1 nT. Greater accuracy and sensitivity in these measurements would lead to improved attitude determination, reduced sensor size, and the feasibility of operation in weaker magnetic anomaly fields.

The importance of vector accuracy has also been demonstrated for planetary explorations.

For example, the Galileo mission, aimed at investigating Jupiter's magnetosphere, revealed intricate magnetic signatures that supported the existence of subsurface oceans on Europa and Callisto [93]. During these flybys, fluctuations in the measured magnetic vector components were observed at a scale of a few nT against a background field of 2000 nT. This observation led to a vector accuracy design goal of 1 part in $10^4$ (100 $\mu$rad) for the mission [97]. Similarly, the Cassini mission, which studied the dynamic interactions in Saturn's magnetosphere, also required comparable vector accuracy [55]. In this mission, the limitation to vector accuracy at the 1 nT level constrained the precision in determining higher order spherical harmonic coefficients for modeling the internal planetary magnetic field at specific flyby distances.

## 1.2 Rabi oscillations as a novel tool for optically pumped magnetometry

### 1.2.1 Background of microwave-Rabi oscillations in vapor cells

This thesis investigates the application of microwave-driven Rabi oscillations for atomic magnetometry in a microfabricated vapor cell platform using $^{87}$Rb. In this work Rabi oscillations refer to coherent population dynamics between two hyperfine sublevels, $|F = 1, m_F\rangle$ and $|F' = 2, m_{F'}\rangle$, when the frequency $\nu_{\mu\mathrm{w}}$ of a microwave field $\vec{\mathcal{B}}(t)$ is tuned to the atomic transition resonance $\nu_0$. Ignoring couplings to adjacent transitions within the multi-level structure of alkali atoms, the probability $P_{|m'\rangle}$ to measure an atom in $|2, m_{F'}\rangle$ during these Rabi oscillations after being initially prepared in the $|1, m_F\rangle$ state is given by

$$P_{|m'\rangle} = \frac{\Omega^2}{\Omega^2 + \Delta^2} \sin^2\left(\frac{2\pi\sqrt{\Omega^2 + \Delta^2}}{2} t\right) \tag{1.4}$$

where $\Delta = \nu_{\mu\mathrm{w}} - \nu_0$ is the detuning of the driving field from the atomic resonance and $\Omega$ is the Rabi frequency. From Eq. (1.4), the oscillation frequency of the population dynamics is given by the generalized Rabi frequency

$$\tilde{\Omega} = \sqrt{\Omega^2 + \Delta^2}. \tag{1.5}$$

Thus, by measuring the detuning dependence of the Rabi oscillation frequencies given by Eq. (1.5), Rabi oscillations can be used for precise hyperfine spectroscopy of the transition resonances $\nu_0$.

Moreover, the Rabi frequency $\Omega$ is linked to a microwave field's polarization structure, mathematically represented as an ellipse, and can be utilized to map out spherical microwave field components ($\mathcal{B}_{\sigma^+}$, $\mathcal{B}_{\pi}$, $\mathcal{B}_{\sigma^-}$). This is achieved by probing $\sigma^{\pm}$ and $\pi$ transitions, characterized by $m_{F'} = m_F \pm 1$ and $m_{F'} = m_F$, respectively. Using microfabricated vapor cells, Rabi oscillation measurements have been employed for sub-millimeter microwave imaging [32, 81], with potential applications in microwave circuit analysis, corrosion monitoring, and medical imaging. Additionally, these measurements have been pivotal in determining the spatial distribution of dephasing mechanisms within vapor cells [80]. Microwave imaging with Rabi oscillations has also proven valuable in characterizing the microwave inhomogeneity in vapor cell atomic clocks [4].

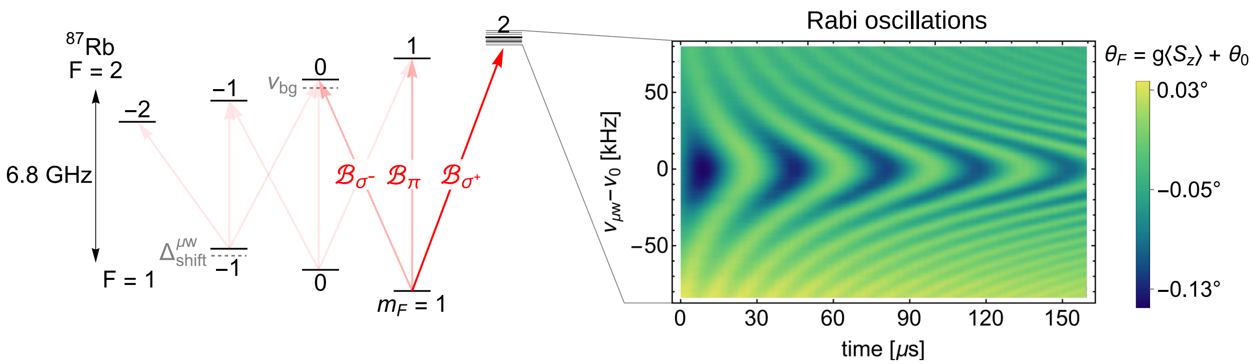


Figure 1.3: Measured Rabi oscillations driven between hyperfine magnetic sublevels in $^{87}$Rb. The Rabi-Chevron pattern (right), measured in our experiment, is well-approximated by Eq. (1.4).

Due to the SI traceability of Rabi measurements stemming from their relation to well-known fundamental constants, they avoid calibration issues when sensing microwave components. To date, however, there has been limited research focused on investigating the systematic errors in detecting Rabi oscillation frequencies in vapor cells. For instance, off-resonant driving in multi-level alkali systems is anticipated to induce frequency shifts in both the Rabi rates and Rabi resonances, deviating from what is predicted by standard two-level formalism in Eq. (1.4) and Eq. (1.5). In addition, nearly all Rabi oscillation measurements in vapor cells have employed absorption detection [4, 32, 81, 115] which severely limits measurement precision due to the many microwave pulse repetitions required to map out the time-dependent Rabi signal. Moreover, absorptive measurements are more susceptible to additional decoherence caused by light scattering and light shifts, while also restricting the measurement bandwidth. In contrast, the Rabi measurements discussed in this thesis employ Faraday rotation, a technique commonly used in OPMs [12, 110, 162], as a nondestructive method to continuously monitor the spin dynamics of Rabi oscillations.

On the other hand accurate microwave interrogation of alkali vapor cells has been extensively explored for application in vapor cell atomic clocks. These techniques often use Ramsey-style interrogation [5, 23, 48] to precisely measure the hyperfine clock transition. To achieve high accuracy measurements, care is taken to design a microwave cavity that produces a linearly polarized microwave field to minimize frequency shifts from off-resonant driving. Furthermore, these experiments operate with a well-defined quantization axis defined by a static magnetic field. These restricted conditions, essential for precise hyperfine spectroscopy in vapor cell atomic clocks, are unfeasible to adapt for magnetometry that requires operation in arbitrary magnetic field directions.

### 1.2.2 This thesis: Rabi techniques for accurate atomic magnetometry

In this thesis, we built a vapor cell experiment to implement microwave-driven Rabi oscillations towards the application of atomic magnetometry. For vector reference, we utilize planar cavity modes that can be excited to create arbitrary microwave polarization ellipses (MPEs) at a microfabricated vapor cell situated at the center of a microwave cavity. Initially, three MPEs are calibrated by making Rabi measurements of over several hyperfine transitions and magnetic field directions. Equipped with the known structure of each MPE, defined by three amplitudes $(\mathcal{B}_x, \mathcal{B}_y, \mathcal{B}_z)$ and two phases $(\phi_x, \phi_y)$, Rabi measurements from each of these MPEs and hyperfine transitions can be used to extract the direction of an unknown magnetic field. Full vector mapping is achieved by combining the Rabi measurements with the magnetic field strengths extracted from free induction decay (FID) measurements introduced in Sec. 1.1. As discussed in Ch. 3, it turns out the vapor cell parameters for the Rabi magnetometer can be very similar to parameters required for sensitive FID scalar magnetometers. Consequently, the measurements can be interleaved in the same system. A schematic of the operational principle of our Rabi magnetometer is shown in

Figure 1.4.

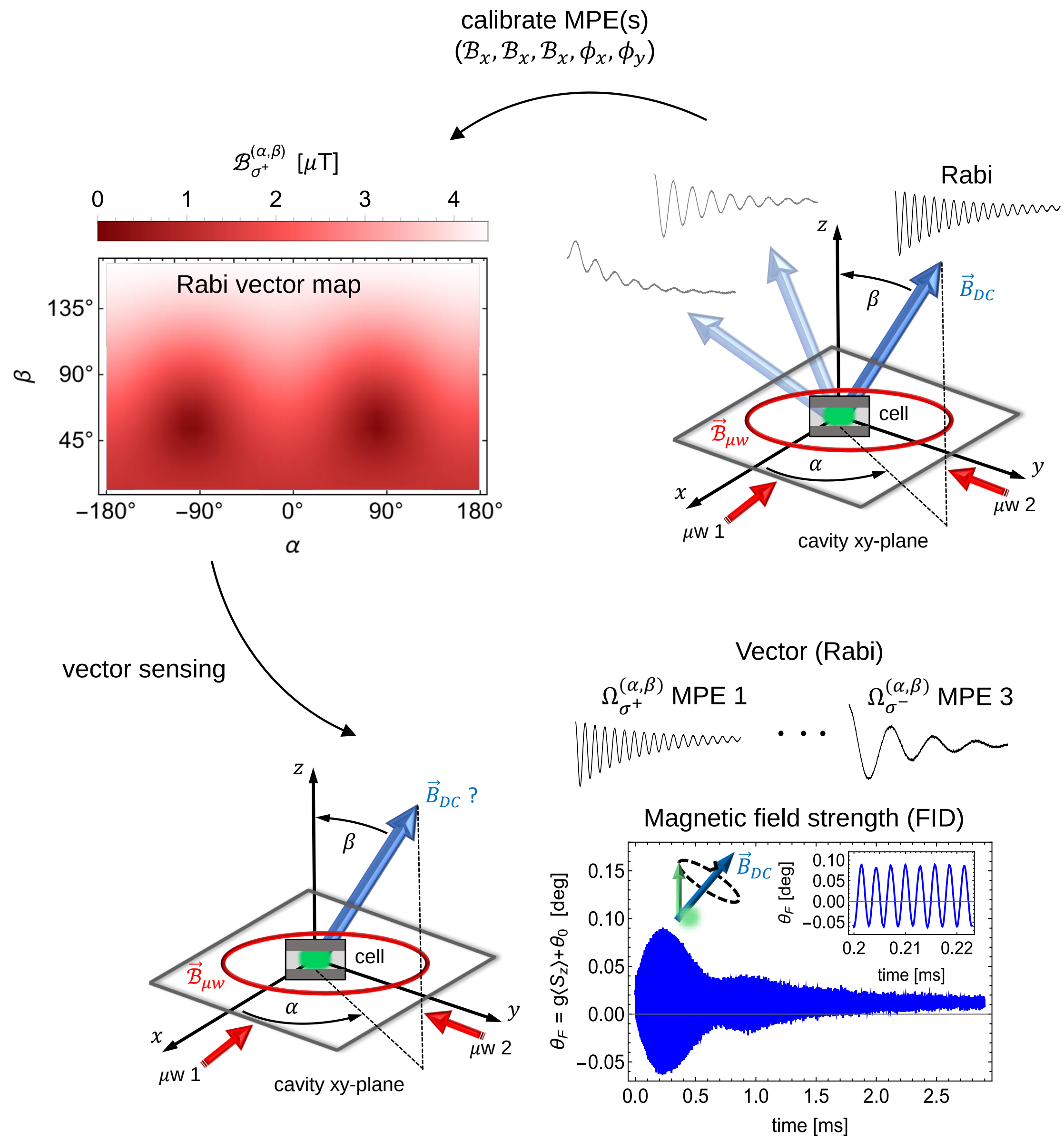


Figure 1.4: Schematic of the operational principle of our Rabi magnetometer. Vector detection requires calibration of the microwave polarization ellipse (MPE) structure ($\mathcal{B}_{\mu\text{w}}$).

The motivation of this work originates from a vector magnetometry experiment implemented with cold single atoms trapped in optical tweezers [170]. In that experiment it was demonstrated that microwave-driven Rabi oscillations could fully calibrate the polarization structure of a microwave field, and that the calibration could in turn be used to extract the direction of a static

(DC) magnetic field. Similar prior work was demonstrated with cold Rydberg atoms to spatially map the electric counterpart of the microwave polarization ellipse [100]. In addition to the DC magnetic field direction, it was also possible to detect and extract various systematic variables stemming from the microwave and coil system apparatus. In this cold atom magnetometry experiment, where measurements were conducted with 5 atoms on average, the sensitivities in this demonstration were poor with the magnetic field strength sensitivity estimated to be 740 $\mathrm{nT}/\sqrt{\mathrm{Hz}}$ and vector sensitivities ranging between $(10, 400)$ $\mathrm{mrad}/\sqrt{\mathrm{Hz}}$. It was an open question how well these techniques could be translated into a vapor cell platform, used for state-of-the-art magnetometer sensitivity, and further, whether Rabi oscillations provided any advantages to accurate vector detection over standard OPM techniques.

For the Rabi oscillation measurements in our apparatus the coherence times were always a few factors less than the coherence times of FID measurements. This motivated us to model Rabi oscillations, in microfabricated vapor cells to fully understand this effect, which likely had implications on the ultimate sensitivity of Rabi measurements. This decoherence discrepancy between the coherence of Rabi and FID measurements ultimately arose from spin-exchange collisions. Hyperfine dephasing from spin exchange collisions has been well-studied from the perspective of vapor cell atomic clocks, but have always assumed steady-state atomic populations in the so-called weak driving approximation [176]. In contrast, Rabi oscillations, by definition, exhibited strong population dynamics. In Ch. 3, we present a theoretical model for Rabi coherence that integrates the effects of strong driving. This model enabled us to correlate subtle characteristics of the time-dependent Rabi signal with specific vapor cell parameters, such as vapor cell temperature and buffer gas pressure. These findings were consistent with independent vapor cell calibrations. Also in Ch. 3, we detail our model for Rabi oscillation frequencies that account for the full atom-microwave coupling in the multi-level $^{87}$Rb structure. This framework enables us to make accurate measurements of Rabi frequencies by accounting for frequency shifts in the atomic hyperfine structure arising from off-resonant driving, nonlinear Zeeman effects, and buffer gas collisions.

In evaluating the accuracy of our Rabi measurements, we compared the magnetic field strengths derived from Rabi resonances with those obtained from FID measurements. This study is described in Ch. 4. The magnetic field strengths in our study were determined from the detuning-dependence of Rabi frequency measurements across four hyperfine transitions. By the fact that Rabi measurements only drive a pair of Zeeman sublevels, it would not suffer from the NLZ heading errors found in standard alkali OPMs. Across random magnetic field orientations, we measured consistent magnetic field strengths near 50 $\mu$T to within 0.3 nT by using microwave fields with three distinct polarization ellipse structures. The consistency achieved in our results implies that our measurements could be more accurate than FID measurements, which are estimated to exhibit heading errors of about 5 nT.

To further assess the accuracy of our magnetic field strength measurements, we implemented a Ramsey interferometry sequence to also probe multiple hyperfine transitions. However, the spin-polarization induced by our optical pumping process led to Larmor precession during the Ramsey sequence, significantly degrading the Ramsey fringe signal and impacting measurement accuracy. To overcome this limitation, we introduced an adiabatic optical pumping method. This involved gradually decreasing the pumping power to align the spin polarization with the magnetic field. The results showed that the magnetic field strengths determined by both Rabi and Ramsey methods were in agreement to within 0.6 nT. Theoretical simulations that assume parameters similar to our experimental conditions indicated systematic errors on the scale of 0.4 nT. The primary systematic influences identified in these simulations were the frequency dependence of microwave cavity modes and spin-exchange frequency shifts. These findings imply that both Rabi and Ramsey spectroscopy techniques could be effectively used to detect and correct heading errors in OPM measurements to the sub-nT level.

To conduct full vector magnetometry, we employed Rabi measurements over four hyperfine transitions, driven by microwave fields with three different MPEs. Although it wasn't the precise vector protocol, the consistency between scalar measurements obtained from Rabi measurements of multiple MPEs bolstered our confidence in the accuracy of our Rabi frequency modeling for application towards accurate vector detection. In contrast to the original cold atom experiment that utilized only one MPE, using multiple MPEs enabled detection of a unique magnetic field direction and enhances the vector sensitivity. One significant challenge we faced was temperature fluctuations in the microwave cavity, leading to drifts in the microwave cavity modes. These drifts limited our ability to know the exact microwave structure during these Rabi measurements. To mitigate this, we employed running MPE calibrations throughout our vector evaluations. These calibrations faced limitations due to the required deadtime in our apparatus, needed both for the electrical heaters to achieve stable cavity temperatures and for the dissipation of eddy currents resulting from rotations of the magnetic field. This approach demonstrated sub-milliradian (0.46 mrad) vector accuracy and vector sensitivities as low as 10 $\mu$rad/$\sqrt{\text{Hz}}$. From these vector evaluations, we also found that the Rabi measurements contain information beyond the DC magnetic field direction that could be used to identity MPE drift in our system without recalibration. These vector accuracy evaluations were made by comparing to our coil system calibration, which we estimate programs magnetic field orientations with 50 $\mu$rad accuracy. We discuss details behind potential systematic errors that currently limit our accuracy to the order of a few hundred microradian, which could be mitigated in future experimental designs.

Also discussed in Ch. 5, is how to extract Rabi frequencies from resonances occuring during simultaneous spin precession and Rabi driving (SPaR). The amplitude of these resonances are maximal at the probe deadzone of Rabi oscillations measurements; an artifact of using a single optical axis. We develop a full model for these resonances and use them to measure magnetic fields with a mean accuracy of 4.3 mrad and vector sensitivities reaching 100 $\mu$rad/$\sqrt{\text{Hz}}$ within the Rabi probing deadzone. While the SPaR measurements show inferior performance to the Rabi oscillation measurements, they perform with accuracies similar to that achieved by other atomic vector magnetometry techniques [87, 120, 199].

We also found that the probing deadzones of the Rabi oscillations can be advantageously used to determine the attitude of our probe beam within the intrinsic magnetometer frame defined by our coil system. The approach, Rabi Amplitude Nulling to determine the Beam attitude (RANBA), addresses the challenge of accurately monitoring drifts in the intrinsic magnetometer frame's orientation that cannot be detected in scalar calibration algorithms [66]. This is a common issue in vector magnetometry that affects absolute accuracy and consistency between multiple vector OPMs. The RANBA technique, as discussed in Ch. 6, could also be useful for aligning a vector gradiometer referenced to a single probe beam. Using the same data set to demonstrate Rabi vector magnetometry in Ch. 5, we use RANBA to determine the attitude of our probe beam with an overall precision of 0.014° (95% confidence). Through both theoretical analysis and experimental validation, we show that RANBA reaches its peak accuracy with Rabi oscillations driven on $\pi$ hyperfine transitions. Theoretical evaluations indicate that, under realistic experimental scenarios, the accuracy can be estimated to fall within 50 $\mu$rad (0.003°). This method not only provides a solution for monitoring drifts in the magnetometer frame but also facilitates calibration relative to external coordinate frames defined by nearby physical objects.

In Ch. 7 I discuss plans to implement Rabi magnetometry with a dielectric resonator that removes the Eddy currents present in our existing metal cavity, and through continuous laser heating, would also eliminate the deadtime arising from using electrical heaters. Such features would enable a more stable microwave setup. In addition, I discuss how the Rabi concept discussed in this thesis could be generalized to a radio-frequency platform to drive Zeeman transition within the hyperfine manifolds. Such a design holds promise for recalibration without sensor or bias field rotations that currently cause mechanical complexity in high accuracy vector OPMs.

## 1.3 Thesis outline

The thesis is structured as follows

- Ch. 2 details the key components of our apparatus to measure both free induction decay (FID) and Rabi oscillations across multiple hyperfine transitions.
- Ch. 3 discusses details behind modeling Rabi oscillations in a microfabricated vapor cell. We then compare this theoretical model with actual experimental Rabi oscillations, showcasing our ability to deduce vapor cell parameters that align with independent calibrations. The

significance of this chapter lies in its contribution to precise modeling of Rabi rates and enhancing our comprehension of the sensitivity limits.

- Ch. 4 describes an experiment utilizing Rabi oscillations and Ramsey interferometry as two separate methodologies for hyperfine spectroscopy, enabling accurate scalar magnetometry within geomagnetic fields. This chapter highlights our capability to rectify heading errors typically found in standard optically pumped magnetometer (OPM) measurements. Through our approach, we achieve scalar accuracies within 0.6 nT. This result is about ten times better than those of standard OPM techniques with heading errors around 5-10 nT.

- Ch. 5 discusses our implementation of Rabi oscillations to map the full magnetic field vector and a discussion of systematic errors in our apparatus. We also show SPaR vector measurements in the probing deadzone of Rabi oscillation measurements.

- Ch. 6 discusses implementation of the RANBA technique to determine the attitude of our probe beam with respect to the intrinsic magnetometer frame defined by our coil system with a precision of 0.014° (95% confidence). This chapter uses the same Rabi measurements used in Ch. 5. This chapter also discusses potential systematic errors of the RANBA technique and how these errors could be mitigated to within 50 $\mu$rad accuracy under realistic experimental conditions.

- Ch. 7 discusses future paths for the Rabi concepts presented in this thesis. These include implementation of a microwave dielectric resonator, an RF Rabi magnetometer, vector recalibration with Rabi measurements without sensor or bias field rotation, and ideas to test the accuracy of our Rabi measurements against Rydberg sensors.

## 1.4 Publications and Talks Related to This Thesis

I started my PhD working for nearly two years on cold atoms in optical tweezers where I gained substantial knowledge about the atomic physics underpinning single-atom trapping and detection, working with high NA optics, and contributed to efficient single-atom loading experiments using gray molasses that led to my co-authorship on [37]. I also gave technical assistance to the Rabi vector magnetometry experiment that was happening right when I joined Cindy's lab. During that time we were interested to learn whether this concept could be realized in thermal atomic vapor. I along with Tobias Thiele over about a year set up this experiment from scratch with microfabricated cells and collaboration with Svenja Knappe. Once we showed successful vapor cell Rabi oscillations I wanted to see how far this concept could go. In the work described above, I have interacted with the OPM community in a number of ways, receiving valuable feedback at multiple conferences. These include the WE-Heraeus workshop on quantum sensing and metrology, DAMOP, the Q-SEnSE community, GRC (invited talk at GRS), and WOPM. This work has been written up thus far in the following manuscripts:

- **C. Kiehl**, D. Wagner, T.-W. Hsu, S. Knappe, C. A. Regal, and T. Thiele, "Coherence of Rabi oscillations with spin exchange", Phys. Rev. Research 5, L012002 (2023)
- **C. Kiehl**, T. S. Menon, S. Knappe, T. Thiele, and C. A. Regal, "Correcting heading errors in optically pumped magnetometers through microwave interrogation", arXiv:2310.11017 (2023)
- **C. Kiehl**, T. S. Menon, S. Knappe, T. Thiele, and C. A. Regal, "A Rabi vector optically pumped magnetometer referenced to multiple microwave polarization ellipses" (unpublished)

# Chapter 2

## Apparatus for Rabi magnetometry

In this chapter, I provide an overview of the essential components of our apparatus (Fig. 2.1) used for implementing Rabi magnetometry within a vapor cell platform. The design was guided by several key objectives, which included

- Full magnetic field control up to magnetic field strengths of 100 $\mu$T with good spatial uniformity in a quiet magnetic environment
- Optical pumping suitable for detection of both FID and hyperfine Rabi oscillations
- A spatially uniform microwave field with 2D polarization ellipse control
- Nondestructive state detection for continuous high accuracy Rabi oscillation measurements
- Uniform vapor cell heating that does not degrade the microwave field at the cell

Our apparatus, designed to fulfill these objectives, features several key components as illustrated in Fig. 2.2(a): a microfabricated vapor cell, a copper rectangular microwave cavity capable of generating an arbitrarily-shaped microwave polarization ellipse (MPE), and a 3D coil system composed of nearly orthogonal pairs of saddle and Helmholtz coils. This MPE is formed in a plane perpendicular to the optical axis at the location of the atoms by stimulating two linearly-polarized cavity modes. To create a magnetically quiet environment, all components were enclosed within a three-layer mu-metal shield produced by Magnetic Shield Corporation. This shield, initially without optical access at one end, required precise drilling by the JILA machine. Concerns about

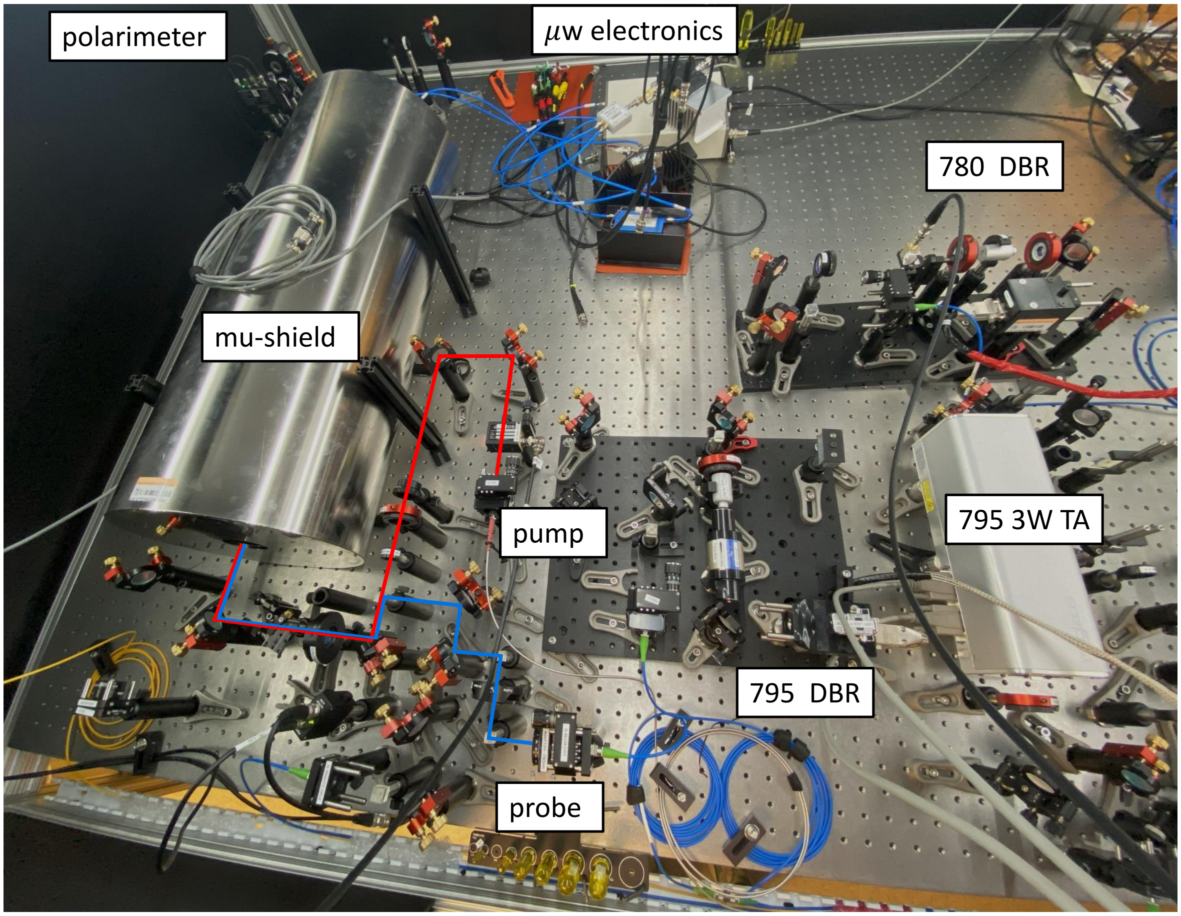


Figure 2.1: Photograph of experiment circa 2023.

reduced magnetic shielding effectiveness along the optical axis, due to these modifications, led us to orient the shield perpendicular to the Earth's magnetic field. In this configuration the measured DC background field inside the shield was around 100 nT (Sec. 2.4.1). To accommodate the wiring for cell heating and the semi-rigid coaxial cables needed for microwave delivery, we operated the shield with one of its end caps removed. With the end cap off, we recorded background magnetic fluctuations at the one nT level using FID measurements, noting only a marginal improvement when the endcap was attached.

For state-preparation and detection, we use a 795 nm elliptically polarized pump beam that is near-resonant with the $D_1$ line and a 780 nm probe beam that is far-detuned from the $D_2$ line, both propagating along a single optical axis ($\hat{z}$ in Fig. 2.2(a)). The subsequent sections provide details on the optical pumping and Faraday rotation of the probe beam employed for non-destructive detection of atomic spin dynamics, along with detailed descriptions and characterizations of the MEMS cell, coil system, and microwave cavity. The chapter concludes by outlining general measurement protocols for achieving stable Rabi oscillations when integrating all these components.

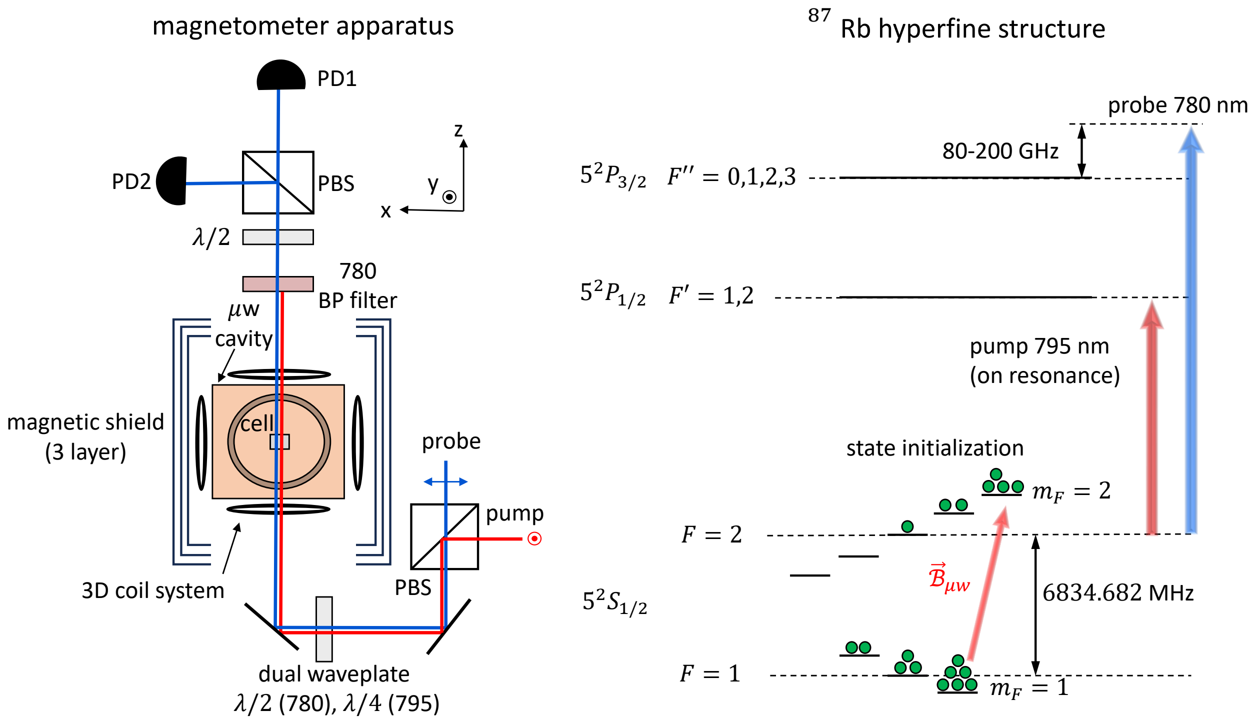


Figure 2.2: Schematic of apparatus and optical scheme. (a) A schematic of our experimental apparatus that includes the key components pictured in Fig. 2.1. (b) $^{87}$Rb energy level diagram of the ground $5^2S_{1/2}$ and excited $5^2P$ states utilized in our experiment. Throughout the measurements in this thesis the probe beam is blue detuned between 80 GHz to 170 GHz from the $D_2$ line. The pump beam is within a few GHz of the $D_1$ line.

## 2.1 The microfabricated cell

To mitigate the effects of microwave spatial inhomogeneity arising from the cavity modes, we utilize a $3 \times 3 \times 2$ mm$^3$ microfabricated vapor cell (Fig. 2.3(a)) to ensure a compact measurement volume. Additionally, given the particular difficulty in mitigating heading error challenges in OPMs when using MEMS cells, our application of a microfabricated cell aims to showcase the effectiveness of Rabi oscillation measurements in addressing these challenges, as detailed in Ch. 4. This vapor cell is heated to near $T_v = 100°$C to supply a high enough atom number density necessary for sensitive measurements (Eq. (1.2)). This number density $n_{\mathrm{Rb}} = P_v(T_v)/kT_v$ is determined by the $^{87}$Rb vapor pressure expressed in Torr units as [168]

$$P_v(T_v) = 10^{(15.88253 - 4529.635/T_v + 0.00058663 T_v - 2.99138 \mathrm{Log10}(T_v))}. \tag{2.1}$$

Practically, the optimal atomic density for measurement sensitivity is determined by a balance between the atomic signal gained and the increase in collisional relaxation discussed in Ch. 3.

To mitigate wall collisions, a major source of spin relaxation in microfabricated cells, we use $N_2$ buffer gas to reduce the mean free path $l_m$ of rubidium atoms given by [176]

$$l_m = v t_d = v \frac{m_{\mathrm{Rb}} D_0}{k_B T_v} \frac{P_1}{P_{\mathrm{N}_2}} \tag{2.2}$$

where $v$ and $m_{\mathrm{Rb}}$ is the average speed and atomic mass of a single Rb atom, $t_d$ is the mean time between Rb atom collisions, and $D_0$ is a diffusion constant, $P_1 = 1$ atm (760 Torr), and $P_{\mathrm{N}_2} \approx 180$ torr is the nitrogen buffer gas pressure for our cell. This cell is utilized for all experiments in this thesis, with the exception of the measurements described in Ch. 7. For the vapor parameters tabulated in Table 3.3 of Ch. 3, $l_m \approx 700$ nm. These Rb-$\mathrm{N}_2$ collisions have minimal impact on atoms in the ground $5^2\mathrm{S}_{1/2}$ states, but lead to rapid collisional mixing for atoms excited to the $5^2$P states. This mixing leads to the broadening of optical transitions by several GHz, significantly surpassing the natural linewidth of $\gamma_{\mathrm{nat}} \approx 6$ MHz arising from spontaneous emission. Additionally, buffer gas collisions induce quenching, where $\mathrm{N}_2$ atoms facilitate de-excitation of excited Rb atoms by absorbing their energy into vibrational and rotational molecular modes [74]. In our experiment, the quenching rate is of the order of a few GHz, meaning that Rb atoms are seldom de-excited through spontaneous emission. Quenching is advantageous for achieving efficient optical pumping, as spontaneous emission can degrade the polarization of the pump beam. In the subsequent subsections, we detail characterizations performed to estimate the nitrogen buffer gas pressure in our cell, which is essential for evaluating quenching and wall collision rates. We also discuss an optical cavity effect observed between uncoated walls of our cell.

### 2.1.1 Buffer gas characterization from $D_1$ optical frequency shift and broadening

A well-known method for determining buffer gas pressures involves measuring the frequency shift and optical broadening of the $D_1$ line, then comparing these observations with known calibrated shifts and linewidths associated with specific buffer gas pressures [125, 149, 151]. For this measurement, we employed a 795 nm VCSEL to examine the $D_1$ optical spectrum through our heated microfabricated cell, alongside a glass cell without buffer gas that serves as an optical frequency reference. To reduce power broadening, the VCSEL power passing through the microfabricated cell was attenuated to 6.8 $\mu$W (with a beam waist of approximately 2 mm). Further reduction of the beam power to 0.7 $\mu$W was found to have negligible impact on the optical broadening. A diagram of the experimental setup is presented in Fig. 2.3(b).

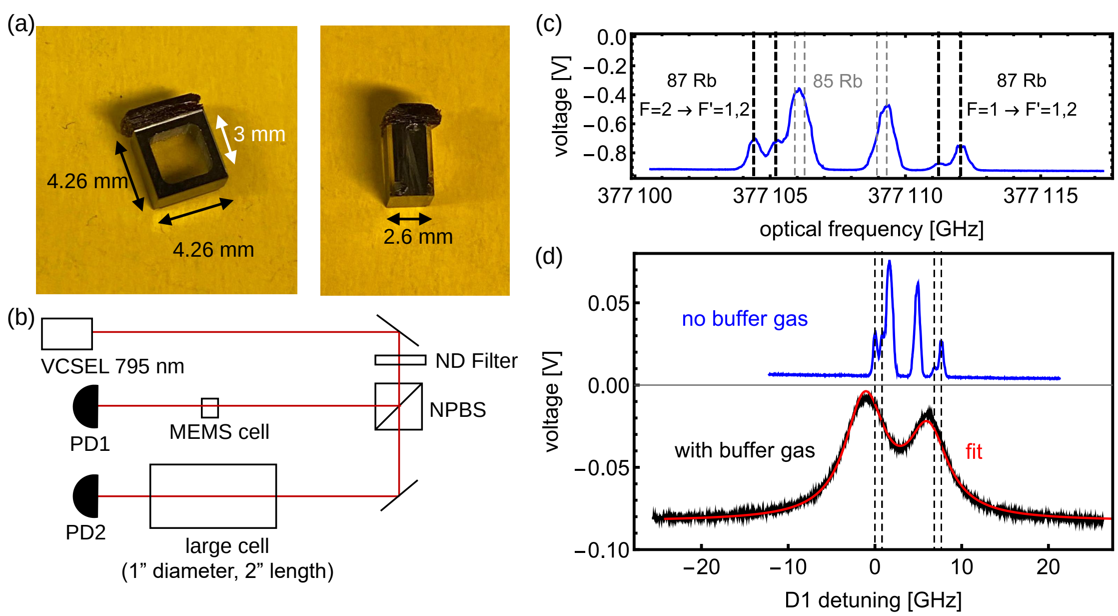


Figure 2.3: Optical measurement of the $D_1$ frequency shift and broadening. (a) The microfabricated vapor cell used in this thesis. The material on top of the cell pictured here is layers of kapton tape used to secure this cell into the cell holder pictured in Fig. 2.12(c). (b) Schematic of the apparatus to measure the $D_1$ optical spectrum from the microfabricated cell with respect to a large cell with no buffer gas inside. (c) The $D_1$ optical spectrum with hyperfine transitions marked by dashed lines. (d) The broadened $D_1$ optical spectrum of the microfabricated cell.

A linear triangle frequency ramp sweeps the VCSEL optical frequency by changing its temperature. From the transmission through the large cell, the $^{87}$Rb and $^{85}$Rb transitions are resolved to calibrate the optical frequency, as shown in Fig 2.3(c,d), by fitting a Lorentizian lineshape

$$L(f, f_{0,F,F'}, A_{F,F'}, \Gamma) = A_{F,F'} \frac{\Gamma/2}{(f - f_{0,F,F'})^2 + (\Gamma/2)^2} + \mathrm{off} \tag{2.3}$$

to each of the four $^{87}$Rb resonances, where $f_{0,F,F'}$, $A_{F,F'}$, and $\Gamma$ are fitting parameters for the resonant frequency, amplitude, and a common width for each resonance. We also include an offset due to bias on the photodiode. Here $F, F'$ denotes the specific fitted parameter for the $F \rightarrow F'$ transition. In retrospect, given that the broadening of these resonances is primarily a result of Doppler shifts, a Gaussian or Voigt fit would have been more appropriate than a Lorentzian fit. However, the systematic errors stemming from this fitting discrepancy are sufficiently small to be deemed inconsequential for our analysis.

To fit the pressure-broadened D1 spectrum in the microfabricated cell we use the following fitting function

$$A_0 \sum_{F,F'=1}^{F,F'=2} L(f, f_{0,F,F'} + f_{\mathrm{N}_2}, A_{F,F'}, \Gamma_{\mathrm{N}_2}) + B_0 f + \mathrm{off} \tag{2.4}$$

where $A_{F,F'}$ and $f_{0,F,F'}$ are the fitted amplitudes and frequencies from the spectrum with no buffer gas. The only fitting parameters here are $A_0$, $B_0$, off, $f_{\mathrm{N}_2} = 1.08$ GHz and $\Gamma_{\mathrm{N}_2} = 5.56$ GHz. In this case a Lorentzian fit is predicted to well-approximate pressure broadening since $\Gamma_{\mathrm{N}_2}$ GHz is much larger than the expected Doppler broadening given by [176]

$$\Delta^{(D)}_{FWHM} = \sqrt{\frac{8 k_B T_v \ln(2)}{m_{\mathrm{Rb}} c^2}} f_{0,F,F'} = 0.56 \text{ GHz} \tag{2.5}$$

In addition, Doppler broadening is expected to be partially diminished from Dicke narrowing with our small mean free path $l_m$ [53, 176].

The $\mathrm{N}_2$ pressure broadening and shift are given by [149] $f_{\mathrm{N}_2} = \alpha n_{\mathrm{N}_2}$ and $\Gamma_{\mathrm{N}_2} = \alpha' n_{\mathrm{N}_2}$, where $\alpha = 17.8 \pm 0.3$ GHz/amg, $\alpha' = -8.25 \pm 0.15$ GHz/amg, and $n_{\mathrm{N}_2} = \frac{\mathrm{P}_{\mathrm{N}_2}}{44.615 N_A k_B T}$ is the buffer gas density in amg units using Avogadro's number $N_A$. From the fitted values for $f_{\mathrm{N}_2}$ and $\Gamma_{\mathrm{N}_2}$, we obtain $\mathrm{P}_{\mathrm{N}_2} = 182 \pm 4$ Torr and $\mathrm{P}_{\mathrm{N}_2} = 332 \pm 4$ Torr respectively. We suspect that part of the discrepancy between these buffer-gas pressures is due to the contamination of hydrocarbons during the in-house manufacturing of the vapor cell. In this case, the extracted $N_2$ buffer-gas pressure could vary between independent measurements since hydrocarbon molecules do not have the same frequency shifts and broadening coefficients ($\alpha$,$\alpha'$) as $N_2$. For example, the $D_1$ optical broadening coefficient for $CH_4$ is nearly twice as large as the broadening coefficient for $N_2$, while the $D_1$ frequency-shift coefficients are nearly equal [151]. The biggest impact on Rabi coherence from unknown hydrocarbon contamination would be a perturbation to the expected wall-collision rate.

### 2.1.2 Buffer gas characterization from the shift in the ground state hyperfine splitting

Perturbations to the alkali electron clouds from Rb-$N_2$ collisions cause a variation of the hyperfine coupling constant $\delta A_{\text{hfs}}\mathbf{S}\cdot\mathbf{I}$, which results in a frequency shift to the hyperfine splitting given by [176]

$$\delta\nu_{\text{hfs}} = \mathrm{P}_0\nu_{\text{hfs}}\big[\beta_0 + \delta_0(\mathcal{T}_v - \mathcal{T}_{v,0}) + O(\mathcal{T}_v^2)\big] \tag{2.6}$$

where $\nu_{\text{hfs}} \approx 6.8$ GHz is the unperturbed hyperfine splitting and $\mathrm{P}_0 = n_{\mathrm{N}_2}k_B\mathcal{T}_{v,0}$ is the buffer-gas pressure at reference temperature $\mathcal{T}_{v,0}$. For $^{87}$Rb with $N_2$ buffer gas measured at reference temperature $\mathcal{T}_{v,0} = 60\ ^\circ$ C [125]

$$\beta_0/\nu_{\text{hfs}} = 81.9 \pm 1.2 \times 10^{-9}\ \text{Torr}^{-1} \tag{2.7}$$

$$\delta_0/\nu_{\text{hfs}} = 79 \pm 2 \times 10^{-12}\ ^\circ\text{C}^{-1}\ \text{Torr}^{-1} \tag{2.8}$$

The actual buffer gas pressure for temperature $\mathcal{T}_v$ is $\mathrm{P}_{N_2} = n_{\mathrm{N}_2}k_B\mathcal{T}_v = \mathrm{P}_0\frac{\mathcal{T}_v}{\mathcal{T}_{v,0}}$. Thus,

$$\mathrm{P}_{N_2} = \frac{1}{\nu_{\text{hfs}}}\frac{\mathcal{T}_v}{\mathcal{T}_{v,0}}\frac{\delta\nu_{\text{hfs}}}{\beta_0 + \delta_0(\mathcal{T}_v - \mathcal{T}_{v,0})} \tag{2.9}$$

A fitted frequency shift $\delta\nu_{\text{hfs}} = 87.22$ kHz (Fig. 3.9 in Ch. 3) implies $\mathrm{P}_{\mathrm{N}_2} = 168$ Torr at $\mathcal{T}_v = 373.15$ Kelvin.

### 2.1.3 Optical cavity from cell windows

During initial characterizations of the vapor cell, we noticed significant fluctuations in the transmission of the pump and probe beam during cell heating. We hypothesized that this effect is due to a Fabry-perot created by the uncoated cell windows. To test this idea, we setup the the layout in Fig. 2.4(a) to measure the transmission through the microfabricated vapor cell with 850 nm light. We chose the 850 nm optical wavelength to avoid light scattering with the rubdium vapor. The cell was heated with a hot plate, whose temperature was monitored by a thermocouple. Fig. 2.4(b) shows the transmission of the 850 nm beam passing through the cell as a function of the thermocouple temperature. During a temperature increase of 60°C, we observed a transmission fringe consistent with the thermal expansion (CTE $= 2.6 \times 10^{-6}$ K$^{-1}$ [133]) of the silicon body of the cell. The phenomenon can be described by

$$CTE \times (60^{\circ}\ \mathrm{K}) \times L = \frac{\lambda}{2} \tag{2.10}$$

With $\lambda = 850$ nm, this formula suggests a silicon thickness of $L = 2.7$ mm, which is in proximity to our actual silicon thickness of 2.6 mm. These results imply that the Fabry-Perot effect is a probable explanation for the observed transmission dependence.

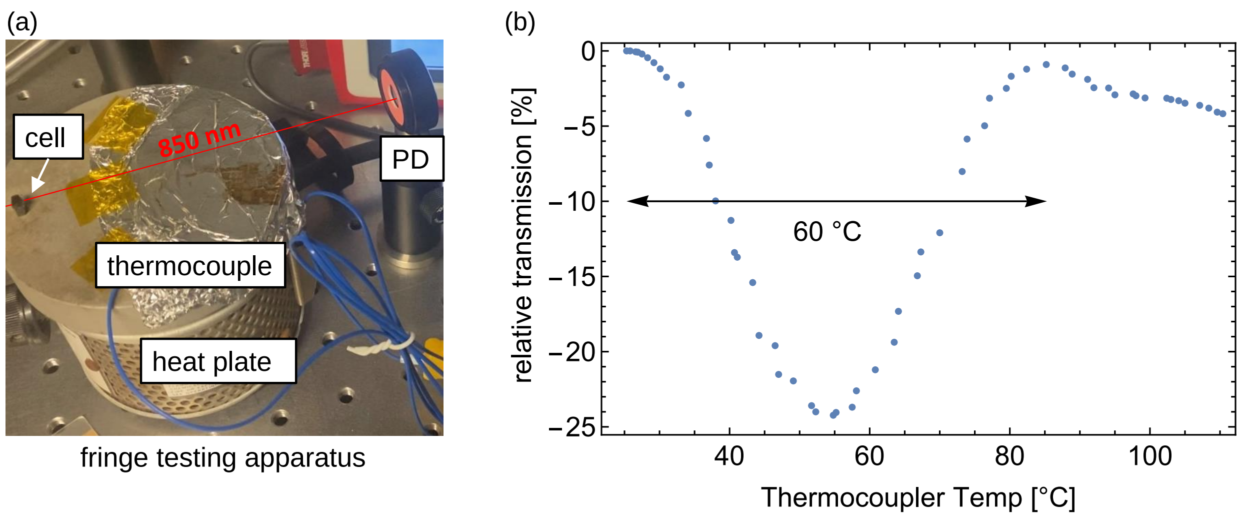


Figure 2.4: Measurement of Fabry-Perot created by the uncoated cell walls. (a) Apparatus consisting of the cell resting on a hot plate. A thermocouple monitors the hot plate temperature. (b) Transmission of 850 nm through the cell as a function of the thermocouple temperature.

## 2.2 Optical pumping

Optical pumping is a key feature of this experiment to optimally prepare the atomic state for FID and Rabi measurements. For FID detection, the signal is proportional to the electron spin $\langle S_z \rangle$ along the probe optical axis. On the other hand, Rabi measurements depend on the population imbalance between the hyperfine manifolds, and do not necessarily require high spin polarization. To achieve high spin polarization we use circularly polarized $\sigma^+$ $D_1$ light shown in Fig. 2.5. Photons are iteratively absorbed by ground state atoms in the $F = 1, 2$ manifolds until ending in the $|2, 2\rangle$ stretched state, which is dark to $\sigma^+$ photons [see Fig. 2.5]. Due to the 5.6 GHz optical broadening ($\Gamma_{N_2}$) arising from the $N_2$ buffer gas collisions, the $D_1$ pump beam alone is sufficient to excite atoms from both ground hyperfine manifolds. The source of our pumping light is a 795 nm tapered amplifier from Moglabs seeded by a Photodigm DBR [see Fig. 2.1]. After fiber coupling, passing through an AOM and several optical elements, we are able to supply up to 500 mW of pump light to the microfabricated cell. The circular polarization is controlled using a dual wavelength waveplate [see Fig. 2.2(a)] from OptiSource that acts as a $\lambda/4$ for 795 nm light and $\lambda/2$ for 780 nm light.

To describe the optical pumping process, we first consider a simpler level structure by ignoring the nuclear spin and considering the $m_J = \pm 1/2$ states shown in Fig. 2.5. A more thorough discussion on optical pumping can be found in references [159] and [74]. The probability that an atom starting in the ground $m_J = -1/2$ state absorbs a $\sigma^+$ photon to the excited $m_{J'} = 1/2$, and decays to the $m_J = 1/2$ ground state is called the optical pumping efficiency $a$. Without buffer gas, dexcitation occurs from spontaneous emission. In this case, the decay branching ratios are proportional to [159]

$$B^+_\pm \propto |\langle m_J = \pm 1/2| \, e\mathbf{r} \, |m_{J'} = 1/2\rangle|^2 \tag{2.11}$$

which predicts a 2/3 probability of decaying to $|m_J = -1/2\rangle$ and 1/3 probability of decaying to $|m_J = 1/2\rangle$, implying the optical pumping efficiency is $a = 1/3$. Including a buffer gas, like $N_2$, causes collisional mixing among the $5P_{1/2}$ excited states such that an excited atom has equal probability of decaying to either $m_J = \pm 1/2$. In this case, the optical pumping efficiency is increased to $a = 1/2$. In terms of a photon absorption rate $R$, the rate of change of the atomic populations in the $m_J = \pm 1/2$ ($\rho_\pm$) states is governed by [159]

$$\dot{\rho}_- = -(1+s)R\rho_- + (1-a)(1+s)R\rho_- + a(1-s)R\rho_+ \tag{2.12}$$

$$\dot{\rho}_+ = -(1-s)R\rho_+ + (1-a)(1-s)R\rho_+ + a(1+s)R\rho_- \tag{2.13}$$

where the average photon spin $s = \mathbf{s} \cdot \hat{z}$ along the pumping axis is defined in terms of the pump polarization $\boldsymbol{\epsilon}$ given by

$$\mathbf{s} = i\boldsymbol{\epsilon} \times \boldsymbol{\epsilon}^\star. \tag{2.14}$$

These rate equations can be expressed in terms of the electron spin through

$$\langle S_z \rangle = \frac{1}{2}(\rho_+ - \rho_-). \tag{2.15}$$

Assuming $a = 1/2$, the electron spin dynamics during optical pumping with a magnetic field $\mathbf{B}$ is given by

$$\dot{\mathbf{S}} = \gamma \mathbf{B} \times \mathbf{S} + \frac{1}{q}\Big[R\Big(\frac{1}{2}s\hat{z} - \mathbf{S}\Big) - \Gamma_{\mathrm{rel}}\mathbf{S}\Big]. \tag{2.16}$$

A phenomenological spin relaxation term with rate $\Gamma_{\mathrm{rel}}$ is included due to relaxation from atomic collisions that tends to equilibrate the atomic populations in the ground $m_J = \pm 1/2$ states [see Fig.2.5].

To account for the influence of the nuclear spin, included in Eq. 2.16 is a nuclear slowing down factor that depends on the electron spin polarization $0 \leq P \leq 1$ through [159]

$$q = \frac{6 + 2P^2}{1 + P^2}. \tag{2.17}$$

Eq.!2.17 is only valid for the $I = 3/2$ nuclear spin of $^{87}$Rb. At high spin-polarizations ($P \approx 1$), $q = 2I + 1$. The gyromagnetic ratio $\gamma_e \approx 28$ kHz per $\mu$T is diminished due to nuclear spin coupling to the value

$$\gamma = \frac{\gamma_e}{2I + 1} \approx 7 \text{ kHz}. \tag{2.18}$$

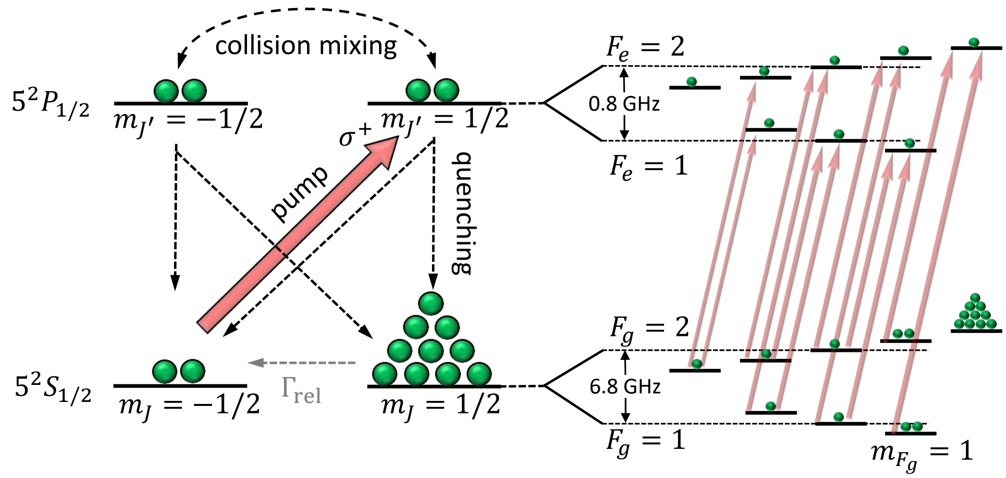


Figure 2.5: (left) Schematic of optical pumping the electron spin with $D_1$ circularly polarized light adapted from Ref. [159]. An atom in $m_J = -1/2$ may absorb a $\sigma^+$ photon to excite into $m_{J'} = 1/2$. Collision mixing from buffer gas collisions rapidly randomizes the excited state populations such there is equal probability for the excited state to decay to either $m_J = \pm 1/2$. Atoms that decay into $m_J = 1/2$ accumulate since they are dark to a $\sigma^+$ photon. Spin relaxation $\Gamma_{\rm rel}$ causes redistribution in the ground states and limits the optical pumping efficiency. (right) $\sigma^+$ optical pumping between the hyperfine manifolds. The $\Gamma_{N_2} = 5.6$ GHz optical broadening enables the pump beam to excite both $F_g = 1, 2$ manifolds.

When the magnetic field is aligned with the pump beam, Eq. (2.16) predicts a build up of electron spin according to [159]

$$\langle S_z \rangle(t) = \frac{sR}{2(R + \Gamma_{\rm rel})}(1 - e^{-(R+\Gamma_{\rm rel})t}). \tag{2.19}$$

Due to the strong coupling between the electron and nuclear spins, the polarization of the electron spin will also polarize the total spin $\langle F_z \rangle$. In Ch. 3, we utilize $\sigma^+$ light such that the above analysis is a close approximation.

In Ch. 4 and Ch. 5 we exploit the partial resolution of the hyperfine manifolds [see Fig. 2.3(d)] to preferentially populate the $F = 1$ manifold over the $F = 2$ using elliptically polarized light so that Rabi oscillations across all hyperfine transitions can be observed. In this case, it is important to account for the optical resolution of the hyperfine splitting in the ground states. Furthermore, it is important to account for relaxation mechanisms, such as spin-exchange collisions, that have nuanced behavior not accounted for in the phenomenological $\Gamma_{\rm rel}$ term in Eq. 2.19. We present a more exact optical pumping model including all 16 ground and excited states [see Fig. 2.5] in Ch. 4.

### 2.2.1 Adiabatic optical pumping

We also utilize a novel form of optical pumping that involves adiabatically ramping off the pump power such that the atomic spin aligns with the magnetic field $\mathbf{B}$. As a result, no Larmor spin precession can occur. This is useful for driving Rabi oscillations in arbitrary magnetic field directions where residual Larmor precession can degrade the Rabi signal.

To understand this spin-alignment with the magnetic field we consider a simpler model stated in Eq. (2.16) for optical pumping without relaxation and the slowing down factor for simplicity

$$\dot{\mathbf{S}} = \gamma \mathbf{B} \times \mathbf{S} + R\Big(\frac{1}{2}s\hat{z} - \mathbf{S}\Big), \tag{2.20}$$

where we assume that the magnetic field $\mathbf{B} = \{B_x, 0, B_z\}$ lies in the $xz$-plane. In steady-state pumping $\dot{\mathbf{S}} = 0$, and we can write

$$\gamma(-B_x S_z \hat{y} + B_x S_y \hat{z} + B_z S_x \hat{y} - B_z S_y \hat{x}) + R(\frac{1}{2}s\hat{z} - \mathbf{S}) = 0. \tag{2.21}$$

Breaking Eq. 2.21 into each vector component gives

$$\begin{aligned} \hat{x}&: \quad -\gamma B_z S_y - R S_x = 0 \\ \hat{y}&: \quad -\gamma (B_x S_z - B_z S_x) - R S_x = 0 \\ \hat{z}&: \quad \gamma B_x S_y + R(\frac{s}{2} - S_z) = 0. \end{aligned} \tag{2.22}$$

The $\hat{x}$-equation implies $S_y = -RS_x/\gamma B_x$. Thus, if $R \to 0$ adiabatically, then $S_y \to 0$. In this limit, the $\hat{y}$-equation predicts $B_z/B_x = S_z/S_x$. Thus, the atomic spin $\mathbf{S}$ will align with the magnetic field $\mathbf{B}$ assuming the pump rate $R$ adiabatically turns off. We also simulate this process with a full optical pumping model in Ch. 4 that incorporates all 16 hyperfine states in the ground and excited state manifolds.

## 2.3 Detecting spin dynamics with Faraday rotation

We nondestructively measure spin dynamics occuring during Rabi oscillations and FID spin precession measurements through the Faraday rotation of the linearly-polarized probe beam [see

Fig. 2.2(b)] that is far-detuned from the $D_2$ line. Faraday rotation refers to the rotation of the polarization of the probe light as it passes through the atomic vapor. This rotation is detected with a polarimeter [see Fig. 2.2(a)] where two photodiodes individually measure the horizontal and vertical components of the probe polarization. The Faraday rotation angle is calculated from these photodiode signals, $P_1$ and $P_2$ as

$$\theta_F = \frac{1}{2}\sin^{-1}\Big(\frac{P_2 - P_1}{P_1 + P_2}\Big). \tag{2.23}$$

### 2.3.1 Theoretical derivation

Faraday rotation of linearly-polarized light passing through atomic vapor is given by [159]

$$\theta_F = \frac{\pi\nu l}{c}(n_+(\nu) - n_-(\nu)) \tag{2.24}$$

where $l$ is the propagation length and $n_\pm(\nu)$ is the index of refraction for circularly-polarized light at optical frequency $\nu$. Faraday rotation arises in spin-polarized atomic vapors due to birefringence birefringence $n_+(\nu) \neq n_-(\nu)$. This birefringence can be expressed through the bulk atomic polarizability [56]

$$n_\pm(\nu) = \sqrt{1 + \alpha^\pm(\nu)} \approx 1 + \frac{1}{2}\alpha^\pm(\nu) \tag{2.25}$$

where the bulk atomic polarizability is expressed as

$$\alpha^\pm(\nu) = \sum_{F,m_F} \rho(F, m_F)\alpha^\pm_{F,m_F}(\nu) \tag{2.26}$$

that is weighted with the atomic populations $\rho(F, m_F)$ and $\alpha^\pm_{F,m_F}(\nu)$ is given by

$$\begin{aligned}\alpha^\pm_{F,m_F}(\nu) &= -\frac{n_{\mathrm{Rb}}}{\epsilon_0 h}\sum_{|F', m_F \pm 1\rangle} |\langle F, m_F| er |F', m_F \pm 1\rangle|^2 \times \mathcal{D}(\nu - \nu_{\mathrm{tr}}) \\ &\approx -\frac{n_{\mathrm{Rb}}}{\epsilon_0 h}\mathcal{D}(\nu - \nu_0)\sum_{|F', m_F \pm 1\rangle} |\langle F, m_F| er |F', m_F \pm 1\rangle|^2\end{aligned} \tag{2.27}$$

Here $\langle F, m_F| er |F', m_F \pm 1\rangle$ is the transition dipole matrix element for $\sigma^\pm$ optical transitions, $n_{\mathrm{Rb}}$ is the alkali atomic density, $\epsilon_0$ is the permitivity of free space, $\mathcal{D}(\nu-\nu_{\mathrm{tr}}) = (\nu-\nu_{\mathrm{tr}})/[(\nu-\nu_{\mathrm{tr}})^2+(\Gamma_0/2)^2]$ is a dispersive lineshape with FWHM $\Gamma_0$, and $\nu - \nu_{\mathrm{tr}}$ is the optical detuning for the transition

$\mathrm{tr} = |F, m_F\rangle \rightarrow |F', m_{F'}\rangle$. In Eq. (2.27), we assumed the case where the optical detuning is much larger than the optical linewidth such that $\nu - \nu_{\mathrm{tr}} \gg \Gamma_{\mathrm{D2}}$. In this case it is valid to assume approximate all atomic transitions by a single optical frequency $\nu_{\mathrm{D2}}$. The transition dipole matrix element is written as [168]

$$|\langle F, m_F| er_q |F', m_{F'}\rangle|^2 = |\langle F|| e\mathbf{r} ||F'\rangle|^2 \times (2F+1) \begin{pmatrix} F' & 1 & F \\ m'_F & m_F - m_{F'} & -m_F \end{pmatrix}^2 \tag{2.28}$$

where

$$|\langle F|| e\mathbf{r} ||F'\rangle|^2 = |\langle J|| e\mathbf{r} ||J'\rangle|^2 (2F'+1)(2J+1) \times \begin{Bmatrix} J & J' & 1 \\ F' & F & I \end{Bmatrix}^2 \tag{2.29}$$

and $|\langle J|| e\mathbf{r} ||J'\rangle|^2 = 3h\epsilon_0 r_e c^2 f_{\mathrm{osc}}/2\pi\nu_0$ with $r_e = 2.82 \times 10^{-15}$ m is the classical electron radius, $f_{osc}$ is the oscillator strength for the optical transition, and $\nu_0$ is the optical transition frequency.

Putting this all together gives

$$\begin{aligned} \theta_F = -\frac{3\nu c r_e f_{\mathrm{osc}} n_{\mathrm{Rb}} l}{4\nu_0} \mathcal{D}(\nu - \nu_{\mathrm{D2}}) \sum_{F,m_F} \rho(F, m_F)(2F+1) \sum_{F',m'_F} (2J+1)(2F'+1) \\ \times \begin{Bmatrix} J & J' & 1 \\ F' & F & I \end{Bmatrix}^2 \left[ \begin{pmatrix} F' & 1 & F \\ m_F+1 & -1 & -m_F \end{pmatrix}^2 - \begin{pmatrix} F' & 1 & F \\ m_F-1 & 1 & -m_F \end{pmatrix}^2 \right]. \end{aligned} \tag{2.30}$$

Then, for $^{87}$Rb atomic ensembles, with nuclear spin $I = 3/2$, prepared in specfic $|F, m_F\rangle$ states

$$\theta_F = \frac{c r_e f_{D1} n_{\mathrm{Rb}} l}{2I+1} \mathcal{D}(\nu - \nu_{D1}) \begin{cases} -m_F \ (\mathrm{F}=1) \\ +m_F \ (\mathrm{F}=2) \end{cases} \tag{2.31}$$

$$\theta_F = \frac{c r_e f_{D2} n_{\mathrm{Rb}} l}{2(2I+1)} \mathcal{D}(\nu - \nu_{D2}) \begin{cases} +m_F \ (\mathrm{F}=1) \\ -m_F \ (\mathrm{F}=2) \end{cases} \tag{2.32}$$

for $D_1$ and $D_2$ transitions respectively ($D_1$ case is consistent with Refs. [102, 162]). This implies that we may write for the $D_2$ case

$$\theta_F \propto \langle \mathcal{F} \rangle = \langle F_{z,b} - F_{z,a} \rangle \tag{2.33}$$

where $\langle F_{z,a}\rangle$ and $\langle F_{z,b}\rangle$ denote the expectation value of the z-component of the hyperfine spin for the $F = 1$ and $F = 2$ manifolds respectively. Note that $\langle \mathcal{F}\rangle \propto \langle S_z\rangle$. Here, off-diagonal elements of $S_z$ expressed in the hyperfine basis average to zero in the rotating wave approximation (Sec. 3.3).

### 2.3.2 Shot noise

Our detector noise is characterized by a standard deviation $\sigma_{\text{noise}} = 0.0043°$ measured over the duration of a typical Rabi oscillation [see Fig. 5.9(b)]. This detector noise is near the optical shot-noise limit characterized by the sensitivity [117]

$$S_{\theta_F,\text{shot}} = \frac{1}{2}\frac{1}{\sqrt{\dot{N}_{\text{ph}}}} \tag{2.34}$$

where $\dot{N}_{\text{ph}} = P/(hc/\lambda)$ is the number of photons in the probe beam per second and $P = 1$ mW is the probe optical power. Eq. 2.34 is derived from Eq. 2.23 by making the small-angle approximation and writing

$$\theta_F \approx \frac{1}{2}\frac{\dot{N}_{\text{ph},2} - \dot{N}_{\text{ph},1}}{\dot{N}_{\text{ph},1} + \dot{N}_{\text{ph},2}} \tag{2.35}$$

and assuming that each photodetector collects $\dot{N}_{\text{ph},i} = \dot{N}_{\text{ph}}/2$ photons per unit time with shot noise uncertainty $\sqrt{\dot{N}_{\text{ph}}/2}$. At our probe power, Eq. (2.34) predicts a standard deviation $\sigma_{\text{shot}} = S_{\theta_F,\text{shot}}\sqrt{f_s} = 0.0046°$ in the Faraday rotation signal, where $f_s = 10$ MHz is the detector sampling rate.

## 2.4 Magnetic field control

For full magnetic field control we use 3D coil system that consists of three near-orthogonal coil pairs that generate fields along coil directions $(\vec{x}_c, \vec{y}_c, \vec{z}_c)$ given in terms of coil currents $(I_x, I_y, I_z)$

$$\vec{B}_{x,c} = I_x a_x(1+\epsilon_x)\vec{x}_c \tag{2.36}$$

$$\vec{B}_{y,c} = I_y a_y(1+\epsilon_y)\vec{y}_c \tag{2.37}$$

$$\vec{B}_{z,c} = I_z a_z(1+\epsilon_z)\vec{z}_c. \tag{2.38}$$

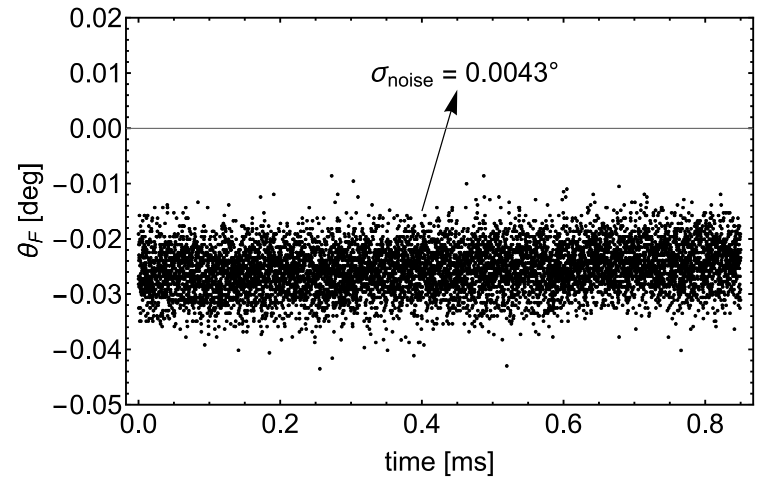


Figure 2.6: Faraday rotation shot-noise measurement

Here $(a_x, a_y, a_z) = (91.6926, 91.2159, 392.773)$ $\mu$T/A are pre-calibrated coil coefficents and $(\epsilon_x, \epsilon_y, \epsilon_z)$ are coil correction terms that are calibrated to account for drift in the coil coefficients. The control of the $B_{x,c}$ and $B_{y,c}$ magnetic fields is managed by saddle coils, characterized by diameter $D = 148$ mm, height $h = 300$ mm, and central angle subtended by the saddle coils $\phi = 120°$ [see Fig. 2.8(a)], and the $B_{z,c}$ control is managed by a Helmholtz coil pair characterized by radius $r_H = 74$ mm. At the midpoint for the Helmholtz pair [183] the magnetic field is predicted to be

$$|\vec{B}_{z,c}| = \left(\frac{4}{5}\right)^{3/2} \frac{\mu_0 N I}{r_H} \tag{2.39}$$

and

$$|\vec{B}_{x,c}| = |\vec{B}_{y,c}| = \frac{4\mu_0 N I}{\pi D}(s-1)^{1/2}(s^{-1/2} + s^{-3/2})\sin(\phi/2) \tag{2.40}$$

for the saddle coil pair [33, 189], where $s$ is a dimensionless aspect ratio parameter given by $s = 1 + (h/D)^2$, $N$ is the number of turns per coil, and $\mu_0 = 4\pi \times 10^{-7}$ H/m. It can be shown that for the saddle coil pair, all spatial derivatives up to fourth order (e.g. $\partial^4 B_x/\partial x^4$) are zero for coil parameters $s = 5$ and $\phi = 120°$. This cancellation of spatial derivatives to fourth order is also true for the Helmholtz pair. In practice, small deviations from these ideal settings occur in actual physical implementations.

To implement this coil system, we used a large 3D printed nylon cylindrical structure with

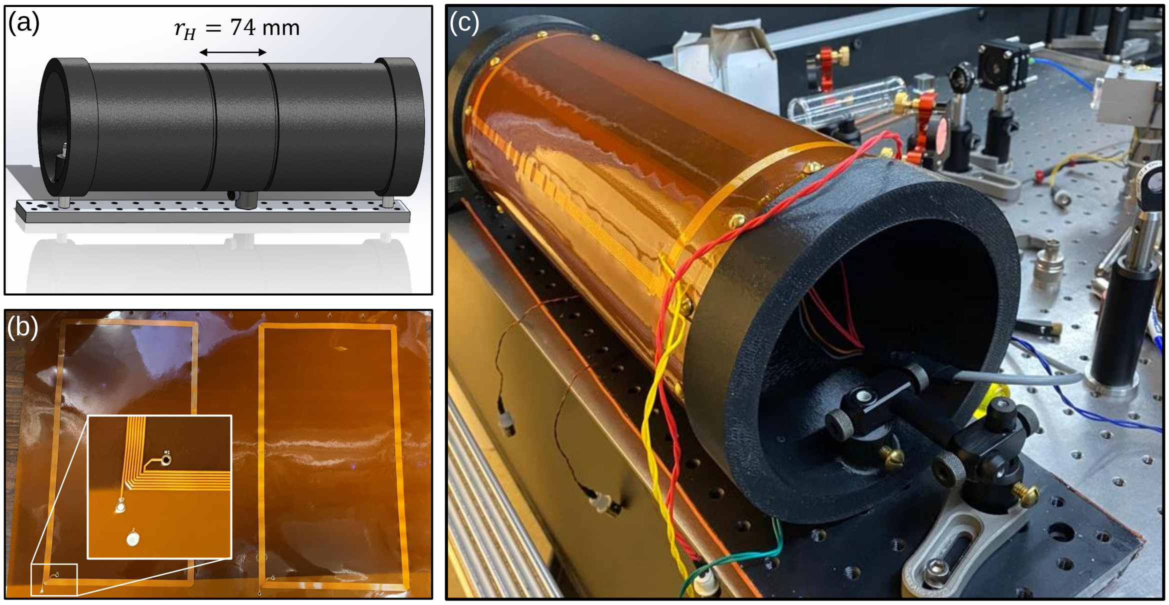


Figure 2.7: 3D coil system. (a) CAD drawing of the cylindrical coil mount. Groves are made to wind Helmholtz coils. (b) The flexible pcb saddle coil. (c) The coil system put together. The mounting cylinder (black) is 3D printed of nylon with the flexible pcb saddle coils wrapped around.

$4 \times 5$ mm$^2$ groves made for the Helmholtz pair [see Fig. 2.7(a)], using approximately 30 turns for wire. The saddle coils were constructed from a flexible six-layer PCB, featuring seven turns per layer and trace widths measuring 0.5 mm [see Fig. 2.7(b,c)]. For the few hundred mA of current used in the Helmholtz pair and saddle coils to produce magnetic field strengths near 50 $\mu$T, we observed coil heating limited to within 3 °C.

### 2.4.1 Coil system calibration

Due to uncertainty in the exact coil factors, coil orthogonality from machining tolerances, and remnant background magnetic fields, we perform a coil system calibration that involves applying different coil current $(I_x, I_y, I_z)$ settings to rotate the effective magnetic field, and detect the resulting magnetic field strength using FID measurements. We establish an orthogonal laboratory frame

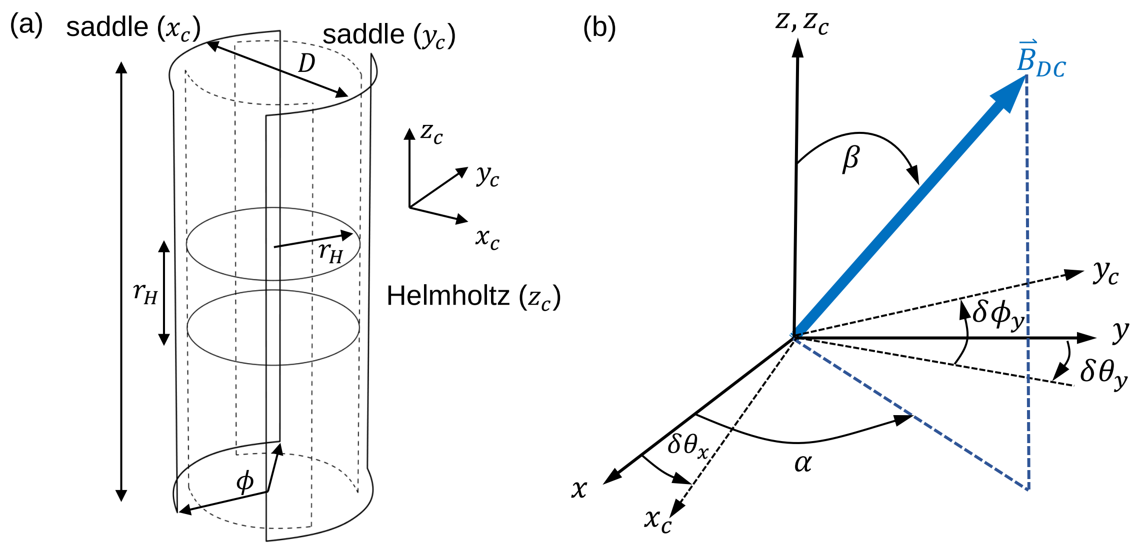


Figure 2.8: (a) Diagram of the 3D coil system consisting of two pairs of saddle coils and a Helmholtz coil pair. (b) Schematic of the non-orthogonal coil coordinate frame $\mathcal{C} = (x_c, y_c, z_c)$ with respect to the orthogonal laboratory frame $\mathcal{L} = (x, y, z)$.

$\mathcal{L} = (x, y, z)$ with respect to the DC coil system frame $\mathcal{C} = (x_c, y_c, z_c)$ as follows [see Fig. 2.8(b)]:

$$\vec{x}_c = R_y(\pi/2 + \delta\theta_x)\hat{z} = \{\cos[\delta\theta_x], 0, -\sin[\delta\theta_x]\} \tag{2.41}$$

$$\vec{y}_c = R_z(\pi/2 + \delta\phi_y)R_y(\pi/2 + \delta\theta_y)\hat{z} = \{-\cos[\delta\theta_y]\sin[\delta\phi_y], \cos[\delta\theta_y]\cos[\delta\phi_y], -\sin[\delta\theta_y]\} \tag{2.42}$$

$$\vec{z}_c = \hat{z} = \{0, 0, 1\} \tag{2.43}$$

where $R_{y,z}$ are rotation matrices about the $\hat{y}$ and $\hat{z}$ directions, and $(\delta\theta_x, \delta\theta_y, \delta\phi_y)$ are non-orthogonality angles.

The total field $|\vec{B}|$ generated by the coil system and a background field $\vec{B}_0 = (B_{x,o}, B_{y,o}, B_{z,o})$ is given by

$$|\vec{B}|^2 = \Big(B_{x,o} + \sum_{k=x,y,z} \vec{B}_{k,c} \cdot \hat{x}\Big)^2 + \Big(B_{y,o} + \sum_{k=x,y,z} \vec{B}_{k,c} \cdot \hat{y}\Big)^2 + \Big(B_{z,o} + \sum_{k=x,y,z} \vec{B}_{k,c} \cdot \hat{z}\Big)^2. \tag{2.44}$$

In this framework there are 9 unknown parameters namely 3 non-orthogonality angles $(\delta\theta_x, \delta\theta_y, \delta\phi_y) = (3.72, -0.99, 3.47)$ mrad, 3 coil corrections $(\epsilon_x, \epsilon_y, \epsilon_z) = (0.57, 0.16, 2.7) \times 10^{-3}$, and three background field components $(B_{x,o}, B_{y,o}, B_{z,o}) = (-84.0, 50.7, -62.2)$ nT. We fit these 9 parameters using scalar measurements ($B$) extracted from FID signals by minimizing

$$C_{\text{coil}} = \sum_{j=1}^{60} w_j \left( |\vec{B}|_j - B_j \right)^2 \tag{2.45}$$

where $j$ denotes a programmed current 3-tuple $(I_x, I_y, I_z)_j$ that corresponds to a random magnetic field direction $(\alpha, \beta)_j$ with norm $B_j \approx 50$ $\mu$T. The weights $w_j = 1/\delta B^2$ weights are given by the variance $\delta B^2$ calculated from 10 repeated FID measurements. The residuals of this calibration are shown in Fig. 2.9(a). To account for drift in the coil system, we conducted scalar calibrations during the 37-minute measurement period.

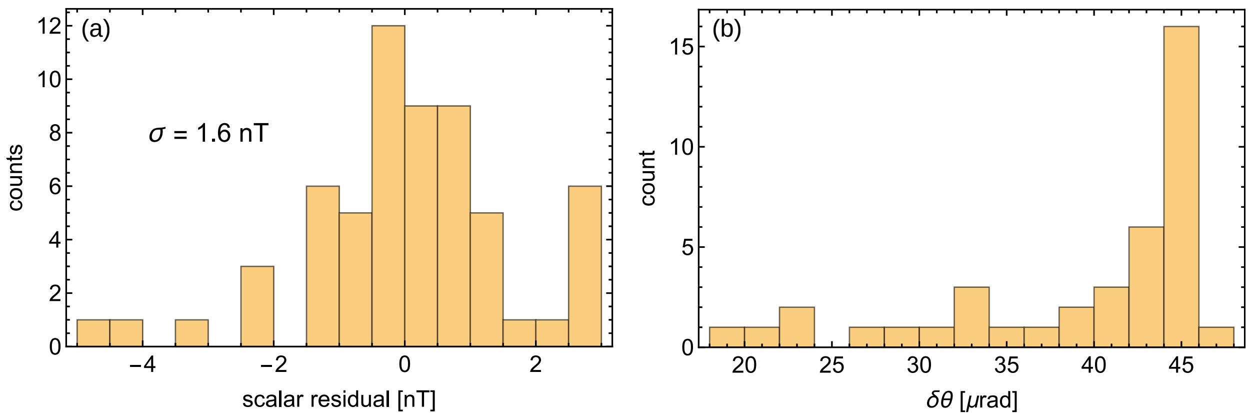


Figure 2.9: Coil system calibration (a) calibration residuals using FID measurements evaluated over 60 random DC magnetic field direction. (b) Estimated errors in the direction of $\vec{B}$ assuming 2.3 nT error in $B_{x,o}$. A similar histogram is obtained for estimated $\delta\theta$ errors assuming an error of $\delta\epsilon_x = 0.06 \times 10^{-3}$ for $\epsilon_x$ bounded by 50 $\mu$rad.

### 2.4.2 Coil system accuracy

The residual few nanotesla, with a standard deviation of 1.6 nT, remains consistent across multiple calibrations employing varying programmed currents. This is significantly larger than the statistical error, less than 100 picotesla ($\delta B < 100$ pT), inferred from 10 repeated FID measurements. The two likely sources of these systematics are heading error in the FID measurement [94] and nonlinearities in the coil current control. To estimate the error in the programmed field direction we purposely shift one of the coil parameters of the coil system model (e.g. $\delta\epsilon_x$ or $\delta B_{x,0}$)

and compare $|\vec{B}|$ to the unperturbed coil model. We selected these parameters as they epitomize two different potential drift scenarios in the coil system: a variation in the coil factors or a shift in the background magnetic field. To produce a root-mean-square deviation (RMSD) of 1.6 nT between scalar measurements predicted by the unperturbed and perturbed coil models, which matched the standard deviation of the measured calibration residuals, required $\delta B_{x,0} = 2.3$ nT or $\delta\epsilon_x = 0.06 \times 10^{-3}$ in the perturbed coil model. The deviations in the directions of the DC magnetic fields between the unperturbed and perturbed coil models is shown in [see Fig. 2.9(b)]. These deviations are confined within 50 $\mu$rad. Consequently, we estimate that the directional accuracy of our coil system is maintained within a margin of 50 $\mu$rad.

### 2.4.3 Coil system uniformity

To test the spatial uniformity of magnetic field produced by the coil system, we used a Bartington MAG612 vector fluxgate magnetometer placed at the center of the coil system and translated 10 mm in each direction. Each of the three coil pairs were measured individually by producing $75 - 85$ $\mu$T in the $B_i$ direction, with $i = x, y, z$ and measuring the spatial variation of that magnetic field component [see Fig. 2.10]. This corresponded to 798 mA applied to the saddle coils at 202 mA applied to the Helmholtz coil pair. For each of these measurements, we calculate the normalized magnetic field gradient.

$$G = \frac{1}{B_i}\sqrt{\left(\frac{\partial B_i}{\partial x}\right)^2 + \left(\frac{\partial B_i}{\partial y}\right)^2 + \left(\frac{\partial B_i}{\partial z}\right)^2} \tag{2.46}$$

Maximum and minimum values of $G$ are plotted in Table 2.1 with the last column showing the estimated magnetic field variation from $(G_{\mathrm{min}} + G_{\mathrm{max}})/2 \times l_i$ over the $l_{x,y} = 3$ mm and $l_z = 2$ mm dimensions of the MEMS cell. The magnetic field variation $\delta B_{x,y}$ that contributes to FID measurements is likely smaller due to the probe beam size with waist $w \approx 1$ mm.

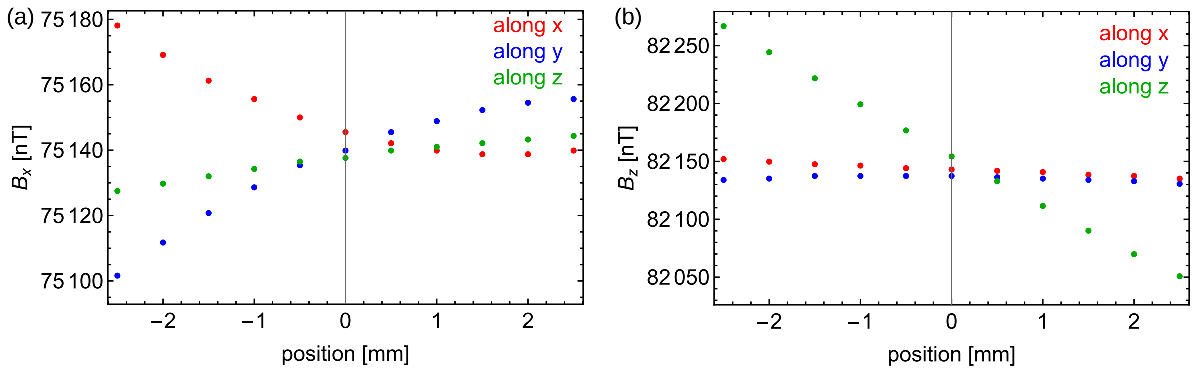


Figure 2.10: Measured spatial dependence of the magnetic $B_x$ and $B_z$ magnetic field components produced by our 3D coil system using a Bartington MAG612 fluxgate magnetometer. The $B_y$ component shows similar homogeneity as $B_x$.

Table 2.1: Table of maximum and minimum $G$-values defined in Eq. 2.46. The last column shows the estimated magnetic field variation from $(G_{\min} + G_{\max})/2 \times l_i$ over the $l_{x,y} = 3$ mm and $l_z = 2$ mm dimensions of the cell.

| coil | $G_{\min}$ (mm$^{-1}$) | $G_{\max}$ (mm$^{-1}$) | $\delta B_i$ [nT] |
|---|---|---|---|
| x saddle | 0.005% | 0.036% | 31 |
| y saddle | 0.001% | 0.017% | 14 |
| z Helmholtz | 0.047% | 0.055% | 51 |

### 2.4.4 Magnetic field sensitivity expected from current noise

The current noise inside the coil system presents a limit to the sensitivity of our magnetic field measurements. We used a home-built current source that allows independent control of the three coil pairs. A transimpedance amplifier circuit (JILA part number RC036A) outputs a current proportional to a low-noise DAC input (Analog Devices EVAL-AD5791) that is controlled by a SparkFun FreeSoC2 development board (474-DEV-13714). The noise performance of the current servo driven across a 50 Ω resistor is shown in Fig. 2.11, where the estimated magnetic field sensitivities are converted using the saddle coil factors.

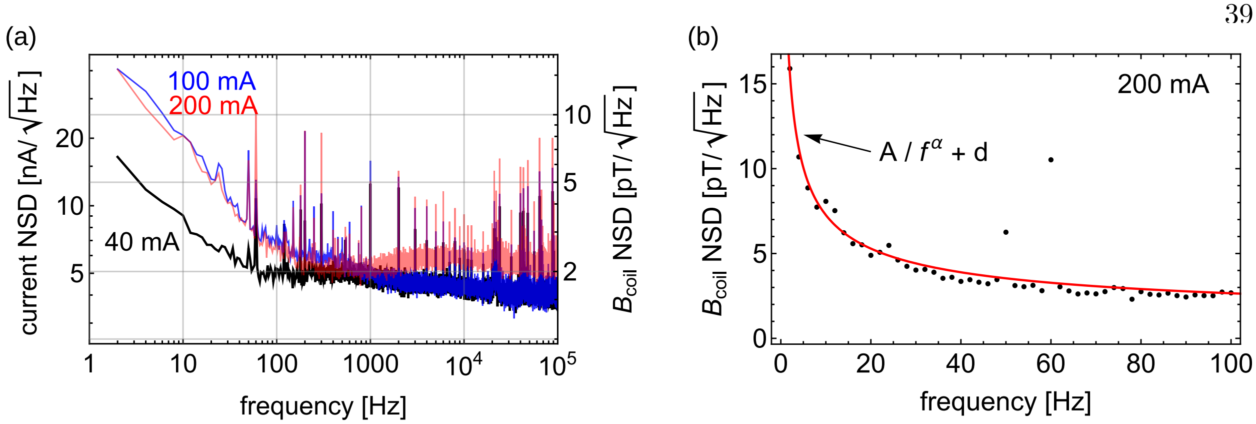


Figure 2.11: (a) Current noise spectral density characterizing the current noise within the coil system. The corresponding magnetic field sensitivity is estimated for the saddle coils with the measured coil factor $a_x = 392.8\ \mu$T/A. (b) A fit to the 200 mA data showing agreement with $1/\sqrt{f}$ behavior. The fitted parameters are $A = 21.4$, $\alpha = 0.502$, and $d = 0.538$.

## 2.5 Microwave cavity

The rectangular microwave cavity [see Fig. 2.12] is designed with inner dimensions $4.8 \times 2.0$ cm$^3$. A single optic-axis is incorporated with the cavity through a one cm$^2$ aperture. With this cavity we excite two near-degenerate transverse magnetic ($B_z = 0$) TM$_{\mathrm{nml}}$ modes characterized by $(m, n, l) = (2, 1, 0)$ $(n, m, l) = (1, 2, 0)$. With perfectly conducting walls, and no material inside the cavity, the resonant microwave frequencies of these modes are given by

$$f_{m,n,l} = \frac{1}{2\pi\sqrt{\epsilon_0\mu_0}}\sqrt{\left(\frac{m\pi}{d_x}\right)^2 + \left(\frac{n\pi}{d_y}\right)^2 + \left(\frac{l\pi}{d_z}\right)^2} \tag{2.47}$$

which, by design, evaluate to $f_{1,2,0} = f_{2,1,0} = 6982.88$ MHz slightly above the ground state hyperfine splitting of $^{87}$Rb $\nu_{\mathrm{hfs}} = 6834.682$ MHz. This design also avoids exciting nearby modes $f_{1,1,0} = 4416.36$ MHz $f_{1,1,1} = 8699.22$ MHz, and $f_{2,2,1} = 8832.72$ MHz are sufficiently far away that. With the electromagnetic wave equation, and assuming appropriate boundary conditions on the cavity walls it is possible to derive through separation of variables the spatial dependence of these TM$_{\mathrm{mnl}}$

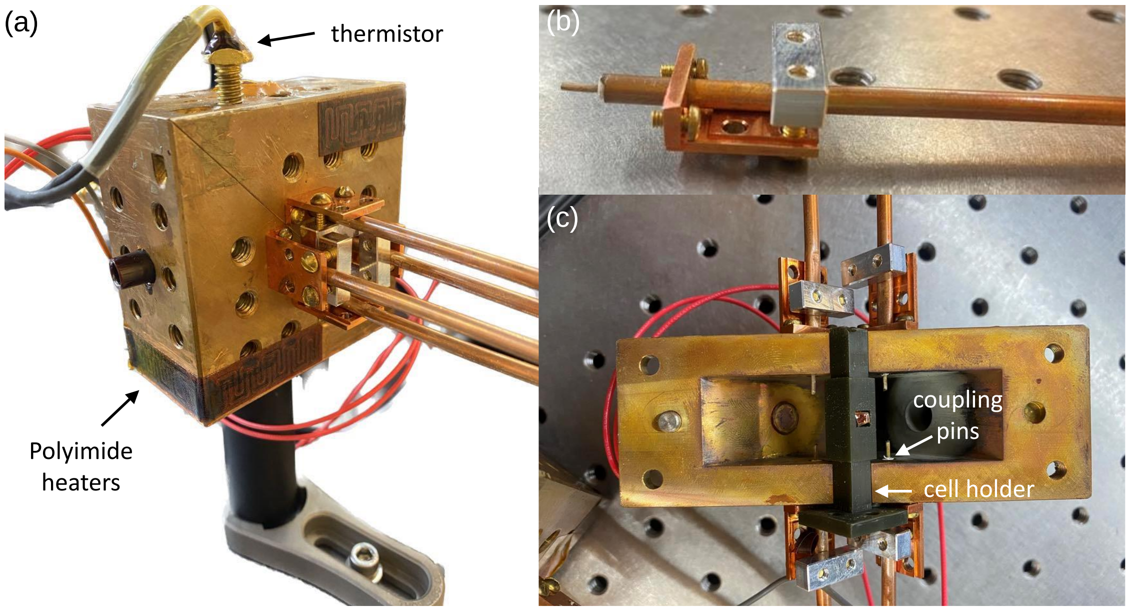


Figure 2.12: Microwave cavity. (a) Assembly of the cavity showing the polymide heaters and embedded thermistor. (b) Microwave coupling is achieved through semi-rigid cables with outer and inner conductors made of beryllium copper. The semi-rigid cables are attached with a mount consisting of copper and aluminum. (c) The cell is placed inside the cavity with a 3D printed holder (dark gray).

$$E_x = \frac{j\omega\mu}{d^2}\left(\frac{n\pi}{d_y}\right) A\cos\left(\frac{m\pi}{d_x}x\right)\sin\left(\frac{n\pi}{d_y}y\right)\sin\left(\frac{l\pi}{d_z}z\right) \tag{2.48}$$

$$E_y = -\frac{j\omega\mu}{d^2}\left(\frac{m\pi}{d_x}\right) A\sin\left(\frac{m\pi}{d_x}x\right)\cos\left(\frac{n\pi}{d_y}y\right)\sin\left(\frac{l\pi}{d_z}z\right) \tag{2.49}$$

$$E_z = A\sin\left(\frac{m\pi}{d_x}x\right)\sin\left(\frac{n\pi}{d_y}y\right)\cos\left(\frac{l\pi}{d_z}z\right) \tag{2.50}$$

$$B_x = -\frac{1}{d^2}\frac{m\pi}{d_x}\frac{l\pi}{d_z} A\sin\left(\frac{m\pi}{d_x}x\right)\cos\left(\frac{n\pi}{d_y}y\right)\cos\left(\frac{l\pi}{d_z}z\right) \tag{2.51}$$

$$B_y = -\frac{1}{d^2}\frac{n\pi}{d_y}\frac{l\pi}{d_z} A\cos\left(\frac{m\pi}{d_x}x\right)\sin\left(\frac{n\pi}{d_y}y\right)\cos\left(\frac{l\pi}{d_z}z\right) \tag{2.52}$$

$$B_z = 0 \tag{2.53}$$

where $d^2 = \left(\frac{m\pi}{d_x}\right)^2 + \left(\frac{n\pi}{d_y}\right)^2$ and $A$ is an arbitrary amplitude. In Fig. 2.13, the $TM_{210}$ and $TM_{120}$ modes are depicted, each showing a linearly polarized magnetic component, $B_x$ and $B_y$ respectively, at the vapor cell's position. The electric field distribution contains only the $E_z$ component.

The vapor cell is placed at the center of the microwave cavity using a 3D printed cell holder.

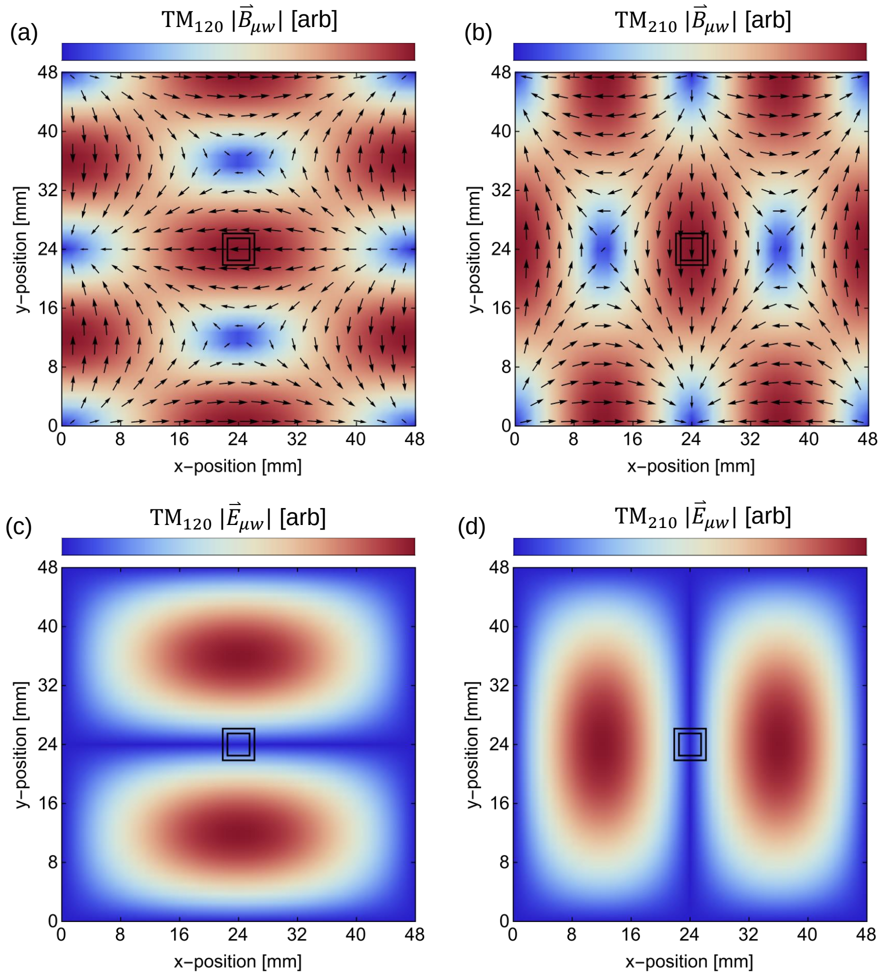


Figure 2.13: TM$_{120}$ and TM$_{210}$ cavity modes overlaid with the outline of the vapor cell located at the center. (a,b) Transverse magnetic field components where $B_z = 0$. (c,d) Electric field components with $E_{x,y} = 0$.

To heat the cell, flexible polyimide heaters with adhesive are attached to the cavity. A thermistor embedded in brass screw is screwed into the cavity walls for monitoring the cavity temperature. We operate the cavity (and the cell) around $T = 100°$C. The resonance frequencies of the cavity modes negatively shift by 10 MHz after heating.

### 2.5.1 Cavity coupling and tuning

To excite the TM$_{120}$ and TM$_{210}$ modes individually, we insert coupling pins [see Fig. 2.12(b,c)] at the location of maximum electric field shown in Figure 2.13(c,d). These coupling pins are copper constructed from the center pin of a semi-rigid coaxial cable (UT-141C-LL). We originally used pins made of brass, but these to be highly magnetic that caused significant magnetic field gradients at the atoms. These semi-rigid cables are secured to the $\mu$w cavity with a home-built copper mount and aluminum bar tightened with brass screws [see Fig. 2.12(b)]. We characterize the coupling and resonant frequencies of the $\mathrm{TM}_{120}$ and $\mathrm{TM}_{210}$ modes with a vector network analyzer (Agilent E8358A) by measuring the $\mathrm{S}_{11}$ parameter on the coaxial cable connected to the coupling pin. We first measure the $\mathrm{S}_{11}$ parameter for a single coupling pin protruding a distance $d$ into the cavity to couple to the $\mathrm{TM}_{120}$ mode [see Fig. 2.14(a)]. We fit this spectrum using

$$S_{11}(\nu_{\mu\mathrm{w}}) = a_0 + a_1\nu_{\mu\mathrm{w}} + a_2\sin(2\pi f_s \nu_{\mu\mathrm{w}}) + \sum_{j=1,2} \frac{A_j}{\pi} \frac{\Gamma_j/2}{(\nu_{\mu\mathrm{w}} - \nu_{0,j})^2 + (\Gamma_j/2)^2} \tag{2.54}$$

which model the $\mathrm{TM}_{120}$ and $\mathrm{TM}_{210}$ resonances as Lorentzian features. The sinusoidal term with amplitude $a_2$ accounts for residual standing waves in the coaxial cable. We observe that resonant frequencies of the $\mathrm{TM}_{120}$ and $\mathrm{TM}_{210}$ modes are degenerate due to small asymmetries in the cavity shape. In Figure 2.14(b) we plot fits of Eq. (2.54) for different coupling pin lengths. As expected, the $\mathrm{TM}_{210}$ mode is minimally affected, while the $\mathrm{TM}_{120}$ exhibits a negative frequency shift and broadening with increased pin length $d$. From this plot we can identify different coupling regimes. We operate the cavity in a strongly over-coupled regime to broaden the linewidth of the cavity and help minimize microwave frequency dependence of the cavity mode across the atomic resonance.

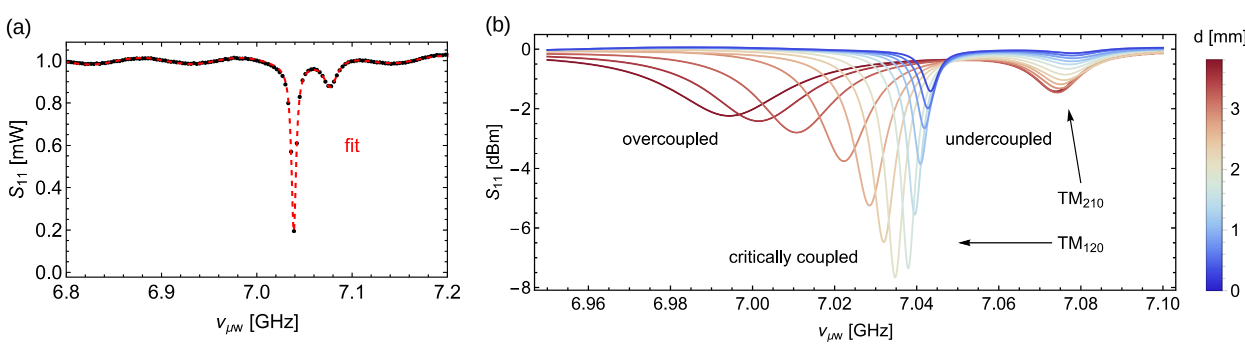


Figure 2.14: $\mathrm{S}_{11}$ spectra of the $\mathrm{TM}_{120}$ and $\mathrm{TM}_{210}$ modes. (a) Overlay of $\mathrm{S}_{11}$ spectra with Eq. (2.54) with fitted parameters. (b) Plots of Eq. (2.54) fits for different coupling pin lengths.

Extracted from the fits in Figure 2.14, Figure 2.15 shows characterization of $\mathrm{TM}_{120}$ mode

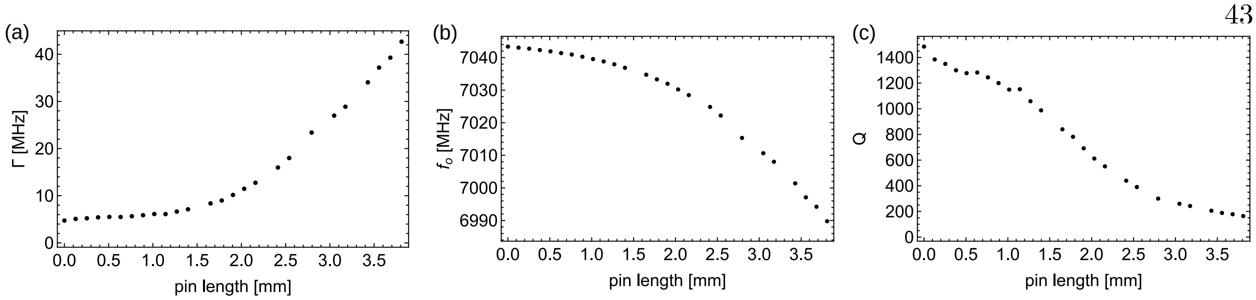


Figure 2.15: Measured linewidth, resonant frequency, and quality factor for different coupling pin lengths of the $\mathrm{TM}_{120}$ cavity mode.

linewidth, resonant frequency, and quality factor as a function of the coupling pin length. Despite these observations, one would naively expect that introducing a metal pin into a cavity would increase the cavity frequency since the overall cavity volume has shrunk. A more careful calculation [143]

$$\frac{\omega - \omega_0}{\omega_0} \simeq \frac{\int_{\Delta V}(\mu|B_0|^2 - \epsilon|E_0|^2)dv}{\int_{\Delta V}(\mu|B_0|^2 + \epsilon|E_0|^2)dv} = \frac{2\Delta V}{V_0} \tag{2.55}$$

where $\Delta V = V_{\text{after}} - V_0$ is the change in the cavity volume from before and after the cavity shape perturbation and $V_0$ is the initial cavity volume. Given the radius of the coupling pins $r_{\text{pin}} = 0.5$ mm Eq. (2.55) predicts a frequency shift per pin length $\delta f_0/l_{\text{pin}} = -0.93$ MHz mm$^{-1}$. This analysis agrees for well with measurements [see Fig. 2.15(b)] for small pin lengths.

To maximize symmetry, overcoupling, and optimized tuning of the $\mathrm{TM}_{120}$ and $\mathrm{TM}_{210}$ resonant frequencies, we use four coupling pins on each face of the cavity [see Fig. 2.12(a,c)]. With this arrangement, final $S_{11}$ and $S_{22}$ spectra are shown in Figure 2.16. From fits of these spectra we find $\mathrm{TM}_{120}$ and $\mathrm{TM}_{210}$ resonances are $f_0 = 6.81$ GHz and $f_0 = 6.89$ GHz with linewdiths of roughly $\Gamma = 110$ MHz, and a loaded quality factor of $Q = 62$. We detect the precise microwave field generated by these cavity modes through Rabi measurements with the atoms in Ch. 4 and Ch. 5.

### 2.5.2 Microwave source

The microwave source to excite the cavity modes was a Windfreak SynthHD Pro signal generator. This signal generator is referenced to a 10 MHz Rubidium standard clock. The Windfreak

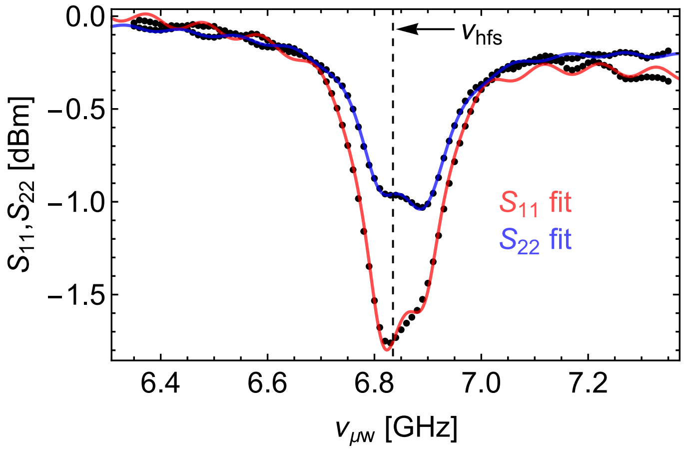


Figure 2.16: S-parameters of the two microwave cavity ports. The coupling pins do not perfectly excite a single mode as two peaks can be seen for each of the S-parameters.

outputs a square wave and thus contains significant harmonics of the microwave frequency $\nu_{\mu\mathrm{w}} \approx 6.8$ GHz. While these harmonics, due to their large detuning, do not influence the atoms within the vapor cell, we pass the output of the Windfreak through a 6.8 GHz bandpass filter to eliminate these harmonics. To ensure relative phase stability between excitation of the two cavity ports across different microwave frequencies we split the output of a single channel on the Windfreak (Mini-Circuits ZN2PD-9G-S+) to send to the two cavity ports. After this power splitter, the two microwave signals go through a switch (Analog Devices ADRF5020) and an amplifier (Mini-Circuits ZVE-8G+). We generally operate the amplifier near the 1 dB compression point to minimize low frequency power fluctuations of the amplifiers. While this is not an ideal arrangement since non-linear distortions of the amplifier output begin to appear past this compression point, we observed improved microwave stability in this arrangement. To decrease the microwave power, while still maintaining this amplifier saturation, we placed attenuators after the amplifier. Circulators are placed before the cavity ports to minimize standing waves created by reflections from the cavity ports. This microwave chain is diagrammed in Figure 2.17.

An important figure of merit of the microwave source is the single-sideband phase noise $\mathcal{L}_{\phi}$. This figure of merit is given by the phase noise amplitude with respect to the carrier (in units of dBc) at a frequency offset. Typically, the phase noise power is evaluated in a 1 Hz

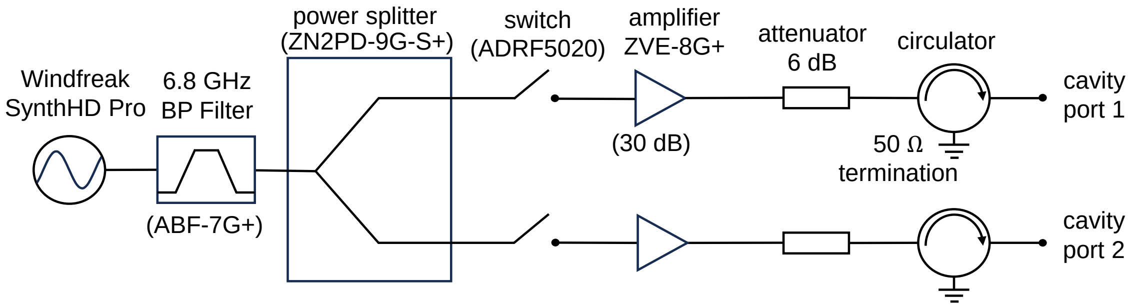


Figure 2.17: Microwave chain employed for excitation of the microwave cavity ports.

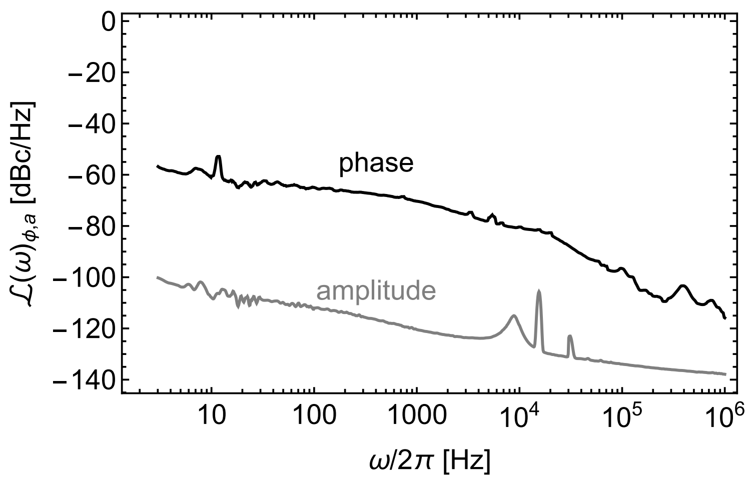


Figure 2.18: The single-sideband (SSB) phase and amplitude noise of the Windfreak measured with a Rhode & Schwarz FSWP26 phase noise analyzer at 6835.82 MHz. Note that these measurements are not to the specifications of the Windfreak Synth Pro datasheet due to a clock issue we are tracking down.

bandwidth. Single-sideband indicates that the depicted phase noise corresponds to the positive frequency components of the associated power spectral density, thereby representing half of the total power. Phase noise is equivalent to frequency jitter of the microwave drive, which leads to microwave detuning fluctuations when driving Rabi oscillations. Amplitude noise on the other hand directly effects the Rabi frequency. Phase noise not only limits the precision of Rabi oscillation measurements, but can also cause systematic frequency shifts. We measure the phase and amplitude noise with a Rhode & Schwarz FSWP26 phase noise analyzer near a typical operation frequency of 6835.82 MHz [see Fig. 2.18]. An analysis of the effects of our measured phase and amplitude noise on Rabi frequency measurements is presented in Ch. 5. Our measured phase noise in Fig. 2.18 is about 20 dB higher than reported in the data sheet of the Windfreak SynthHD Pro due to issues with our Rubidium clock that we are tracking down. While unfortunate, this level of phase noise is not a dominant noise source for our Rabi oscillation measurements as discussed in Ch. 5.

## 2.6 Additional logistics behind FID and Rabi measurements

Our apparatus enables control and detection of hundreds of Rabi oscillation and free induction decay (FID) and measurements in just a few hundred milliseconds. This functionality is important to probe Rabi measurements across multiple hyperfine transitions and cavity mode excitations, as well as to obtain proper measurement statistics. Details on how to use these comprehensive data sets to extract vapor cell parameters, perform high accuracy vector magnetometry, and calibrate microwave polarization ellipses (MPEs) are discussed in the subsequent chapters. In this section, we explore a few logistical facets involved in the FID and Rabi oscillation measurements.

### 2.6.1 Limited data acquisition rate due to Eddy currents and cavity temperature stabilization

To mitigate unwanted magnetic fields from the electric currents running through the polyimide heaters, as well as Eddy currents in the copper body of the microwave cavity when changing the DC magnetic field direction, we deactivate heater currents and program coil currents at least 40 ms prior to recording Rabi and FID measurements. This 40 ms number is based FID measurements initiated after a variable wait time when turning on coil currents [see Fig. 2.19].

Another factor that limits the rate of data collection is the fact that the heater currents are turned off during measurements. If not accounted for, this would result in cavity cooling, which affects the cavity modes driving the Rabi oscillations. To account for this cooling, a deadtime on the order of 1-2 seconds between each recorded Rabi-FID measurement sequence is introduced to allow the heaters enough time to restabilize the cavity temperature.

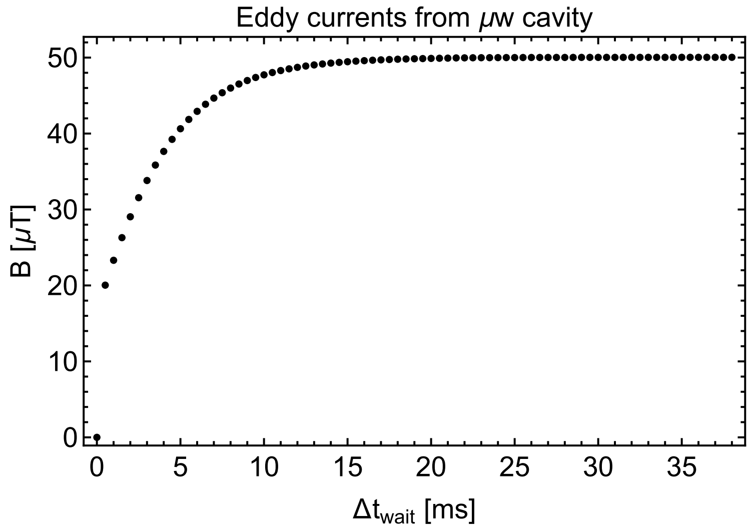


Figure 2.19: The magnetic field strength after turning on the current in the x saddle coil pair. The transient observed is due to Eddy currents induced primarily in the copper body of the microwave cavity. After 40 ms, these transients stabilize to within the stability of coil system.

### 2.6.2 Rabi oscillation filtering

To remove high frequency noise and residual Larmor precession from Rabi oscillation measurements, we use a digital equiripple finite impulse response (FIR) filter. This filter is characterized by a passband frequency of 10 kHz, and a stopband frequency of 1 MHz. The length of the filter is 100. To implement this filter we used the Mathematica EquirippleFilterKernel function to produce the filter kernel that is convolved with the measurement data. The filter's impulse response, along with its application to a Rabi oscillation measurement, is displayed in Fig. 2.20.

### 2.6.3 Spatial inhomogeneity of the microwave cavity modes

Fundamentally, the spatial uniformity of the microwave field is constrained by the dimensions of the microwave cavity modes. These dimensions are determined by matching the $f_{210}$ and $f_{120}$ mode resonant frequencies with the 6.8 GHz hyperfine resonances of $^{87}$Rb. The microwave cavity modes, however, are strongly perturbed by the eight coupling pins situated within a centimeter of the vapor cell, depicted in Fig. 2.13, which is likely the dominant contribution to the microwave spatial inhomogeneity. Although mapping the precise spatial inhomogeneity is challeng-

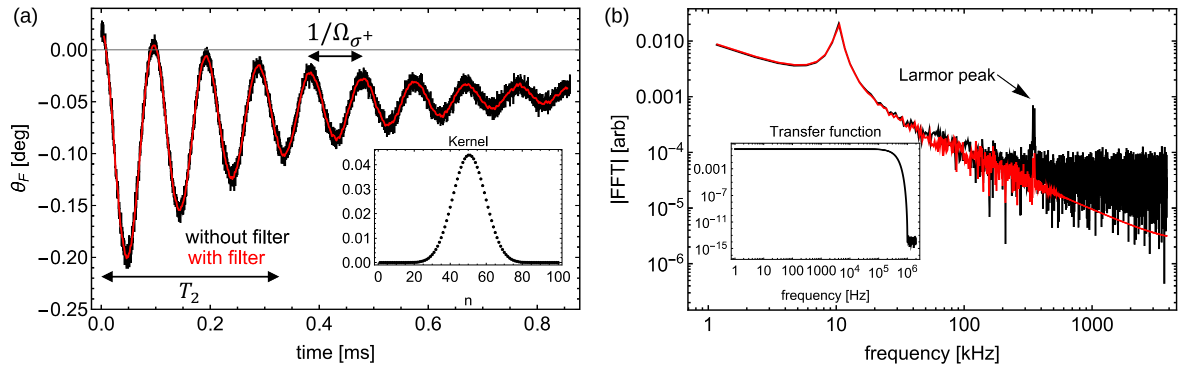


Figure 2.20: Finite implulse response (FIR) filtering of Rabi oscillation measurements evaluated in the (a) time-domain and (b) frequency-domain.

ing, it significantly affects the $T_2$ dephasing times of Rabi oscillations, especially at higher oscillation frequencies. Fig. 2.21 illustrates the measured dephasing time in relation to the Rabi frequency of the $\sigma^+$ $|1,1\rangle - |2,2\rangle$ transition [see Fig. 2.20(a)].

At lower Rabi frequencies, the $T_2$ dephasing time is chiefly governed by collisional dephasing that agree well with theoretical expected values at vapor cell temperatures near the 100 °C cavity temperature known approximately to within a few °C. The model used to calculate collisional dephasing is discussed in Ch. 3. The exact vapor cell temperature is unknown due to thermal gradients between the thermistor, embedded within the body of the microwave, and the vapor cell. Additionally, variations in the vapor cell temperature between the experiments described in Ch. 3, Ch. 4, and Ch. 5 are probable, owing to the replacement of electrical heaters, which necessitated the substitution and re-location of the microwave cavity thermistor as well. For Rabi frequencies exceeding 50 kHz, the influence of microwave inhomogeneity becomes apparent. Throughout this thesis, Rabi frequencies across all hyperfine transitions are within 90 kHz. As highlighted in Ch. 5, microwave inhomogeneity introduces systematic errors in calibrating microwave polarization ellipses, a crucial part of Rabi vector magnetometry measurements.

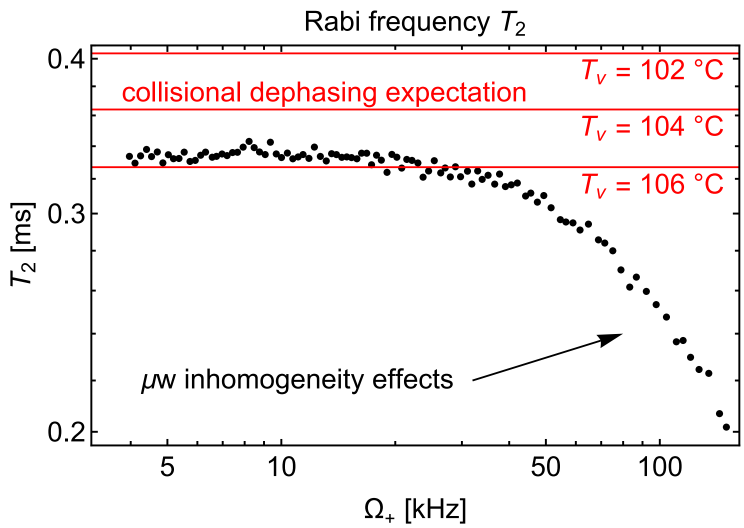


Figure 2.21: Rabi oscillation $T_2$ time as a function of the Rabi oscillation frequency $\Omega_{\sigma+}$ between transitions $|1,1\rangle$ and $|2,2\rangle$. Broadening from spatial inhomogeneity of the microwave cavity modes becomes apparent at $\Omega_{\sigma+} > 50$ kHz. The $T_2$ time agrees with theoretical expectations for collisional relaxation estimated at different vapor temperatures ($T_\mathrm{v}$). The predicted $T_2$ times were obtained by fitting Rabi oscillations simulated using Eq. 3.21 with parameters $\vec{B} = B\hat{z}$, $B = 50$ $\mu$T, $\nu_{\mu\mathrm{w}} =$ 6835.82 MHz, pressure shift $\delta\nu_\mathrm{hfs} = 88$ kHz, buffer gas pressure $P_{\mathrm{N}_2} = 180$ Torr, and vapor cell volume $(3 \times 3 \times 2)$ mm$^3$. While the cavity temperature is controlled to maintain a thermistor embedded within the copper body of the microwave cavity to 98 °C, the actual temperature of the vapor cell inside the cavity is uncertain due to thermal gradients across the cavity body. While there can be systematic effects, not accounted for in our dephasing estimates, such as higher order wall collisions, our measured dephasing rates are consistent with a vapor temperature near 105 °C.

# Chapter 3

## Modeling Rabi oscillations in vapor cells

Rabi measurements in atomic vapor cells are of current interest in a range of microwave imaging and sensing experiments, but are increasingly in a parameter space outside of theoretical studies of coherence defined by spin-exchange (SE) collisions. In particular, in our initial measurements, we noticed that Rabi measurement decayed a few times faster than FID measurements. This discrepancy is primarily due to spin-exchange collsions, which are are the dominant limitation of sensitivity for sensors based on hot atomic vapors [73, 176]. Spin-exchange collisions originate from the acquired phase shift between singlet and triplet interaction potentials of the electrons of colliding alkali atoms. The exchange interaction conserves the total spin of the colliding atoms, but causes random transitions between the hyperfine ground states that have recently been leveraged in hot atomic vapor cells for generating many-body entanglement [102] and modeling phase transition dynamics [79]. Decoherence effects of SE collisions within a Zeeman manifold have been studied in the context of optically-pumped magnetometers (OPMs), and notably even found to disappear in the spin-exchange-relaxation-free (SERF) regime at low magnetic fields [41, 72, 156]. Further, the consequences of spin-exchange collisions on the coherence between two hyperfine ground manifolds have also been well-studied in the context of masers [175, 177] and atomic clocks [88, 176]. In these studies, SE decay rates were modeled based on stationary atomic populations such as a spin-temperature (ST) distribution, which is valid when continuous optical pumping and a weak driving field prevent Rabi oscillations, and SE collisions dominate over other collision and scattering rates. However, this approximation is invalid in the case of a strong driving field, such as a near-resonant microwave field, that causes significant population transfer. As a result, the coherence of Rabi oscillations is expected to deviate from the assumptions of weak driving and exhibit nontrivial detuning and spin-polarization dependence.

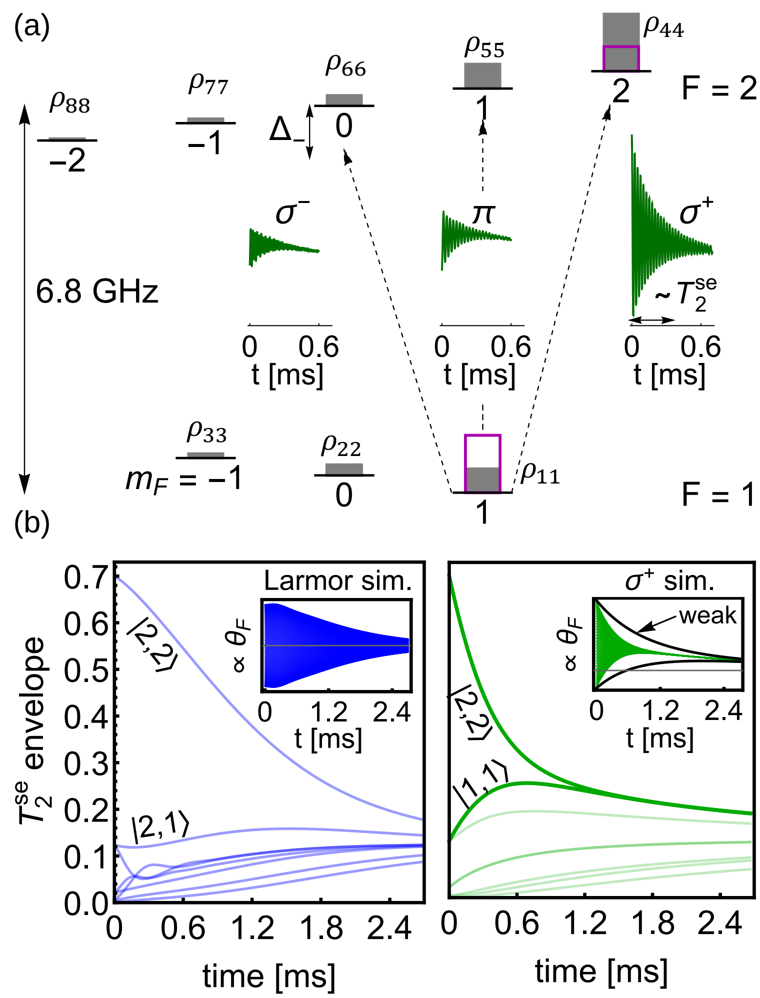


Figure 3.1: (a) Energy-level diagram for $^{87}$Rb showing the relevant microwave transitions and Rabi oscillations driving atomic populations ($\rho_{ii}$) measured in our apparatus (green insets). A microwave sweep performs adiabatic rapid passage (ARP) to switch the $\sigma^+$ populations prior to driving the $\sigma^-$ and $\pi$ transitions (magenta). (b) The envelopes of simulated atomic population dynamics due purely to SE collisions during Larmor precession (left) which decays slower than during a $\sigma^+$ Rabi oscillation (right). Comparison of the envelopes for each state population to the simulated Faraday rotation signal (insets) shows nuanced population dynamics that are easier to individually observe with Rabi oscillations that couple a pair of states. The initial populations and SE rate here are set by a ST distribution with polarization p = 0.7 and vapor temperature $\mathcal{T}_v = 110°$C

In this chapter, we explore the coherence of Rabi oscillations in a heated vapor cell driven on

$\sigma^-, \pi$, and $\sigma^+$ hyperfine transitions of $^{87}$Rb [see Fig. 3.1] that do not adhere to the weak-driving approximation. First we describe the full atom-microwave Hamiltonian that accurately models various frequency shifts arising from off-resonant driving within multi-level structure of $^{87}$Rb. Next, we discuss modeling of various collisional dephasing mechanisms including the effects of spin-exchange collisions. With this full theoretical analysis of SE that accounts for the time-dependent SE dephasing rate caused by population dynamics during Rabi oscillations, we observe excellent agreement between the model and the measured coherence in the continuous Faraday signal. With this full understanding in hand, we illustrate that the Rabi lineshape is connected to many vapor parameters and show that driving multiple transitions can pinpoint useful information. Specifically, we extract from SE coherence consistent values for the vapor temperature, buffer gas pressure, and the atomic state prepared by optical pumping by using the fact that the Rabi envelope reflects the initial atomic populations, as well as their subsequent SE redistribution predicted from our model. While similar population dynamics occurs with OPMs that sense Larmor spin precession, such SE effects are more apparent and distinguishable with Rabi oscillations that probe discrete states.

## 3.1 Modeling Rabi oscillations

The atomic structure of the ground hyperfine manifolds in the presence of a static magnetic field $\vec{B}$ and a microwave field $\vec{\mathcal{B}}(t)$ is described by the following Hamiltonian

$$\begin{aligned} H(t) &= (A + h\nu_{\mathrm{bg}}/2)\mathbf{I}\cdot\mathbf{S} + \mu_B(g_s\mathbf{S} + g_I\mathbf{I})\cdot(\vec{B} + \vec{\mathcal{B}}(t)) \\ &= H_{\mathrm{hfs}} + H_{\mathrm{zeeman}} + H_{\mu\mathrm{w}} \end{aligned} \tag{3.1}$$

where the first term, $H_{\mathrm{hfs}}$, describes the hyperfine interaction characterized by electronic $\mathbf{S} = (S_x, S_y, S_z)$ and nuclear $\mathbf{I} = (I_x, I_y, I_z)$ spin operators, the magnetic dipole hyperfine constant $A$, and the buffer gas frequency shift $\nu_{\mathrm{bg}} \approx 88$ kHz. Further details behind evaluating these spin matrices in the hyperfine basis $|F, m_F\rangle$ is discussed in the Appendix A. The term proportional to $\vec{B}$, $H_{\mathrm{zeeman}}$, describes the Zeeman interaction from a DC magnetic field expressed as

$$\vec{B} = B\big[\sin(\beta)\cos(\alpha)\hat{x} + \sin(\beta)\sin(\alpha)\hat{y} + \cos(\beta)\hat{z}\big], \tag{3.2}$$

where $B$ is the magnetic field strength, $g_s$ and $g_i$ are the electron and nuclear Landé g-factors, and $\mu_B$ is the Bohr magneton. The microwave field $\vec{\mathcal{B}}(t)$, contained in $H_{\mu\mathrm{w}}$, oscillating at frequency $\omega_\mu = 2\pi\nu_\mu$ is expressed in terms of a complex phasor $\vec{\mathcal{B}} = (\mathcal{B}_x e^{-i\phi_x}, \mathcal{B}_y e^{-i\phi_y}, \mathcal{B}_z)$ that is completely determined by three amplitudes $(\mathcal{B}_x, \mathcal{B}_y, \mathcal{B}_z)$ and two relative phases $(\phi_x, \phi_z)$

$$\vec{\mathcal{B}}(t) = \frac{1}{2}\left[\vec{\mathcal{B}}e^{-i\omega_\mu t} + \vec{\mathcal{B}}^\star e^{i\omega_\mu t}\right] = \sum_{j=x,y,z} \mathcal{B}_j \cos(\omega_\mu t + \phi_j), \tag{3.3}$$

where $\phi_z = 0$ without loss of generality.

### 3.1.1 Rotating wave approximation take 1: numerical averaging

The Hamiltonian in Eq. (3.1) can be made time-independent by making the rotating wave approximation (RWA), which eliminates rapidly oscillating terms at $2\omega_{\mu\mathrm{w}}$ in a rotating frame. The transition to this rotating frame is achieved with the unitary operator $\mathcal{U}$, characterized by its diagonal elements $\mathcal{U}_{ii} = 1$ ($\mathcal{U}_{ii} = e^{-i\omega_{\mu\mathrm{w}} t}$) for states in the $F = 1$ ($F = 2$) manifold, and making the transformation

$$H'(t) = \mathcal{U}^\dagger H(t) \mathcal{U} - i\mathcal{U}^\dagger \frac{d\mathcal{U}}{dt}. \tag{3.4}$$

We eliminate the counter-rotating terms by numerically averaging $H'(t)$ with time-steps $\Delta t = 1/(\nu_\mu N_{\mathrm{ave}})$, where $N_{\mathrm{ave}}$ is the number of averages

$$H_{\mathrm{RWA}} = \frac{1}{N_{\mathrm{ave}}} \sum_{k=0}^{N_{\mathrm{ave}}-1} H'(k\Delta t) \tag{3.5}$$

such that high-frequency terms $\propto e^{\pm in\omega_\mu t}$ oscillating at multiple integers of $\nu_{\mu\mathrm{w}}$ are eliminated. Here we use $N_{\mathrm{ave}} = 4$, where $e^{\pm in\omega_\mu t}$ terms in this rotated frame are efficiently averaged away using time-steps $\Delta t$. By doing this we have eliminated microwave coupling terms between magnetic sublevels within each hyperfine manifold $\langle F, m| H_{\mu\mathrm{w}} |F, m'\rangle$ that are otherwise far-detuned ($\Delta_{\mu\mathrm{w}} \approx 2A_{\mathrm{hfs}}/h$) from the single-photon transition resonance. We have also eliminated coupling between the hyperfine levels arising from off-diagonal elements in $H_{\mathrm{zeeman}}$: $\langle 2I-1, m_F| H_{\mathrm{zeeman}} |2I+1, m_{F'}\rangle$. An unintended consequence of this is that nonlinear Zeeman (NLZ) shifts within each manifold have also been eliminated. NLZ effects are not important for studying Rabi oscillation dephasing, but play a significant role for performing accurate hyperfine spectroscopy using Rabi oscillations as done in the next chapter.

### 3.1.2 Rotating wave approximation take 2: keeping NLZ shifts

In order to preserve NLZ shifts after making the RWA, we work in an atom frame $\mathcal{A} = (x_a, y_a, z_a)$ whose z-axis is aligned with the static magnetic field $\vec{B}$ that is oriented in a laboratory frame $\mathcal{L} = (x, y, z)$. Within this atom-frame we work in a modified hyperfine basis $|\overline{F, m}\rangle = \mathcal{M}\,|F, m\rangle$ with $\mathcal{M}$ being defined as the operator that diagonalizes the Hamiltonian defined only by the static hyperfine and Zeeman terms in Eq. (3.1), namely $H(t) - H_{\mu\text{w}}(t) = H_{\text{hfs}} + H_{\text{zeeman}}$. After making this basis change, namely

$$\tilde{H}(t) = \mathcal{M}H(t)\mathcal{M}^{\dagger}, \tag{3.6}$$

we repeat the rotating frame transformation and averaging steps in Eq. (3.4) and Eq. (3.5). The final Hamiltonian is compactly expressed as

$$\begin{aligned} H =&\mathcal{M}\big[(A + h\frac{\nu_{\text{bg}}}{2})\mathbf{S}\cdot\mathbf{I} + \mu_B(g_s S_z + g_i I_z)B\big]\mathcal{M}^{\dagger} - \\ &I_2 h\nu_{\mu\text{w}} + \sum_{|m-m'|\leq 1} \frac{h}{2}\Big[\,|\overline{2, m'}\rangle\,\Omega_m^{m'}\,\langle\overline{1, m}| + \text{h.c.}\Big] \end{aligned} \tag{3.7}$$

where $I_2$ is the $F = 2$ identity operator. The Rabi frequency $\Omega_m^{m'}$ that characterizes the coupling between hyperfine sublevels $|1, m\rangle$ and $|2, m'\rangle$ is given by

$$\Omega_m^{m'} = \mu_m^{m'}\mathcal{B}_k^{(\alpha,\beta)}/h \tag{3.8}$$

where $\mu_m^{m'}$ denotes the corresponding magnetic transition dipole moment defined in Sec. 3.1.3 and $k = \pm, \pi$ denotes the polarization of the hyperfine transition. The spherical microwave components [see Fig. 3.2(a)] are defined by

$$\mathcal{B}_k^{(\alpha,\beta)} = R_y(-\beta)R_z(-\alpha)\{\mathcal{B}_x e^{-i\phi_x}, \mathcal{B}_y e^{-i\phi_y}, \mathcal{B}_z\}\cdot\hat{\epsilon}_k \tag{3.9}$$

where $R_{y,z}$ are 3D rotation operators about the $y, z$ axes, $k = \pm, \pi$, and $\epsilon_{\pm} = \{\frac{1}{\sqrt{2}}, \mp\frac{i}{\sqrt{2}}, 0\}$ and $\epsilon_{\pi} = \{0, 0, 1\}$ are spherical projection operators defined in $\mathcal{A}$.

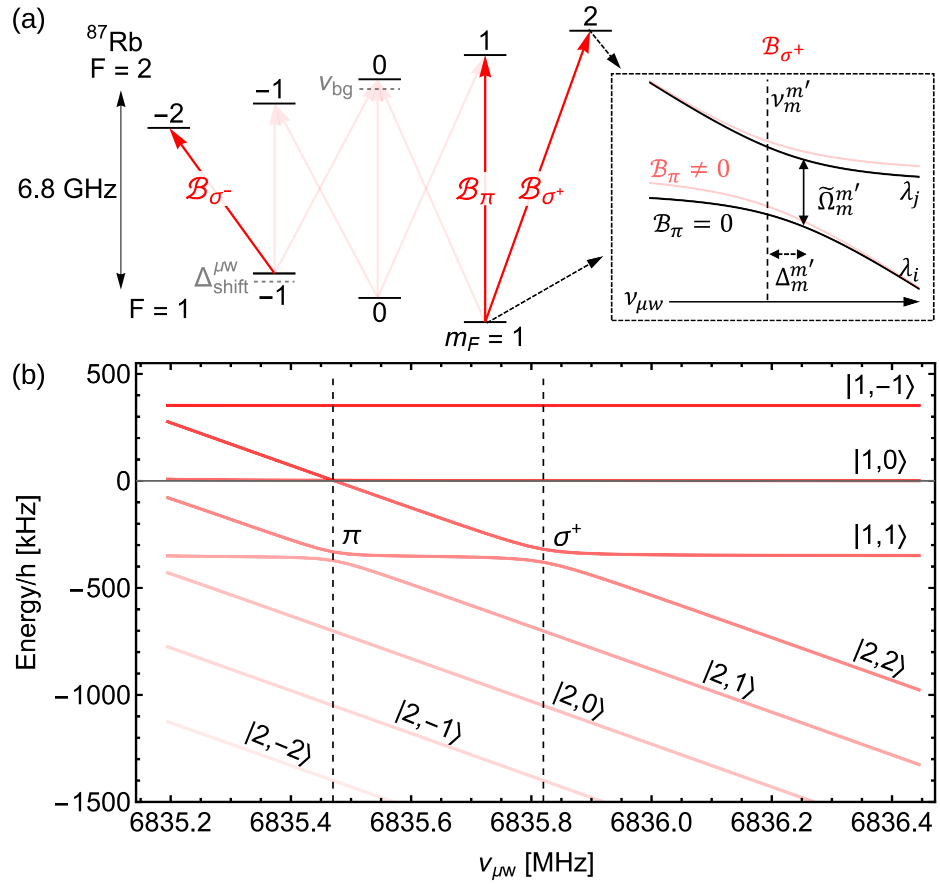


Figure 3.2: Atom-microwave coupling within the hyperfine manifolds of $^{87}$Rb. (a) Energy-level diagram showing all possible hyperfine transitions (red arrows), and specific examples of $\sigma^{\pm}$ and $\pi$ transitions (solid red). Inset shows anti-crossing of the atom-microwave Hamiltonian eigen-states ($\lambda_j$) near a hyperfine transition resonance. Rabi rates are given in terms of this anti-crossing $\Omega_m^{m'} = (\lambda_j - \lambda_i)/h$ (b) Energy eigenvalues ($\lambda_i$) plotted in a frame rotating at $\nu_{\mu\text{w}}$ for a magnetic field strength $B = 50\ \mu$T and microwave parameters $\mathcal{B}_x = 3.5\ \mu$T, $\mathcal{B}_x = 5.9\ \mu$T, $\mathcal{B}_z = 0.1\ \mu$T, $\phi_x = 2.6$ rad, $\phi_y = 4.0$ rad. Anti-crossings occur at the hyperfine resonances (dashed lines).

The diagonal elements of $H$ are given in terms of the energies $E_{\pm,m_F}$ of the $|I \pm 1/2, m_F\rangle$ due to hyperfine and Zeeman splitting and a displaced Kronecker delta function centered about $F = 2$

$$H_{ii} = E_{\pm,m_F} - \delta(F-2)h\nu_{\mu\text{w}}. \tag{3.10}$$

The energies $E_{\pm,m_F}$ are given by the Breit-Rabi formula

$$E_{\pm,m_F} = -\frac{\Delta E}{2(2I+1)} + g_i\mu_B m_F B \pm \frac{\Delta E}{2}\left(1 + \frac{4m_F x}{2I+1} + x^2\right)^{1/2} \tag{3.11}$$

where $x = (g_s - g_i)\mu_B B/\Delta E$, and $\Delta E = A(I + 1/2)$. These are the eigenvalues of $H$ when the microwave field is off ($\Omega_m^{m'} = 0$). With the microwave field on, the eigenvalues of H exhibit anti-crossings at the hyperfine transition resonances [see Fig. 3.2(b)]. We will use energy separation of these anti-crossings to calculate the exact Rabi oscillation frequency at a driving microwave frequency $\nu_{\mu\text{w}}$ with shifts arising from off-resonant driving. As defined in Eq. 3.7, the magnetic field is along $\hat{z}$. Simulation of spin-dynamics in arbitrary magnetic fields directions is achieved with the rotated Hamiltonian

$$H^{(\alpha,\beta)} = e^{-iF_z\alpha}e^{-iF_y\beta}He^{iF_y\beta}e^{iF_z\alpha} \tag{3.12}$$

where $F_x$, $F_y$, and $F_z$ denote the Cartesian components of the total atomic spin operator $\vec{F} = \vec{S} + \vec{I}$.

### 3.1.3 Transition dipole moments

Table 3.1: The magnetic transition dipole moments $\mu_m^{m'}$ for hyperfine transitions $|1, m\rangle \leftrightarrow |2, m'\rangle$. The middle column displays $\mu_m^{m'}$ in the limit of $B = 0$. The rightmost column displays the relative change in $\mu_m^{m'}$ at 50 $\mu$T given by $\delta\mu_m^{m'} = [\mu_m^{m'}(B = 50\ \mu\text{T})]/[\mu_m^{m'}(B = 0)]$.

| transition | $\mu_m^{m'}(B = 0)$ | $\delta\mu_m^{m'} - 1$ [%] |
|---|---|---|
| $\|1,1\rangle \leftrightarrow \|2,2\rangle$ | $-\sqrt{\frac{3}{8}}(g_s - g_i)\mu_B$ | $0.42 \times 10^{-2}$ |
| $\|1,1\rangle \leftrightarrow \|2,1\rangle$ | $\frac{\sqrt{3}}{4}(g_s - g_i)\mu_B$ | $-1.22 \times 10^{-2}$ |
| $\|1,1\rangle \leftrightarrow \|2,0\rangle$ | $\frac{1}{4}(g_s - g_i)\mu_B$ | $-2.66 \times 10^{-2}$ |
| $\|1,0\rangle \leftrightarrow \|2,1\rangle$ | $-\frac{\sqrt{3}}{4}(g_s - g_i)\mu_B$ | $1.44 \times 10^{-2}$ |
| $\|1,0\rangle \leftrightarrow \|2,0\rangle$ | $\frac{1}{2}(g_s - g_i)\mu_B$ | $0.10 \times 10^{-2}$ |
| $\|1,0\rangle \leftrightarrow \|2,-1\rangle$ | $\frac{\sqrt{3}}{4}(g_s - g_i)\mu_B$ | $-1.63 \times 10^{-2}$ |
| $\|1,-1\rangle \leftrightarrow \|2,0\rangle$ | $-\frac{1}{4}(g_s - g_i)\mu_B$ | $2.47 \times 10^{-2}$ |
| $\|1,-1\rangle \leftrightarrow \|2,-1\rangle$ | $\frac{\sqrt{3}}{4}(g_s - g_i)\mu_B$ | $0.93 \times 10^{-2}$ |
| $\|1,-1\rangle \leftrightarrow \|2,-2\rangle$ | $\sqrt{\frac{3}{8}}(g_s - g_i)\mu_B$ | $0.61 \times 10^{-2}$ |

These transition dipole moments for the $\pi$ $(m' = m)$ and $\sigma^{\pm}$ $(m' = m \pm 1)$ transitions are given by

$$\mu_m^m = \mu_B \langle\overline{2,m}|\, \mathcal{M}(g_s S_\pi + g_i I_\pi)\mathcal{M}^\dagger\, |\overline{1,m}\rangle \tag{3.13}$$

$$\mu_m^{m\pm1} = \frac{\mu_B \langle\overline{2,m\pm1}|\, \mathcal{M}(g_s S_\pm + g_i I_\pm)\mathcal{M}^\dagger\, |\overline{1,m}\rangle}{\sqrt{2}} \tag{3.14}$$

where $S_\pi = S_z$ and $S_\pm = S_x \pm iS_y$ are the electron-spin raising and lowering operators with analogous definitions for the nuclear-spin operators $I_\pi$ and $I_\pm$. Table 3.1 tabulates these dipole moments for all $5^2S_{1/2}$ hyperfine transitions in $^{87}$Rb [see Fig. 3.2(a)].

Calculation of these dipole moments requires the knowledge of the operator $\mathcal{M}$ that diagonalizes $H_{\text{hfs}} + H_{\text{zeeman}}$. While the effect of the pressure shift $\nu_{\text{bg}} \approx 88$ kHz on $\mathcal{M}$ is negligible, the magnetic field-strength dependence of $\mathcal{M}$ is also small, but not negligible. The third column of Table 3.1 diplays the relative change of $\mu_m^{m'}$ at $B = 50$ $\mu$T from $B = 0$. Table 3.2 shows the magnetic field-strength dependence of $\mathcal{M}$ that is calculated by fitting polynomial terms to the $\mathcal{M}$-matrix elements for $B \in \{0, 1\}$ mT. The explicit functions for this magnetic field dependence are given by

$$
\begin{aligned}
\mathcal{M}_{11}(B) &= 1 - 1.57774B^2 + 6.47256B^3 - 6.35276B^4 \\
\mathcal{M}_{22}(B) &= 1 - 2.10366B^2 - 0.0000379091B^3 + 24.3589B^4 \\
\mathcal{M}_{33}(B) &= 1 - 1.57774B^2 - 6.47264B^3 - 6.04991B^4 \\
\mathcal{M}_{55}(B) &= \mathcal{M}_{11}(B) \\
\mathcal{M}_{66}(B) &= \mathcal{M}_{22}(B) \\
\mathcal{M}_{77}(B) &= \mathcal{M}_{33}(B) \\
\mathcal{M}_{15}(B) &= 1.77637B - 3.64364B^2 - 0.933969B^3 + 36.1278B^4 \\
\mathcal{M}_{26}(B) &= 2.05117B + 1.16664 \times 10^{-7}B^2 - 12.9456B^3 + 0.35176B^4 \\
\mathcal{M}_{37}(B) &= 1.77637B + 3.64364B^2 - 0.933969B^3 - 36.6891B^4
\end{aligned}
\tag{3.15}
$$

where $B$ is in units of Tesla.

### 3.1.4 Spin dynamics without decoherence

To study spin-dynamics we use the density-matrix formalism that describes the state of an atomic ensemble by the density matrix

$$\rho = \frac{1}{N}\sum_{i=1}^{N} |\psi_i\rangle \langle\psi_i| \tag{3.16}$$

Table 3.2: The operator $\mathcal{M}$, that transforms the hyperfine basis $|F, m_F\rangle$ into the basis $|\overline{F, m_F}\rangle$ that diagonalizes the hyperfine and Zeeman part of the Hamiltonian defined by Eq. 3.7.

| | $\|1,1\rangle$ | $\|1,0\rangle$ | $\|1,-1\rangle$ | $\|2,2\rangle$ | $\|2,1\rangle$ | $\|2,0\rangle$ | $\|2,-1\rangle$ | $\|2,-2\rangle$ |
|---|---|---|---|---|---|---|---|---|
| $\|\overline{1,1}\rangle$ | $\mathcal{M}_{11}(B)$ | 0 | 0 | 0 | $-\mathcal{M}_{15}(B)$ | 0 | 0 | 0 |
| $\|\overline{1,0}\rangle$ | 0 | $\mathcal{M}_{22}(B)$ | 0 | 0 | 0 | $-\mathcal{M}_{26}(B)$ | 0 | 0 |
| $\|\overline{1,-1}\rangle$ | 0 | 0 | $\mathcal{M}_{33}(B)$ | 0 | 0 | 0 | $-\mathcal{M}_{37}(B)$ | 0 |
| $\|\overline{2,2}\rangle$ | 0 | 0 | 0 | 1 | 0 | 0 | 0 | 0 |
| $\|\overline{2,1}\rangle$ | $\mathcal{M}_{15}(B)$ | 0 | 0 | 0 | $\mathcal{M}_{55}(B)$ | 0 | 0 | 0 |
| $\|\overline{2,0}\rangle$ | 0 | $\mathcal{M}_{26}(B)$ | 0 | 0 | 0 | $\mathcal{M}_{66}(B)$ | 0 | 0 |
| $\|\overline{2,-1}\rangle$ | 0 | 0 | $\mathcal{M}_{37}(B)$ | 0 | 0 | 0 | $\mathcal{M}_{77}(B)$ | 0 |
| $\|\overline{2,-2}\rangle$ | 0 | 0 | 0 | 0 | 0 | 0 | 0 | 1 |

where $|\psi_i\rangle$ is the quantum state of the $i^{th}$ atom. We consider the eight Zeeman sublevels $|F, m_F\rangle$ within the $F = 1, 2$ hyperfine manifolds, such that $\rho$ is expressed as an $8 \times 8$ matrix. We use the index notation $|F, m_F\rangle \to i = 4F - m_F - 2$, where for example $\langle 2, 2| \rho |2, 2\rangle \to \rho_{44}$, and $\langle 1, 1| \rho |2, 2\rangle \to \rho_{14}$. In this formalism the diagonal elements $\rho_{ii}$ are the atomic populations of each sublevel, and off-diagonal elements $\rho_{ij}$ describe coherences between two sublevels. Expectation values of atomic observables $\mathcal{O}$, such as the z-component of the electron spin $S_z$, are calculated by taking the trace of the product $\rho\mathcal{O}$: $\langle\mathcal{O}\rangle = \mathrm{Tr}[\rho\mathcal{O}]$. Time-evolution of an initial atomic state $\rho_i$ is calculated through the commutation of the Hamiltonian $H^{(\alpha,\beta)}$ (Eq. (3.12)) with the density matrix $\rho$ known as the Liouville-von Neumann equation

$$\frac{d\rho}{dt} = \frac{[H^{(\alpha,\beta)}, \rho]}{i\hbar}. \tag{3.17}$$

In the case that $H^{(\alpha,\beta)}$ is time-independent, time-evolution of an initial atomic state $\rho_0$ is calculated by

$$\rho(t) = e^{-iH^{(\alpha,\beta)}t/\hbar}\rho_0 e^{i(H^{(\alpha,\beta)})^\dagger t/\hbar}. \tag{3.18}$$

Eq. (3.18) can be written more concretely if we diagonalize the atom-microwave Hamiltonian $H^{(\alpha,\beta)} \to H_d^{(\alpha,\beta)}$ through $H_d^{(\alpha,\beta)} = D^* H^{(\alpha,\beta)} D^T$. Then, the diagonal elements $\{\lambda_1, ..., \lambda_8\}$ of $H_d^{(\alpha,\beta)}$

are the eigenvalues of $H^{(\alpha,\beta)}$. If we put the Faraday rotation operator $\mathcal{F}_d = D^*\mathcal{F}_d D^T$ and the initial density matrix $\rho_{i,d} = D^*\rho_i D^T$ also into this basis, then the resulting Faraday rotation angle is given by

$$\theta_F(t) \propto \sum_{i=1}^{8}(\mathcal{F}_d)_{ii}(\rho_{0,d})_{ii} + \sum_{i\neq j}^{8}\left|(\mathcal{F}_d)_{ij}(\rho_{0,d})_{ji}\right|\cos\Big(2\pi t\big(\lambda_j-\lambda_i\big)/h - \mathrm{Arg}\big((\mathcal{F}_d)_{ij}(\rho_{0,d})_{ji}\big)\Big) \quad (3.19)$$

where the first sum represents a DC offset, while the second summand represents oscillatory signals with frequencies given by the eigenvalues of $H^{(\alpha,\beta)}$. The amplitude and phases of these oscillations are given by magnitude and argument of the complex numbers: $(\mathcal{F}_d)_{ij}(\rho_{0,d})_{ji}$.

We consider, as a concrete example, the specific case where atomic spin polarization is initialized along $\hat{z}$ with the atomic population occupying $|1,1\rangle$ with $\rho_{11} = 0.3$ and $|2,2\rangle$ with $\rho_{44} = 0.7$. We also assume that the magnetic field is aligned along $\hat{z}$ with field strength $B = 50\ \mu$T. If only the $\mathcal{B}_x = 2\ \mu$T of the microwave field is nonzero, then from Eq. (3.8) and Eq. (3.9), the Rabi rate defining the $\sigma^+$ transition $|1,1\rangle - |2,2\rangle$ transition is $\Omega_m^{m'} = \Omega_1^2 = 24.283$ kHz. For a microwave frequency $\nu_{\mu\mathrm{w}} = 6835.82$ MHz that is near-resonant ($\Delta = 0$ kHz) with this $\sigma^+$ transition and the detuned case $\nu_{\mu\mathrm{w}} = 6835.845$ MHz ($\Delta = 25$ kHz), Eq. (3.19) predicts the Rabi oscillations shown in Fig. 3.3(a). In this case, only Eq. (3.19) contains only one frequency component corresponding to a specfic pair of eigenvalues $(\lambda_j - \lambda_i)/h$. This frequency component is the generalized Rabi frequency.

In contrast, if the microwave field is turned off and the magnetic field oriented with polar angle $\beta = 1$ rad (57.3°), then we observe Larmor precession [see Fig. 3.3(b)]. In this case six frequency components are nonzero corresponding to the Zeeman frequencies $\approx 350$ kHz. In Fig. 3.3(b) beating is observed due to the 1.4 kHz difference between the Zeeman splittings of the $F = 1$ and $F = 2$ manifolds.

## 3.2 Selection of eigenvalues for Rabi modeling

In the previous section, we saw that the generalized Rabi frequency can be modeled by the atom-microwave Hamiltonian through a pair of eigenvalues

$$\tilde{\Omega}_m^{m'} = \delta\lambda_m^{m'} \equiv (\lambda_j - \lambda_i)/h. \quad (3.20)$$

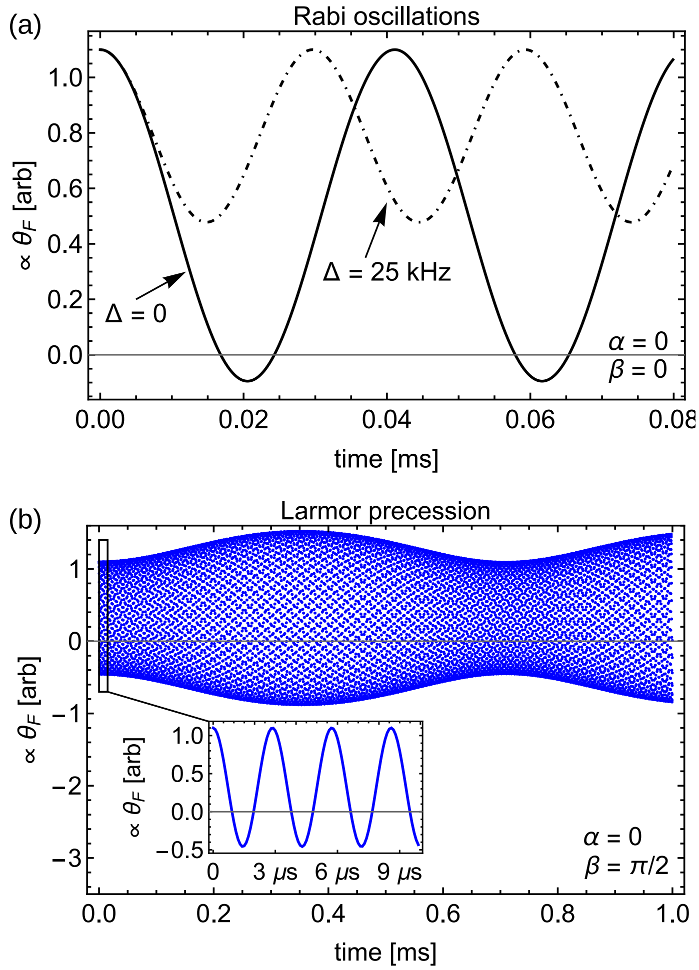


Figure 3.3: Rabi and FID spin dynamics without decoherence using Eq. 3.19. Initial atomic population given by $\rho_{11} = 0.3$ and $\rho_{44} = 0.7$ and off-diagonal coherences are set to zero. Assumes a 50 $\mu$T field and pressure shift $\nu_{\rm bg} = 88$ kHz. (a) Rabi oscillation dynamics of the $|1,1\rangle - |2,2\rangle$ driven on resonance with $\nu_{\mu\rm w} = 6835.82$ MHz ($\Delta = 0$) and $\nu_{\mu\rm w} = 6835.845$ MHz ($\Delta = 25$). (b) Larmor precession with 1.4 kHz beating from the difference in Zeeman splittings between the $F = 1$ and $F = 2$ manifolds.

where we use the shorthand notation $\delta\lambda_m^{m'}$ to denote the eigenvalue defference coresponding to the hyperfine transition defined by $|1,m\rangle$ and $|2,m'\rangle$. In this section, we discuss a general approach to find the correct eigenvalue pair for any hyperfine transition. First, we diagonalize the atom-microwave Hamiltonian $H \rightarrow H_d$ through $H_d = D^* H D^T$. Then, the diagonal elements $\{\lambda_1, ..., \lambda_8\}$ of $H_d$ are the eigenvalues of $H$. Next, let $\rho_m^{m'}$ be the density matrix with all the atomic population in the $|2,m'\rangle$ and $S_{z,d} = \mathrm{diag}(S_z)$ consisting of the diagonal elements of z-component of the electron spin operator $S_z$. Let $i, j$ be the matrix indices such that$|(D^*\rho_m^{m'}D^T)_{ij} \times (D^*S_{z,d}D^T)_{ji}|$ is maximized. Then those indices correspond to the appropriate pair of eigenvalues from the $\{\lambda_1, ..., \lambda_8\}$ list obtained from the diagonal elements of $H_d$ such that $\tilde{\Omega}_m^{m'} = (\lambda_j - \lambda_i)/h$.

### 3.3 Rabi oscillations with collisional relaxation

The time evolution of the atomic ensemble including multiple sources of collisional relaxation is given by Refs. [12, 40, 89]

$$\begin{aligned}\dot{\rho} =& \frac{[H,\rho]}{i\hbar} + \frac{[\delta\mathcal{E}_{\rm se},\rho]}{i\hbar} + \dot{\rho}_{\rm se} + \dot{\rho}_{\rm sd} + \dot{\rho}_{\rm c} + \dot{\rho}_{\rm D} \\ =& \frac{[H,\rho]}{i\hbar} + \frac{[n_{\rm Rb}\lambda_{\rm se}v_r\langle\mathbf{S}\rangle\cdot\mathbf{S},\rho]}{i\hbar} + \Gamma_{\rm se}\big(\phi(1+4\langle\mathbf{S}\rangle\cdot\mathbf{S}) - \rho\big) + \\ & \Gamma_{\rm sd}\big(\phi-\rho\big) - \frac{\eta_I^2[I]^2}{8}\Gamma_{\rm C}\rho^{(\rm m)} + \Gamma_D(\rho^e - \rho)\end{aligned} \tag{3.21}$$

where $H$ is the atom-microwave Hamiltonian defined in Eq. (3.7) and $\phi = \rho/4 + \mathbf{S}\cdot\rho\mathbf{S}$ is known as the nuclear part of the density matrix for which $\mathrm{Tr}[\phi\mathbf{S}] = 0$ and $\mathrm{Tr}[\phi] = 1$ [15]. The terms $\dot{\rho}_{\rm se}$ and $\dot{\rho}_{\rm sd}$ in Equation (3.21) represent the relaxation processes due to spin-exchange (SE) and spin-damping (SD) collisions. The mechanism of SE collisions involves a spin-spin coupling interaction, described by $J(r)\mathbf{S}'\cdot\mathbf{S}$, which ensures the conservation of total spin for the interacting electron spins, denoted by $\mathbf{S}'$ and $\mathbf{S}$. In contrast, SD collisions, which result in the loss of electron spin polarization, occur due to a spin-rotation interaction ($\gamma(r)\mathbf{N}\cdot\mathbf{S}$). Here, the electron spin angular momentum $\mathbf{S}$ is transferred to the angular momentum of the colliding pair $\mathbf{N}$. The collision rates $\Gamma_{\rm se(sd)} = n_{\rm a(N_2)}\sigma_{\rm se(sd)}v_r$ for these processes are defined by the cross sections $\sigma_{\rm se(sd)}$, the mean relative velocity $v_r$ of the colliding entities, and $n_a$ ($n_{\rm N_2}$), representing the atomic density for alkali and buffer gas collisions, respectively [12].

Additionally, the term $\delta\mathcal{E}_{\rm se}$ of Eqn. (3.21) accounts for frequency shifts from SE collisions [15, 176] proportional to a spin-exchange frequency shift cross-section $\lambda_{\rm se} = 0.69\times10^{-18}$ m$^2$ [124]. The next chapter will explore their influence in Rabi frequency spectroscopy. The term $\dot{\rho}_{\rm c}$ models pure dephasing of microwave transitions due to buffer gas collisions, where $\rho^{(\rm m)}$ signifies the density matrix with off-diagonal terms representing the coherences between the upper and lower hyperfine

Table 3.3: Cross-sections, diffusion constant, and the corresponding collision rates $\Gamma$ for the different collisional processes for a vapor cell with volume ($3 \times 3 \times 2$ mm$^3$), vapor temperature $\mathcal{T}_v = 107$ °C, buffer gas pressure $P_{N_2} = 180$ Torr (24 kPa), and diffusion constant $D_0 = 0.221$ cm$^2$s$^{-1}$ for Rb-$N_2$ buffer gas collisions scaled to our vapor temperature [142].

| Collision | $\sigma$ [$10^{-18}$ m$^2$] | $\Gamma = n\sigma v^r$ [Hz] |
|---|---|---|
| $(\text{Rb-Rb})_{\text{se}}$ | 1.9 [65] ($\lambda_{\text{se}} = 0.69$ [124]) | $6.2 \times 10^3$ |
| $(\text{Rb-Rb})_{\text{sd}}$ | $1.77 \times 10^{-3}$ [180] | 5.8 |
| $(\text{N}_2\text{-Rb})_{\text{sd}}$ | $1.44 \times 10^{-8}$ [180] | 41 |
| $(\text{N}_2\text{-Rb})_{\text{carver}}$ | $\Gamma_{\text{C}}/[\text{N}_2] = 394$ amg$^{-1}$s$^{-1}$ [181] | $\Gamma_{\text{C}} = 67$ |
| wall | $D_0 P_0 = 0.017$ m$^2$Torr [142] | $\Gamma_{\text{D}} = 4.4 \times 10^2$ |

manifolds. Here, $\Gamma_{\text{C}}$ is the Carver rate, and $\eta_I = \mu_I/(2I\mu_N)$ is the isotope coefficient [89, 181] where $\mu_I$ and $\mu_N$ are the nuclear magnetic moment and the nuclear magneton respectively.

The final term models diffusion into the cell walls where alkali spins are completely randomized. Here $\rho^e$ is the equilibrium density matrix with all populations $\rho^e_{ii}$ equal and $\Gamma_{\text{D}} = D\pi^2/(l_x^2 + l_y^2 + l_z^2)$ is the fundamental decay mode defined by the vapor cell dimensions $l_x$, $l_y$, and $l_z$ [60]. The diffusion constant $D = D_0 \text{P}_0/\text{P}_{\text{N}_2}$ is attenuated by the buffer gas pressure where $\text{P}_0 = 1$ atm. This study also considers higher-order diffusion modes due to focused pumping through the vapor cell. For context, Table 3.3 contains the collision rates, cross-sections, and diffusion constant assuming the vapor cell parameters and the Rb-$N_2$ alkali-buffer gas mixture used in our experiment. Doppler broadening is an insignificant factor in decoherence for the $5^2\text{S}_{1/2}$ hyperfine transitions, attributed to the relatively low transition frequencies. This leads to considerable Dicke narrowing [53, 176], particularly since the microwave wavelengths greatly exceed the 700 nm mean free path (Eq. (2.2)) of Rb atoms in our vapor cell.

To solve Eq. (3.21) we must place the decoherence operators, e.g. $\Gamma_{\text{se}}\big(\phi(1 + 4\langle \mathbf{S}\rangle \cdot \mathbf{S}) - \rho\big)$, in the rotating frame and make the RWA accordingly. To do this we first put the spin matrices in the rotating frame $\tilde{\mathbf{S}}(t) = \mathcal{U}^\dagger \mathbf{S} \mathcal{U}$ and then numerically average the decoherence operators with time-steps $\Delta t = 1/(\nu_\mu N_{\text{ave}})$, where $N_{\text{ave}}$ is the number of averages. We cannot average the spin-matrices individually since the decoherence operators contain higher-order products like $\tilde{S}_x(t)\rho(t)\tilde{S}_x(t)$ that contain nontrivial cancellation of counter-rotating terms before averaging. Instead, we calculate

$$\tilde{S}_x(t)\rho(t)\tilde{S}_x(t) \rightarrow \frac{1}{N_{\text{ave}}} \sum_{k=0}^{N_{\text{ave}}-1} \tilde{S}_x(k\Delta t)\rho(t)\tilde{S}_x(k\Delta t) \tag{3.22}$$

such that high-frequency terms $\propto e^{\pm in\omega_\mu t}$ oscillating at multiple integers of $\nu_\mu$ are eliminated. Note that since we are using the time-independent Hamiltonian $\tilde{H}$, $\rho(t)$ in the rotated frame contains no counter-rotating terms and is left fixed at time $t$ during the averaging. Here we again use $N_{\text{ave}} = 4$, where $e^{\pm in\omega_\mu t}$ terms in this rotated frame are efficiently averaged away using time-steps $\Delta t$. Using more averaging terms only increases computation time.

### 3.3.1 Spin-exchange weak-driving approximation

Due to the nonlinear nature of the collisional relaxation operators in Eq. (3.21) (such as $\langle \mathbf{S} \rangle \cdot \mathbf{S}$), finding exact analytical solutions is not feasible. In this section, we explore the weak-driving approximation. This approach assumes constant atomic populations, allowing us to derive an analytical formula for the spin-exchange dephasing rate, denoted as $\gamma_{se} \equiv 1/T_2^{\text{se}}$. Our primary focus is on spin-exchange collisions, the predominant cause of collisional decoherence. However, the methodologies discussed here could also be adapted for calculating SD dephasing rates. Additionally, this chapter concentrates on the hyperfine transitions illustrated in Fig. 3.1(a).

To analytically describe hyperfine decoherence due to SE collisions for weak driving, the typical path [176] is to first write $\dot{\rho}_{\text{se}} = \Gamma_{\text{se}}\big[\phi(1 + 4\langle \mathbf{S} \rangle \cdot \mathbf{S}) - \rho\big]$ in the approximation such that $\rho$ is diagonal except for the coherence $\rho_{ij}$ that corresponds to the driven transition, and assuming fixed populations:

$$\rho \to \rho_+^{\mathrm{wk}} = \begin{bmatrix} \rho_{11} & 0 & 0 & \rho_{14} & 0 & 0 & 0 & 0 \\ 0 & \rho_{22} & 0 & 0 & 0 & 0 & 0 & 0 \\ 0 & 0 & \rho_{33} & 0 & 0 & 0 & 0 & 0 \\ \rho_{41} & 0 & 0 & \rho_{44} & 0 & 0 & 0 & 0 \\ 0 & 0 & 0 & 0 & \rho_{55} & 0 & 0 & 0 \\ 0 & 0 & 0 & 0 & 0 & \rho_{66} & 0 & 0 \\ 0 & 0 & 0 & 0 & 0 & 0 & \rho_{77} & 0 \\ 0 & 0 & 0 & 0 & 0 & 0 & 0 & \rho_{88} \end{bmatrix} \tag{3.23}$$

The proper application of the rotating wave approximation (RWA) to $\dot{\rho}_{\mathrm{se}}$, as detailed in a prior section, is also necessary in these calculations. However, this is only crucial for the case where $k = \pi$. For the dephasing rates associated with $k = \pm$, the weak-driving approximation remains unaffected by the RWA. When we assess $\dot{\rho}_{\mathrm{se}}$ using $\rho \to \rho{+}^{\mathrm{wk}}$, it leads to the derivation of an exponential decay equation for the $\sigma^+$ coherence:

$$\dot{\rho_{14}} = -\gamma_{\mathrm{se},+}^{\mathrm{wk}}\rho_{41} = \rho_{41}\Gamma_{\mathrm{se}}\left[\frac{7}{8}(\rho_{44}-1) + \frac{\rho_{11}}{2} + \frac{\rho_{33}-\rho_{77}}{16} + \frac{\rho_{55}}{4} - \frac{\rho_{88}}{8}\right] \tag{3.24}$$

The exponential decay rate, $\gamma_{\mathrm{se},+}^{\mathrm{wk}}$, equals the rate reported by Y. Y. Jau et al. for weak microwave driving [88]. This same analysis for the $\sigma^-$ transition gives

$$\dot{\rho_{16}} = \rho_{61}\Gamma_{\mathrm{se}}\left[\frac{3}{32}\rho_{11} + \frac{\rho_{22}-\rho_{33}}{16} + \frac{\rho_{88}-\rho_{44}}{8} + \frac{\rho_{55}}{32} - \frac{3}{4} + \frac{\rho_{66}+\rho_{77}}{16}\right] \tag{3.25}$$

For the $\pi$ transition this analysis with RWA gives

$$\dot{\rho_{15}} = -\rho_{15}\frac{\Gamma_{\mathrm{se}}}{32}\left[26 - 6\rho_{11} - 3(\rho_{22} + 2(\rho_{44}+\rho_{55}) + \rho_{66})\right] \tag{3.26}$$

For context, other works involving atomic clocks [176] assume that optical pumping simply depopulates the lower hyperfine manifold ($F = 1$) and leaves the upper manifold ($F = 2$) equally populated. While this is physically not the situation in this work, the equations simplify to pure exponential decay equations that are unaffected by the RWA.

$$\begin{aligned} \frac{d\rho_{62}}{dt} &= -\frac{5}{8}\rho_{62} \qquad (|1,0\rangle \rightarrow |2,0\rangle) \\ \frac{d\rho_{51}}{dt} &= -\frac{23}{32}\rho_{51} \qquad (|1,1\rangle \rightarrow |2,1\rangle) \end{aligned} \tag{3.27}$$

The weak-driving approximation can also be used to calculate frequency shifts from spin-exchange collisions defined in Eq. (3.21). For example, to calculate the frequency shift on the $|1,0\rangle - |2,0\rangle$ clock transition we evaluate

$$\frac{d\rho^{\mathrm{wk}}}{dt} = -\frac{i}{\hbar}[H_{\mathrm{ex}}, \rho^{\mathrm{wk}}]. \tag{3.28}$$

where $\mathcal{E}_{\mathrm{ex}} = hn_{\mathrm{Rb}}v_{\mathrm{r}}\lambda_{\mathrm{ex}}\langle\tilde{\mathbf{S}}\rangle \cdot \tilde{\mathbf{S}}$ and $\rho^{\mathrm{wk}}$ is the density matrix under the weak-driving approximation where the only non-zero off-diagonal element is $\rho_{26}$ $\rho_{62}$ corresponding to the $|1,0\rangle - |2,0\rangle$ transition. We find that evaluating Eq. (3.28) gives

$$\frac{d\rho_{26}^{\mathrm{wk}}}{dt} = -i\rho_{26}^{\mathrm{wk}}\Big[\frac{1}{4}n_{\mathrm{Rb}}v_{\mathrm{r}}\lambda_{\mathrm{ex}}(\rho_{66} - \rho_{22})\Big] \tag{3.29}$$

which matches the result in [124].

### 3.3.2 Theoretical microwave detuning dependence

Next, we compare the weak-driving models derived above, with the exact numerical solution of Eq. (3.21). Here we theoretically study the dephasing rate $\gamma \equiv 1/T_2$ of Rabi oscillations with the atomic ensemble initialized in the steady-state solution when SE collisions dominate over other types of collisions and scattering rates. This solution, known as a spin-temperature distribution, is defined by the atomic populations as $\rho_{ii}(0) = \rho_{ii}^{(\mathrm{p})} \propto e^{\beta(\mathrm{p})m_i}$, where $\beta(\mathrm{p}) = \ln\big[\frac{1+\mathrm{p}}{1-\mathrm{p}}\big]$ and $\mathrm{p} \in [0,1]$ is the electron spin polarization. This situation is a close approximation for many vapor cell experiments that optically pump with high buffer gas pressure [22, 88]. We specifically study the $\sigma^{\pm}$ and $\pi$ transitions in Fig. 3.4. For the $\pi$ and $\sigma^{-}$ Rabi oscillations, we set the initial atomic state away from a ST distribution in our simulation by switching the atomic populations of the $\sigma^{+}$ transition ($\rho_{44} \leftrightarrow \rho_{11}$). This switch mimics the adiabatic rapid passage sequence utilized in our measurements and discussed in the next section. Using Eq. 3.21 we investigate $\gamma_{\mathrm{se}}$ as a function of

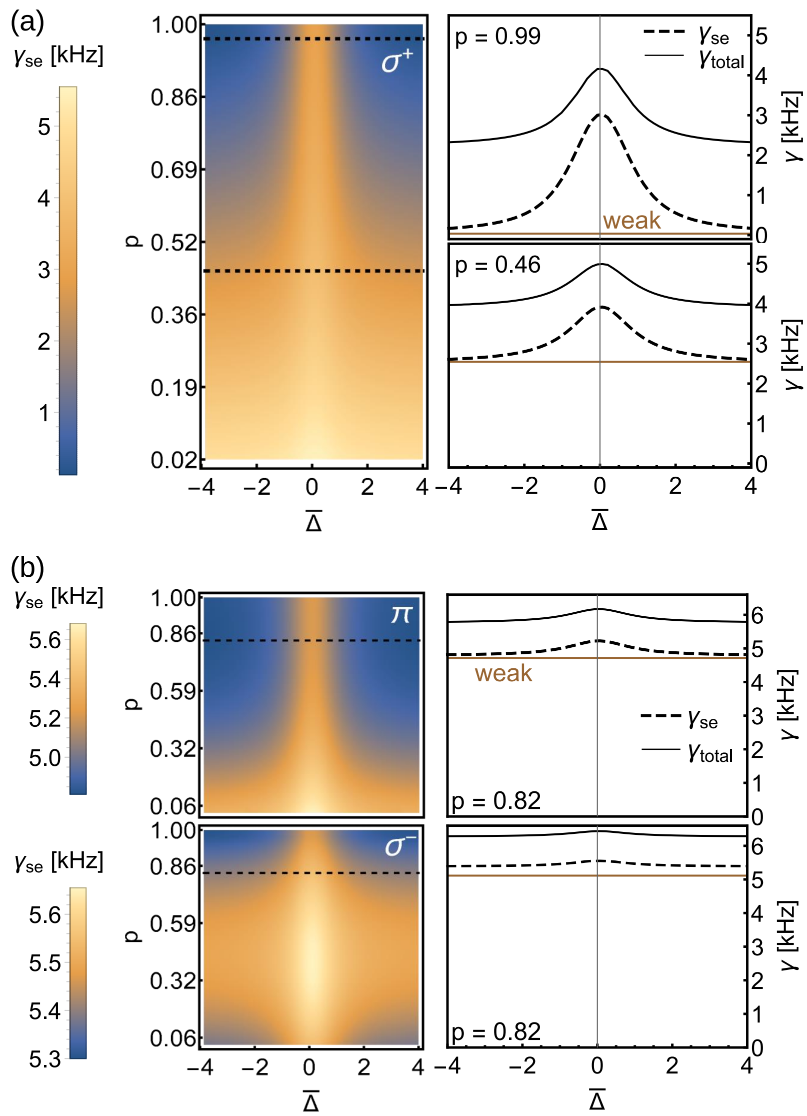


Figure 3.4: Numerical simulation of the dependence of Rabi coherence with electron spin polarization (p) and normalized microwave detuning ($\overline{\Delta}$). The left density plots show the SE dephasing rate $\gamma_{\rm se}$ with black dashed lines indicating p-cuts for the corresponding plots on the right. The right plots simultaneously show the $\gamma_{\rm se}^{\rm wk}$ (brown), the exact SE dephasing rate (black dashed), and the total decay rate $\gamma_{\rm total}$ including SD, pure dephasing from buffer gas collisions, and wall collisions (black solid). For these plots we only include the fundamental diffusion mode to model wall collisions. The cell parameters used in these plots are $\mathcal{T}_{\rm v} = 110°{\rm C}$ and $P_{N_2} = 100$ Torr (13.3 kPa). (a) $\sigma^+$ transition with two p-cuts (b) $\pi$, $\sigma^-$ transitions each with one p-cut.

the electron spin-polarization p and the normalized microwave detuning $\overline{\Delta} = \Delta/\Omega$ as the primary variables affecting atomic population dynamics [see Fig. 3.4]. For this investigation we assume vapor parameters $\mathcal{T}_v = 110$ °C and $P_{N_2} = 100$ Torr (13.3 kPa) and consider Rabi oscillations between the hyperfine ground states of $^{87}$Rb.

By neglecting the $\dot{\rho}_{\rm sd}$, $\dot{\rho}_{\rm c}$, and $\dot{\rho}_{\rm d}$ terms in Eq. (3.21), we can compare the dephasing rate due to SE alone (black dashed) to the case with all collisional processes (black solid) as shown in Fig. 3.4. We also plot the predictions of the weak-driving approximation $\gamma_{\rm se}^{\rm wk}$ (brown) to show the large discrepancy between previous studies of SE dephasing rates with the full-numerical solution shown in this work in the regime of strong coherent driving. Such coherent dynamics and atomic population redistribution from SE collisions leads to an increased dephasing rate $\gamma_{se}$ near $\overline{\Delta} = 0$ that is symmetric with $\overline{\Delta}$ for the transitions and initial states considered here [see Fig. 3.4].

This effect is heightened for the $\sigma^+$ transition where no hyperfine-changing collisions occur for atoms purely in the initial 'stretched' state $|2, 2\rangle$, when all electron spins are aligned, but are coherently coupled into $|1, 1\rangle$ with projections onto states with oppositely aligned electron spins. If the initial atomic populations are not a ST distribution, then the hyperfine coherence will have multiple decay rates because the atomic populations are time-dependent even in the far-detuned limit. This explains the small discrepancy between the weak-driving approximation and the far-detuned Rabi driving in the case of the $\pi$ and $\sigma^-$ transitions due to the $\sigma^+$ population switch [see Fig. 3.4(b)].

## 3.4 Rabi oscillation measurements

To validate this theoretical description, we experimentally drive Rabi oscillations on the $\sigma^\pm$ and $\pi$ microwave transitions near resonance where the theoretical model predicts larger SE dephasing rates than the weak-driving approximation. Due to the planar polarization structure of the microwave field from the microwave cavity, we tilt the magnetic field from the pump-beam axis by 25° such that a non-zero microwave field component drives all microwave hyperfine transitions with respect to $|1, 1\rangle$ [see Fig. 3.1(a)]. In each measurement, we first prepare a spin-polarized atomic ensemble by continuously optically pumping with circularly-polarized light that is near-resonant with the $D_1$ line (795 nm) for 100 $\mu$s. Immediately after, we perform adiabatic pumping by turning

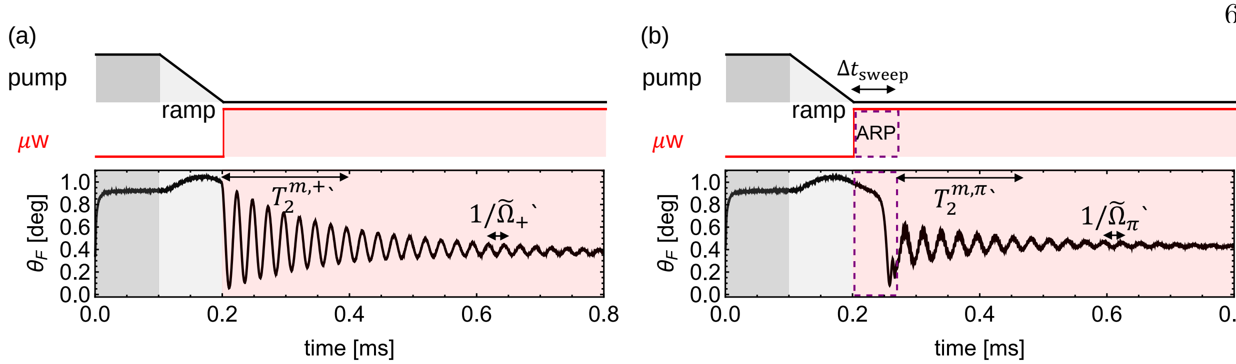


Figure 3.5: Rabi oscillation pulse sequences for the (a) $\sigma^+$ $|11\rangle - |22\rangle$ transition and (b) the $\pi$ $|11\rangle - |21\rangle$ transition. For all measurements first optically pump for 100 $\mu$s and then ramp off the pump power over the next 100 $\mu$s. For the $\pi$ and $\sigma^-$ measurements we switch the $|11\rangle$ and $|22\rangle$ atomic populations using adiabatic rapid passage (ARP).

off the pumping light over the next 100 $\mu$s to align the atomic spins with the static magnetic field and avoid Larmor precession. After preparation of the macroscopic atomic spin in the $|2,2\rangle$ state, we prepare the ensemble in the $|1,1\rangle$ state using adiabatic rapid passage (ARP) microwave sequence [see Fig. 3.6]. Note, to study the $\sigma^+$ transition that couples $|1,1\rangle$ to $|2,2\rangle$, we do not perform an ARP. These pumping and microwave pulse sequences are presented for the $\sigma^+$ and $\pi$ measurement Fig. 3.5. The $\sigma^-$ Rabi measurement uses the same protocol as the $\pi$. For these measurements, the probe beam $\approx$ 80 GHz detuned from the $D_2$ line (780 nm).

In order to compare our theoretical model, as outlined in Eq. (3.21), with our experimental observations, several key parameters must be determined. These include the Rabi rates $\tilde{\Omega}_m^{m'}$, the magnetic field strength denoted as $B$, and the pressure shift $\nu_{\text{bg}}$, all of which define the Hamiltonian $H$ in Eq. (3.7). We extract generalized Rabi frequencies $f \rightarrow \tilde{\Omega}$ from time-domain Rabi signals, such as the ones shown in Fig. 3.5, with the following model

$$\begin{aligned}\theta_F(t) =& a_0 + a_1 e^{-t/t_1} + a_2 e^{-t/t_2} + \\ & e^{-t/t_3}(a_3 \sin[2\pi t f] + a_4 \cos[2\pi t f]).\end{aligned} \tag{3.30}$$

Here, two DC-offset decay constants $t_1$ and $t_2$ are required to account for the atomic population redistribution arising from spin-exchange collisions [95]. Additionally, it's necessary to understand the time-dependent spin decay observed in our setup, which likely results from a mix of higher-order wall collision modes and residual light scattering by the probe beam. Furthermore, accurately estimating the initial atomic state is crucial. Following a detailed discussion on the adiabatic rapid passage sequence, we will delve into the process of extracting these various parameters, enabling a comprehensive comparison of the theoretical model with our Rabi oscillation measurements.

### 3.4.1 Adiabatic rapid passage details

The principle behind adiabatic rapid passage (ARP) involves gradually sweeping the microwave frequency across the $|1,1\rangle - |2,2\rangle$ transition in an adiabatic manner such that the atomic state remains in the same eigenstate throughout the sweep. Initially, the atomic state is set in $|2,2\rangle$, with the microwave frequency far from resonance. By the end of the sweep, the energy levels of $|1,1\rangle$ and $|2,2\rangle$ have effectively switched roles. Consequently, the atomic state, which started in $|2,2\rangle$, ends up in $|1,1\rangle$, having followed the gradual shift in energy levels without jumping across to the alternate eigenstate mid-sweep. If $\Omega$ represents the Rabi frequency induced by the microwave drive, and $\Delta(t) = \nu_{\nu\mathrm{w}}(t) - \nu_0$ is the detuning of the microwave from the $\sigma^+$ resonance, then for adiabaticity to be maintained, the condition required is that the Rabi frequency significantly exceeds the rate at which the microwave detuning changes. This means [119]:

$$\Omega^2 \gg \dot{\Delta}(t)/2\pi. \tag{3.31}$$

To implement ARP, we start the microwave drive at a detuning $\Delta^{(i)} = 490$ kHz above the $\sigma^+$ resonance and then linearly chirp it to $\Delta^{(f)} = -150$ kHz below the $\sigma^+$ resonance within $\Delta t_{\mathrm{sweep}} = 70$ $\mu$s. Then, we continue to study the dynamics of Rabi oscillations by tuning the microwave drive to the hyperfine transition resonance. In the acquired data, we filter out high-frequency oscillations due to off-resonant coupling to adjacent microwave transitions [see Fig. 3.6(c)]. Note, to study the $\sigma^+$ transition that couples $|1,1\rangle$ to $|2,2\rangle$, we do not perform an ARP.

A pertinent question raised from observing Fig. 3.6(c) concerns the notably large high-frequency oscillations during the $\pi$ Rabi oscillation. The amplitude $A_R$ of the Rabi oscillations

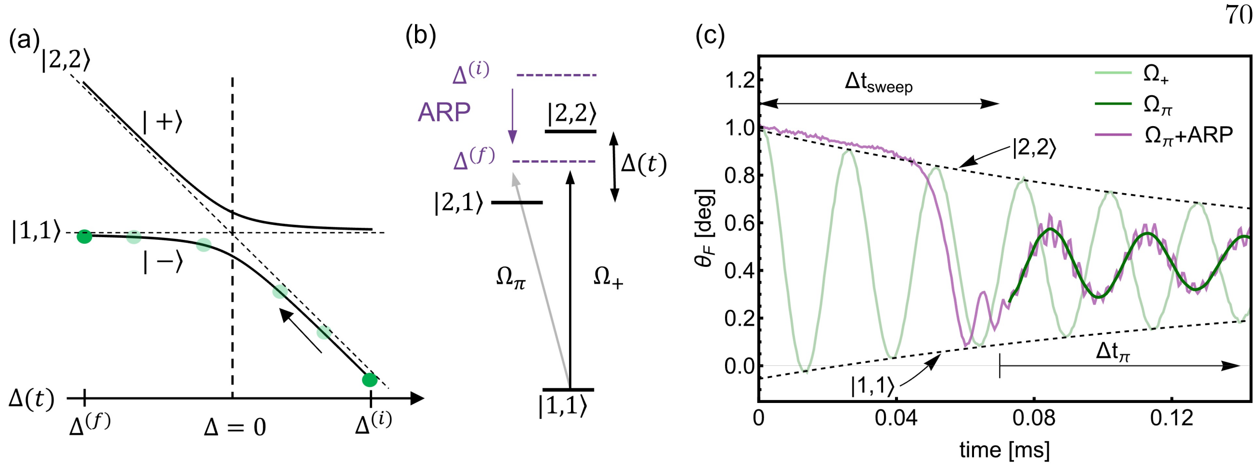


Figure 3.6: Atomic population transfer from $|2,2\rangle$ to $|1,1\rangle$ with adiabatic rapid passage (ARP). (a) A schematic of ARP featuring dressed states $|\pm\rangle$. When there's a large positive detuning, like $\Delta^{(i)}$, the dressed state $|-\rangle$ is a close approximation of $|2,2\rangle$. Conversely, with large negative detunings, such as $\Delta^{(f)}$, $|-\rangle$ aligns closely with $|1,1\rangle$. If the initial state consistently stays in $|-\rangle$ during the sweep of the microwave detuning, there is an efficient transfer of the atomic population from $|2,2\rangle$ to $|1,1\rangle$. (b) Energy level diagram for adiabatic rapid passage (ARP). (c) Using ARP to maximize the $|1,1\rangle$ population and enhance the $\Omega_\pi$ signal. Overlaying with $\Omega_+$ (light green) denotes $\theta_F$ values for $|2,2\rangle$ and $|1,1\rangle$ occupation, where we observe ARP transfer (purple) after the microwave frequency sweep. Extracting the pure $\pi$ oscillation (dark green) requires filtering off-resonance driving of adjacent transitions.

driven in a two-level system is given in terms of the Rabi rate $\Omega$ and the detuning $\Delta$

$$A_R \propto \frac{\Omega^2}{\Omega^2 + \Delta^2}. \tag{3.32}$$

Given that the Rabi frequency $\Omega_+$ is approximately 40 kHz and the detuning of the $\pi$ transition from the $\sigma^+$ transition is $\Delta_+ = 350$ kHz, the expected population dynamics from off-resonant driving at the $\pi$ transition frequency is predicted, from Eq. (3.32), to be about 1% of what they would be if $\Delta_+ = 0$. However, in reality, the observed detuned $\sigma^+$ Rabi oscillations are closer to 15% of the on-resonance value, which is significantly higher than the calculated expectation.

This can be understood within the context of Rabi oscillations within a two-level system defined by the following system of differential equations

$$
\begin{aligned}
i\dot{\rho}_{11} &= -\pi\Omega(\rho_{12} + \rho_{21}) \\
i\dot{\rho}_{12} &= \pi(-\Omega\rho_{11} + \Delta 2\rho_{12} + \Omega\rho_{22}) \\
i\dot{\rho}_{21} &= \pi(\Omega\rho_{11} - \Delta 2\rho_{21} - \Omega\rho_{22}) \\
i\dot{\rho}_{22} &= \pi\Omega(\rho_{12} - \rho_{21})
\end{aligned}
\tag{3.33}
$$

Solving these equations with initial populations set at $\rho_{11} = 0.4$ and $\rho_{22} = 0.6$, and zero initial coherences ($\rho_{12} = \rho_{21} = 0$), results in Rabi oscillations characterized by amplitudes as outlined in Eq. (3.32). This scenario is depicted by the black curve in Fig. 3.7(a). Alternatively, if we start with initial coherences of $\rho_{12} = \rho_{21} = 0.2$, the resulting Rabi oscillations change significantly, as shown by the blue curve in the same figure. In this case, the Rabi amplitude tends to decrease as $1/\Delta$ rather than $1/\Delta^2$ when the detuning is large.

A simpler case to consider is when the atomic populations are equal ($\rho_{11} = \rho_{22} = 0.5$) and the coherences are both set to 0.5 ($\rho_{12} = \rho_{21} = 0.5$). This configuration leads to the Rabi amplitude behavior illustrated in Fig. 3.7(b).

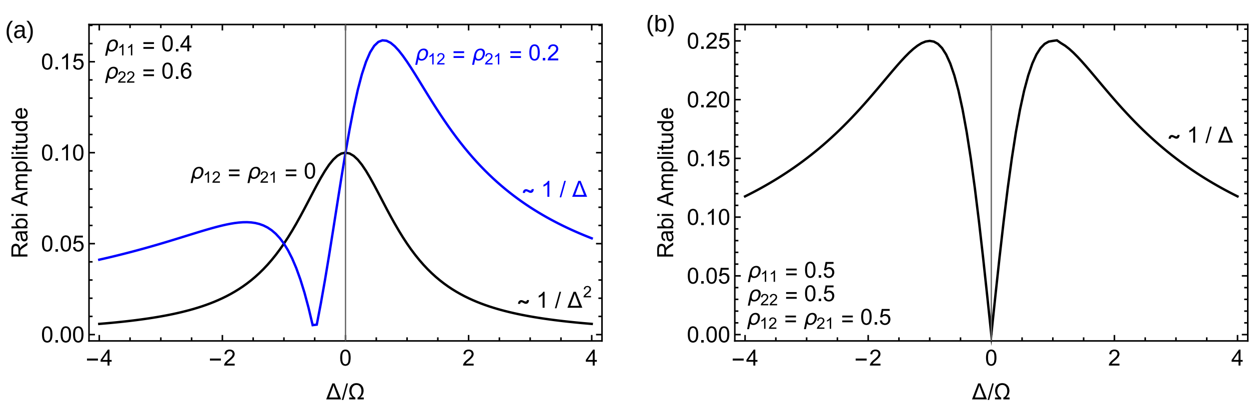


Figure 3.7: Detuning-dependence of the Rabi oscillation amplitude for a two-level system. (a) If initial coherences are zeroed, then the Rabi amplitude falls off as $1/\Delta^2$ as predicted by Eq. 3.32. If however, the initial coherences are non-zero, the Rabi amplitude changes shape and falls off as $1/\Delta$ at large detunings. (b) The detuning-dependence of the Rabi oscillation amplitude when the two-level system is initialized in a perfect superposition state.

This scenario is illustrated on the Bloch sphere in Fig. 3.8(a), where the initial state aligns along the $\hat{x}$ axis. In this framework, Rabi dynamics are interpreted as rotations around the vector $\vec{\Omega} = (\Omega, 0, -\Delta)$. When $\Delta = 0$, there are no population dynamics because the vector $\vec{\Omega}$ is parallel to the atomic state vector. At $\Delta = \Omega$, the Rabi vector forms a 45-degree angle with the atomic state vector, leading to dynamics that trace the red dashed circle in Fig. 3.8(b). As $\Delta$ increases indefinitely, $\vec{\Omega}$ aligns along $\hat{z}$, restricting population dynamics to the x-y plane, and resulting in a Rabi amplitude of zero. The geometry of the Bloch sphere suggests that the Rabi amplitude is proportional to:

$$A_R \propto \frac{\overline{\Delta}}{1 + \overline{\Delta}^2} \tag{3.34}$$

where $\overline{\Delta} = \Delta/\Omega$. Consequently, the pronounced high-frequency oscillations observed in Fig. 3.6(c) are likely attributable to the initial coherences between $|1, 1\rangle$ and $|2, 2\rangle$ generated by the ARP microwave sweep.

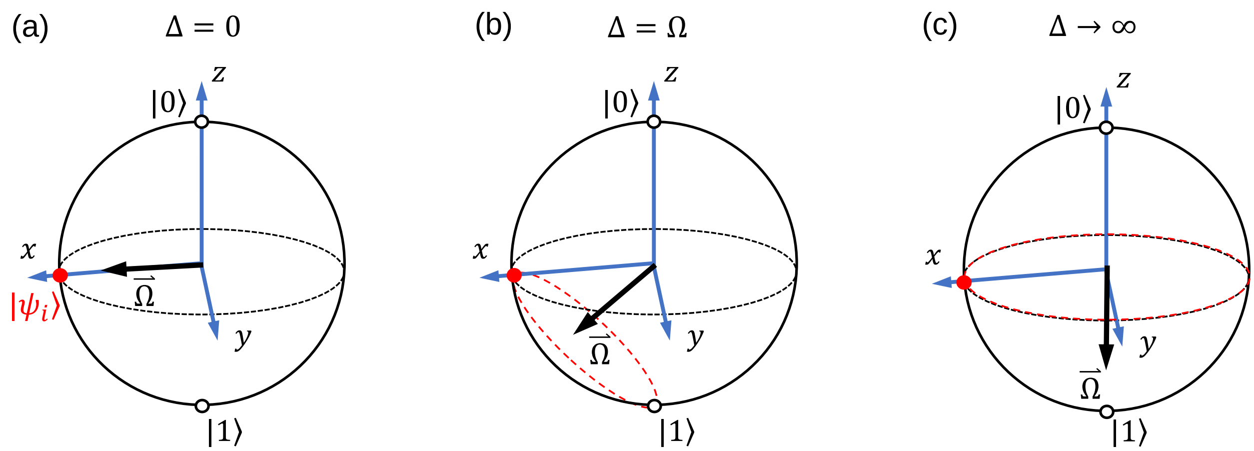


Figure 3.8: Bloch sphere description of the detuning-dependence of the Rabi oscillation amplitude for the case $\rho_{11} = \rho_{22} = \rho_{12} = \rho_{21} = 0.5$ [see Fig. 3.7(b)]. (a) For $\Delta = 0$ no Rabi oscillations occur because the Rabi vector $\vec{\Omega} = (\Omega, 0, 0)$ is parallel with $|\psi_i\rangle$. (b) For $\Delta = \Omega$ Rabi oscillations occur with maximum amplitude. In this picture the initial state $|\psi_i\rangle$ precesses about $\vec{\Omega}$. In this case the Rabi vector $\vec{\Omega} = (\Omega, 0, -\Delta)$. At infinite detuning the Rabi vector is aligned with the z-axis resulting in Bloch sphere rotations in the xy-plane. In this case, the Rabi oscillation amplitude is zero because the atomic populations in states $|0\rangle$ and $|1\rangle$ are always equal.

### 3.4.2 Rabi frequency measurements

Next, we turn our attention to fitting free parameters in the atomic-microwave Hamiltonian $H$ defined in Eq. (3.7). This is achieved by using the eigenvalues of $H$ to model the Rabi oscillations frequencies observed in the $\sigma^{\pm}$ and $\pi$ transitions. As elaborated in Sec. 3.1.4, the generalized Rabi frequency $\tilde{\Omega}_k = (\lambda_j - \lambda_i)/h$ is defined as the difference between a specific pair $(\lambda_i, \lambda_j)$ of $H$ eigenvalues. Special consideration is required when choosing the eigenvalue pair for the $|11\rangle - |20\rangle$ $\sigma^-$ transition due to the closely matched $\sigma^+$ $|10\rangle - |21\rangle$ transition at the same resonance frequency. For this analysis all Rabi rates $\Omega_m^{m'}$ are assumed to be real in $H$. Therefore, it suffices to fit the three Rabi rates $\Omega_+$, $\Omega_\pi$, and $\Omega_-$, as the known transition dipole moments $\mu_m^{m'}$ proportionally scale the Rabi rates for other transitions driven by the same spherical microwave component $\mathcal{B}_k$ defined in Eq. 3.9.

We extract these Rabi rates, in addition to the magnetic field strength $B$ and buffer gas pressure shift $\nu_{\text{bg}}$, by fitting to generalized Rabi frequency measurements $\tilde{\Omega}_j$ with $j \in \{\pm, \pi\}$ at seven different detunings near resonance for each transition. We show in Fig. 3.9(a) these eigenvalues, or rather dressed-states, as a function of microwave frequency $\nu_\mu$ for the fitted parameters [see Fig. 3.9(c-e)] $\Omega_- = 54.565$ kHz, $\Omega_\pi = 35.025$ kHz, $\Omega_+ = 39.552$ kHz, $|\vec{B}| = 49.626$ $\mu T$, $\delta\nu_{\text{hfs}} = 87.219$ kHz. We explicitly show the generalized Rabi frequencies as the difference between two dressed states at an anti-crossing as shown in Fig. 3.9(b). The specific Rabi oscillations driven near-resonance that we use for comparing to the decoherence model (Eq. (3.21)) are the circled points in Fig. 3.9(c-e).

### 3.4.3 Spin decay measurements and modeling wall-collision decoherence

To properly model Rabi oscillation measurements requires correctly modeling the time-dependent spin decay. To measure spin decay, we align $\vec{B}^{\text{dc}}$ with our pump and probe beam such that no Larmor precession occurs. Then we measure the decay of the probe Faraday rotation $\theta_F(t)$ after turning off the pump beam as shown in Fig. 3.10(a). In this configuration, the Fara-

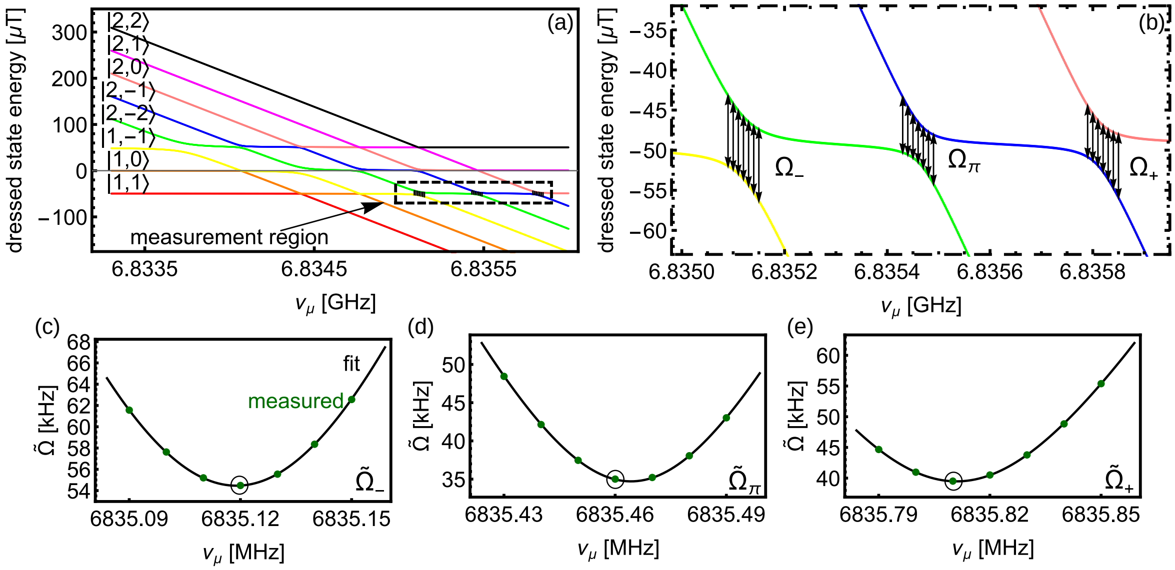


Figure 3.9: Extraction of $\nu_{\rm bg}$, $|\vec{B}|$, and Rabi frequencies. (a) Eigenvalues (dressed states) of the total microwave-coupled Hamiltonian. Units are reported in $\mu T = [E/\mu_B]$. (b) Enlargement of the measurement region of (a) where the specific microwave frequencies for each microwave transition are shown. (c-e) Fits (black) using the dressed states of the full Hamiltonian overlayed with measured generalized Rabi frequencies (green).

day angle senses the magnitude of the macroscopic spin state. We fit $\theta_F(t) = a0 + \sum_i A_i e^{-t/\tau_i}$ to the spin decay [see Fig. 3.10(a)], where we obtain a good fit using at least 3 decay rates. We attribute this time-dependent spin-decay to be primarily due to higher-order wall-collision modes and residual light scattering from the probe beam. Because the pump beam is slightly focused into the vapor cell to achieve a higher pumping rate, we expect the presence of higher-order diffusion modes in our measurements. Since we cannot easily distinguish decoherence due to wall collisions from light scattering, we model spin decay as an effective time-dependent wall collision decay rate [see Fig. 3.10(b)].

Spin decay from wall collisions occurs due to large time-dependent electric and magnetic fields experienced by the atom when colliding with the cell wall surface that effectively randomizes the atomic spin. The diffusion of the atomic spin polarization $p(x, y, z, t)$ spreads throughout the vapor cell according to the diffusion equation $\partial p/\partial t = D\nabla^2 p$, where $D = D_0 P_0/P_{\rm buff}$ is a diffusion constant that is inversely proportional to the buffer-gas pressure, and $P_0 = 1$ atm. The boundary condition $p = 0$ at the cell walls is assumed, which leads to solutions due to the diffusion equation of the form:

$$p(x, y, z, t) = \sum_{i,j,k} A_{ijk} e^{-D\pi^2\left(\frac{i^2}{x_c^2}+\frac{j^2}{y_c^2}+\frac{k^2}{z_c^2}\right)t} \sin\left(\frac{i\pi x}{x_c}\right)\sin\left(\frac{j\pi y}{y_c}\right)\sin\left(\frac{k\pi z}{z_c}\right) \tag{3.35}$$

where $x_c$, $y_c$, and $z_c$ are the Cartesian dimensions of the cell chamber, and the mode amplitudes ($A_{ijk}$) are determined by the initial spin distribution ($p(x, y, z, 0)$) configured by the pumping beam. If only the fundamental mode ($i, j, k = 1$) is excited, then the expected spin decay rate is given by

$$\Gamma_D = \frac{\pi^2 D_0 P_0}{P_{N_2}} \frac{1}{\frac{1}{x_c^2} + \frac{1}{y_c^2} + \frac{1}{z_c^2}} \tag{3.36}$$

To model wall collisions in our measurements, it is not necessary to know which higher-order modes are excited, rather we use a phenomenological model where we assume only the fundamental diffusion mode (Eq. (3.36)) but with a time-dependent buffer-gas pressure $P_{\mathrm{N}_2}(t) \propto 1/\Gamma_D(t)$. We model the time-dependence of $\Gamma_D(t)$ as proportional to the measured instantaneous spin-decay rate shown in Fig. 3.10(b), where we subdivide this signal into sections of $\Delta t = 35$ $\mu$s and fit a single exponential time constant over each of these time intervals and plot these time-constants over the duration of the spin decay. In this framework, the spin-decay rate at $t \to \infty$ is given by the fundamental diffusion mode determined by an effective buffer-gas pressure likely to be an underestimate since residual light scattering is lumped into this wall-collision rate.

### 3.4.4 Initial atomic state estimation

The lineshapes of the Rabi oscillations measured in this work are very sensitive to the initial atomic state. There are two initial states to consider: (1) the state after optical pumping $\rho^{\mathrm{OP}}$ that initializes the $\sigma^+$ Rabi oscillation, and (2) the state after adiabatic rapid passage $\rho^{\mathrm{ARP}}$ that initializes the $\sigma^-$ and $\pi$ Rabi oscillations. To simplify these initial states, we assume that atomic coherences are set to zero such that the task at hand is to find the atomic populations $\rho_{ii}^{\mathrm{OP}}$ and $\rho_{ii}^{\mathrm{ARP}}$

To incorporate the effect of spin-decay that occurs during the 70 $\mu$s ARP pulse, we model

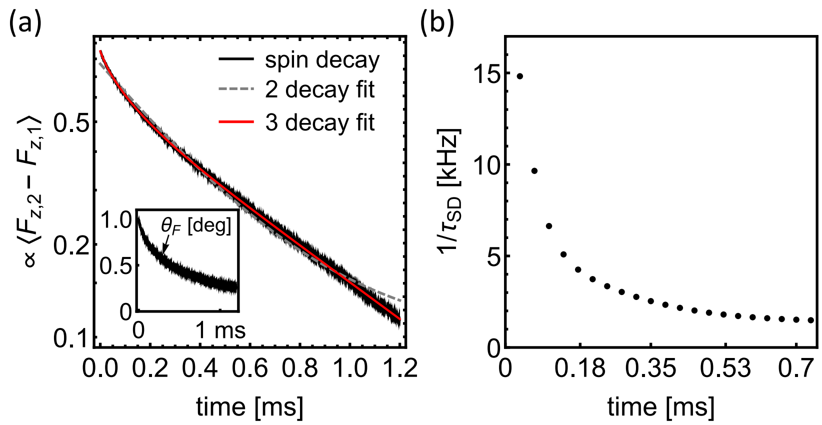


Figure 3.10: Spin decay from wall collisions. (a) Spin decay after optical pumping. Inset shows Faraday rotation $\theta_F \propto a_0 + b_0\langle\mathcal{F}\rangle$ when $\vec{B}^{dc}$ is parallel with the pump beam. We use a decay fitting function $a0 + \sum_i A_i e^{-t/\tau_i}$ and fit to the Faraday rotation data of the inset. The main log-plot displays the spin decay ($\propto \mathcal{F}$) with the constant offset $a_0$ removed to show the deviation from a pure exponential decay due to higher-order wall-collision modes. (b) Instantaneous spin-decay rate obtained by fitting a single exponential decay to 35 $\mu$s sections of the '3 decay' fit.

$\rho^{\mathrm{ARP}}$ in terms of the decayed atomic populations

$$\tilde{\rho}_{ii}^{\mathrm{OP}} = (\rho_{ii}^{\mathrm{OP}} - 1/8)e^{-s} + 1/8 \tag{3.37}$$

Here, we set $e^{-s} \approx 0.78$ to account for the atomic spin polarization decreasing by 22% during the initial 70 $\mu$s after optical pumping as measured from the data in Fig. 3.10. We assume that the primary effect of ARP is to flip the $|2,2\rangle \leftrightarrow |1,1\rangle$ atomic populations with efficiency $\epsilon$, while having no effect on the other atomic populations. We write this quantitatively as

$$\begin{aligned} \rho_{11}^{\mathrm{ARP}} &= \tilde{\rho}_{11}^{\mathrm{OP}} + \epsilon(\tilde{\rho}_{44}^{\mathrm{OP}} - \tilde{\rho}_{11}^{\mathrm{OP}}) \\ \rho_{44}^{\mathrm{ARP}} &= \tilde{\rho}_{44}^{\mathrm{OP}} - \epsilon(\tilde{\rho}_{44}^{\mathrm{OP}} - \tilde{\rho}_{11}^{\mathrm{OP}}) \end{aligned} \tag{3.38}$$

and for all other populations $\rho_{ii}^{\mathrm{ARP}} = \tilde{\rho}_{ii}^{\mathrm{OP}}$. Thus, finding unique solutions for $\rho_{ii}^{\mathrm{OP}}$ and $\epsilon$ fully defines $\rho^{\mathrm{OP}}$ and $\rho^{\mathrm{ARP}}$ with this model.

Next, we show that we can fit $\rho_{ii}^{\mathrm{op}}$ from our Rabi data. To do this, we first extract an estimate for the Rabi oscillations without decoherence as shown in Fig. 3.10. Here, we fit an exponential decay model $\theta_F(t) = A_0 + A_1 e^{-t/T_1} + A_2 e^{-t/T_2}\cos(2\pi f t)$ to the initial 100 $\mu$s of each Rabi oscillation,

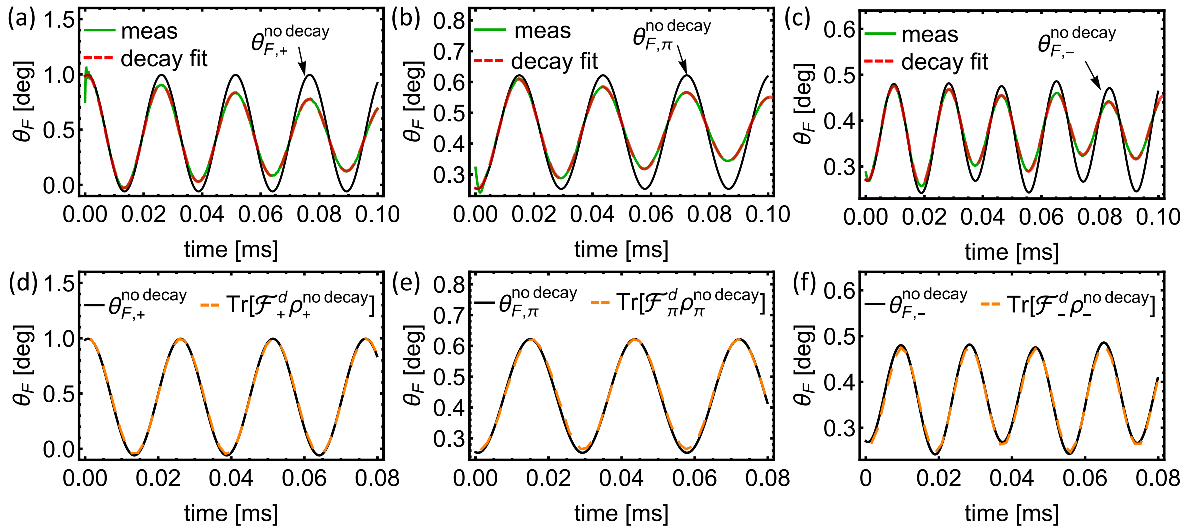


Figure 3.11: Estimate of atomic dynamics during Rabi oscillation without decoherence. (a-c) An exponential decaying sine (red-dashed) is fitted to the measured Faraday rotation signal (green). The decay constants in these fits are set to zero to estimate the Rabi oscillation signal without decoherence $\theta_{F,j}^{\text{no decay}}$ (black). (d-e) To estimate the initial atomic state prior to each Rabi oscillation, we fit the atomic dynamics without decoherence $\mathrm{Tr}[\mathcal{F}_j^d \rho_j^{\text{no decay}}]$ (orange-dashed) to $\theta_{F,j}^{\text{no decay}}$ (black).

and use the $\theta_F^{\text{no decay}}(t) = A_0 + A_1 + A_2\cos(2\pi f t)$ as an estimate for the Rabi oscillation without decoherence.

From fitting to the Rabi data in Fig 3.9, we apriori know the full time-independent Hamiltonian $\tilde{H}$ for each Rabi oscillation. We diagonalize $\tilde{H} \to \tilde{H}_d$ and transform the initial atomic state $\rho_0 = \rho^{\text{OP}}$ (or $\rho^{\text{ARP}}$) into this diagonalized basis $\rho_0 \to \rho_{0,d}$. Then the atomic dynamics without decoherence is given by

$$\rho^{\text{no decay}}(t) = e^{-i\tilde{H}_d t/\hbar}\rho_{0,d}e^{i\tilde{H}_d t/\hbar} \tag{3.39}$$

By writing $\rho_{0,d}$ as a function of the unknown atomic populations $\rho_{jj}^{\text{OP}}$, we can fit $a_0\mathrm{Tr}[\mathcal{F}_d\rho^{\text{no decay}}(t)]+ b_0$ to $\theta^{\text{no decay}}(t)$ for each Rabi oscillation to extract $\rho_{jj}^{\text{OP}}$ and $\epsilon$. Here the Faraday rotation offset $b_0$ is known from the polarimeter reading prior to optical pumping, but the scaling variable $a_0$ is an additional fitting parameter. The cost function that we minimize is

$$\sum_{r=\pm,\pi}\sum_{k=1}^{50} w_r\left[b_0 + a_0\mathrm{Tr}[\mathcal{F}_r^d\rho_r^{\text{no decay}}(t_k)] - \theta_r^{\text{no decay}}(t_k)\right]^2 \tag{3.40}$$

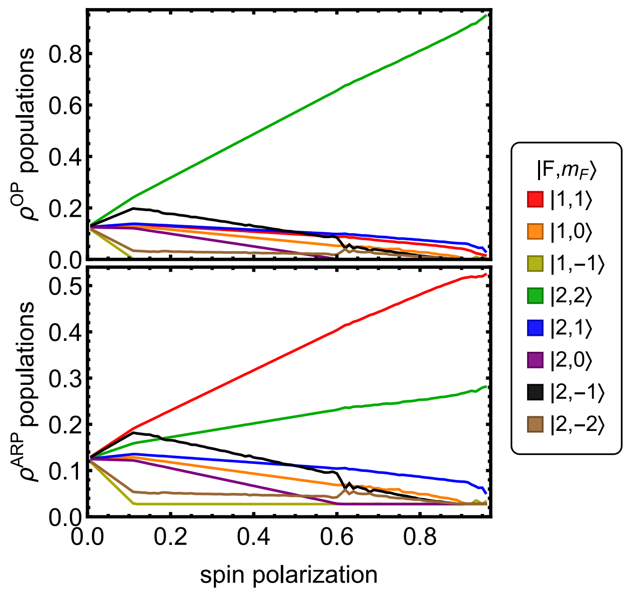


Figure 3.12: Fitted atomic populations subsequent to optical pumping (top) and adiabatic-rapid-passage (bottom) as a function of the electron spin polarization (p) produced at the end of optical pumping

that samples 50 sequential time steps seperated by $t_{k+1} - t_k = 1.6$ $\mu$s. Here $w_+ = 1$, $w_\pi = 2 = A_{2,+}/A_{2,\pi}$, and $w_- = 4 = A_{2,+}/A_{2,-}$ are weights chosen based on the fitting amplitude $A_2$ of each Rabi oscillation in $\theta^{\text{no decay}}(t)$. The results of this fitting is shown in Fig. 3.11. We find unique solutions for $\rho_{jj}^{\text{op}}$ if we also fix the atomic spin polarization $p$ shown in Fig. 3.12.

### 3.4.5 Fitting optimal vapor parameters from Rabi oscillations

After spin preparation, we model the full atomic spin dynamics by solving Eq. (3.21) that provides $\langle \mathcal{F}(t) \rangle$, where $\mathcal{F} = F_{z,b} - F_{z,a}$ is the difference between the z-component of the hyperfine spin $F_z$ in the $b = I + 1/2$ and $a = I - 1/2$ manifolds. We model Faraday rotation by $a_0 + b_0 \langle \mathcal{F}(t) \rangle = \theta_F^{\text{sim}}(t)$, where $a_0$ is a scaling constant that we fit originating from the light-atom coupling and $b_0$ is a measured initial polarization offset of the probe beam. To account for higher-order diffusion modes affecting the wall-collision rate and residual light scattering from the probe, we independently measure the non-exponential dependence of macroscopic spin decay and model as an effective time-dependent wall collision rate $\Gamma_{\text{D}}(t)$. We use fitted values 49.63 $\mu T$ for the static magnetic field, 87.22 kHz for the hyperfine frequency shift from buffer gas collisions, and $\{\Omega_-,\ \Omega_\pi,\ \Omega_+\} = \{54.57,\ 35.03,\ 39.55\}$ kHz extracted from Rabi oscillations driven at multiple detunings.

The parameters $\{\mathcal{T}_v, \mathrm{P}_{\mathrm{N}_2}, p\}$ affect both the Rabi coherence through the collision rates and the overall population dynamics. To find the optimal values for these parameters within our model, we minimize the RMS error

$$e_{\theta_F} = \sqrt{\frac{\sum_{r=\pm,\pi} \sum_{j=1}^{N} (\theta_{F,r}^{\mathrm{sim}}(t_j) - \theta_{F,r}(t_j))^2}{3N}} \tag{3.41}$$

by utilizing the lineshapes of all three hyperfine transitions at sampled times $t_j$ where $t_{j+1} - t_j = 1$ $\mu$s. Here $\theta_F(t)$ is the measured Faraday rotation and $\theta_F^{\mathrm{sim}}(t)$ is the simulated Rabi oscillation Faraday signal. In $\theta_F^{\mathrm{sim}}(t)$ we use the same scaling factor $a_0$ fitted during the extraction of initial atomic populations (see Eq. (3.40)). We minimize $e_{\theta_F}$ by evaluating $e_{\theta_F}$ over a 2D scan of $\mathcal{T}_v$ and $\mathrm{P}_{\mathrm{N}_2}$ at a given electron spin polarization $p$ [see Fig. 3.13(a)]. We use piecewise polynomial interpolation of order 3 to estimate the global minimum appearing in these 2D scans shown as a green circle in Fig. 3.13(a). We plot the global minimum of $e_{\theta_F}$ at different $p$ in Fig. 3.13b and the corresponding values of $\mathcal{T}_v$ and $P_{\mathrm{N}_2}$ in Fig. 3.13(b-c), where the vertical green-dashed line indicates the optimal values. An overlay of the simulated with the measured Rabi oscillations for different vapor parameters (colored circles in Fig. 3.13(a)) at an electron spin polarization $p = 0.79$ is shown in Fig. 3.13(d-f) to visually illustrate how unique values of $\{\mathcal{T}_v, \mathrm{P}_{\mathrm{N}_2}, p\}$ fit our data.

Our model extracts $\mathcal{T}_v = 107$ °C, $P_{N_2} = 190$ Torr, and p = 0.79 from the measurements by utilizing all three Rabi lineshapes to minimize the root-mean-square error (RMSE) between the simulated $\theta_F^{\mathrm{sim}}$ and the measured $\theta_F$. The inset of Fig. 3.14(b) displays the RMSE over variations of the vapor temperature $\mathcal{T}_{\mathrm{v}}$ and the buffer gas pressure $\mathrm{P}_{\mathrm{N}_2}$, where the green circle marks the optimal values. The dephasing rates $\gamma_{t,j} = 1/T_2^{t,j}$ and nuanced features of the lineshapes predicted theoretically agree with the measured dephasing times $\gamma_{m,j} = 1/T_2^{m,j}$ and lineshapes (black/green lines Fig. 3.14). In contrast, the corresponding weak-driving approximation predicts a total dephasing time $\gamma_{t,+}^{\mathrm{wk}}$ for the $\sigma^+$ Rabi oscillation that underestimates $\gamma_{m,+}$ [see Fig. 3.14(b)]. Here,

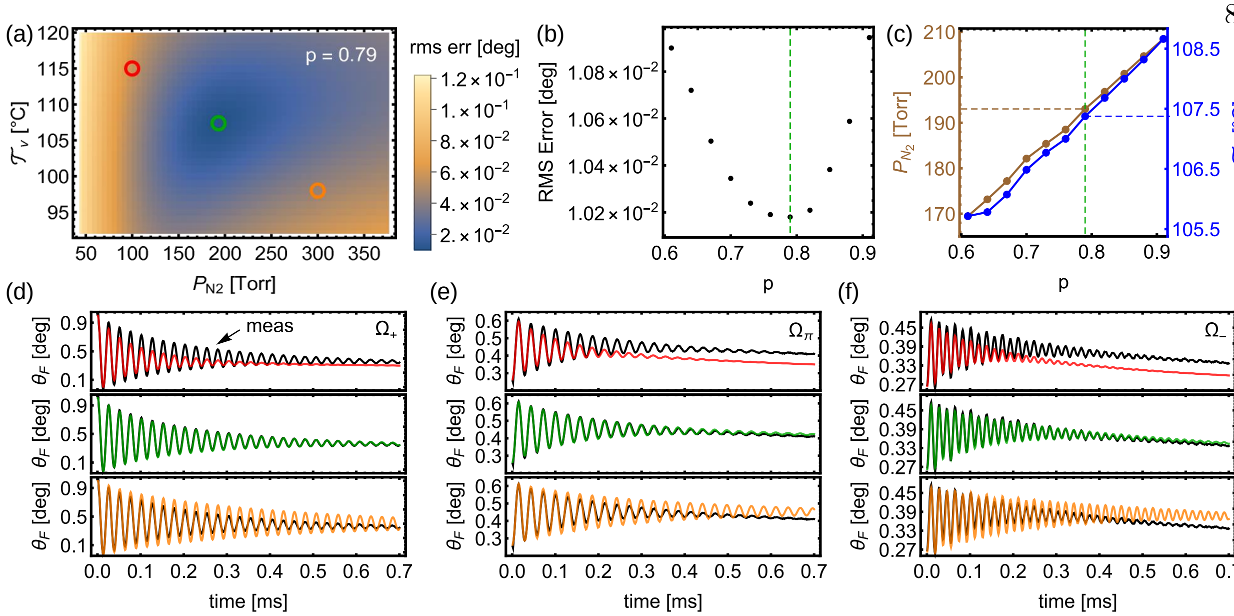


Figure 3.13: Fitting vapor cell parameters (a) The RMS error $e_{\theta_F}$ between the simulated and measured Rabi oscillations as a function of vapor temperature $\mathcal{T}_v$ and buffer gas pressure $\mathrm{P}_{\mathrm{N}_2}$ for an electron spin polarization of p = 0.79. Circles denote optimal (green) and non-optimal (red and orange) vapor cell parameters within the theoretical model (b) the RMS error $e_{\theta_F}$ at optimal $\mathcal{T}_v$ and $\mathrm{P}_{\mathrm{N}_2}$ for different spin polarization p. (c) Optimal $\mathcal{T}_v$ and $\mathrm{P}_{\mathrm{N}_2}$ values as a function of the electron spin polarization. (d-f) Comparison of measured (black) and simulated Rabi oscillations for different vapor parameters given by the circles in (a). Optimal values are the green center curves.

$\gamma_{t,+}^{\mathrm{wk}}$ is extracted from fitting a single decay rate to a theoretical Rabi oscillation given by an exponentially decaying sine with instantaneous decay rate $\gamma_{\mathrm{se}}^{\mathrm{wk}} + \gamma_{\mathrm{sd}} + \gamma_{\mathrm{C}} + \Gamma_{\mathrm{D}}(t)$ accounting for all sources of collisional decoherence but using the weak driving approximation for the spin-exchange dephasing rate. In fact, in order for $\gamma_{t,+}^{\mathrm{wk}}$ to match the measured Rabi coherence would require $\mathcal{T}_v \to 122$°C to sufficiently increase the SE collision rate. This is far from the thermistor temperature $\mathcal{T}_{\mathrm{therm}} = 98$°C, which we expect is cooler than the vapor temperature $\mathcal{T}_v$ by only a few °C due to thermal gradients across the microwave cavity. Furthermore, an electron spin polarization of p = 0.79 is reasonable given the uncoated glass walls of our cell and the misalignment between the pump beam and the static magnetic field, and $\mathrm{P}_{\mathrm{N}_2} = 190$ Torr (25.3 kPa) is in close agreement with buffer gas pressures {170, 180, 330} Torr extracted independently from broadening and frequency shifts in both microwave and optical measurements.

### 3.4.6 Vapor temperature sensing

Finally, we demonstrate the application of Rabi coherence to intra-cell thermometry [see Fig. 3.14(c)], which is generally useful for characterizing the performance of atomic vapor sensing platforms and is particularly useful for stabilizing and optimizing the accuracy of atomic clocks [70, 188]. In contrast, external sensors such as thermistors do not sense the actual vapor temperature. Here we cool the vapor cell by switching off the heat tape attached to the microwave cavity. While the cell cools, we record the Rabi dephasing time $T_2^{m,+}$ by generating a half-second long train of 500 $\sigma^+$ Rabi oscillations triggered every four seconds over a seven minute cooling period of 3.5 °C. We map the measured dephasing time $T_2^{m,+} \rightarrow \mathcal{T}_v$ to the intra-cell vapor temperature by varying $\mathcal{T}_v$ within the calibrated theoretical model and fitting an interpolating polynomial $\mathcal{P}$ to the simulated dephasing time $\mathcal{T}_v = \mathcal{P}(T_2^{t,+})$. The temperature dependence of $1/T_2^{m,+} \propto n_{\mathrm{Rb}}\sigma_{\mathrm{se}}v^r$ arises from the atomic density, which decreases as the vapor cell cools. From a single 500 ms train of Rabi oscillations we measure a temperature sensitivity of 1.2 mK/$\sqrt{\mathrm{Hz}}$ [see Fig. 3.14(c) inset]. This is a competitive sensitivity with other techniques [155, 188], and demonstrates Rabi coherence as a novel platform for intra-cell thermometry.

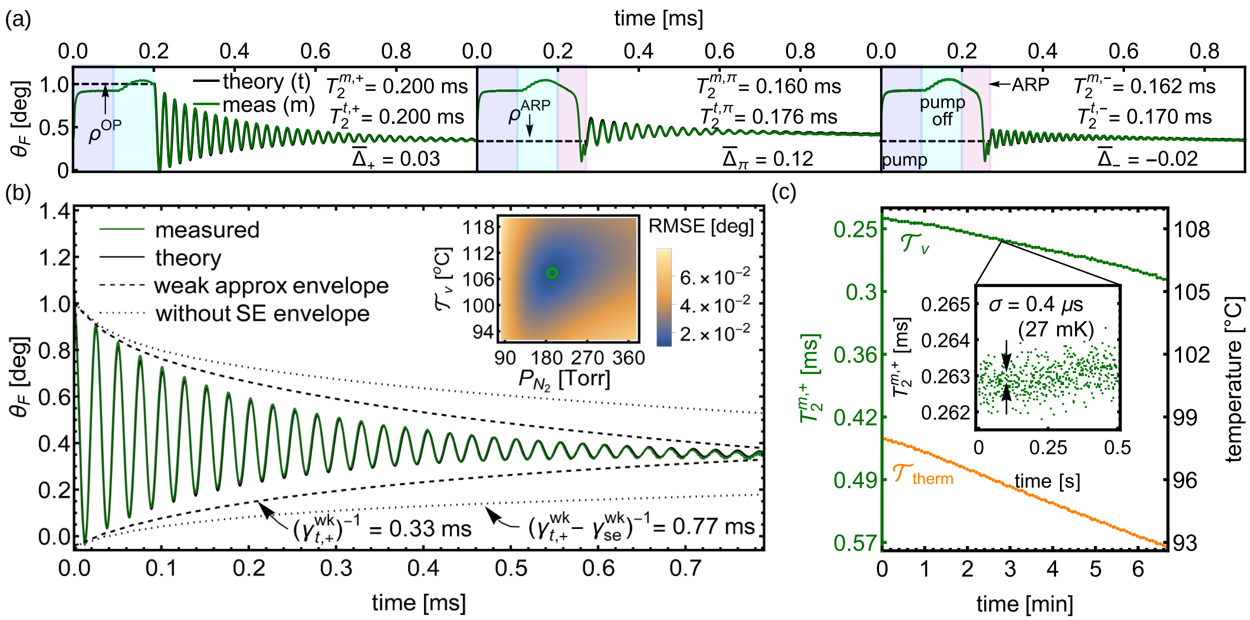


Figure 3.14: (a) A mirror comparison of the simulated (black-dashed) and measured (green) $\sigma^+$, $\pi$, and $\sigma^-$ Rabi oscillations. Here $\overline{\Delta}_{\pm,\pi} = \Delta_{\pm,\pi}/\Omega_{\pm,\pi}$ is the normalized microwave detuning. (b) A plot of the $\sigma^+$ Rabi oscillation alongside other relevant decay rates. Importantly, the weak-driving approximation predicts much higher coherence compared to our measurements. The inset shows the RMSE between the simulated and measured Rabi oscillations for different vapor temperatures $\mathcal{T}_v$ and buffer gas pressures $P_{N_2}$ at a fixed spin polarization p = 0.79. By finding these optimal values where the theory and measured Rabi oscillations highly overlap, our model estimates these parameters for our cell. (c) Intra-cell thermometry with SE coherence measurements. The intra-cell temperature $\mathcal{T}_v$ is inferred from measured dephasing times $T_2^{m,+}$ using the calibrated model. The inset displays $T_2^{m,+}$ fluctuations over a 0.5 second period.

# Chapter 4

## Rabi and Ramsey heading error correction

The previous chapter delved into the theoretical aspects of Rabi oscillations in microfabricated vapor cell platforms, establishing a connection between vapor cell parameters and the dephasing and population redistribution occurring during these oscillations. This chapter is inspired by the potential to measure geomagnetic field strengths with improved accuracy over traditional scalar OPM techniques, by detecting the Zeeman splitting across several transitions with hyperfine spectroscopy.

Sensitive hyperfine spectroscopy in microfabricated cells has been demonstrated with pulsed [23] and continuous [6, 80, 95] microwave interrogation. In particular E. B. Aleksandrov et. al. built a hyperfine structure (HFS) OPM using continuous microwave interrogation of the end-hyperfine resonances of $^{87}$Rb that achieved 6 pT resolution over 0.1 seconds of measurement time [6]. The detuning dependence of Rabi oscillations is another approach to measure hyperfine resonances, and further, have been shown to enable self-calibrated vector magnetometry [170]. To date, however, careful modeling of frequency shifts from off-resonant driving in multi-level atomic systems is lacking to characterize the ultimate magnetometer accuracy limits using hyperfine transitions. By utilizing short periods of microwave interrogation, Ramsey interferometry protocols, as implemented in vapor cell atomic clocks [5, 23, 48], mitigate systematic errors from off-resonant driving, but require linearly polarized microwave sources along a well-defined magnetic field. These design requirements have made the application of Ramsey protocols towards magnetometry impractical. In this chapter, we solve these microwave interrogation challenges associated with off-resonant driving and directly measure the heading error of a microfabricated OPM based on free induction decay (FID) with sub-nT accuracy.

Practical use of OPMs in geomagnetic fields such as navigation [42, 146], geophysics [61, 169], space [27, 55, 103], and unexploded ordinance detection [28, 144] requires addressing systematic errors that depend on the orientation of the sensor with respect to the magnetic field known as heading errors. For the most common OPMs operating on the Zeeman transitions of alkali atoms the dominant heading error at geomagnetic fields is on the order of 10 nT. This systematic error manifests from unknown strengths of unresolved frequency components in the magnetometer signal arising from nonlinear Zeeman (NLZ) shifts from each of the ground state hyperfine manifolds [8, 107].

Only in regimes of narrow magnetic resonances [1] and high spin polarization can this heading error be accurately modeled to 0.1 nT [107]. In MEMS vapor cells, these regimes often become unfeasible due to line broadening from atomic collisions and the challenges associated with implementing fast, high-fidelity optical pumping using modest pump powers. Various other approaches have been developed to mitigate heading error including spin locking [20, 21], light polarization modulation [132], double-pass configurations [150], double-modulated synchronous pumping [160], and leverage of tensor lightshifts [90], but all these approaches neglect frequency shifts arising from the different Zeeman resonances between the $F = I \pm 1/2$ manifolds and have their own practical challenges. Furthermore, methods that utilize higher-order polarization moments [2, 191, 197] are not feasible in compact OPM packages with high buffer gas pressures [153]. CPT magnetometry [111, 140] holds promise for high scalar accuracy by detecting multiple hyperfine resonances to address NLZ systematics, though sub-nT accuracy in microfabricated cells remains elusive to date.

To address the challenges associated with heading errors, we employ Rabi and Ramsey frequency spectroscopy independently, each utilizing continuous and pulsed microwave interrogation to detect Zeeman shifts between four hyperfine transitions of $^{87}$Rb shown in Fig. 4.1(a). Both techniques can be applied at the same set of vapor cell parameters used for sensitive FID measurements. In Rabi frequency spectroscopy, an atom-microwave Hamiltonian accurately models Rabi oscilla-

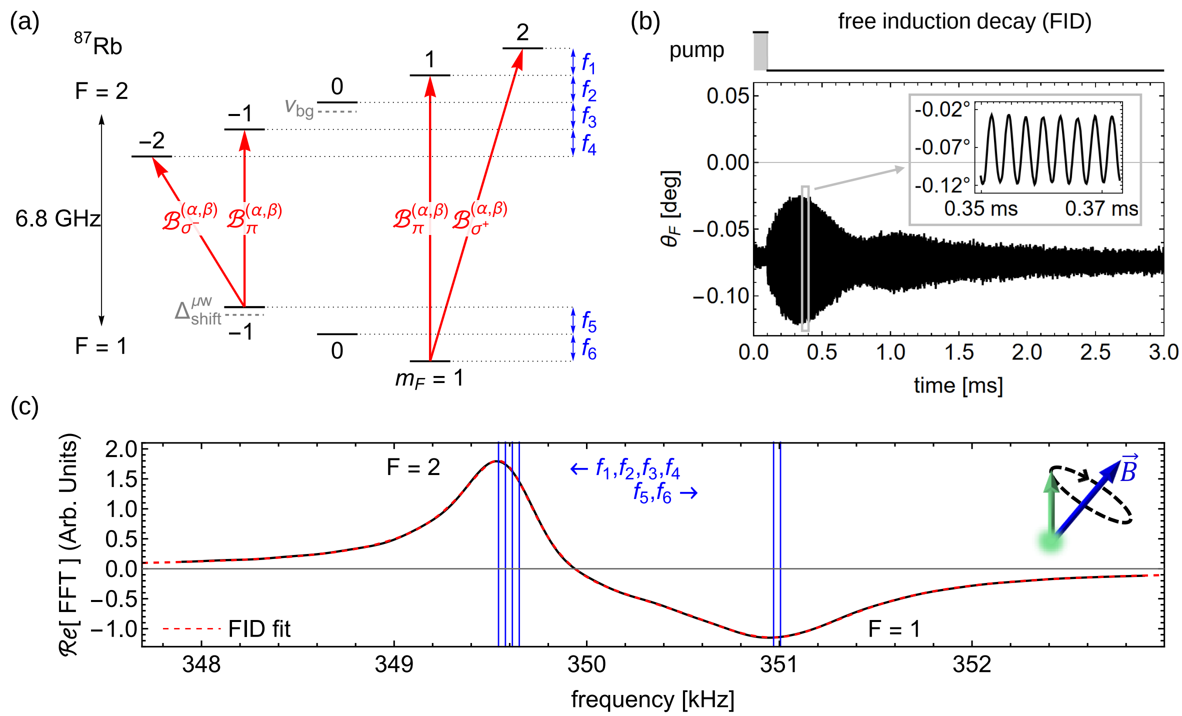


Figure 4.1: (a) Energy-level diagram showing the four hyperfine transitions used in Rabi and Ramsey frequency spectroscopy to correct FID heading error. Nonlinear Zeeman splittings $f_i$ (blue) contribute to the Larmor FID signal. Buffer gas pressure shift $\nu_{\rm bg} \approx 88$ kHz further shifts the hyperfine manifolds. (b) Pump timing diagram and FID signal measured at $\beta = 106°$ in the regime of low-polarization pumping that contains both $F = 1$ and $F = 2$ precession frequencies. (c) Real-part of the fast Fourier transform (FFT) of the FID signal shown in (b). Heading errors arise due to the uncertainty in the amplitudes and relative phases of the nonlinear Zeeman frequencies (blue lines).

tion frequencies despite frequency shifts due to off-resonant driving. To ensure proper modeling of the atom-microwave coupling, we check the consistency between Rabi measurements driven by three distinct microwave polarization ellipses (MPEs) [170], which each induce unique frequency shifts due to off-resonant driving. In contrast, Ramsey frequency spectroscopy does not directly model atom-microwave coupling, but instead mitigates systematic errors within a $\pi/2 - t_R - 3\pi/2$ Ramsey sequence [194]. To prevent signal degradation in arbitrary magnetic field directions, both techniques employ adiabatic power ramps during optical pumping to suppress Larmor precession. We compare these two methods to FID measurements over a range of DC magnetic field directions at 50 $\mu$T. We find the Rabi and Ramsey techniques, despite their distinct concepts, both measure the FID heading error with agreement to within 0.6 nT. From theoretical simulations, we find that the fundamental accuracy of both approaches is within 0.4 nT due to spin-exchange frequency shifts [15, 124].

## 4.1 FID comparative study

For comparative demonstration, we study FID spin-precession signals with low atomic spin polarization where no accurate physical models for heading errors exist. To initiate FID measurements in this low polarization regime, a 100 $\mu$s pulse of elliptically-polarized pump light at 400 mW polarizes atomic spins along the pump beam [see Fig. 4.1(b)]. The pump frequency is tuned near-resonance to the $D_1$ line to depopulate the $F = 2$ manifold and enable strong Rabi signals across all hyperfine transitions. Complete depopulation of the $F = 2$ manifold is limited by the 5.6 GHz optical broadening due to quenching from Rb-$N_2$ collisions. In this study, the probe beam was blue-detuned by 170 GHz from the 780 nm $D_2$ line with 1 mW of power.

In this low spin polarization regime, the FID spectrum [see Fig. 4.1(c)] consists of both $F = 1$ and $F = 2$ Zeeman resonances that are separated at 50 $\mu$T by 1.4 kHz. The NLZ effect splits these resonances into frequency components $\{f_1, ..., f_6\}$ separated by 36 Hz. We model the FID spectrum as two resonances $f_{L,\pm}(B) \approx \mu_B(g_s - g_i \pm 4g_i)B/4h$ that are the mean Zeeman splitting across the magnetic sublevels for the $F = I \pm 1/2$ manifolds, where $I = 3/2$ is the nuclear spin, $g_s$ and $g_i$ are the electronic and nuclear Landé g-factors, $h$ is Planck's constant, $\mu_B$ is the Bohr magneton, and $B$ is the magnetic field strength. The real component of the FID signal's Fourier transform in this model is given by

$$\mathcal{R}e[\text{FFT}] = \sum_{j=\pm} a_j \frac{\cos[\phi_j] - \sin[\phi_j](f - f_{L,j})}{(f - f_{L,j})^2 + w_j^2/4} \tag{4.1}$$

where $\phi_\pm = 2\pi f_{L,\pm} t_0 \pm \phi/2$ are phase shifts due to a starting time offset $t_0$ with $\phi$ being a relative phase between the $I \pm 1/2$ resonances respectively. Here the strength and broadening of this signal is given by amplitudes $a_\pm$ and linewidths $w_\pm \approx 1$ kHz. The linewidths $\omega_j$ in the frequency-domain are related to dephasing times $T_2$ in the time-domain through

$$T_2 = \frac{1}{\pi\omega_j}. \tag{4.2}$$

Based on the initial atomic state and the direction of $\vec{B}$, heading error arises in this model from the unresolved NLZ frequency components that bias the observed resonances from $f_{L,\pm}$. Rabi and Ramsey frequency spectroscopy avoid these heading errors by detecting Zeeman shifts between resolved hyperfine transitions highlighted in Fig. 4.1(a).

## 4.2 Ramsey frequency spectroscopy

In this section we describe details behind magnetic field strength measurements using Ramsey frequency spectroscopy. First we discuss the theoretical background of Ramsey interferometry, and show theoretical simulation of expected accuracy. Then, we discuss details behind experimental measurements.

### 4.2.1 Theoretical background of Ramsey interferometry

We first describe the principle of Ramsey interferometry within the context of a standard two-level system, which includes atomic states $|g\rangle = \binom{0}{1}$ and $|e\rangle = \binom{1}{0}$, separated by an energy difference of $\hbar\omega_0$. The principle behind Ramsey interferometry is to initialize the two-level system in its ground state $|g\rangle$, prepare a coherent superposition of $|g\rangle$ and $|e\rangle$ with an initial $\pi/2$ pulse, let this relative phase accumulate, apply a final $\pi/2$ pulse, and detect the excitate state population. The Hamiltonian in the rotating-wave approximation, evaluated at the driving field at frequency $\omega$, is given by

$$H_2 = -\hbar\frac{\Delta}{2}\sigma_z + \hbar\frac{\Omega}{2}\sigma_x \tag{4.3}$$

where $\Delta = \omega - \omega_0$ and $\Omega$ is the complex Rabi frequency coupling the two-level system. The coherent evolution of the two-level system applied to this driving field is given by the unitary operator

$$U_\tau^{\text{on}} = e^{iH_2\tau/\hbar} = \cos(\tilde{\Omega}\tau/2)\mathbb{I} + i\sin(\tilde{\Omega}\tau/2)\Big(\frac{\Delta}{\tilde{\Omega}}\sigma_z - \frac{\Omega}{\tilde{\Omega}}\sigma_x\Big) \tag{4.4}$$

where $\tilde{\Omega} = \sqrt{\Omega^2 + \Delta^2}$. Free evolution for duration $t_R$ with the driving field turned-off is given by

$$U^{\text{off}}_{t_R} = e^{it_R\Delta/2} \left|e\right\rangle \left\langle e\right| + e^{-it_R\Delta/2} \left|g\right\rangle \left\langle g\right|. \tag{4.5}$$

Traditional $\pi/2 - t_R - \pi/2$ Ramsey interferometry is described by

$$n_e = \left| \left\langle e\right| U^{\text{off}}_{\tau_2} U^{\text{off}}_{t_R} U^{\text{on}}_{\tau_1} \left|g\right\rangle \right|^2 = \frac{\Omega^2(2\Delta^2 + \Omega^2)}{(\Delta^2 + \Omega^2)^2} \cos^2(t_R\Delta/2) \tag{4.6}$$

where $\tau_1 = \tau_2 = 1/4\tilde{\Omega}$.

Practically, it is often the case that the driving field induces a frequency shift $\Delta_s$ during the $\pi/2$ pulse that causes a systematic shift $\delta\omega_0$ in the Ramsey central fringe. It can be shown that to first order in $(\Delta_s/\Omega)$ this shift is given by [194]

$$\delta\omega_0 \propto -\frac{1}{t_R}\frac{\Delta_s}{\Omega} \sin(\Omega(\tau_1 + \tau_2)/2) \tag{4.7}$$

which is maximized for the standard $\pi/2 - t_R - \pi/2$ sequence. Based on Eq. (4.7) this shift is canceled to first-order (leaving third-order contributions) by choosing

$$\Omega(\tau_1 + \tau_2) = 2\pi n \tag{4.8}$$

where $n$ is a positive integer. In our work we satisfy Eq.(4.8) by utilizing a $\pi/2 - t_R - 3\pi/2$ sequence. Any Ramsey sequence that deviates from the standard $\pi/2 - t_R - \pi/2$ sequence through pulse duration, excitation frequency, phases to eliminate frequency shifts from the driving field is often referred as a hyper-Ramsey sequence [194].

To further study systematic errors associated with a $\pi/2 - t_R - 3\pi/2$ hyper-Ramsey sequence within the multi-level $^{87}$Rb hyperfine ground states, we time-evolve an initial $8 \times 8$ density matrix $\rho_i$ to produce $\rho_{\text{ram}}(t_R)$ defined by

$$\rho_{\text{ram}}(t_m) = (U^{\text{off}}_{t_m})(U^{\text{on}}_{t_{3\pi/2}})(U^{\text{off}}_{t_R})(U^{\text{on}}_{t_{\pi/2}})\rho_i(U^{\text{on}}_{t_{\pi/2}})^\dagger(U^{\text{off}}_{t_R})^\dagger(U^{\text{on}}_{t_{3\pi/2}})^\dagger(U^{\text{off}}_{t_m})^\dagger \tag{4.9}$$

where $U^{\text{on/off}}_t = e^{-iH_{\text{on/off}}t/\hbar}$ is the unitary time-evolution operator (same as Eq. (3.18)) that denotes whether the microwave field is on or off in the Hamiltonian defined in Eq. (3.7). Included in the above sequence is a final time-evolution of length $t_m$ that is used to average the measured Faraday rotation signal. This step is important in practice since in arbitrary field directions residual Larmor precession can severely degrade the Ramsey fringes.

We theoretically investigate the standard and hyper-Ramsey sequence for realistic off-resonant driving conditions characterized by $\sigma^+$, $\pi$, and $\sigma^-$ Rabi rates $\Omega_1^2 = 25$ kHz, $\Omega_1^1 = 25$ kHz, and $\Omega_1^0 = 40$ kHz, with a DC magnetic field of 50 $\mu$T. We calculate Eq. (4.9) for these parameters at microwave detunings ranging from [-1.5,1.5] kHz about the $|1,1\rangle - |2,2\rangle$ $\sigma^+$ transition [see Fig. 4.2]. The Ramsey time was set to $t_R = 0.3$ ms and $\pi/2$ time $t_{\pi/2} = 10$ $\mu$s. To extract the resonance $f_0$ of the central fringe, we fit

$$\theta_F = a\cos^2(b(f - f_0)) + d \tag{4.10}$$

with free parameters $a$, $b$, and $d$. These fits are shown as dashed and solid lines for the standard and hyper Ramsey protocols respectively. The central fringe of the standard $\pi/2 - t_R - \pi/2$ sequence is shifted 42 Hz from resonance, while the central fringe of the hyper-Ramsey sequence is shifted by 0.5 Hz. This study highlights the enhanced mitigation of systematic shifts of the central fringe using the $\pi/2 - t_R - 3\pi/2$ hyper Ramsey sequence, particularly when varying the microwave detuning.

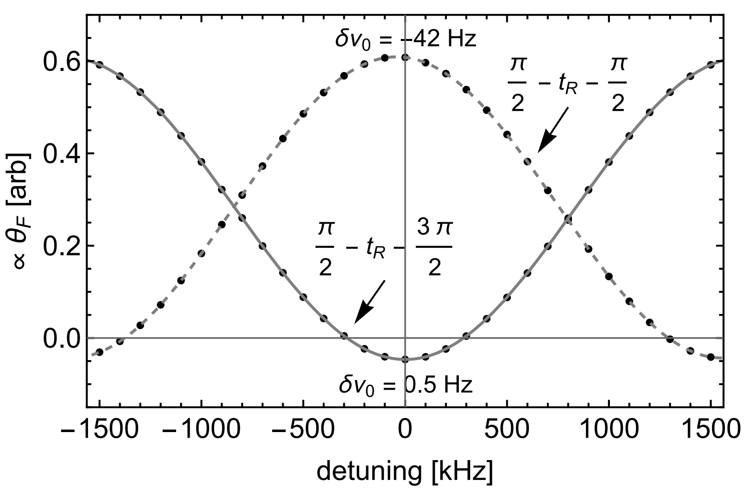


Figure 4.2: Comparison of standard $\pi/2 - t_R - \pi/2$ (dashed) vs hyper-Ramsey $\pi/2 - t_R - 3\pi/2$ (solid) sequences evaluated for the $\sigma^+$ $|1,1\rangle - |2,2\rangle$ transition. The central fringe with the standard Ramsey sequence is shifted 42 Hz from the transition resonance, while the central fringe of the hyper-Ramsey sequence is shifted by 0.5 Hz.

Instead of detecting the transition resonance through the location of the central fringe, we observed superior accuracy when fitting to Ramsey fringes generated from varying the Ramsey time $t_R$. The frequency of these fringes $\Delta_R$ is expected to match the microwave detuning $\Delta$ as shown in Eq. (4.6). This technique offers reduced sensitivity to systematic errors because it is a frequency measurement of the Ramsey fringes in contrast to detecting the location of a central fringe, which is a phase measurement. We extract the transition resonance by fitting a linear line to the Ramsey fringe frequency $\Delta_R$ for several microwave detunings $\Delta$ above and below the transition resonance [see Fig. 4.3(a)], where the x-intercept marks the transition resonance.

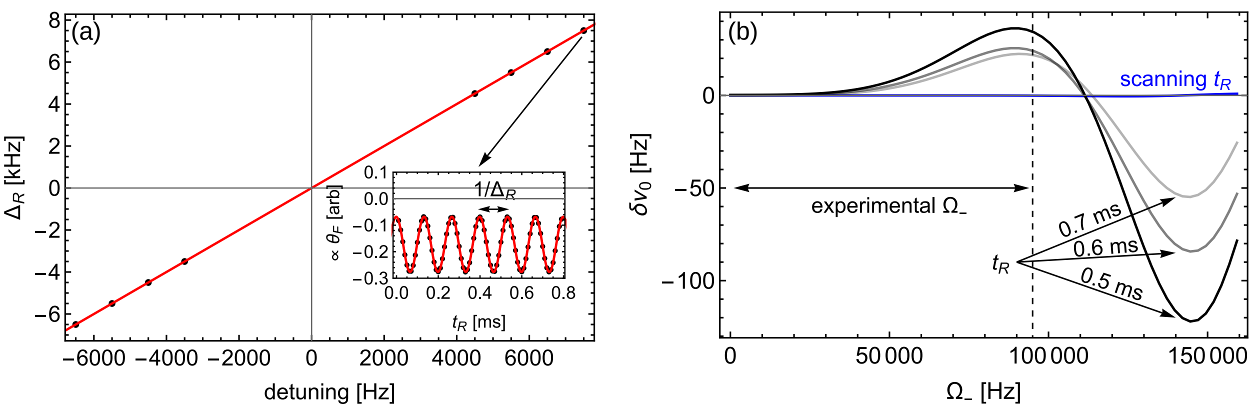


Figure 4.3: Scanning $t_R$ Ramsey interferometry within a $\pi/2-t_R-3\pi/2$ sequence. (a) Ramsey fringe frequency $\Delta_R$ vs microwave detuning from the $|1,1\rangle - |2,1\rangle$ transition. The x-intercept, extracted from a linear fit (red), measures the transition frequency. (b) Systematic shift of the $|1,1\rangle - |2,1\rangle$ transition resonance extracted from Ramsey frequency spectroscopy for various $\Omega_- = \Omega_{m=1}^{m'=0}$ Rabi frequencies that correlate to varying amounts of off-resonant driving. Ramsey interferometry based on detecting the central fringe location (black) at fixed Ramsey times $t_R$ exhibit 100 Hz scale systematics over this range of $\Omega_-$ values. In contrast, the scanning $t_R$ method (blue) mitigates systematic shifts to the sub-Hz level.

This method is depicted in Fig. 4.3, where it's applied to the $|1,1\rangle - |2,1\rangle$ $\pi$ transition. We use Eq. (4.9) and set the Rabi Rates at $\Omega_{m=1}^{m'=2} = 18$ kHz and $\Omega_{m=1}^{m'=1} = 25$ kHz, with a $\pi/2$ pulse duration of $t_{\pi/2} = 10$ $\mu$ s, and a magnetic field strength of $B = 50$ $\mu$T. The Ramsey time $t_R$ is varied up to 0.8 ms. To assess the effectiveness of this technique in compensating for systematic errors due to off-resonant driving, we adjust the adjacent $\sigma^-$ transition Rabi rate $\Omega_{m=1}^{m'=0}$ up to 160 kHz, as shown in Fig. 4.2(b). In this example, central fringe $\pi/2-t_R-3\pi/2$ Ramsey interferometry exhibits systematic shifts around 100 Hz, whereas the scanning $t_R$ Ramsey interferometry approach mitigates systematic shifts at a sub-Hz level. This analysis motivates scanning $t_R$ Ramsey interferometry over central fringe Ramsey interferometry as an accurate method for the spectroscopy of hyperfine transitions. We have observed in similar simulations that the scanning $t_R$ Ramsey interferometry performs with similar accuracy for either a $\pi/2 - t_R - \pi/2$ or a $\pi/2 - t_R - 3\pi/2$ Ramsey sequence.

### 4.2.2 Experimental implementation of Ramsey frequency spectroscopy

Next, we discuss hyperfine spectroscopy measurements on the four transitions $\nu_m^{m'} \approx 6.8$ GHz between sublevels $|1, m\rangle$ and $|2, m'\rangle$ marked in Fig. 4.1(a) using scanning $t_R$ Ramsey interferometry. These measurements utilize a $\pi/2 - t_R - 3\pi/2$ Ramsey sequence with a $\pi/2$ pulse length of $t_{\pi/2} = 4\tilde{\Omega}_m^{m'} \approx 10$ $\mu$s [see Fig. 4.4(a)]. Satisfying this particular $t_{\pi/2}$ required manual adjustments to the microwave power at each magnetic field direction and hyperfine transition such that the generalized Rabi frequency satisfied $\tilde{\Omega}_m^{m'} \approx 25$ kHz. Importantly, after each pulse sequence, we average the resulting Faraday signal for 50 $\mu$s to filter out residual 350 kHz Larmor precession. As shown in the pulse diagram in Fig. 4.4(a) we employ adiabatic optical pumping, which consists of a 100 mW pump pulse lasting 50 $\mu$s followed by a 50 $\mu$s interval where the pump power is linearly ramped off.

We fit these Ramsey fringes [insets of Fig. 4.4(b)] in the time-domain using an exponentially decaying sinusoid (Eq. (3.30)) and force the fringe frequencies $\Delta_R$ to be either positive or negative according to the sign of the microwave detuning $\Delta_m^{m'} = \nu_{\mu\text{w}} - \nu_m^{m'}$. Without influence from systematic shifts, $\Delta_R = \Delta_m^{m'}$. We choose 6 microwave detunings $\Delta_m^{m'} \in [5, 10]$ kHz below and above each transition resonance as shown for the $\sigma^+$ transition in Fig. 4.4(b). All of these measurements are taken in random order to mitigate systematic errors from time-dependent drifts in the microwave field. By linear fitting $\Delta_R$ as a function of the microwave frequency $\nu_{\mu\text{w}}$, the x-intercept measures $\nu_m^{m'}$. The magnetic field $B$ and the pressure shift arising from $N_2$ buffer gas collisions $\nu_{\text{bg}} \approx 88$ kHz are obtained by fitting [see Fig. 4.6(a)] $\nu_m^{m'}$ measurements to

$$\frac{h\nu_m^{m'}}{\Delta E} = \frac{m' - m}{g_s/g_i - 1} x + \frac{1}{2} \sum_{M=m,m'} \sqrt{1 + \frac{4Mx}{2I+1} + x^2} \tag{4.11}$$

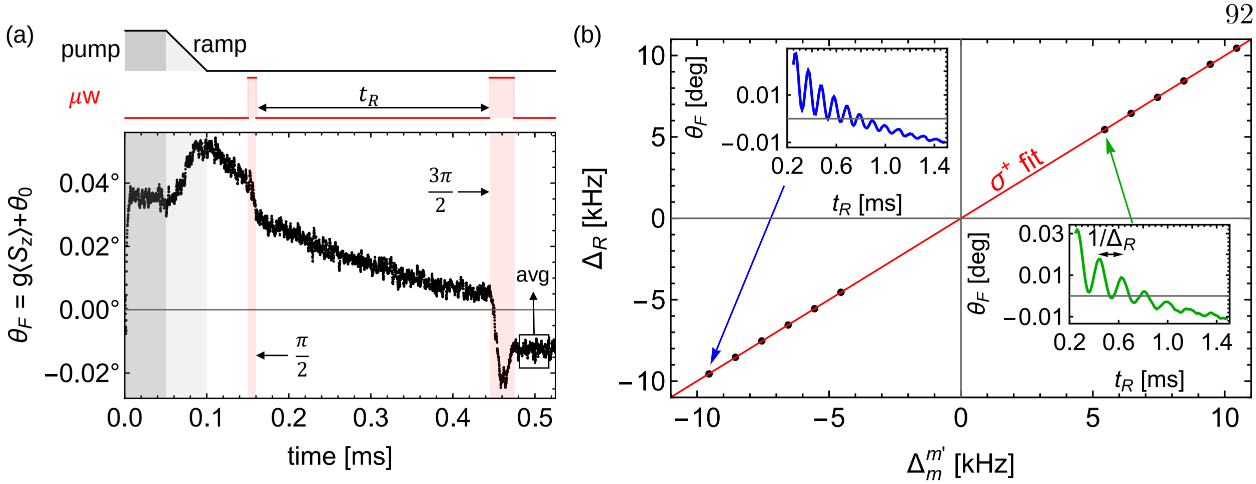


Figure 4.4: (a) Ramsey interferometry Faraday rotation measurement and associated timing diagram. (b) Ramsey frequency vs microwave detuning for the $\sigma^+$ transition. Insets show measured Ramsey fringes as a function of the Ramsey time $t_R$. A linear fit (red) extracts the transition resonance.Both (a) and (b) were measurement at $\beta = 35°$.

where $x = (g_s - g_i)\mu_B B/\Delta E$ and $\Delta E = (A + h\nu_{\rm bg}/2)(I + 1/2)$ is the hyperfine splitting expressed in terms of the magnetic dipole hyperfine constant $A$.

The measurement sequence [see Fig. 4.5] to perform Ramsey frequency spectroscopy involves several Ramsey-FID acquisition periods with a repetition rate of 1 second. This includes a 0.9 second dead-time between each acquisition period, necessary to ensure that the electrical heating keeps the cavity temperature stable at 100°C. Each Ramsey-FID acquisition period, lasting 105 ms, includes 48 Ramsey sequences evaluated with unique microwave detunings. These 48 detunings correspond to 12 microwave frequencies for each of the four hyperfine transitions, randomly sequenced in time. Following these 48 Ramsey sequences, three FID measurements are carried out. Each acquisition period is repeated 124 times corresponding to the variation of 124 Ramsey free evolution times within the 48 Ramsey sequences. The Ramsey free evolution times range from 0.2 ms to 1.43 ms and spaced by 10 $\mu$s. For averaging, all 124 acquisition periods are repeated 10 times, resulting in a total of 1240 acquisition periods ($\approx$ 34 minutes) for each magnetic field measurement. This process, repeated over 14 magnetic field directions, resulted in a total measurement duration of approximately 4.8 hours.

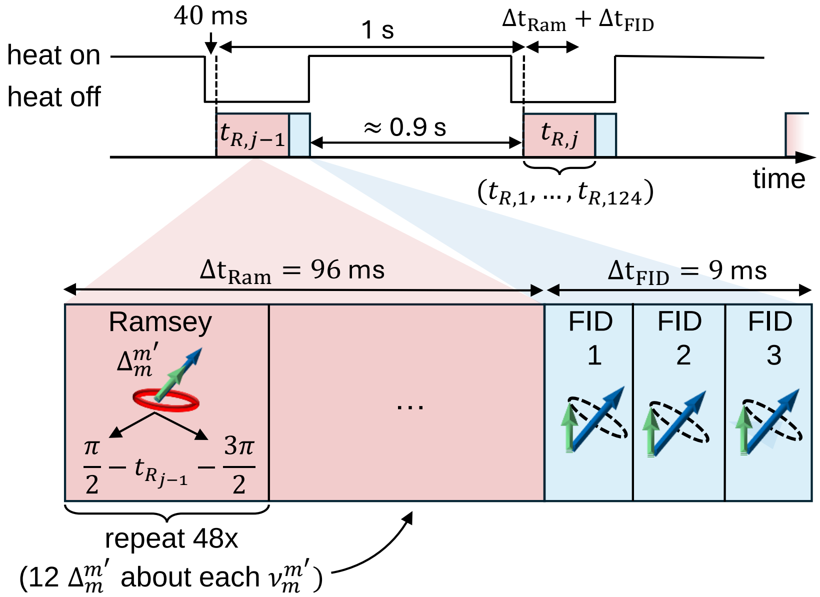


Figure 4.5: Timing diagram for Ramsey frequency spectroscopy. (Top) Ramsey measurements are segmented into acquisition periods lasting $\Delta t_{\mathrm{Ram}} + \Delta t_{\mathrm{FID}} = 105$ ms and repeated every 1 second. A total of 124 acquisition periods are taken that correspond to 124 different Ramsey times $T_{R,j}$ spanning 0.2 ms to 1.43 ms. All 124 acquisition periods are repeated 10 times for averaging. (Bottom) Each acquisition period consists of 48 Ramsey sequences corresponding to the 12 microwave detunings for each of the 4 hyperfine transitions $\nu_m^{m'}$. At the end of each acquisition period are 3 FID measurements.

We map the discrepancy between the magnetic field strength measurments using Ramsey frequency spectroscopy against the FID measurements over 14 magnetic field directions [see Fig. 4.6(b)]. This discrepancy, presumably FID heading error, monotonically scales with the polar angle $\beta$ and is contained within 5 nT. Fluctuations in the Ramsey measurements for different magnetic field directions are observed larger than the statistical error bars. This is likely due to instabilities in state preparation occuring over the 4.8 hour duration it took to make these Ramsey measurements.

Our coil system exhibits drifts between repeated measurements on the order of a few nT as seen in the inset of Fig. 4.6(b). Despite this, Ramsey magnetic field measurements follow the drifts of the corresponding FID measurements. We also observe drifts in the extracted pressure shift $\nu_{\mathrm{bg}}$ due to temperature instability of our microwave cavity [see Fig. 4.6(c)]. Due to the long duration

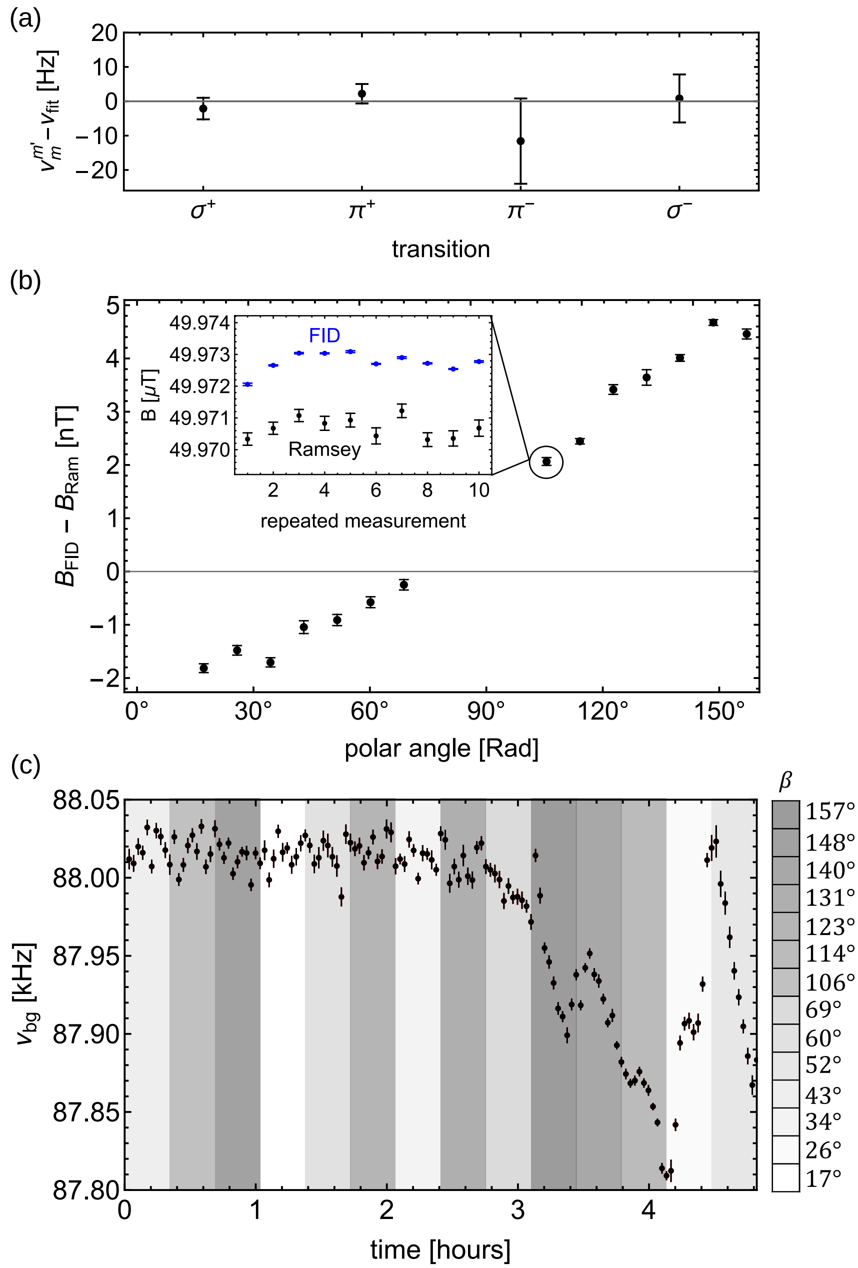


Figure 4.6: Magnetic field strength and pressure shift evaluated over 14 different magnetic field orientations with Ramsey frequency spectroscopy. Error bars show 68% confidence interval. (a) Residuals of fitting Eq. (4.11) to the hyperfine resonances. (b) FID measurements and Ramsey frequency spectroscopy magnetic field strength residuals over 14 different magnetic field orientations with respect to the single optical axis. Inset shows repeated FID and Ramsey measurements. (c) The corresponding buffer gas pressure shifts $\nu_{\mathrm{bg}}$ obtained with the magnetic field strength measurements during Ramsey frequency spectroscopy. The magnetic field orientation during these measurements is indicated by the shaded color. Drift in $\nu_{\mathrm{bg}}$, seen here, is due to a few °C temperature drift of the microwave cavity during the total measurement duration of 4.8 hours.

it takes to measure Ramsey fringes, it is possible that drifts in $\nu_{\text{bg}}$ during this measurement period may cause systematic errors in the magnetic field strengths. In the next section, we discuss scalar measurements using Rabi frequency spectroscopy taken on a different day. Consistency between FID heading error measurements between Ramsey and Rabi frequency spectroscopy contests to their accuracy, even with drifts in our apparatus.

### 4.3 Rabi frequency spectroscopy

Next, we discuss Rabi frequency spectroscopy, which measures hyperfine resonances $\nu_m^{m'}$ from the detuning $\Delta_m^{m'}$ dependence of generalized Rabi frequencies $(\tilde{\Omega}_m^{m'})^2 \approx (\Delta_m^{m'})^2 + |\Omega_m^{m'}|^2$. The generalized Rabi frequencies $\tilde{\Omega}_m^{m'}$ are fitted from Rabi oscillations using an exponentially decaying sinusoid (Eq. (3.30)), and utilize the same adiabatic pumping parameters as used for the Ramsey measurements [see Fig. 4.7(a)]. Unlike Ramsey frequency spectroscopy, this approach demands precise modeling of atom-microwave coupling to accommodate for frequency shifts from off-resonant driving. This atom-microwave coupling is theoretically described by the eigenvalue differences of the atom-microwave Hamiltonian (Eq. (3.7)) discussed in Ch. 3 [see Fig. 4.7(b,c)]. Rabi measurements at each microwave detuning are made independently with three microwave polarization ellipses (MPEs) generated from different excitations of the microwave cavity ports. Consistency of magnetic field and pressure shifts extracted from Rabi frequency spectroscopy for each of these MPEs serves as an accuracy check that frequency shifts from off-resonant driving are correctly compensated.

Generalized Rabi frequency measurements $\tilde{\Omega}_m^{m'}$ are shown in Figure 4.8 for all three MPEs. We purposely choose weaker microwave fields such that Rabi rates $\Omega_m^{m'} < 25$ kHz to enable narrow Rabi resonances. The limit to how small the Rabi frequencies can be is constrained by the $T_2 \approx .25$ ms coherence time. The atom-microwave Hamiltonian defined in Eq. (3.7) accounts for systematic shifts in the Rabi oscillations from off-resonant driving through the expression $h\tilde{\Omega}_m^{m'} = \lambda_j - \lambda_i$, where eigenvalues $\lambda_j$ and $\lambda_i$ of $H$ correspond to the pair of dressed states coupled by the microwave field. With this model, the magnetic field strength $B$ and the pressure shift $\nu_{\text{bg}}$ are fitted from generalized Rabi frequencies $\tilde{\Omega}_m^{m'}$, driven at 25 microwave detunings $\Delta_m^{m'}$ spaced by 800 Hz, with

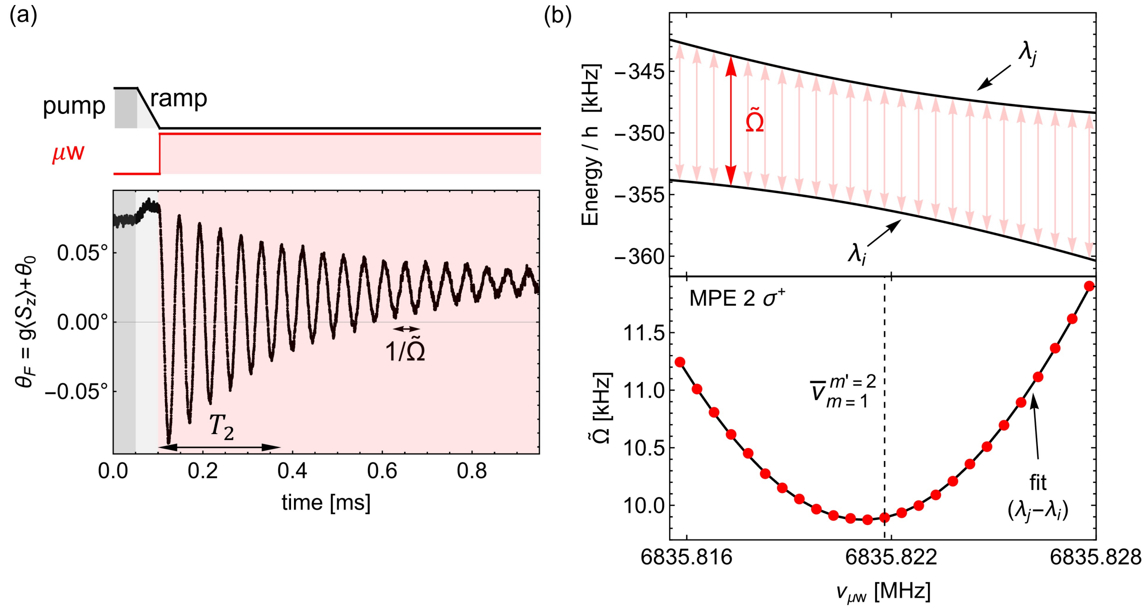


Figure 4.7: (a) Rabi frequency spectroscopy pulse sequence. (b) $\sigma^+$ Rabi measurements and corresponding eigenvalue differences $\lambda_j - \lambda_i$ of $H$ ( Eq. (3.7)) versus the microwave frequency $\nu_{\mu\mathrm{w}}$.

center frequency $\overline{\nu}_m^{m'}$ that is near-resonant with the hyperfine transitions $\nu_m^{m'}$ [see Fig. 4.8].

We utilize the sequence of Rabi acquisition periods diagrammed in Fig. 4.9 to make all of these Rabi measurements. Each Rabi acquisition period is comprised of 300 Rabi frequency measurements, corresponding to the 25 microwave detunings for each hyperfine transition across MPE 1, 2, and 3, lasting $\Delta t_{\mathrm{Rabi}} = 400$ ms. Unlike Ramsey frequency spectroscopy, all Rabi data across the hyperfine transitions is contained within the $\Delta t_{\mathrm{Rabi}}$ acquisition period. Like the Ramsey measurements, a deadtime of roughly 2.6 seconds is incorporated between each measured Rabi acquisition period to maintain the cavity temperature to near 100 °C. To allow the microwave components to thermally stabilize, and minimize microwave field drift, we make the Rabi acquisition period twice before executing and recording the final Rabi acquisition period. The microwave frequencies used in the Rabi measurements are arranged in a random temporal sequence, and MPE measurements are interlaced to minimize the time any given microwave component is turned off. A 1 ms dead-time, for technical reasons that are not relevant, was incorporated between each set of three MPE measurements, as shown in Fig. 4.9. Following the Rabi measurements, three FID

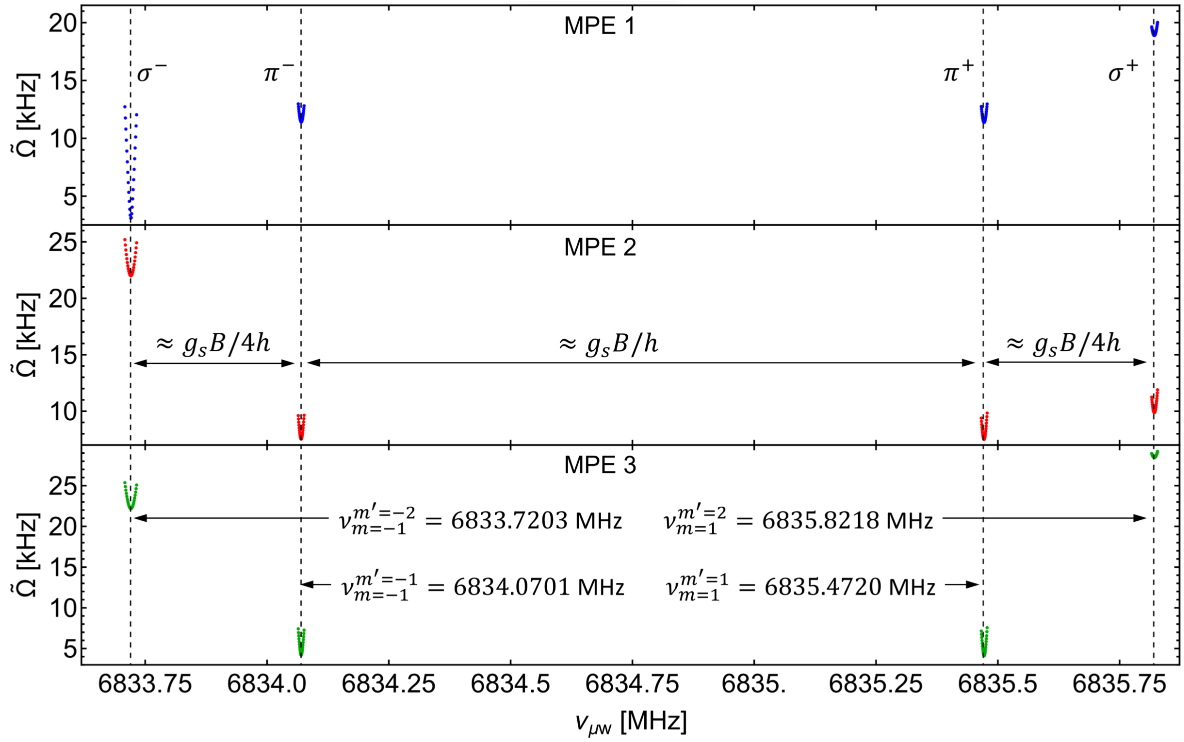


Figure 4.8: Rabi frequency spectroscopy by MPE 1, MPE 2, and MPE 3 at $\beta = 35°$. All microwave detunings are centered about microwave frequencies $\overline{\nu}_m^{m'}$ (dashed lines).

measurements are conducted over $\Delta t_{\mathrm{FID}} = 9$ ms. For each of the 14 magnetic field orientations, the combined Rabi+FID measurement sequence is repeated eight times for averaging.

### 4.3.1 Fitting $B$ and $\nu_{\mathrm{bg}}$ from Rabi frequency measurements

We fit the magnetic field strength $B$ and the pressure shift $\nu_{\mathrm{bg}}$ from the measured generalized Rabi frequencies $\tilde{\Omega}_m^{m'}(\nu_{\mu\mathrm{w}})$, evaluated at microwave frequencies $\nu_{\mu\mathrm{w}}$, by minimizing the following cost function

$$r_B = \sum_{(m,m')} \sum_{k=-12}^{12} w_{m,m',k} \left[ \delta\lambda_m^{m'}(B, \nu_{\mathrm{bg}}, \mathcal{B}_{\sigma^+}, \mathcal{B}_{\pi}, \mathcal{B}_{\sigma^-}, \nu_{\mu\mathrm{w}}) - \tilde{\Omega}_m^{m'}(\nu_{\mu\mathrm{w}}) \right] \Bigg|_{\nu_{\mu\mathrm{w}} = \overline{\nu}_m^{m'} + k(800\ \mathrm{Hz})} \tag{4.12}$$

where $\delta\lambda_m^{m'} = (\lambda_j - \lambda_i)/h$, where $\lambda_j$ and $\lambda_i$ are the eigenvalue pair correponding to $\tilde{\Omega}_m^{m'}$. We use the algorithm detailed in to select the correct pair of eigenvalues. The spherical microwave components $\sigma^{\pm}$ and $\pi$, assumed to be real and positive, are additional free parameters in the fit.

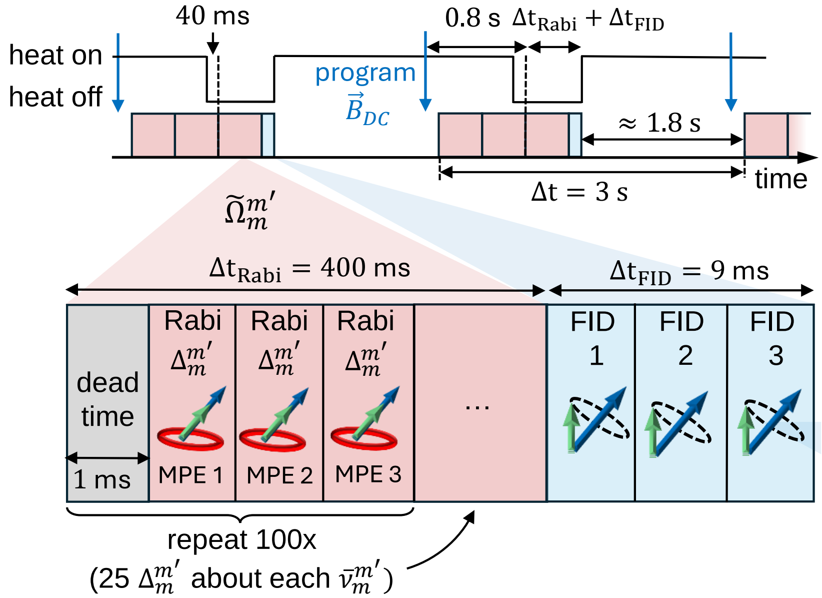


Figure 4.9: Timing diagram for Rabi frequency spectroscopy measurements. The Rabi measurement sequence consists of 100 Rabi measurements for each of the 3 MPEs. These 100 Rabi measurements correspond to 25 microwave detunings about each of the four hyperfine transitions in Fig. 4.1(a). As shown in the second row of the timing diagram these Rabi measurements of different MPEs are interlaced at a given microwave frequency. At the end of the acquisition period are 10 FID measurements. Bottom: Rabi oscillation measurement with a moving average of 10 data-points and measured at a magnetic field orientation of $\beta = 35°$.

The transitions $(m, m')$ in Eq. (4.12) are either summed over the $(\sigma^-, \pi^-, \sigma^+)$ or the $(\sigma^-, \pi^+, \sigma^+)$ transitions [see Fig. 4.1(a)]. Weights $w_{m,m',k} = (1/\delta\tilde{\Omega}_m^{m'})^2$ are given in terms of the generalized Rabi frequency fitting error $\delta\tilde{\Omega}_m^{m'}$. The reason for this is due to the microwave frequency dependence of the microwave cavity modes, which causes the $\pi$ spherical microwave component to be different at the microwave frequencies for the $\pi^\pm$ transitions. Thus, fitting all four hyperfine transitions at once, with only one $\mathcal{B}_\pi$ parameter leads to fitting errors. We assume that the MPE parameters are constant for microwave frequencies near $\bar{\nu}_m^{m'}$. Sec. 4.6 explores potential systematic errors of this assumption. Scalar and buffer gas pressure measurements for different magnetic field orientations are shown in Fig. 4.10.

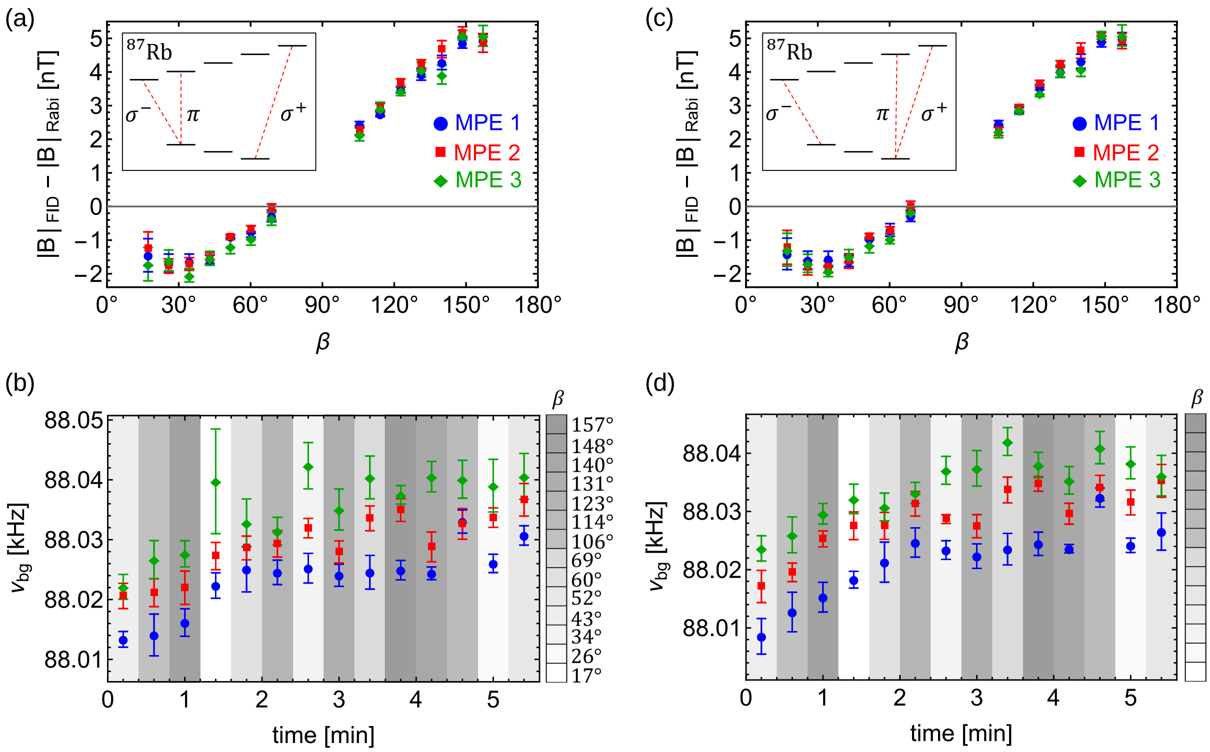


Figure 4.10: Magnetic field $B$ and pressure shift $\nu_{\mathrm{bg}}$ measurements using Rabi frequency spectroscopy with (a,b) $(\sigma^-, \pi^-, \sigma^+)$ transitions and (c,d) $(\sigma^-, \pi^+, \sigma^+)$ transitions. Pressure shift measurements are reported with respect to the measurement time to show the measurement duration compared to the Ramsey measurements in Fig. 4.6(c). Drift in the pressure shifts denote small temperature drifts of the vapor cell and cavity.

### 4.3.2 Characterization of microwave polarization ellipses (MPEs)

This section concludes with the characterization of the MPEs utilized in Rabi frequency spectroscopy. For these calibrations, we fit the 5 MPE parameters $(\mathcal{B}_x, \mathcal{B}_y, \mathcal{B}_z, \phi_x, \phi_y)$ from generalized Rabi frequency measurements at each of the 14 different magnetic field directions against the eigenvalue value model $\delta\lambda_m^{m'}$ of $H$ [see Fig. 4.11]. We make 12 independent MPE calibrations corresponding to Rabi measurements driven at the four microwave frequencies $\nu_{\mu\mathrm{w}} = \overline{\nu}_m^{m'}$, and the three unique cavity excitations (MPE 1, MPE 2, and MPE 3).

Due to the fact that the magnetic field determines the atomic quantization axis, this calibration requires knowledge of the magnetic field strength $B$ and the magnetic field direction $(\alpha, \beta)$. For this we use the FID measurements to estimate $B$, and the coil system calibration to estimate

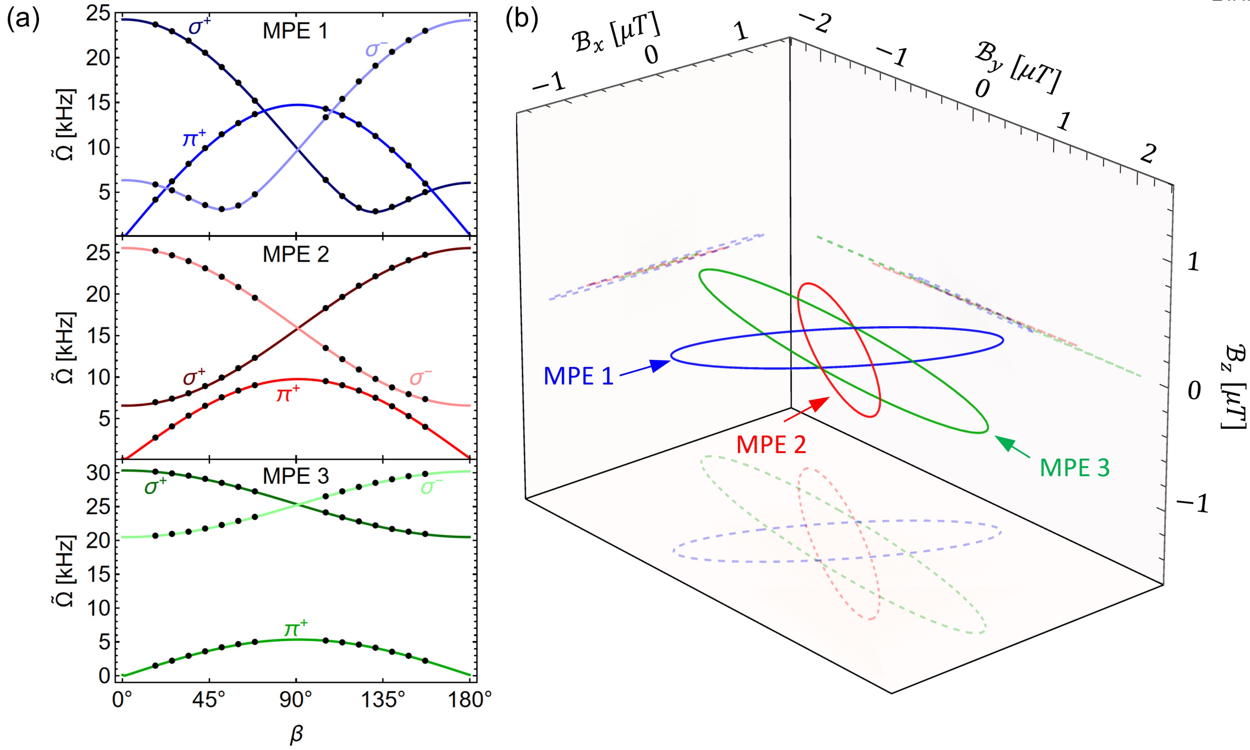


Figure 4.11: (a) Polar angle dependence of Rabi-frequency measurements for the $\sigma^+, \pi^+$, and $\sigma^-$ hyperfine transitions. Solid lines show fits to calibrate the polarization ellipses. (b) Calibrated microwave polarization ellipses used for Rabi frequency spectroscopy.

$(\alpha, \beta)$. FID systematic errors are not a concern for these calibrations since $\tilde{\Omega}_m^{m'}$ depends on $\Delta_m^{m'}$ in second-order near the transition resonance. We denote the 14 different magnetic field directions with corresponding magnetic field strengths used in the calibration as $(\alpha_k, \beta_k)$ and $B_k$ respectively. We solve for free parameters $\nu_{\rm bg}, \mathcal{B}_x, \mathcal{B}_x, \mathcal{B}_x, \phi_x, \phi_y$ with the cost function $r_{\rm MPE}$ given by

$$r_{\rm MPE} = \sum_{k=1}^{14} w_{m,m',k} \left[ \delta\lambda_{m,m'}(B_k, \nu_{\rm bg}, \mathcal{B}_x, \mathcal{B}_x, \mathcal{B}_x, \phi_x, \phi_y, \alpha_k, \beta_k, \nu_{\mu \rm w} = \overline{\nu}_m^{m'}) - (\tilde{\Omega}_m^{m'})\Big|_{(\alpha_k, \beta_k)} \right]^2 \quad (4.13)$$

where we write the eigenvalue function $\delta\lambda_{m,m'}$ explicitly in terms of the free microwave, pressure shift, and magnetic field parameters. While we leave the buffer gas pressure shift $\nu_{\rm bg}$ as a free parameter, these calibrations fit $\nu_{\rm bg} \approx 88$ kHz to an accuracy within a few hundred Hz from the fact that the generalized Rabi frequencies $\tilde{\Omega}_m^{m'}$ are only measured at a single microwave frequency $\overline{\nu}_m^{m'}$ that is near resonance of the hyperfine transition. Weights $w_{m,m',k} = (1/\delta\tilde{\Omega}_m^{m'})^2\big|_{(\alpha_k, \beta_k)}$ are given in terms of the generalized Rabi frequency fitting error $\delta\tilde{\Omega}_m^{m'}|_{(\alpha_k, \beta_k)}$. The calibrated MPE parameters for each of the three MPEs at each microwave frequency $\nu_{\mu\text{w}}$ are tabulated in Table 4.1 and plotted in Fig. 4.11.

Table 4.1: Measured MPE 1, 2, and 3 parameters used in Rabi frequency spectroscopy calibrated at microwave frequencies $\overline{\nu}_m^{m'}$.

| $\nu_{\mu\text{w}}$ [MHz] | $\mathcal{B}_x$ [$\mu$T] | $\mathcal{B}_y$ [$\mu$T] | $\mathcal{B}_z$ [$\mu$T] | $\phi_x$ [rad] | $\phi_y$ [rad] |
|---|---|---|---|---|---|
| $\overline{\nu}_{-1}^{-2} = 6833.7203$ | 1.2177 | 0.7973 | 0.01884 | 3.549 | 2.292 |
| $\overline{\nu}_{-1}^{-1} = 6834.0701$ | 1.2158 | 0.7810 | 0.020 | 3.467 | 2.340 |
| $\overline{\nu}_{1}^{1} = 6835.472$ | 1.2136 | 0.7938 | 0.0207 | 3.445 | 2.373 |
| $\overline{\nu}_{1}^{2} = 6835.8218$ | 1.2100 | 0.8091 | 0.0232 | 3.751 | 2.480 |
| $\overline{\nu}_{-1}^{-2} = 6833.7203$ | 0.8046 | 1.3086 | 0.0298 | 4.077 | 5.842 |
| $\overline{\nu}_{-1}^{-1} = 6834.0701$ | 0.8076 | 1.3747 | 0.0221 | 3.764 | 5.538 |
| $\overline{\nu}_{1}^{1} = 6835.472$ | 0.8038 | 1.3021 | 0.0210 | 3.744 | 5.989 |
| $\overline{\nu}_{1}^{2} = 6835.8218$ | 0.7952 | 1.3142 | 0.0236 | 3.843 | 5.263 |
| $\overline{\nu}_{-1}^{-2} = 6833.7203$ | 0.4125 | 2.0849 | 0.0116 | 3.346 | 2.018 |
| $\overline{\nu}_{-1}^{-1} = 6834.0701$ | 0.4465 | 2.0543 | 0.0070 | 3.104 | 2.115 |
| $\overline{\nu}_{1}^{1} = 6835.472$ | 0.4402 | 2.0363 | 0.0092 | 3.020 | 2.136 |
| $\overline{\nu}_{1}^{2} = 6835.8218$ | 0.4352 | 2.0871 | 0.0033 | 3.229 | 2.025 |

In Sec. 4.6, we utilize these calibrated MPE parameters to study a potential systematic error in Rabi frequency spectroscopy due to the microwave frequency dependence of the cavity modes arising from the 110 MHz finite cavity mode linewidth (Sec. 2.5). For comparison, the microwave frequencies of our Rabi measurements span nearly 2 MHz [see Fig. 4.8]. Other factors, such as standing waves in the SMA cables and frequency dependent amplitude and phase shifts from the bandpass filters and microwave amplifiers, may also contribute to the frequency dependence of the MPE parameters.

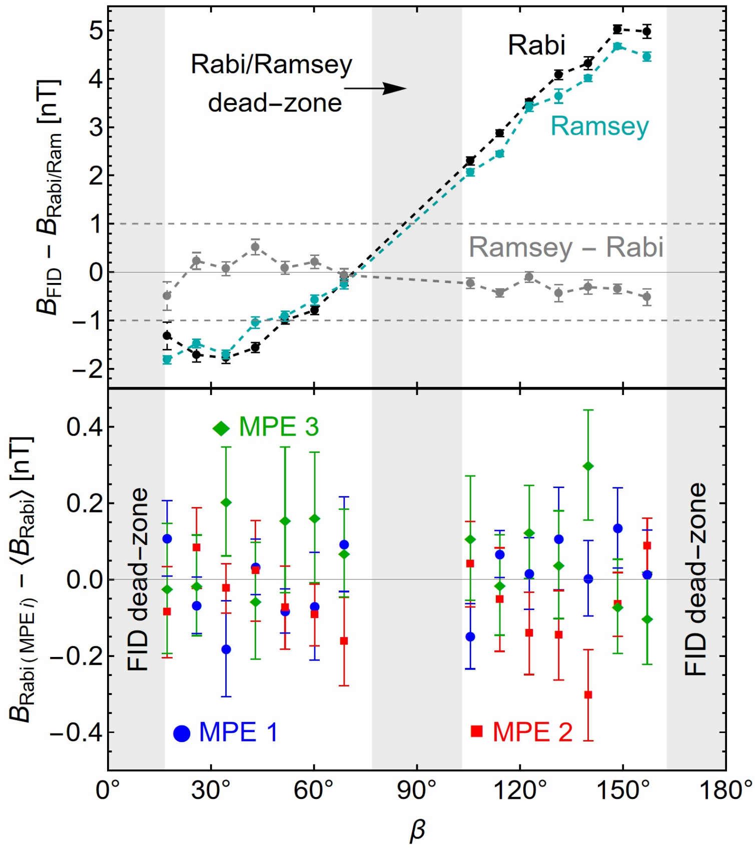


Figure 4.12: Comparison of FID, Rabi, and Ramsey scalar measurements over different magnetic field directions. Error bars show 68% confidence intervals. (Top) Differences between FID measurements with Ramsey (cyan) and Rabi (black) scalar measurements, and differences between Ramsey and Rabi scalar measurements (gray). (Bottom) Differences between Rabi scalar measurements for each MPE with respect to the average scalar across all three MPEs.

## 4.4 Comparison of magnetic field strengths extracted from Rabi and Ramsey frequency spectroscopy

Final results comparing FID measurements against the Rabi and Ramsey scalar measurements are shown in Fig. 4.12(a). The final $B$ and $\nu_{\mathrm{bg}}$ values in the Rabi frequency spectroscopy average the $(\sigma^-, \pi^-, \sigma^+)$ and $(\sigma^-, \pi^+, \sigma^+)$ measurements displayed in Fig. 4.10. The discrepancy between the Rabi and Ramsey scalar data are within 0.6 nT, while the FID measurements differ from both the Rabi and Ramsey scalar data by up to 5 nT over the 14 $\vec{B}$ directions. Heading errors qualitatively similar to Fig. 4.12(a) are predicted from simulations in Sec. 4.6 using our experimental parameters. Despite different systematic errors from off-resonant microwave driving, the Rabi scalar measurements across different MPEs are consistent to within 0.3 nT [see Fig. 4.12(b)]. Figure 4.13 emphasizes the critical role of accounting for off-resonant driving using Eq. (4.12). In contrast, fitting Rabi measurements from each hyperfine transition with the two-level Rabi formula, as specified in Eq. (1.5), results in discrepancies up to 3 nT in the estimated magnetic field strength. From theoretical simulations accounting for MPE $\nu_{\mu\mathrm{w}}$-dependence, spin-exchange frequency shifts [15, 124], as well as lineshape distortions from atomic collisions, we estimate scalar errors to be contained within 0.5 nT for the Rabi and Ramsey methods. These simulations show that a large portion of errors ($< 0.4$ nT) arise due to frequency shifts from spin-exchange collisions. These estimates, along with drifts of the optical-pumping parameters, are consistent with the measured differences, bounded by 0.6 nT, between the Ramsey and Rabi measurements [see Fig. 4.12(a)].

## 4.5 Rabi frequency spectroscopy sensitivity analysis

The magnetic field strength and pressure shift sensitivities from the Rabi frequency spectroscopy data are reported in Fig. 4.14 with the best sensitivities observed to be near 60 pT/$\sqrt{\mathrm{Hz}}$ and 1.0 Hz/$\sqrt{\mathrm{Hz}}$. The magnetic field strength sensitivity $S_B = \sigma_B\sqrt{t_m}$ is calculated from the standard error $\sigma_B$, using eight repeated measurements of $B$ over a total measurement time $t_m = 8 \times 100$ ms. The sensitivities $S_{\nu_{\mathrm{bg}}}$ of the buffer gas pressure shifts are calculated similarly. Measurement repetitions are separated by $\Delta t = 3$ seconds [see Fig. 4.9], covering deadtime allocated for cavity heating between measurements. This downtime is excluded from the active measurement period, $t_m$, when calculating $S_B$ and $S_{\nu_{\mathrm{bg}}}$. Included in Fig. 4.14 are the corresponding scalar sensitivities from eight repeated FID measurements, also separated by 3 seconds, evaluated from an active measurement time $t_m = 8 \times 9$ ms. Each FID scalar value is derived from a 9 ms FID train consisting of three FIDs each lasting 3 ms as diagrammed in [see Fig. 4.9]. Error bars for these sensitivity measurements denote a 95% confidence interval from the uncertainty in the standard error calculated from only 8 repeated measurements. This confidence interval is calculated by analyzing the

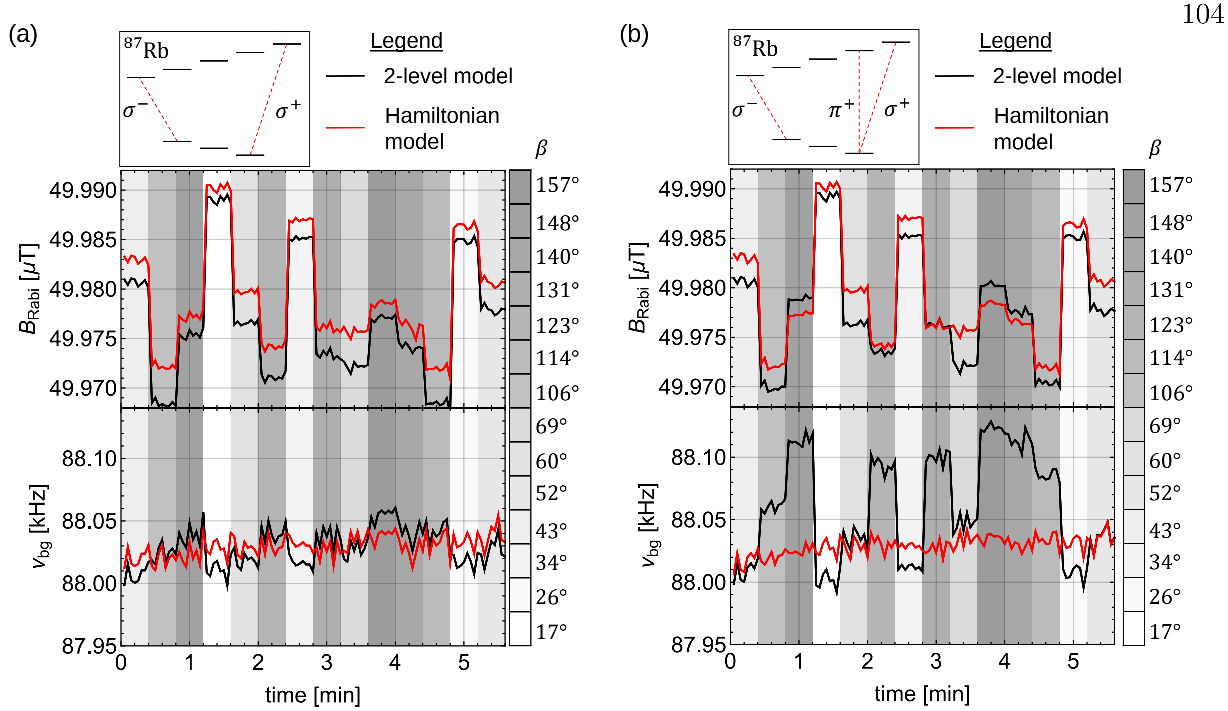


Figure 4.13: Comparison of Rabi fitting using the two-level Rabi formula given by Eq. (1.5) (black) versus the multi-level Hamiltonian model given by Eq. (4.12) (red). For these fits, the two-level Rabi formula assumes that the hyperfine transition resonance is given by the Breit-Rabi formula Eq. (4.11). All of the measurements in these plots are with the MPE 2 data. We compare (a) fitting with only $\sigma^{\pm}$ with (b) fitting with $\sigma^{\pm}$ and $\pi^{+}$. In both cases the two-level model deviates from the full Hamiltonian model up to 4 nT because of frequency shifts from off-resonant driving. When $\pi$ measurements are included the pressure shift $\nu_{\mathrm{bg}}$ exhibits errors around 100 Hz for some magnetic field directions.

standard deviation of many repeated standard errors, calculated from eight fake data points with Gaussian noise. Overlaid in Fig. 4.14 is the estimated $S_B$ contribution from our coil system derived from noise of our current source at 0.3 Hz taking the form

$$S_{B_{coil}}(\beta) = \sqrt{(S_{B_{x,coil}}\sin(\beta))^2 + (S_{B_{z,coil}}\cos(\beta))^2} \tag{4.14}$$

accounting for the fact that the $x$ and $z$ coil pairs have different coil factors $a_x = 91.7\ \mu\mathrm{T/A}$ and $a_z = 392.8\ \mu\mathrm{T/A}$ [Sec. 2.4.1].

To assess the inherent precision of the Rabi scalar method, we first determine the minimum variance $\sigma_\Omega^2$ (Cramer-Rao lower bound, CRLB) for the frequency uncertainty of a Rabi oscillation.

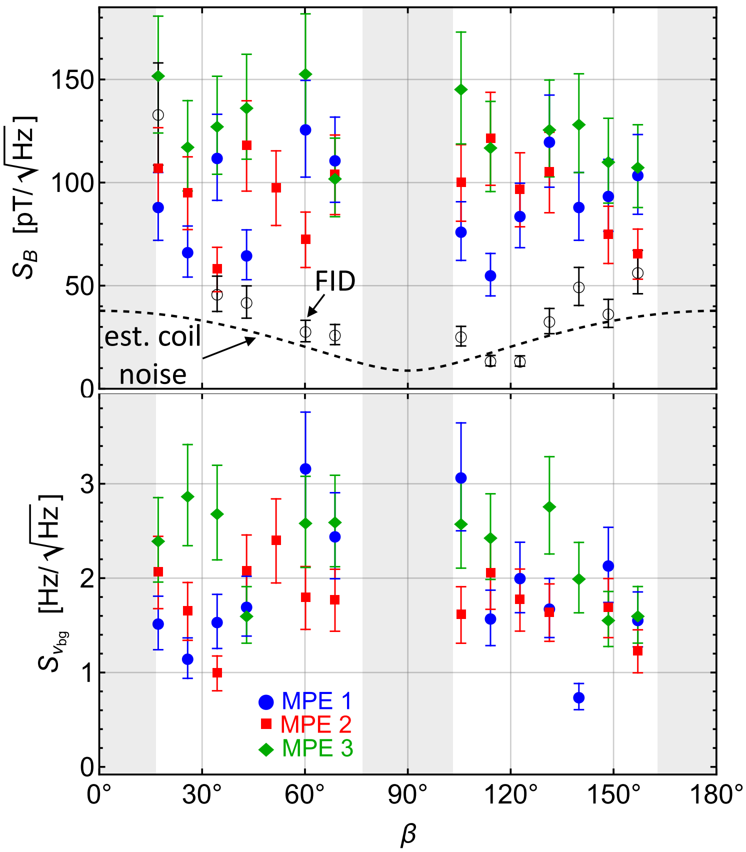


Figure 4.14: Magnetic field strength and pressure shift sensitivities from Rabi frequency spectroscopy measurements. Top and bottom plots show the sensitivities of the magnetic field strength and buffer gas pressure shift respectively. The scalar sensitivities from the FID measurements (black circles) and the expected coil noise (black dashed), assessed at our 0.3 Hz measurement repetition rate, are overlaid for comparison. Error bars denote a 95% confidence interval due to the fact that the sensitivities were calculated from the noise in only eight repeated measurements.

The CRLB for a damped sinusoid is given by [62, 68]

$$\sigma_\Omega^2 \geq \frac{12}{(2\pi)^2 (A_\theta/\sigma_\theta)^2 f_s T_r^3} C \tag{4.15}$$

Where $A_\theta/\sigma_\theta$ is the signal-to-noise ratio (SNR), $T_r = 0.85$ ms is the measurement time, and $f_s = 10$ MHz is sampling rate. The factor $C$ is an overall constant given in terms of the dephasing time $\gamma_2 = 1/T_2$ and the number of samples $N = f_s T_r = 8500$

$$C = \frac{N^3}{12} \frac{(1-z^3)^3(1-z^{2N})}{z^2(1-z^{2N})^2 - N^2 z^{2N}(1-z^2)^2} \tag{4.16}$$

where $z = e^{-\gamma_2/f_s}$.

We first consider an ideal case where all atomic population is evenly distributed within the $F = 1$ manifold after pumping. In this scenario, the Rabi oscillation amplitude of the $\sigma^{\pm}$ transitions at a vapor temperature of $T_{\mathrm{v}} = 105$ °C is predicted to be $A_\theta \approx 0.16°$, as calculated from Eq. (2.32). Using the average measured Rabi oscillation dephasing time $1/\gamma_2 = 0.3$ ms across all four hyperfine transitions at $\beta = 42.4°$ and the shot noise of our Faraday polarimeter $\sigma_\theta = 0.0043°$ [Sec. 2.3.2], we calculate a CRLB standard error of $\sigma_\Omega = 1.1$ Hz.

Next, given the generalized Rabi frequency uncertainty $\sigma_\Omega$, we estimate the frequency uncertainty in a hyperfine transition $\nu_0$ estimated from the detuning dependence of 25 generalized Rabi frequencies. For simplicity, we model the 25 generalized Rabi frequency measurements about the hyperfine transition $\nu_0$ as

$$\tilde{\Omega} = \sqrt{\Omega^2 + (j\Omega/12)^2} \tag{4.17}$$

where the detunings $(\nu - \nu_0) = j\Omega/12$ are expressed by the integer $-12 < j < 12$. We assume that the generalized Rabi frequency measurement uncertainty $\sigma_{\tilde{\Omega}}$ scales as

$$\sigma_{\tilde{\Omega}} = \sigma_\Omega \frac{\Omega^2 + (j\Omega/12)^2}{\Omega^2} \tag{4.18}$$

consistent with the expected population dynamics in a two-level system. By fitting fake data calculated from Eq. (4.17) with added $\delta\tilde{\Omega}$ as Gaussian noise, we find that the frequency uncertainty $\sigma_\nu$ in the transition resonance $\nu_0$ is $\sigma_\nu/\sigma_\Omega \approx 0.65$ independent of the Rabi rate $\Omega$ because of how the detunings are assumed to scale with the Rabi rate $\Omega$. The fake data within these fits were weighted according to the modeled variance $w = 1/\sigma^2_{\tilde{\Omega}}$.

We estimate an uncertainty for the pressure shift $\nu_{\mathrm{bg}}$ and magnetic field strength $B$ subtracting and adding the $\sigma^{\pm}$ transition resonances and propagating the hyperfine resonance uncertainty $\sigma_\nu$ to the magnetic field strength and pressure shift shift uncertainties $\sigma_B$ and $\sigma_{\nu_{\mathrm{bg}}}$, namely

$$(\nu_{m=1}^{m'=2} - \nu_{m=-1}^{m'-2}) \pm \sqrt{2}\sigma_\nu \approx 6\gamma(B \pm \sigma_B) \tag{4.19}$$

$$(\nu_{m=1}^{m'=2} + \nu_{m=-1}^{m'-2}) \pm \sqrt{2}\sigma_\nu \approx 2(\nu_{\mathrm{hfs}} + \nu_{\mathrm{bg}} \pm \sigma_{\nu_{\mathrm{bg}}}). \tag{4.20}$$

Here $\gamma \approx 7$ Hz/nT and the unperturbed hyperfine frequency $\nu_{\mathrm{hfs}}$ is taken to have no uncertainty. Assuming a total measurement time of $t_m = 50$ ms to make all 50 $\sigma^{\pm}$ Rabi oscillation measurements we find that the shot-noise limited sensitivities $S_B$ and $S_{\nu_{\rm bg}}$ are given by

$$S_B = \sigma_B \sqrt{t_m} = \sigma_\Omega \frac{0.65}{3\sqrt{2}\gamma}\sqrt{t_m} = 5.3\ \text{pT}/\sqrt{\text{Hz}} \tag{4.21}$$

$$S_{\nu_{\rm bg}} = \sigma_{\nu_{\rm bg}} \sqrt{t_m} = \sigma_\Omega \frac{0.65}{\sqrt{2}}\sqrt{t_m} = 110\ \text{mHz}/\sqrt{\text{Hz}}. \tag{4.22}$$

Factors that inhibit our measurements from reaching the ideal limits expressed in Eq. (4.21) and Eq. (4.22) are imperfect state-preparation into the $F = 1$ manifold, utilizing Rabi measurements from both $\pi$ and $\sigma^\pm$ transitions, coil system noise, and microwave field drifts. Optical pumping in this experiment utilized elliptical polarized light to give some spin orientation for FID detection, and optical broadening from buffer gas collisions prevented complete depopulation of the $F = 2$ manifold. Taking the Rabi measurements at $\beta = 42.4°$ as an example, the mean Rabi amplitude across all four hyperfine transitions was $A_\theta = 0.042°$, which results in a CRLB uncertainty of $\sigma_\Omega = 4.2$ Hz. This CRLB uncertainty, which is about four times higher than assumed to calculate the ideal sensitivities in Eq. (4.21) and Eq. (4.22), corresponds to magnetic and pressure shift sensitivities

$$S_B = \sigma_B \sqrt{t_m} = \sigma_\Omega \frac{0.65}{3\sqrt{2}\gamma}\sqrt{t_m} = 20.7\ \text{pT}/\sqrt{\text{Hz}} \tag{4.23}$$

$$S_{\nu_{\rm bg}} = \sigma_{\nu_{\rm bg}} \sqrt{t_m} = \sigma_\Omega \frac{0.65}{\sqrt{2}}\sqrt{t_m} = 440\ \text{mHz}/\sqrt{\text{Hz}}. \tag{4.24}$$

Instead of using all four hyperfine transitions, higher SNR is expected with Rabi oscillations on the $\sigma^\pm$ hyperfine transitions over the $\pi$ transitions due to the higher $m_F = 2$ sublevels. The biggest noise source is likely from microwave field drifts occuring over the Rabi measurement aqcuisition period. Because microwave detunings are sampled randomly over time, these drifts manifest solely as noise.

For completeness, we also apply the CRLB sensitivity analysis to our FID measurements, as done in previous work [68, 86]. A noteable feature of our FID signals, arising from significant $F = 1$ atomic population, are that they contain two frequency components corresponding to the spin precession in both of the $F = 1$ and $F = 2$ hyperfine manifolds [see Fig. 4.1]. We estimate the magnetic sensitivity $S_B$ from the calculated sensitivities from each of the FID frequency components

$S_{B,1}$ and $S_{B,2}$ as

$$S_B = \frac{1}{1/S_{B,1} + 1/S_{B,2}}. \tag{4.25}$$

The sensitivities $S_{B,i} = \gamma\sigma_L$ are calculated from the CRLB standard in the Larmor precession frequency $\sigma_L$ and the gyromagnetic ratio $\gamma = 7$ Hz/nT. For the FID measurements at $\beta = 105°$, the $F = 2$ frequency component has an amplitude and dephasing time $A_\theta = 0.033°$ and $T_2 = 0.51$ ms, while the $F = 1$ frequency component has an amplitude and dephasing time $A_\theta = 0.039°$ and $T_2 = 0.26$ ms. With the measurement time for a single FID being $T_r = 3$ ms, these parameters correspond to a CRLB standard error $\sigma_L = 2.3$ Hz ($S_{B,2} = 18$ pT/$\sqrt{\text{Hz}}$) and $\sigma_L = 5.4$ Hz ($S_{B,1} = 43$ pT/$\sqrt{\text{Hz}}$) for the $F = 2$ and $F = 1$ frequency components respectively. From Eq. (4.25), we estimate the CRLB magnetic sensitivity for this FID measurement to be $S_B = 13$ pT/$\sqrt{\text{Hz}}$. If instead we had perfect optical pumping for the FID measurements, i.e. all atomic population starts in $|2,2\rangle$, then, using Eq. (2.32) at a vapor temperature of $T_v = 105°$, we would have an FID signal amplitude of $A_\theta = 1.3°$. For this case, we assume an increased $T_2 \approx 0.7$ ms because of measured FID dephasing times in our apparatus when using circularly polarized optical pumping that arises from decreased dephasing from spin-exchange collisions. Using these amplitude and dephasing parameters we calculate an CRLB magnetic sensitivity of 0.28 pT/$\sqrt{\text{Hz}}$. A summary of this CRLB sensitivity analysis for both the Rabi and FID measurements is shown in Table 4.2.

Table 4.2: Cramer-Rao lower bound (CRLB) sensitivitiy estimates for Rabi frequency spectroscopy and FID measurements for ideal and measured signal amplitudes. The first column denotes the case of ideal state preparation for Rabi measurements where all atomic population is evenly distributed in $F = 1$. The third column lists the ideal FID measurement when all atomic population begins in $|2,2\rangle$ with the polar angle of $\vec{B}_{\text{DC}}$ set at $\beta = 90°$. The second and fourth column denote Rabi frequency spectroscopy and FID sensitivities using measured signal amplitudes and dephasing times. All estimates assume a Faraday shot-noise floor of $\sigma_\theta = 0.0043°$.

| Sensitivity | Rabi (ideal) | Rabi ($\beta = 42.4°$) | FID (ideal) | FID ($\beta = 105°$) |
|---|---|---|---|---|
| $S_B$ [pT/$\sqrt{\text{Hz}}$] | 5.3 | 20.7 | 0.28 | 13 |
| $S_{\nu_{\text{bg}}}$ [Hz/$\sqrt{\text{Hz}}$] | 0.11 | 0.44 | — | — |

## 4.6 Rabi, Ramsey, and FID theoretical modeling and simulation

In this section we discuss the details behind simulations of the Rabi and Ramsey frequency spectroscopy protocols, as well as Larmor FID heading error. These simulations use parameters similar to those used in our apparatus with the goal of estimating the size of potential systematic errors arising from MPE frequency dependence and collisional spin-exchange frequency shifts. For these simulations, we assume that the magnetic field strength is $B = 50\ \mu$T and the buffer-gas pressure shift is $\nu_{\rm bg} = 88$ kHz. First, the optical-pumping model is discussed that includes optical excitation to the $D_1$ hyperfine states. Adiabatic optical pumping is simulated to estimate the initial state $\rho_i$ for the Rabi and Ramsey measurements at each of the 14 magnetic field directions $(\alpha, \beta)$. Next, we simulate FID heading error using experimental pumping parameters without the adiabatic power ramps. Finally, we simulate the Rabi-oscillation and Ramsey-fringe signals. By using measured MPE parameters (Table 4.1), these simulations emulate realistic off-resonant driving.

### 4.6.1 Full optical pumping model with excited and ground hyperfine sublevels

We utilize a mean-field approach similar to that formulated in [74, 79] to simulate the spin dynamics of the $16 \times 16$ density matrix $\rho$ for a single atom. An energy level diagram that highlights the different components of this optical pumping model is shown in Fig. 4.15. The density matrix

$$\rho = \begin{pmatrix} \rho_{gg} & \rho_{ge} \\ \rho_{eg} & \rho_{ee} \end{pmatrix} \tag{4.26}$$

is defined in terms of the eight spin states in the $5^2\mathrm{S}_{1/2}$ $F_g = 1, 2$ hyperfine manifolds denoted as $\rho_{gg}$ and the eight spin states in the $5^2\mathrm{P}_{1/2}$ $F_e = 1, 2$ hyperfine manifolds denoted as $\rho_{ee}$. The optical coherences are described by $\rho_{eg}$ and $\rho_{ge}$ submatrices. Under the rotating-wave approximation, the master equation that governs the time-evolution of $\rho$ is given by

$$\frac{\partial \rho}{\partial t} = -\frac{i}{\hbar}[\mathcal{H}, \rho] + \mathcal{L}(\rho). \tag{4.27}$$

The Hamiltonian $\mathcal{H}$

$$\mathcal{H} = \begin{pmatrix} \mathcal{H}_{gg} & \mathcal{H}_{ge}/2 \\ \mathcal{H}_{eg}/2 & \mathcal{H}_{ee} - 2\pi\Delta\mathcal{I}_e \end{pmatrix} \tag{4.28}$$

is written in terms of the ground and excited-state Hamiltonians $\mathcal{H}_{gg}$ and $\mathcal{H}_{ee}$, the optical detuning $\Delta$ from the $|F_g = 1, 1\rangle - |F_e = 1, 1\rangle$ transition, where $\mathcal{I}_e$ is the excited state identity operator, and the optical coupling interaction $\mathcal{H}_{ge} = \mathcal{H}_{eg}^{\dagger}$. The ground and excited-state Hamiltonians

$$\mathcal{H}_{gg} = A_g \mathbf{I}_g \cdot \mathbf{S}_g + \mu_B (g_s^{(g)} \mathbf{S}_g + g_i^{(g)} \mathbf{I}_g) \cdot \vec{B} - 2\pi \mathcal{I}_g E_{g,|1,1\rangle} \tag{4.29}$$

$$\mathcal{H}_{ee} = A_e \mathbf{I}_e \cdot \mathbf{S}_e + \mu_B (g_s^{(e)} \mathbf{S}_g + g_i^{(e)} \mathbf{I}_e) \cdot \vec{B} - 2\pi \mathcal{I}_e E_{e,|1,1\rangle} \tag{4.30}$$

consist of the hyperfine interaction $A\mathbf{I} \cdot \mathbf{S}$ and Zeeman interaction $\mu_B(g_s\mathbf{S} + g_i\mathbf{I}) \cdot \vec{B}$. The total energies of $\mathcal{H}_{gg}$ and $\mathcal{H}_{ee}$ are shifted such that at $\Delta = 0$ the energy of the ground $5\mathrm{S}_{1/2}\,|1, 1\rangle$ and the excited $5\mathrm{P}_{1/2}\,|1, 1\rangle$ states are equal. The hyperfine coupling constants and Landé g-factors are given by $A_g = 3.417$ GHz and $g_s^{(g)} = 2.00232$ for $\mathcal{H}_{gg}$ and $A_e = 0.4083$ GHz and $g_s^{(e)} = 0.6659$ for $\mathcal{H}_{ee}$. In both cases $g_i^{(g)} = g_i^{(e)} = -0.00099514$. The total electron and nuclear-spin operators for the ground manifolds are denoted as $\mathbf{S}_g$ and $\mathbf{I}_g$, respectively, with similar definitions for the excited state spin operators.

The optical coupling $\mathcal{H}_{ge} = \mathcal{H}_{eg}^{\dagger}$ is defined in terms of a complex electric field

$$\vec{\mathcal{E}} = \{E_x, E_y e^{-i\phi}, 0\} \tag{4.31}$$

of the pump laser and the electric dipole transition operator $\mathbf{D} = e\mathbf{r}$

$$\langle F_g, m_{F_g}|\, \mathcal{H}_{ge}\, |F_e, m_{F_e}\rangle = \mathcal{E}_k \langle F_g, m_{F_g}|\, er_k\, |F_e, m_{F_e}\rangle /2. \tag{4.32}$$

Here $k = \sigma^{\pm}, \pi$ denotes transitions characterized by $m_{F_e} = m_{F_g} \pm 1$ for $k = \sigma^{\pm}$ and $m_{F_e} = m_{F_g}$ for $k = \pi$. It is convenient to write $\vec{\mathcal{E}}$ in a spherical basis, namely $\mathcal{E}_{\pm} = \vec{\mathcal{E}} \cdot \epsilon_{\mp}$ and $\mathcal{E}_{\pi} = \vec{\mathcal{E}} \cdot \epsilon_{\pi}$ with $\epsilon_{\pm} = \{\frac{1}{\sqrt{2}}, \pm\frac{i}{\sqrt{2}}, 0\}$ and $\epsilon_{\pi} = \{0, 0, 1\}$. To simulate realistic optical pumping, we use pump polarization parameters $E_y/E_x = 1.68$ and $\phi = 0.8$ rad measured of our pump beam in front of the vapor cell using a SK010PA-NIR polarization analyzer from Schafter and Kirchoff. The electric

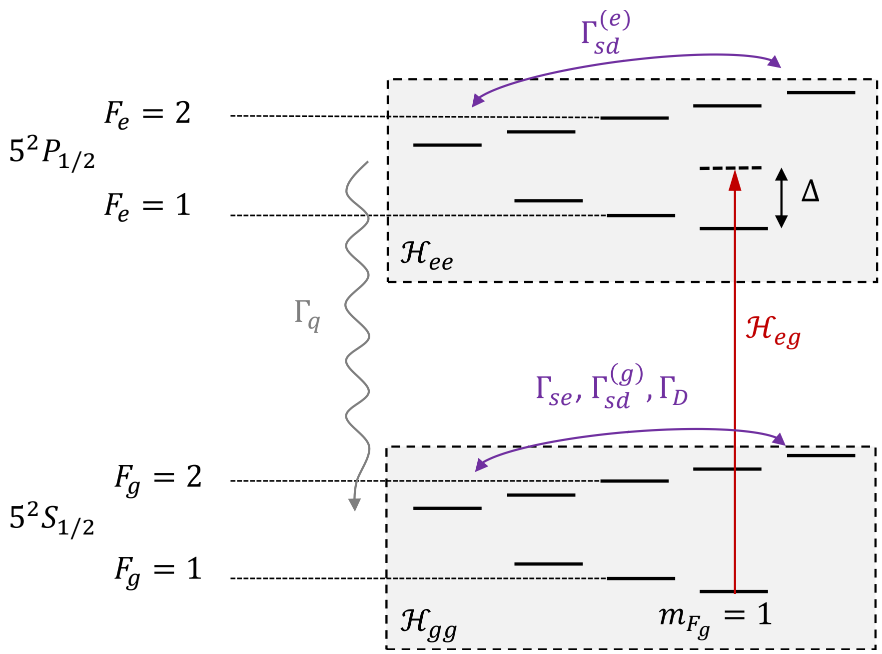


Figure 4.15: Energy level diagram depicting the eight $5^2S_{1/2}$ ground atomic states and the eight excited $5^2P_{1/2}$ states. The atomic structure is quantified by Hamiltonians $\mathcal{H}_{gg}$ and $\mathcal{H}_{ee}$. The quenching rate is denoted by $\Gamma_q$ and collisional mixing of the excited states is characterized by $\Gamma_{\mathrm{sd}}^{(e)}$.

field norm is estimated from the laser power $P$ through

$$|\mathbf{E}| = \sqrt{\frac{2P}{\pi w^2 c\epsilon_0}} \tag{4.33}$$

assuming a Gaussian waist $w = 1.5$ mm. The matrix elements of $\mathbf{D}$ is given by

$$\langle F_g, m_{F_g}| e r_k |F_e, m_{F_e}\rangle = \langle F_g|| e\mathbf{r} ||F_e\rangle \langle F_g, m_{F_g}|F_e, 1, m_{F_e}, k\rangle \tag{4.34}$$

which is expressed by the Clebsch-Gordan coefficient written terms of a Wigner 3-j symbol as

$$\langle F_g, m_{F_g}|F_e, 1, m_{F_e}, k\rangle = (-1)^{F_e-1+m_F}\sqrt{2F+1}\begin{pmatrix} F_e & 1 & F_g \\ m_{F_e} & m_{F_g} - m_{F_e} & -m_{F_g} \end{pmatrix} \tag{4.35}$$

and a reduced density matrix element

$$\langle F_g|| e\mathbf{r} ||F_e\rangle = \langle J_g|| e\mathbf{r} ||J_e\rangle (-1)^{F_e+J_g+1+I}\sqrt{(2F_e+1)(2J_g+1)}\begin{Bmatrix} J_g & J_e & 1 \\ F_e & F_g & I \end{Bmatrix}. \tag{4.36}$$

Here $\mathcal{D}$ as the D1 transition dipole reduced matrix element [168]

$$\mathcal{D} = \langle J_g = 1/2 || \, er \, || J_e = 1/2 \rangle = 2.992 e a_0. \tag{4.37}$$

where $a_0$ is the Bohr radius.

The relaxation superoperator $\mathcal{L}(\rho)$, expressed as

$$\mathcal{L}(\rho) = \begin{pmatrix} \mathcal{L}_{gg}(\rho) & \mathcal{L}_{ge}(\rho) \\ \mathcal{L}_{eg}(\rho) & \mathcal{L}_{ee}(\rho) \end{pmatrix}, \tag{4.38}$$

describes relaxation through radiation and collision channels in the ground and excited states, as well as optical broadening $\mathcal{L}_{eg} = \mathcal{L}_{ge} = -\Gamma_o/2$ with linewidth $\Gamma_o/2\pi = 5.6$ GHz due to Rb-$N_2$ collisions. Excited-state relaxation is expressed as

$$\mathcal{L}_e(\rho) = -\Gamma_q \rho_{ee} - \Gamma_p(\frac{3}{4}\rho_{ee} - \mathbf{S}\rho_{ee}\mathbf{S}) \tag{4.39}$$

where $\Gamma_q$ is the de-excitaton rate (quenching) from Rb-$N_2$ collisions and $\Gamma_p$ is the spin-destruction (SD) rate from Rb-$N_2$ collisions. Relaxation in the ground manifolds is given by

$$\begin{aligned} \mathcal{L}_g(\rho) =& \frac{\Gamma_q}{\mathcal{D}^2}\mathbf{D}^\dagger \rho_{ee}\mathbf{D} - \Gamma_{sd}(\frac{3}{4}\rho_{gg} - \mathbf{S}_g\rho_{gg}\mathbf{S}_g) \\ &- \Gamma_{se}(\rho_{gg}/4 + \mathbf{S}_g \cdot \rho_{gg}\mathbf{S})(1 + 4\langle \mathbf{S}_g \rangle \cdot \mathbf{S}_g) - \Gamma_D(\rho_{gg}^e - \rho_{gg}) \end{aligned} \tag{4.40}$$

where $\Gamma_{\mathrm{sd}}$ is the spin-destruction rate due to Rb-$N_2$ and Rb-Rb collisions, $\Gamma_{\mathrm{se}}$ is the spin-exchange collision rate, and $\Gamma_D$ is the wall collision rate. All collision rate parameters are tabulated in Table 4.3.

### 4.6.2 Simulation of FID heading error

We use pumping model just described to estimate realistic initial atomic states $\rho_i = \overline{\rho}_{gg}$ at the start of FID measurements and Ramsey and Rabi frequency spectroscopy. We start by simulating the initial atomic state prior to the FID measurements, where we assume experimental pump pulse settings of 100 $\mu$s with power $P = 0.4$ W [see Fig. 4.16(a)]. After pumping, we free-evolve the atomic state for 3 ms to generate the FID signal. We fit the resulting FID signal with the same

Table 4.3: The collision mechanisms, cross sections $\sigma_i$, and the calculated collision rates for a vapor cell with volume $3 \times 3 \times 2$ mm$^3$, vapor temperature $\mathcal{T}_v = 100°$C, buffer gas pressure $P_{N_2} = 180$ Torr (24 kPa), and diffusion constant $D_0 = 0.216$ cm$^2$s$^{-1}$ for Rb-$N_2$ buffer gas collisions scaled to our vapor temperature [142]. The tabulated mechanisms are quenching, optical dephasing (OD), spin-destruction (SD), spin-exchange (SE), wall collisions (WC), and Carver relaxation.

| Collision type | cross-section $[10^{-18}$ m$]$ | collision rate |
|---|---|---|
| $5P_{1/2}$ quench (Rb-$N_2$) | $\sigma_q = 0.58$ [83, 159] | $\Gamma_q = n_{N_2}\sigma_q v_r = 3.2$ GHz |
| $5P_{1/2}$ OD (Rb-$N_2$) | - | $\Gamma_o = 2\pi \cdot 5.6$ GHz (measured) |
| $5P_{1/2}$ SD (Rb-$N_2$) | $\sigma_p = 0.64$ [74] | $\Gamma_p = n_{N_2}\sigma_p v_r = 3.5$ GHz |
| $5S_{1/2}$ SD (Rb-$N_2$) | $\sigma_{sd} = 1.44 \times 10^{-8}$ [179] | $\Gamma_{sd} = n_{N_2}\sigma_{sd} v_r = 41$ Hz |
| $5S_{1/2}$ SD (Rb-Rb) | $\sigma_{sd} = 1.77 \times 10^{-3}$ [179] | $\Gamma_{sd} = n_{Rb}\sigma_{sd} v_r = 3.6$ Hz |
| $5S_{1/2}$ SE (Rb-Rb) | $\sigma_{se} = 1.9$ [65] | $\Gamma_{se} = n_{Rb}\sigma_{se} v_r = 3.89$ kHz |
| $5S_{1/2}$ WC | $D_0 P_0 = 0.016$ m$^2$Torr [142] | $\Gamma_D = \frac{D_0 P_0 \pi^2}{P_{N_2}(l_x^2+l_y^2+l_z^2)} = 0.45$ kHz [95] |
| $5S_{1/2}$ Carver (Rb-$N_2$) | $\Gamma_C/[N_2] = 394$ amg$^{-1}$s$^{-1}$ [181] | $\Gamma_C = 69$ Hz |

fitting protocol described in Eq. (4.1). In Figure 4.16(b) we plot the magnetic field strength error from the simulated FID signals at $B_{\text{true}} = 50$ $\mu$T for different pump relative phases from $\phi = 0.8$ rad.

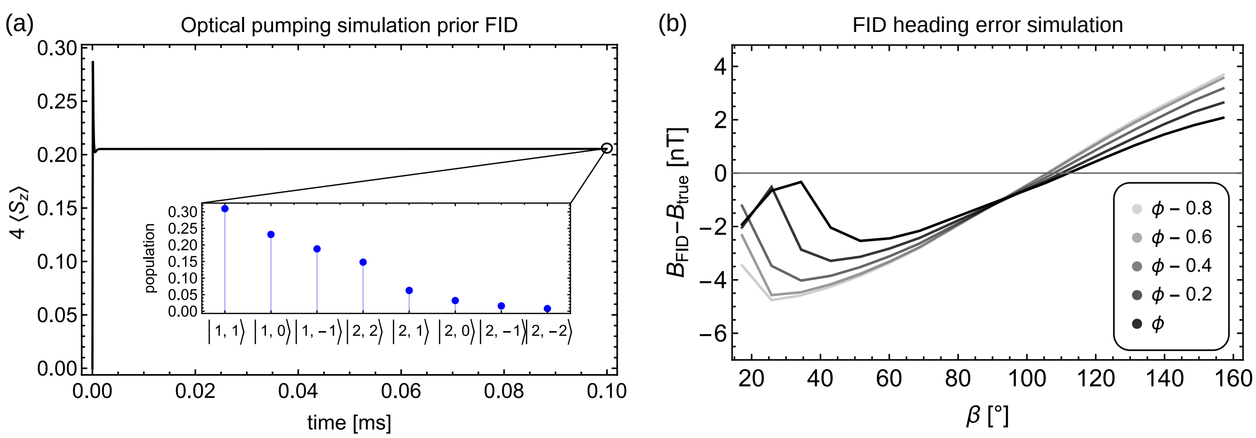


Figure 4.16: Simulated FID heading error. (a) Time-evolution of the optical pumping when the magnetic field is oriented at $\beta = 100°$. Inset shows the steady-state atomic populations at the end of the 100 $\mu$s pump pulse. (b) FID heading error for different pump relative phases between $E_x$ and $E_y$ from the value $\phi = 0.8$ rad measured in our apparatus prior to entering the cell.

In general there is some uncertainty in the pump beam parameters leading to uncertainty in the heading error shape predicted in Fig. 4.16(b). For example, there is uncertainty in the pump electric field polarization at the location of the atoms due to optical reflections off the uncoated glass walls of the vapor cell that create a small etalon [see Fig. 2.4]. In addition, there is some uncertainty in the pump optical frequency on the order of few GHz due to the wavemeter uncertainty and drift. Furthermore, spatial dependence of the pump power inside the vapor cell due to absorption is not considered here. We vary pump relative phase within the FID heading error simulations to show, as one example, the uncertainty in the predicted heading error shape from the uncertainty of these pump beam parameters in our apparatus. Desite some ambiguity in the pump beam parameters, we simulate [see Fig. 4.16] qualitatively similar heading errors to that predicted from Rabi and Ramsey frequency spectroscopy measurements in Fig. 4.12.

The heading error simulation depicted in Fig. 4.16(b) exhibits several subtle characteristics, particularly the distinctive shape observed at low $\beta$. The Rabi scalar measurements in Fig. 4.12 appear to show a similar shape as that marked for "$\phi - 0.8$". The shape of the heading error can be attributed to several interrelated factors that result in a complex atomic state characterized by nontrivial atomic coherences and populations. These factors include the use of a single pump pulse, the partial optical resolution of the $F = 1$ and $F = 2$ manifolds despite the 5.6 GHz optical broadening [see Fig. 2.3(d)], and perturbation to the effective magnetic field during pumping caused by the vector light shift from the 400 mW pump beam. A single pump pulse results in nontrivial coherences and populations in the final density matrix because FID spin precession occurs after an atom randomly absorbs a pump photon. In contrast, synchronous pumping uses short pump pulses repeated at the Larmor frequency, and tends to cause all pumped atoms to precess together during pumping. As illustrated in Fig. 4.1(c), heading error arises due to uncertainty in the unresolved six amplitudes and phases of the FID frequency components comprising the $F = 1, 2$ manifolds, as determined from the final density matrix after pumping. It is nontrivial how the FID fitting model, which only assumes on two FID frequency components and a single relative phase [Eq. (4.1)], will produce systematic errors while fitting to FID signals without the simulating optical pumping as we have.

### 4.6.3 Simulation of Rabi and Ramsey frequency spectroscopy

Next, we explore simulations of adiabatic optical pumping to estimate the initial atomic states for both of the Rabi and Ramsey measurements. These simulations, using the model discussed in Sec. 4.6.1, utilize the same experimental parameters for adiabatic pumping, which include sustaining constant optical pumping for 50 µs at 0.1 W, and then linearly ramping off the optical power over a 50 µs, as depicted in Fig. 4.17. A comparison of simulated Larmor FID signals initialized with either constant or adiabatic optical pumping are shown in Fig. 4.17(d) for a 50 $\mu$T magnetic field with direction $(\alpha, \beta) = (0°, 51.6°)$. The hyperfine spin-vector $\mathbf{F}$ after 50 $\mu$s of constant pumping has a steady-state direction given by $(68.8°, 24.6°)$. Meanwhile the steady-state spin vector direction after also applying the 50 $\mu$s linear pump ramp during adiabatic pumping is $(0.5°, 52.4°)$, which closely aligns with the magnetic field direction. This spin alignment results in very little Larmor precession, which improves the quality of the Ramsey and Rabi signals in arbitrary magnetic field directions.

Rabi oscillations are simulated using Eq. (3.21) with the initial density matrix obtained from the adiabatic optical pumping simulations. These Rabi simulations are done at the same microwave frequencies used in the measurements, namely 25 detunings separated by 800 Hz about each $\overline{\nu}_m^{m'}$. Realistic MPE 1, 2, and 3 parameters at each microwave frequency are estimated using polynomial interpolation [see Fig. 4.18] of the calibrated parameters listed in Table 4.1. The estimated systematic error from the frequency dependence of the MPE parameters is shown in Fig. 4.22. We also assume a linear drift of 0.4 % of the microwave field amplitude in these simulations to mimic possible experimental drift. This linear drift appears randomly in the analysis because the microwave frequencies are taken in random order, and hence causes negligible systematic errors.

Examples of simulated Rabi oscillations and corresponding generalized Rabi frequency fits at $\beta = 34°$ are shown in Fig. 4.19(a-h). We observe small systematic errors in these fits on the order of a few Hz as shown in Fig. 4.19(i-l). These errors likely arise from the nontrivial lineshape deviations of the simulated Rabi oscillations from the exponential-decay fitting model (Eq. (3.30))

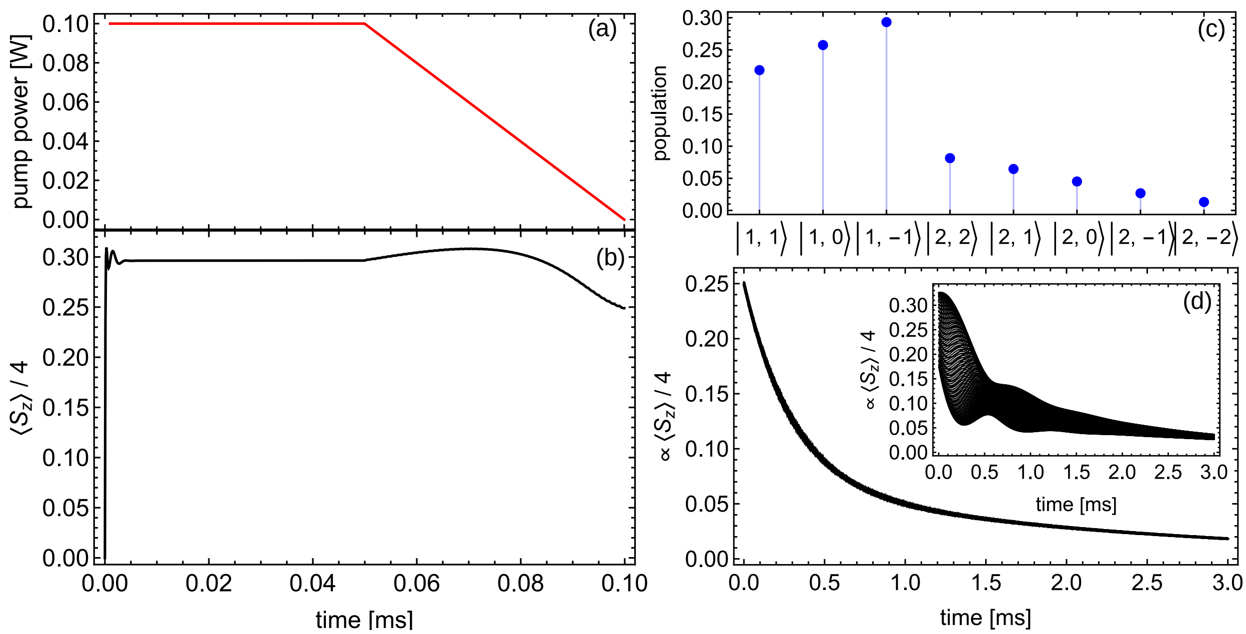


Figure 4.17: Adiabatic optical pumping simulation for $(\alpha, \beta) = (0°, 51.6°)$ (a) Pump power during optical pumping simulation. (b) Simulated Faraday rotation $\theta_F \propto \langle S_z \rangle$ during optical pumping. (c) Steady-state atomic populations after adiabatic pumping. (d) Spin decay after adiabatic optical pumping shows very little Larmor precession. The inset shows resulting Larmor precession without adiabatic pump ramp shown in (a)

due to atomic collisions. As shown in Fig. 4.22, however, these fitting errors only cause scalar systematics at the tens of pT level.

For the Ramsey frequency spectroscopy simulations, we also use Eq. (3.21) to simulate the $\frac{\pi}{2} - t_R - \frac{3\pi}{2}$ Ramsey sequence (Eq. (4.9)) as shown in Fig. 4.20(a). These simulations use the $\overline{\nu}_{m=-1}^{m'=-2}$ MPE 1 calibrated microwave parameters (first row of Table 4.1) to drive the $\mu$w pulses in the Ramsey sequence. To satisfy $t_{\pi/2} \approx 10\ \mu$s in the experiment, the power of the $\mu$w synthesizer $P_{\text{synth}}$ at each hyperfine transition is manually chosen. To mimic this process in the Ramsey simulations, we assume that changing $P_{\text{synth}}$ does not affect the MPE structure, but only affects the microwave amplitude $|\mathcal{B}| = \sqrt{\mathcal{B}_x^2 + \mathcal{B}_y^2 + \mathcal{B}_z^2}$. To estimate the dependence of $|\mathcal{B}|$ on $P_{\text{synth}}$, we measure the $\tilde{\Omega}_{m=1}^{m'=1}$ generalized Rabi frequency at $\nu_{\mu\text{w}} = \overline{\nu}_{m=1}^{m'=1}$ as a function of $P_{\text{synth}}$ [see Fig. 4.20(b)]. Here we assume that the percent change in $\tilde{\Omega}_{m=1}^{m'=1}$ gives the percent change in $|\mathcal{B}|$. Thus, from knowledge of the $P_{\text{synth}}$ settings in the Ramsey measurements it is possible to use comparable MPE parameters

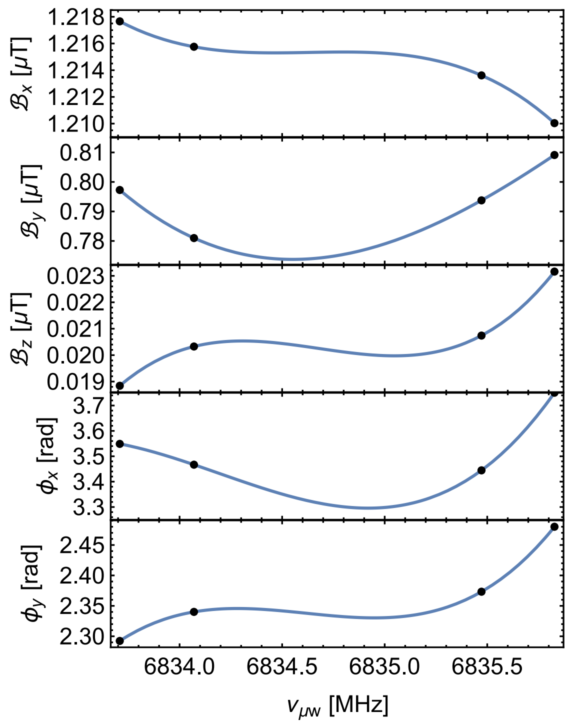


Figure 4.18: Estimated frequency dependence of the 5 MPE parameters from measured calibrations (black dots) of MPE 1. To generate a continuous model of the frequency dependence we use polynomial interpolation of the calibrations performed at 4 different microwave frequencies. Although these polynomial interpolations are not necessarily accurate to the true frequency dependence in the experiment, they are realistic for the purposes of estimating the size of the systematic errors arising from MPE frequency dependence.

in the simulations. Fig. 4.21 displays simulated Ramsey fringes at $\beta = 34.5°$ with 7 kHz microwave detuning from each hyperfine transition.

We estimate magnetic field strength and pressure shift systematic errors by applying the fitting protocols in Sec. 4.2.2 and Sec. 4.3.1 to the Ramsey and Rabi simulated data. In addition to systematic shifts due to off-resonant driving, Fig. 4.22 also displays the effect of microwave frequency dependence and spin-exchange frequency shifts as potential sources of systematic errors. Our simulations estimate that off-resonant driving leads to systematic errors on the order of 100 pT in the Ramsey frequency spectroscopy measurements as seen in the blue points of Fig. 4.22. Meanwhile, Rabi frequency spectroscopy has systematic errors on the order of 10 pT, which likely arise from the time-domain fitting errors attributed to collisional lineshape distortions shown in

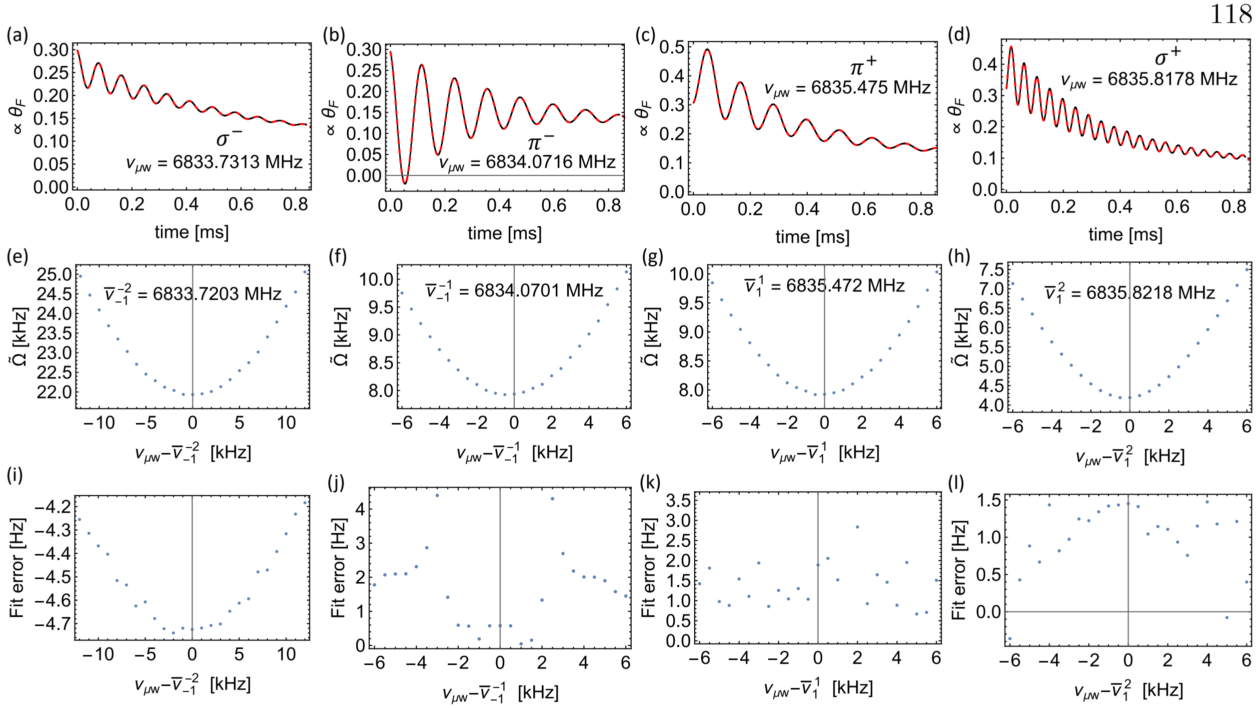


Figure 4.19: Simulated Rabi oscillations and generalized Rabi frequency fits for $(\alpha, \beta) = (0, 34°)$. (a-d) Simulated Rabi oscillations and fits (red dashed) for the hyperfine transitions measured in this work. (e-h) Detuning dependence of generalized Rabi frequency fits using simulated Rabi oscillations about $\overline{\nu}_m^{m'}$. The reason the detuning dependence looks funky in (h) is due to assumed microwave field amplitude drift that appears as random Rabi frequency noise. (i-l) Frequency fit errors of simulated generalized Rabi frequencies.

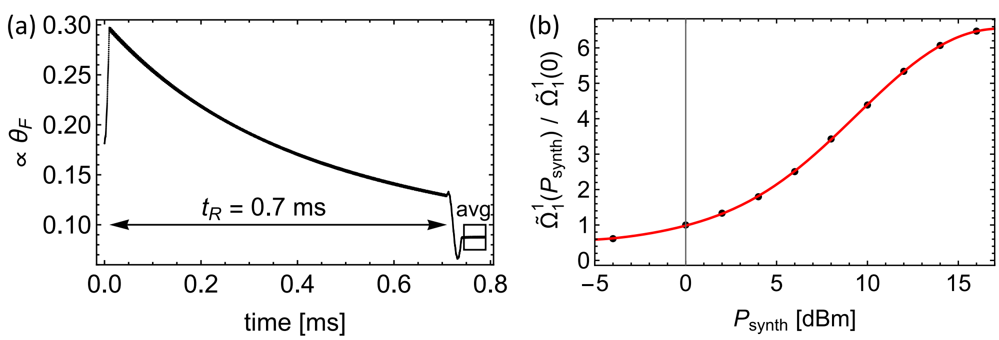


Figure 4.20: (a) Simulated Faraday rotation angle during the Ramsey pulse sequence for $t_R = 0.7$ ms at $(\alpha, \beta) = (0, 34°)$. (b) Estimated microwave field amplitude dependence on the power setting of the microwave synthesizer. This is estimated by measuring the change of the $\pi$ generalized Rabi frequency near-resonant with $\Delta_{m=1}^{m'=1} \approx 0$ at different microwave power settings ($P_{\mathrm{synth}}$). The red line generated from polynomial interpolation.

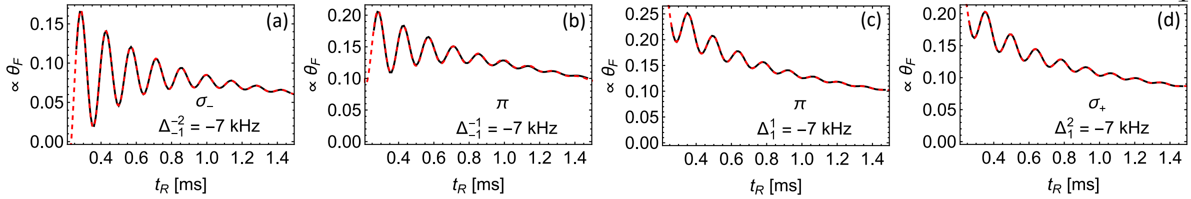


Figure 4.21: Simulated Ramsey fringes with frequency fits (red dashed) for $(\alpha, \beta) = (0, 34°)$.

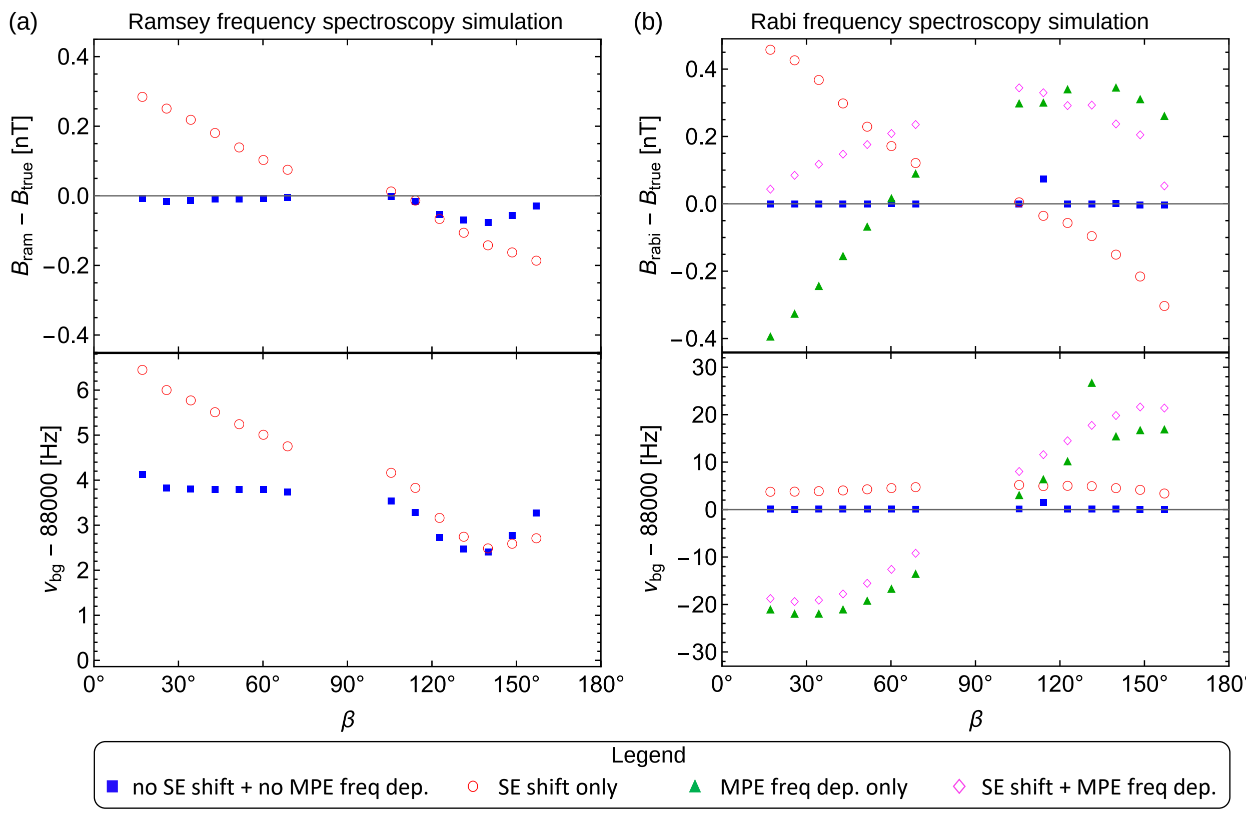


Figure 4.22: Simulated magnetic field strength and pressure shift errors using Ramsey and Rabi frequency spectroscopy. (a) Errors in the Ramsey frequency spectroscopy sequence. Assuming no spin-exchange frequency shifts, errors primarily from off-resonant microwave driving are contained within 100 pT (blue). Spin-exchange frequency shifts at our vapor cell temperature produce errors within 300 pT across different DC field directions. (b) Simulated magnetic field strength errors in Rabi frequency spectroscopy sequence. Shown are the error of the average magnetic field strength deduced from Rabi measurements across the 3 MPEs. Only $\sigma^{\pm}$ transitions are used. With no MPE frequency dependence and SE frequency shifts, our magnetic field strength errors are at the 10 pT level (blue). Errors from SE frequency shifts are at a similar level as the Ramsey measurements. The MPE frequency dependence [see Fig. 4.18] contributed a major source of systematics at the 0.6 nT level (green).

Fig. 4.19. Including spin-exchange frequency shifts (red circles in Fig. 4.22) increases the Ramsey and Rabi systematic shifts to similar levels within $\pm$ 0.4 nT. For the Rabi frequency spectroscopy, the simulated microwave frequency dependence of the MPE parameters causes a systematic error ($<$ 0.4 nT) similar in magnitude to the spin-exchange frequency shifts (green triangles in Fig. 4.22). Microwave frequency dependence could be mitigated with improved flatness of the microwave-cavity mode, or could be compensated by performing MPE calibrations at each microwave frequency used in Rabi frequency spectroscopy. MPE frequency dependence is not expected to be a systematic for the Ramsey protocol because Rabi fringe frequencies are independently fit at a single microwave frequency.

Pressure shifts are predicted to be more accurately measured with Rabi frequency spectroscopy than Ramsey frequency spectroscopy when microwave frequency dependence of MPE parameters and spin-exchange frequency shifts are not included. This is due to the atom-microwave coupling being modeled with greater accuracy compared to the compensation for frequency shifts from off-resonant driving in Ramsey frequency spectroscopy. Pressure shift errors $<$ 20 Hz are expected from microwave frequency dependence of the MPE parameters. This is consistent with the 10 Hz scale discrepancies in Fig. 4.10 between pressure shift measurements of different MPEs.

We are also able to compare discrepancies in the simulated data of the fitted magnetic field strengths and pressure shifts using a two-level Rabi model (Eq. (1.5)) versus the full Hamiltonian model (Eq. (4.12)) in Fig. 4.23. We observe nearly perfect agreement of these descrepancies between the fits of simulated and measured data implying that the differences in Fig. 4.13 are truly due to errors in off-resonant driving. This comparison leads us to conclude that inadequate modeling of off-resonant driving could have resulted in magnetic field strength errors of up to 4 nT.

These results demonstrate how tailored atom-microwave interrogation through Rabi and Ramsey spectroscopy reduces OPM heading error to the sub-nT regime at geomagnetic fields and other challenging domains such as the high buffer gas pressure environments utilized in microfabricated vapor cells and regimes of weak optical pumping. We estimate that systematic errors of the Ramsey and Rabi frequency spectroscopy are within 0.5 nT from the simulations reported in

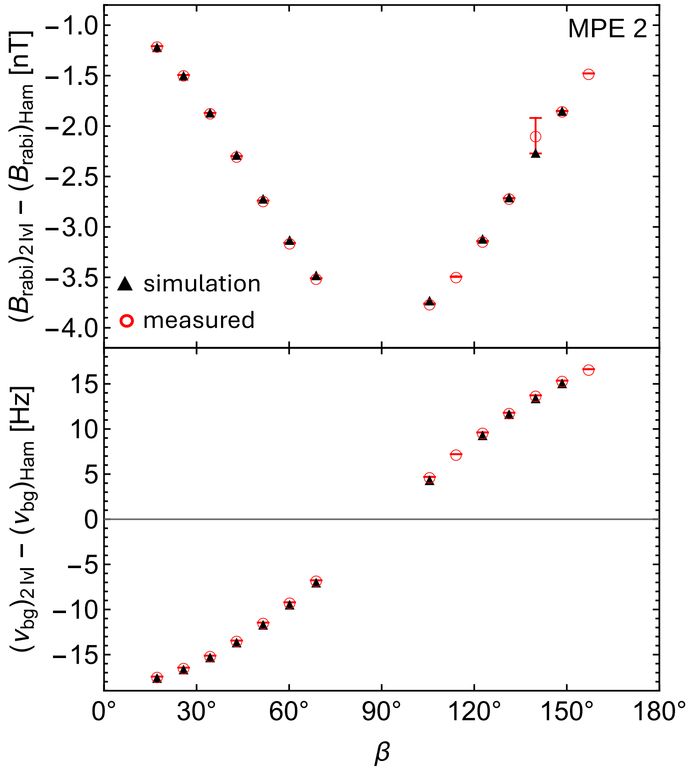


Figure 4.23: Difference between magnetic field strengths and pressure shift fits using the two-level Rabi model and the full Hamiltonian model evaluated on simulated (black triangle) and measured (red circle) data. These fits only utilize the $\sigma^{\pm}$ transitions as shown for the data in Fig. 4.13(a). This comparison confirms that failing to accurately model off-resonant driving would have led to errors in magnetic field strength measurements up to 4 nT.

Fig. 4.22. The fact that the Rabi measurements across different MPEs and Ramsey measurements all agree to within 0.6 nT in Fig. 4.12 is confirmation towards this error estimate. Even so, some experimental discrepancy between Rabi and Ramsey scalar measurements could be due to experimental drift since these measurements were taken on different days. We further showed that errors due to off-resonant driving would have resulted scalar systematic errors up to 4 nT. From these results, we expect that these techniques will be useful for benchmarking the absolute accuracy of standard OPMs based on FID detection, as well as HFS magnetometers like that presented in [6]. Future work focused on improving MPE frequency dependence and including spin-exchange frequency shift compensation would likely reduce these systematic errors in the Rabi and Ramsey frequency spectroscopy to the 100 pT scale. Demonstration of accurate scalar measurements using

Rabi frequency spectroscopy establishes a solid foundation to use Rabi oscillations for accurate vector magnetometry presented in Ch. 5.

# Chapter 5

## A Rabi vector magnetometer referenced to multiple microwave polarization ellipses

In Ch. 4, microwave-driven Rabi oscillations were shown to measure geomagnetic fields with a scalar accuracy bounded by 0.6 nT [94], which is nearly ten times more accurate than standard OPM measurements that reach accuracies on the 5-10 nT scale. In this chapter, we map the full magnetic field vector using Rabi measurements by employing multiple microwave polarization ellipses (MPEs) as a directional reference. This method utilizes Rabi oscillations driven across four hyperfine transitions of $^{87}$Rb [Fig 5.1(a,b)] to calibrate and reference MPEs to an unknown magnetic field direction $(\alpha, \beta)$. For a given MPE structure $(\vec{\mathcal{B}}^{\mu\mathrm{w}})$, the atomic quantization axis, defined by $(\alpha, \beta)$, gives rise to spherical microwave components $(\mathcal{B}_{\sigma^+}^{(\alpha,\beta)}, \mathcal{B}_{\pi}^{(\alpha,\beta)}, \mathcal{B}_{\sigma^-}^{(\alpha,\beta)})$ that can be linked to Rabi rates $\Omega_m^{m'}$ coupling hyperfine states $|1, m\rangle$ and $|2, m'\rangle$ through

$$\Omega_m^{m'} = \mu_m^{m'} \mathcal{B}_k^{(\alpha,\beta)} / h \tag{5.1}$$

where $h$ is Planck's constant, $\mu_m^{m'}$ is the transition magnetic dipole moment, and $k = \sigma^{\pm}, \pi$ denotes hyperfine transitions characterized by $m' = m \pm 1$ and $m' = m$ respectively. Initially, the MPE structure undergoes calibration using Rabi rates measured over many known DC magnetic field orientations. Subsequently, these measured Rabi rates, in conjunction with the directional maps [see Fig. 5.1(c)] supplied by the calibrated MPEs, determine the orientation of any magnetic field direction. This technique can be combined with any scalar OPM measurement, such as free-induction decay (FID), to obtain the full magnetic field vector.

This work follows many previous efforts, ranging from all optical approaches based on various atom-light interactions to different coil modulation techniques, to convert scalar OPMs to vector

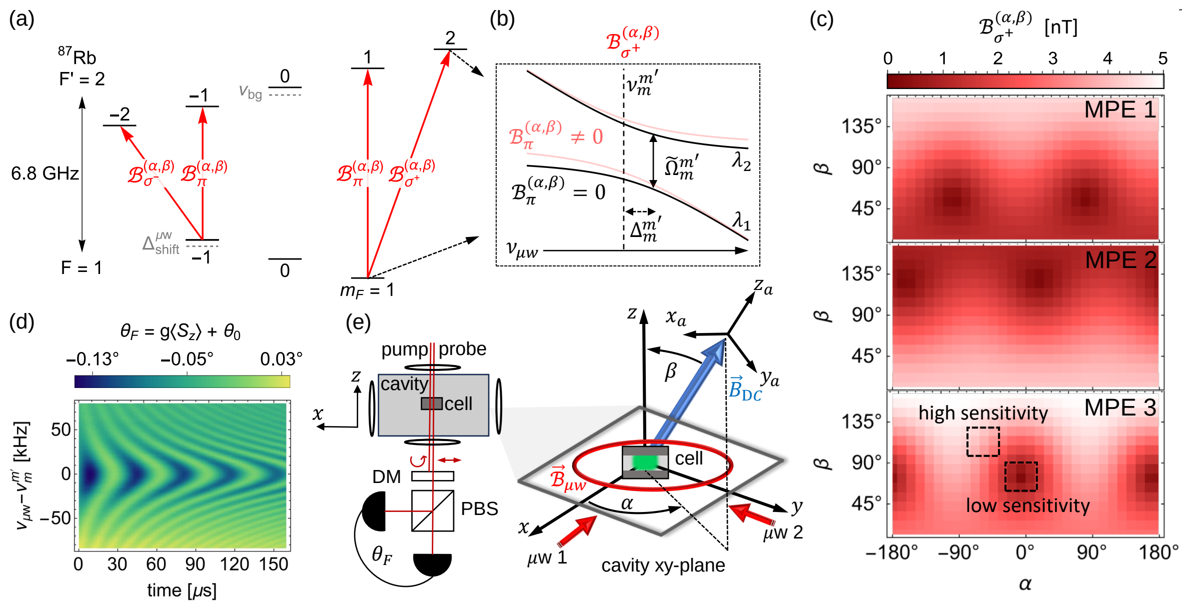


Figure 5.1: Rabi vector magnetometry referenced to multiple MPEs. (a) Energy-level diagram showing the four hyperfine transitions utilized for Rabi detection. Off-resonant $\mu$w driving causes energy-level perturbations ($\Delta^{\mu\mathrm{w}}_{\mathrm{shift}}$) and buffer gas collisions cause a frequency shift in the hyperfine splitting ($\nu_{\mathrm{bg}}$). (b) Generalized Rabi frequencies $\tilde{\Omega}^{m'}_{m}$ are quantified by the difference between dressed-state energies $\lambda_j$ and $\lambda_i$. Off-resonant driving (red) from $\mathcal{B}^{(\alpha,\beta)}_{\pi}$ induces shifts in these dressed states. (c) The measured $\mathcal{B}^{(\alpha,\beta)}_{\sigma^+}$ spherical microwave component at different magnetic field directions for each of the three MPEs. (d) Measured Rabi-Chevron pattern. (e) The magnetometer apparatus. An angled dichroic mirror (DM) reflects the pump.

operation that were discussed in Sec. 1.1.1. To date, as discussed in Sec. 1.2.2, this Rabi technique has only been implemented in the controlled environment of ultracold atoms with limited sensitivity [100, 170]. The promise of Rabi measurements to compete with the precision of standard vector techniques in vapor-cell platforms is evidenced by the coherence times of Rabi oscillations in vapor cells being similar to those of conventional Larmor free-induction decay (FID) measurements [80, 95]. In addition, hyperfine transitions exhibit larger magnetic couplings (e.g., $\mu^{m'=2}_{m=1}/h \approx 17$ Hz/nT) than the gyromagnetic ratios $\gamma \approx 7$ Hz/nT characterizing Zeeman transitions.

In our approach, Rabi rates across the four hyperfine transitions are accurately extracted despite being more prone to systematic errors than scalar measurements on Zeeman transitions. We achieve this by using a full atom-microwave Hamiltonian to model various systematic shifts arising in the multilevel $^{87}$Rb atomic structure including a buffer-gas pressure shift $\nu_{\mathrm{bg}}$, nonlinear

Zeeman shift $\Delta_{\mathrm{NLZ}}$, and frequency shifts from off-resonant driving $\Delta^{\mu\mathrm{w}}_{\mathrm{shift}}$ [see Fig. 5.1(b)]. Recently, this approach to model Rabi rates was used to measure geomagnetic fields with improved scalar accuracy over standard OPM measurements from 5 nT down to 0.6 nT [94]. In this work we attain a mean vector accuracy of 0.48 mrad, exceeding the 1-degree (17 mrad) accuracy constraining many types of vector OPMs. To mitigate systematic errors from microwave drift, we employ running MPE calibrations to track microwave field drifts over a 37.5-minute period, which are consistent with a drift observable derived from the Rabi measurements. We envision that these drift observables could be useful to avoid constant recalibration that are employed in high-accuracy vector magnetometers [109, 134].

Similar to many OPM configurations that use a single optical axis [31], Rabi oscillation signals exhibit a probing deadzone that appears when the magnetic field is aligned perpendicular to this axis. To facilitate deadzone-free operation, we explore a novel detection scheme, which extracts Rabi rates from resonances that occur during simultaneous Larmor precession and Rabi driving (SPaR). This SPaR technique has maximal sensitivity at the probing deadzone. With Rabi oscillation measurements, we demonstrate vector sensitivities reaching 10 $\mu\mathrm{rad}/\sqrt{\mathrm{Hz}}$, and correspondingly 100 $\mu\mathrm{rad}/\sqrt{\mathrm{Hz}}$ using SPaR near the Rabi deadzone. The use of three distinct MPEs helps mitigate regions where the spherical microwave components, connected to Rabi rates through Eq. (5.1), weakly depend on the magnetic field direction (e.g. $\partial\mathcal{B}_k^{(\alpha,\beta)}/\partial\beta \approx 0$) as indicated in Fig. 5.1(c). Utilizing multiple MPE structures that do not all mutually have these regions for the same $(\alpha, \beta)$ enables high vector sensitivity measurements for all field directions.

## 5.1 Measurement protocol and details

In this experiment, we drive Rabi and SPaR measurements with microwave fields, labeled MPE 1, MPE 2, and MPE 3, produced by three different cavity excitations. Details of the microwave cavity are discussed in Sec. 2.5. The microwave fields of MPE 1 and MPE 2 are produced by individually exciting two microwave ports designed to excite these orthogonally polarized modes [see Fig. 5.1(e)]. The microwave field for MPE 3 is generated by simultaneously exciting both of these cavity ports, resulting in the microwave field of MPE 3 being effectively approximated by the combined fields of MPE 1 and MPE 2. Optical pumping and probing follow the same laser configuration as detailed Ch. 4, namely a 795 nm elliptically-polarized pump beam overlapped with a 1-mW probe beam, blue-detuned by 170 GHz from the 780 nm $D_2$ line. Like the Rabi scalar measurements in Ch. 4, the pump frequency is tuned near resonance with the $D_1$ line to bias most of atomic population into the the $F = 1$ manifold and enable Rabi signals with good SNR across all hyperfine transitions.

Before initiating Rabi oscillations, we implement adiabatic optical pumping as described in Sec. 2.2.1 and Sec. 4.6.3. This involves a 100-mW pump pulse lasting for 50 $\mu$s, followed by a linear ramp-off of the pump over an additional 50 $\mu$s [see Fig. 5.2(a)]. In contrast, a single pump pulse lasting 100 $\mu$s at 400 mW optically pumps the atomic ensemble for SPaR and FID measurements. After pumping, the microwave field from one of the three MPEs is turned on for 0.85 ms and 1.85 ms for Rabi oscillation and SPaR measurements respectively. We detect Rabi and SPaR signals for each hyperfine transition highlighted in Fig. 5.1(a) using a single microwave frequency $\overline{\nu}_m^{m'}$ that is near-resonant to the unperturbed hyperfine transition frequency $\nu_m^{m'}$, namely $\overline{\nu}_{-1}^{-2} = 6833.7201$ MHz, $\overline{\nu}_{-1}^{-1} = 6834.0701$ MHz, $\overline{\nu}_1^{1} = 6835.4701$ MHz, and $\overline{\nu}_1^{2} = 6835.8204$ MHz.

Vector magnetometry is carried out with these Rabi, SPaR, and FID measurements over a range of DC magnetic field orientations so that we can conduct running MPE calibrations and evaluate the vector sensitivity and accuracy over all directions of magnetic fields [see Fig. 5.2(b)]. At each $\vec{B}_{\rm DC}$ direction, Rabi oscillation and SPaR measurements for each $\overline{\nu}_m^{m'}$ and MPE are repeated 10 times over a $\Delta t_R = 400$ ms period followed by 10 repeated FID measurements over a $\Delta t_{\rm FID} = 30$ ms period [see Fig. 5.2(b)]. The 400 ms Rabi measurement sequence is initiated twice before capturing the final Rabi-SPaR-FID sequence to allow the microwave components to thermally stabilize. To avoid Eddy currents during measurements, deactivation of electrical heating and magnetic field rotations are made 40 ms and 1 second before this final sequence. The cooling resulting from the deactivation of electrical heating during the Rabi-SPaR-FID sequence restricts the repetition rate of these sequences to $\Delta t = 2.5$ seconds. This time period is essential for ensuring that the electrical heating sustains the cavity temperature at 100 °C. However, it also limits how fast MPE calibrations are performed as detailed in Section 5.2.

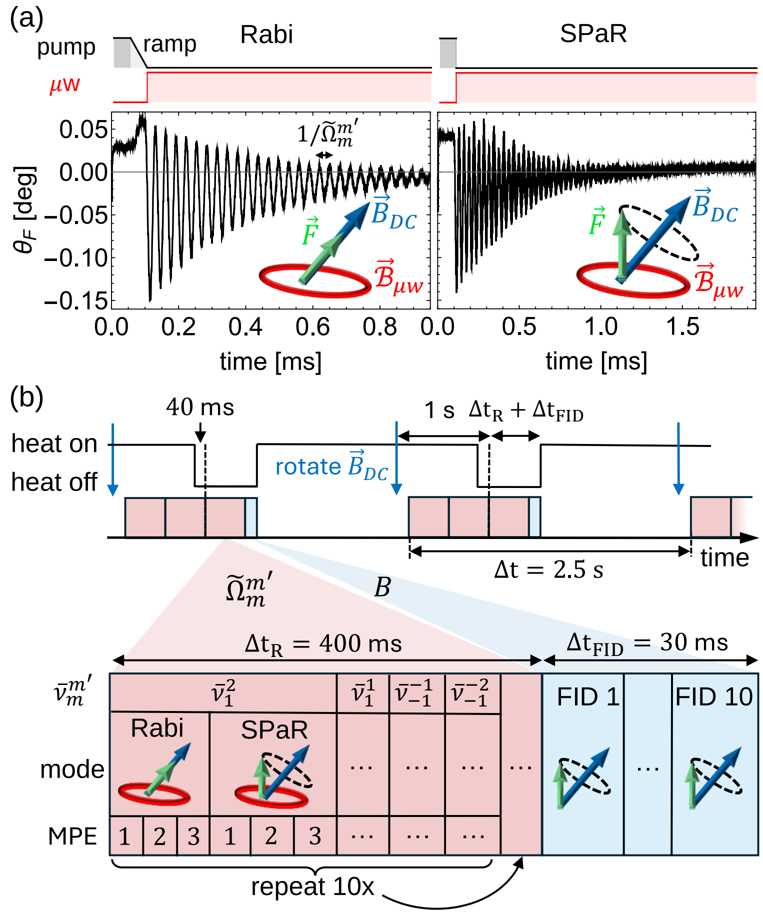


Figure 5.2: (a) Rabi oscillation and SPaR pulse sequences measured at $(\alpha, \beta) = (0°, 57°)$. (b) A timing diagram of the Rabi, SPaR, and FID measurement sequences. All Rabi, SPaR, and FID measurements are taken within a $\Delta t_R + \Delta t_{\text{FID}} = 430$ ms period. Magnetic field rotations (blue arrow) and deactivation of electrical heating are initiated 1 s and 40 ms before each measurement period to minimize Eddy currents during acquisition. All 12 Rabi and SPaR measurements corresponding to the three MPEs and four hyperfine transitions are repeated 10x.

## 5.2 MPE calibration and long-term drift

For clarity, throughout this chapter we denote the microwave phasor

$$\vec{\mathcal{B}} = \{\mathcal{B}_x, \mathcal{B}_y, \mathcal{B}_z, \phi_x, \phi_y\} \tag{5.2}$$

and generalized Rabi frequency $\tilde{\Omega}_m^{m'}$ corresponding to the $s^{\text{th}}$ MPE, where $s = 1, 2, 3$, as $(\vec{\mathcal{B}}_m^{m'})_s$ and $(\tilde{\Omega}_m^{m'})_s$ respectively. Due to the microwave parameters being influenced by the frequency dependence of the cavity modes, this notation also specifies the microwave frequency $\nu_{\mu\text{w}} = \overline{\nu}_m^{m'}$ associated with driving a specific hyperfine transition. The microwave phasor in Eq. (5.2) defines the spherical microwave components in Eq. (5.1) through Eq. (3.9).

The first step towards measuring $\vec{B}_{\text{DC}}$ is to calibrate the 12 microwave phasors $(\vec{\mathcal{B}}_m^{m'})_s$, corresponding to each MPE [see Fig. 5.3(b)] and microwave frequency $\nu_{\mu\text{w}} = \overline{\nu}_m^{m'}$, within the orthogonal reference frame $\mathcal{L}$ defined by the coil system. In total, 60 microwave parameters are involved in these calibrations. During the MPE calibrations, the angles $(\alpha, \beta)$ are determined with an accuracy of 50 $\mu$rad from known coil system parameters. We fit each $(\vec{\mathcal{B}}_m^{m'})_s$ using Eq. (3.20) over $N = 12$ DC field directions by minimizing the following cost function

$$(r_m^{m'})_s = \sum_{j=1}^{N} (w_m^{m'})_s \Big( \delta\lambda_m^{m'}((\vec{\mathcal{B}}_m^{m'})_s, \alpha, \beta) - (\tilde{\Omega}_m^{m'})_s \Big)^2 \Big|_{(\alpha_j, \beta_j)}. \tag{5.3}$$

In Eq. (5.3) we explicitly denote the magnetic field direction and microwave field dependence of $\delta\lambda_m^{m'}$. Generalized Rabi frequencies $(\tilde{\Omega}_m^{m'})_s$ and corresponding weights $(w_m^{m'})_s = 1/(\delta(\tilde{\Omega}_m^{m'})_s)^2$ are evaluated from the mean and variance $(\delta(\tilde{\Omega}_m^{m'})_s)^2$ of 10 repeated measurements.

To account for MPE drifts, we make Rabi measurements over an $(\alpha, \beta)$ sequence consisting of random $\vec{B}_{\text{DC}}$ directions interspersed with two repeated constant directions [see Fig. 5.3(a)]. At each random $(\alpha, \beta)$, we estimate $(\vec{\mathcal{B}}_m^{m'})_s$ by using Rabi measurements taken at the 12 previous directions to calibrate a phasor $(\vec{\mathcal{B}}_m^{m'})_{s,1}$ with squared residual error (Eq. (5.3)) $(r_m^{m'})_{s,1}$ and the subsequent 12 directions to calibrate $(\vec{\mathcal{B}}_m^{m'})_{s,2}$ with the corresponding error $(r_m^{m'})_{s,2}$, and calculate the weighted average

$$(\vec{\mathcal{B}}_m^{m'})_s = \frac{((r_m^{m'})_{s,2}(\vec{\mathcal{B}}_m^{m'})_{s,1} + (r_m^{m'})_{s,1}(\vec{\mathcal{B}}_m^{m'})_{s,2})}{((r_m^{m'})_{s,1} + (r_m^{m'})_{s,2})}. \tag{5.4}$$

This method circumvents overfitting by ensuring that the calibrated MPE parameters in $(\vec{\mathcal{B}}_m^{m'})_s$ are evaluated solely against Rabi measurements that were not part of the calibration process.

Over 37.5 minutes, we observe nT-scale drifts of the microwave field components and mrad-scale drifts in the phases as exemplified for MPE 2 in Fig. 5.3(d). The microwave field drift

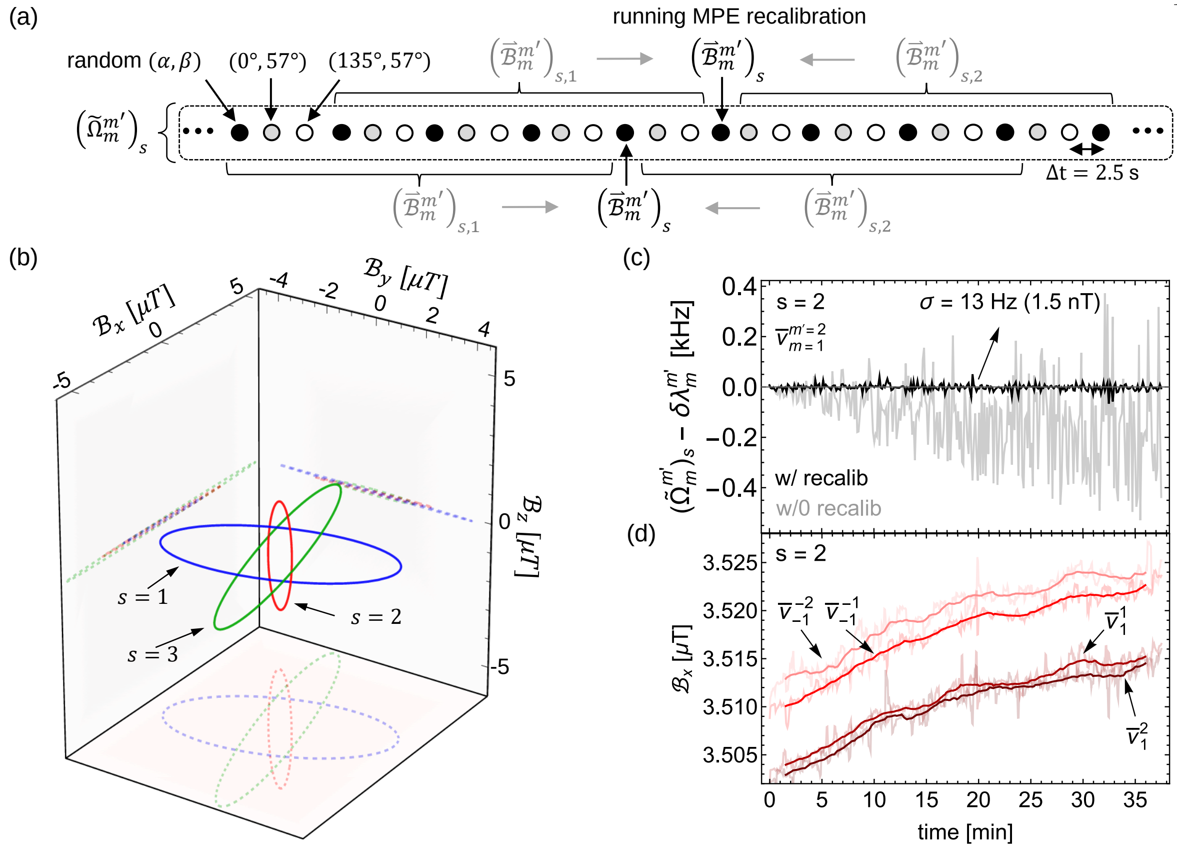


Figure 5.3: (a) The sequence of $\vec{B}_{\rm DC}$ directions $(\alpha, \beta)$ consisting of random directions (black circles) interspersed with directions $(0°, 57°)$ and $(135°, 57°)$. While all $\vec{B}_{\rm DC}$ directions in this sequence are utilized in the MPE calibrations, vector measurements are only evaluated at the random $(\alpha, \beta)$. Conversely, the repeated field directions (gray and white circles) are used to consistently monitor microwave drifts. To avoid overfitting, the microwave phasor $(\vec{\mathcal{B}}_m^{m'})_s$ at each random $\vec{B}_{\rm DC}$ direction in this sequence is determined from the weighted average of the two phasors $(\vec{\mathcal{B}}_m^{m'})_{s,1}$ and $(\vec{\mathcal{B}}_m^{m'})_{s,2}$ extracted from the MPE calibrations that consist of the $N = 12$ angles immediately before and after the random $(\alpha, \beta)$. The calibration length $N$ is limited by the finite time $\Delta t = 2.5$ s that is dominated by measurement deadtime used to electrically heat the cavity. (b) Measured MPEs. The nT-scale variation of the microwave field components arising from the frequency dependence of the cavity modes are not discernible in this plot. (c) Residuals of the $\sigma^+$ generalized Rabi frequency $(\tilde{\Omega}_{m=1}^{m'=2})_s$ at random DC magnetic field directions with and without MPE recalibration. (d) Drift of the $\mathcal{B}_x$ microwave component evaluated at different $\nu_{\mu\rm w} = \overline{\nu}_m^{m'}$. MPE 2 measurements are used as a representative example in (b,c).

is dominated by the contraction of the microwave cavity modes due to a few °C cooling of the microwave cavity. Monitoring the temperature drift from the Rabi dephasing rate and accounting for temperature-dependent shifts in $\nu_{\rm bg}$ are discussed in Sec. 5.2.2. For these calibrations, we found that it was sufficient to recalibrate only the relative phase $\delta\phi = \phi_y - \phi_x$ by leaving $\phi_x$ fixed after an initial calibration instead of resolving for both $\phi_x$ and $\phi_y$. We note that most of this 37.5 minute duration is spent heating the cavity and not taking measurements. One path to eliminate this in future work is to employ continuous laser heating [123] that does not perturb the atomic measurements.

To assess the calibration accuracy, we show residuals of $\sigma^+$ generalized Rabi frequencies $(\tilde{\Omega}_{m=1}^{m'=2})_{s=2}$ against the $\delta\lambda_{m=1}^{m'=2}$ model utilizing recalibrated MPE 2 parameters in Fig. 5.3(c) as a representative example. Over 37.5 minutes these residuals exhibit a standard deviation of $\sigma = 13$ Hz, which corresponds to $\sigma = 1.5$ nT fluctuations for spherical microwave component $\mathcal{B}_{\sigma^+}$. These fluctuations are approximately three times greater than the anticipated $\sigma = 5$ Hz (0.6 nT), a figure expected due to the limited calibration length ($N = 12$) and measurement noise [Sec. 5.2.3]. This discrepancy suggests that the systematic errors in the calibrated MPE parameters, attributed to inaccuracies in the Rabi measurements, are estimated to be $\delta\mathcal{B}_x = 0.3$ nT, $\delta\mathcal{B}_y = 0.3$ nT, $\delta\mathcal{B}_z = 0.2$ nT, and $\delta(\phi_y - \phi_x) = 0.2$ mrad.

### 5.2.1 Expressing MPE 3 in terms of MPE 1 and MPE 2

In this work, MPE 1 and MPE 2 are the microwave fields generated by individually exciting independent microwave ports designed to excite orthogonally polarized modes within the cavity xy-plane. We generate the microwave field of MPE 3 by exciting these two ports at the same time. Thus, calibrated MPE 3 parameters should be well-approximated by summing the microwave fields predicted from the parameters of MPE 1 and MPE 2. This is mathematically formulated as

$$\begin{aligned}\vec{\mathcal{B}}_3 =& \vec{\mathcal{B}}_1 + \vec{\mathcal{B}}_2 = \{\mathcal{B}_{x,1}e^{-i\phi_{x,1}}, \mathcal{B}_{y,1}e^{-i\phi_{y,1}}, \mathcal{B}_{z,1}\} + \\ &\{\mathcal{B}_{x,2}e^{-i(\phi_{x,2}+\phi_r)}, \mathcal{B}_{y,2}e^{-i(\phi_{y,2}+\phi_r)}, \mathcal{B}_{z,2}e^{-i\phi_r}\}\end{aligned} \tag{5.5}$$

The MPE 3 parameters are then given by

$$\begin{aligned}
\mathcal{B}_{x,3} &= \sqrt{(\mathcal{B}_{x,1}\cos(\phi_{x,1}) + \mathcal{B}_{x,2}\cos(\phi_{x,2}+\phi_r))^2 + (\mathcal{B}_{x,1}\sin(\phi_{x,1}) + \mathcal{B}_{x,2}\sin(\phi_{x,2}+\phi_r))^2} \\
\mathcal{B}_{y,3} &= \sqrt{(\mathcal{B}_{y,1}\cos(\phi_{y,1}) + \mathcal{B}_{y,2}\cos(\phi_{y,2}+\phi_r))^2 + (\mathcal{B}_{y,1}\sin(\phi_{y,1}) + \mathcal{B}_{y,2}\sin(\phi_{y,2}+\phi_r))^2} \\
\mathcal{B}_{z,3} &= \sqrt{(\mathcal{B}_{z,1} + \mathcal{B}_{z,2}\cos(\phi_r))^2 + (\mathcal{B}_{z,2}\sin(\phi_r))^2} \\
\phi_{x,3} &= \arg(\mathcal{B}_{x,1}\cos(\phi_{x,1}) + \mathcal{B}_{x,2}\cos(\phi_{x,2}+\phi_r) + i(\mathcal{B}_{x,1}\sin(\phi_{x,1}) + \mathcal{B}_{x,2}\sin(\phi_{x,2}+\phi_r))) \\
\phi_{y,3} &= \arg(\mathcal{B}_{y,1}\cos(\phi_{y,1}) + \mathcal{B}_{y,2}\cos(\phi_{y,2}+\phi_r) + i(\mathcal{B}_{y,1}\sin(\phi_{y,1}) + \mathcal{B}_{y,2}\sin(\phi_{y,2}+\phi_r))) \\
\phi_{z,3} &= \arg(\mathcal{B}_{z,1} + \mathcal{B}_{z,2}\cos(\phi_r) + i(\mathcal{B}_{z,2}\sin(\phi_r)))
\end{aligned} \tag{5.6}$$

To compare to calibrated MPE 3 parameters that assume $\phi_{z,3} = 0$ we make the transformation

$$\begin{aligned}
\phi_{x,3} &\to \phi_{x,3} - \phi_{z,3} \\
\phi_{y,3} &\to \phi_{y,3} - \phi_{z,3}.
\end{aligned} \tag{5.7}$$

For initial calibrated MPE 1 and MPE 2 parameters in Table 5.2 we calculate with (5.6) and (5.7) $(\mathcal{B}_{x,3}, \mathcal{B}_{y,3}, \mathcal{B}_{z,3}) = (5.5820, 1.6327, 0.1002)$ $\mu$T, $(\phi_{x,3}, \phi_{y,3}) = (2.7707, 4.7489)$ rad, and $\phi_r = 1.0580$ rad. These values closely align with the MPE 3 parameters that were independently calibrated, as listed in Table 5.2.

### 5.2.2 Vapor cell temperature monitoring

The primary reason for the microwave field drift depicted in Fig. 5.3(d) is cooling of the microwave cavity by a few °C cooling over 37.5 minutes. This section discusses how to monitor the drift of the temperature $T_\mathrm{v}$ of the vapor cell contained inside the microwave cavity through the dephasing time $T_2$ of the Rabi oscillations [see Fig. 5.4]. These dephasing times also allow us to estimate relative changes in the buffer gas pressure shift $\nu_\mathrm{bg}$, which affects the microwave detuning, due to drifts in the vapor temperature $T_\mathrm{v}$.

The buffer gas pressure shift at the start of these measurements is initially assumed to be $\nu_\mathrm{bg} = 88$ kHz from independent pressure shift characterizations. Relative changes in $\nu_\mathrm{bg}$ due to drifts in the vapor temperature $T_\mathrm{v}$ [see Fig. 5.4(b)] are estimated from the Rabi oscillation dephasing rate $1/T_2 = n_\mathrm{Rb}\sigma_\mathrm{se}v_r$ [Sec. 3.3] where $n_\mathrm{Rb} = P_\mathrm{Rb}(T_\mathrm{v})/k_B T_\mathrm{v}$ is the atomic density expressed in terms

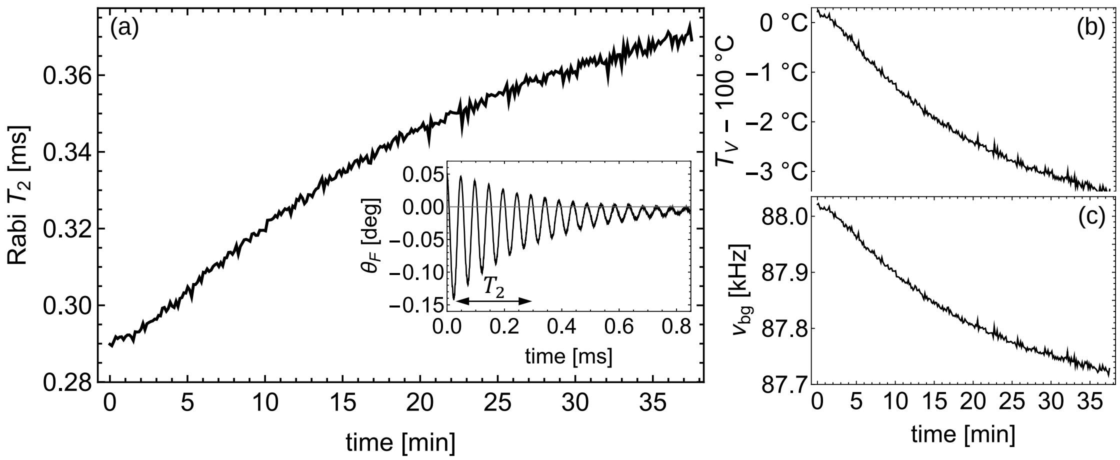


Figure 5.4: Detection of vapor cell cooling through the Rabi dephasing time $T_2$ . (a) Rabi dephasing time over the duration of the vector measurements. These measurements used MPE 1 $\sigma^+$ Rabi oscillations at the magnetic field direction $(135°, 57°)$. (b) and (c) show the predicted vapor temperature and buffer gas pressure shift respectively.

of the Rb vapor pressure $P_{\mathrm{Rb}}(T_{\mathrm{v}})$ [Eq. (2.1)] and Boltzmann constant $k_B$, $\sigma_{\mathrm{se}} = 1.9 \times 10^{-18}$ cm$^2$ is the Rb spin-exchange (SE) collisonal cross-section [65], and $v_r = \sqrt{8k_BT_{\mathrm{v}}/\pi m_r}$ is the mean speed between colliding Rb atoms with reduced mass $m_r$. As an approximation, we focus solely on dephasing from spin-exchange (SE) collisions in our temperature estimation, as it represents the predominant mechanism of decoherence [Table 3.3]. By driving Rabi oscillations near resonance, the generalized Rabi frequency $(\tilde{\Omega}_m^{m'})s$ is only sensitive to changes in the microwave detuning to second-order, as evidenced by expanding the generalized Rabi frequency formula Eq. (1.5) for a two-level system. Therefore, errors in estimating $\nu_{\mathrm{bg}}$ by about 100 Hz would correspond to only minor modeling errors in $(\tilde{\Omega}_m^{m'})_s$, estimated at around a few Hz. We estimate changes in $\nu_{\mathrm{bg}}$ from drifts in $T_{\mathrm{v}}$ through [176]

$$\frac{\nu_{\mathrm{bg}}}{\nu_0} = P_0[\beta_0 + \delta_0(T_{\mathrm{v}} - T_{\mathrm{v},0})] \tag{5.8}$$

where $\nu_0 = 6834.682$ MHz is the $5^2\mathrm{S}_{1/2}$ hyperfine splitting for $^{87}$Rb, $T_{\mathrm{v},0} = 60$ °C, $P_0 = 151.39$ Torr (buffer gas pressure at $T_{\mathrm{v},0}$), $\beta_0/\nu_0 = 81.9 \times 10^{-9}$ Torr$^{-1}$, and $\delta_0/\nu_0 = 79 \times 10^{-12}$ °C$^{-1}$Torr$^{-1}$.

### 5.2.3 Expected Rabi modeling errors due to finite MPE calibration length and measurement noise

In this section, we utilize fake Rabi frequency data with added noise to investigate the size of the generalized Rabi frequency residuals

$$(\delta_m^{m'})_s = (\tilde{\Omega}_m^{m'})_s - \delta\lambda_m^{m'}((\vec{\mathcal{B}}_m^{m'})_s, \alpha, \beta) \tag{5.9}$$

evaluated over random DC magnetic field directions $(\alpha, \beta)$ shown in Fig. 5.3(c). In Fig. 5.3(c), these residuals are evaluated for the case of $\sigma^+$ MPE 2 measurements and exhibited a standard deviation of $\sigma = 13$ Hz. The analysis in this section focuses on the contribution to the $\sigma = 13$ Hz from MPE calibration errors due to the finite calibration length of $N = 12$. In this section, we are focusing our analysis on the $\sigma^+$ MPE 2 data. Expected residual $\sigma$ lower than $\sigma = 13$ Hz in the fake data implies systematic errors in the Rabi measurements. For notational simplicity, we use $(\tilde{\Omega}_{m=1}^{m'=2})_{s=2} \to \Omega_{\sigma^+}$ with analogous notation for the microwave phasor, transition dipole moments, etc.

To begin, we first reiterate the approach from Sec. 5.2 that the MPE phasor $\vec{\mathcal{B}}$ associated with each Rabi measurement at a randomly chosen angle $(\alpha, \beta)_r$ was determined using two MPE phasors, $\vec{\mathcal{B}}^{(1)}$ and $\vec{\mathcal{B}}^{(2)}$. Phasors $\vec{\mathcal{B}}^{(1)}$ and $\vec{\mathcal{B}}^{(2)}$ were each calibrated with generalized Rabi frequencies measured at 12 DC magnetic field orientations other than $(\alpha, \beta)_r$. For the analysis in this section, we neglect $\vec{\mathcal{B}}^{(2)}$ and use the measured $\vec{\mathcal{B}}^{(1)}$'s to generate fake $\sigma^+$ Rabi data corresponding to all $12 + 12 = 24$ Rabi frequencies corresponding to the 24 DC magnetic field directions. We analyze residuals from Rabi rate fake data instead of generalized Rabi frequencies to simplify the analysis. This fake Rabi rate data $\Omega_{\sigma^+,G}$ with added Gaussian noise, characterized by variance $(\delta\Omega_{\sigma^+})^2$, is given by

$$\Omega_{\sigma^+,G} = G\Big(|\mu_{\sigma^+}\mathcal{B}_{\sigma^+}^{(\alpha,\beta)}/h|, (\delta\Omega_{\sigma^+})^2\Big) \tag{5.10}$$

where

$$\mathcal{B}_{\sigma^+}^{(\alpha,\beta)} = R_y(-\beta)R_z(-\alpha)\vec{\mathcal{B}}^{(1)} \cdot \epsilon_+ \tag{5.11}$$

is the $\sigma^+$ microwave component calculated from $\mathcal{B}^{(1)}$ parameters with $\epsilon_+ = \{\frac{1}{\sqrt{2}}, -\frac{i}{\sqrt{2}}, 0\}$. Here $\delta\Omega_{\sigma^+}$ is the corresponding standard error calculated from 10 repeated Rabi measurements.

With this set of fake Rabi data, we recalibrate each $\mathcal{B}^{(1)} \rightarrow \mathcal{B}^{(1')}$, using the associated $N = 24$ DC magnetic field directions. Each $\mathcal{B}^{(1')} \neq \mathcal{B}^{(1)}$ due to the added noise and finite calibration length. Finally, we generate fake residual data with new Rabi rates $\Omega'_{\sigma^+,G}$ generated by $\mathcal{B}^{(1')}$ and evaluating

$$\delta_{\sigma^+,G} = \Omega'_{\sigma^+,G} - \frac{\mu_{\sigma^+}}{h} R_y(-\beta) R_z(-\alpha) \vec{\mathcal{B}}^{(1)} \cdot \epsilon_+. \tag{5.12}$$

From this analysis we find that the expected standard deviation of the residuals Eq. (5.9) evaluated over 300 random field directions is $\sigma = 5$ Hz due to measurement noise and finite MPE calibration length. If we compare Rabi residuals without added noise using

Table 5.1: Comparison of Rabi frequency residuals evaluated over random DC magnetic field orientations. Residuals generated with fake Rabi data show the contribution from model discrepancy due to the calibration errors from the finite MPE calibration length. If systematic errors in the vector measurements were only from the finite MPE calibration length, then the second and third row would have equal $\sigma$.

| Type of Rabi frequency residuals evaluated over random $(\alpha, \beta)$ | $\sigma$ [Hz] |
|---|---|
| fake data (w/o measurement noise): $\delta_{\sigma^+}$ (Eq. (5.13)) | 3.4 |
| fake data: $\delta_{\sigma^+,G}$ (Eq. (5.12)) | 5 |
| measured: $(\delta_m^{m'})_s$ (Eq. (5.9)) | 13 |

$$\delta_{\sigma^+} = \frac{\mu_{\sigma^+}}{h} (|R_y(-\beta) R_z(-\alpha) \vec{\mathcal{B}}^{(1')} \cdot \epsilon_+| - |R_y(-\beta) R_z(-\alpha) \vec{\mathcal{B}}^{(1)} \cdot \epsilon_+|), \tag{5.13}$$

then $\sigma = 3.4$ Hz. This $\sigma = 3.4$ Hz represents systematic errors from finite MPE calibration length alone. We summarize these results in Table 5.1. The fact that these predicted $\sigma$ are less than the measured $\sigma = 13$ Hz, as reported in Sec. 5.2, implies systematic errors. By incorporating a larger $\delta\Omega_{\sigma^+}$ into the simulated Rabi data, ensuring the predicted Rabi residual noise matches with the observed value of $\sigma = 13$ Hz, and analyzing how the distribution of MPE calibrations deviates from the actual MPE parameters, we can gauge the magnitude of systematic errors present in the calibrated MPE parameters. This analyis predicts systematic errors of $\delta\mathcal{B}_x = 0.3$ nT, $\delta\mathcal{B}_y = 0.3$

nT, $\delta\mathcal{B}_z = 0.2$ nT, $\delta(\phi_y - \phi_x) = 0.2$ mrad as deduced from the standard deviations of each of the distribution of MPE parameter errors. We explore potential systematic error sources in Sec. 5.6.

## 5.3 Simultaneous precession and Rabi (SPaR)

For the single optical-axis geometry utilized in this work, Rabi oscillations, and corresponding vector measurements, exhibit a deadzone when $\beta \to 90°$ [see Fig. 5.5(a)]. In this section we discuss how SPaR is an effective method to detect Rabi rates $\Omega_m^{m'}$ within this probing deadzone through precessional frequency components that appear around the Larmor frequency $\nu_L$ labeled $\nu_{\text{low}}$ and $\nu_{\text{hi}}$ in Fig. 5.5(a). Like FID measurements, the amplitude of these SPaR peaks are maximal when $\beta = 90°$.

These SPaR peaks occur due to couplings between the microwave-dressed states and the surrounding Zeeman sublevels, which are conceptually diagrammed in Fig. 5.5(b) from the perspective of a rotating reference frame near the $\sigma^+$ transition frequency $\nu_{\mu\text{w}} = \overline{\nu}_{m=1}^{m'=2}$. Akin to the Rabi modeling described in Ch. 3, the SPaR frequency components are modeled from the differences between pairs of eigenvalues of $H$, depicted by arrows diagrammed in Fig. 5.5(b). This diagram illustrates that the frequency separations of the $\nu_{\text{hi}}$ and $\nu_{\text{low}}$ components closely approximate the $\sigma^+$ Rabi frequency. The eigenvalue analysis with known magnetic and microwave-field parameters indicates that each of the SPaR peaks, labeled by $j \in$ (low, hi), consist of two frequency components $\nu_{\text{j}}^{(1)}$ and $\nu_{\text{j}}^{(2)}$ displayed as vertical lines in the $\sigma^+$ SPaR spectrum shown in Fig. 5.5(d). The $\sigma^-$ transition, also consisting of the stretched $|m'| = 2$ sublevel, has a SPaR spectrum that is qualitatively the same. SPaR measurements and modeling details for the $\pi$ transitions are further discussed in Sec. 5.3.3.

To fit Rabi rates $\Omega_m^{m'}$ with SPaR, we begin by estimating the three spherical microwave components $\mathcal{B}_k^{(\alpha,\beta)}$, defined in Eq. (3.9), from the $\sigma^+$ and $\sigma^-$ SPaR spectra. We do this by first estimating the centers of the $\nu_{\text{low}}$ and $\nu_{\text{hi}}$ peaks in the SPaR FFT signal using a peak-finding algorithm. Then, we approximate $\nu_{\text{hi}} - \nu_{\text{low}} \approx \Omega_m^{m'}$ along with Eq. (5.1) to estimate $\mathcal{B}_{\sigma^\pm}^{(\alpha,\beta)}$. From the total microwave field amplitude $|\vec{\mathcal{B}}|$, known from MPE calibrations described in Sec. 5.2, $\mathcal{B}_\pi^{(\alpha,\beta)}$

is calculated using $|\mathcal{B}_{\pi}^{(\alpha,\beta)}|^2 = |\vec{\mathcal{B}}|^2 - |\mathcal{B}_{\sigma^+}^{(\alpha,\beta)}|^2 - |\mathcal{B}_{\sigma^-}^{(\alpha,\beta)}|^2$. By assuming that the spherical components are positive instead of complex numbers, we can estimate all Rabi rates in Eq. (3.7) with 1 kHz accuracy, and further, estimate all eigenvalues $\lambda_j$ of $H$. We linearize these eigenvalues about these estimates to enable faster computation during SPaR fitting that is described in Sec. 5.3.1.

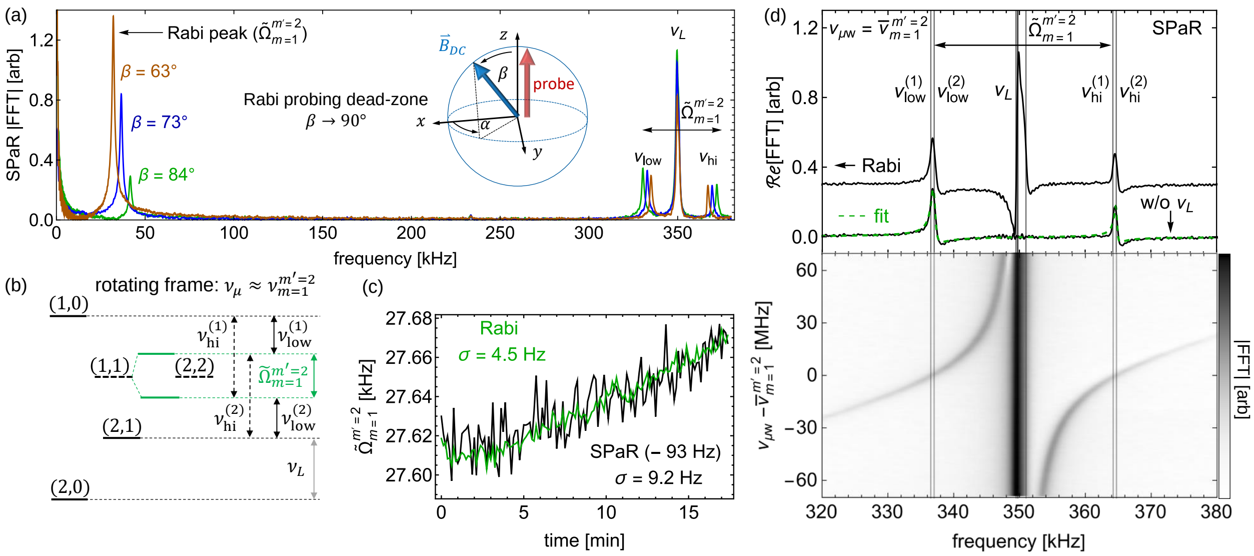


Figure 5.5: Rabi rate detection using SPaR. (a) Directional dependence of Rabi oscillation and SPaR signal amplitude. This plot shows the fast Fourier transform (FFT) of SPaR time-domain signals like the one shown in Fig. 5.2(a). (b) Energy-level diagram in the rotating frame near the $\sigma^+$ transition frequency. Coupling between microwave dressed states (green) with Zeeman sublevels (black) are indicated by double-sided arrows that indicate $\nu_{\text{hi}}$ (long, dashed) and $\nu_{\text{low}}$ (short, solid) frequency components. (c) Generalized Rabi frequency measurements using Rabi oscillations (green) and SPaR (black). SPaR measurements are shifted by the values in parenthesis. (d) Measured SPaR spectrum for the $\sigma^+$ transition. Vertical lines indicate $\nu_{\text{low}}$ and $\nu_{\text{hi}}$ precessional frequencies calculated from the eigenstates of $H$.

Next, we remove the broadened Larmor resonance $\nu_L \approx 350$ kHz appearing in each SPaR spectra [Sec. 5.3.2] and use the following fitting equation to fit the $\sigma^\pm$ SPaR spectra

$$\mathcal{R}e[\text{FFT}] = \sum_{j\in\{\text{low,hi}\}} a_j \frac{\cos[\phi_j] - \sin[\phi_j](f - \bar{\nu}_j + f_{\text{shift}})}{(f - \bar{\nu}_j + f_{\text{shift}})^2 + w_j^2/4} \tag{5.14}$$

where $\bar{\nu}_j$ is the mean frequency of the two $\nu_j^{(1)}$ and $\nu_j^{(2)}$ frequency components, $f_{\text{shift}}$ is a phenomenological frequency shift, $\phi_j$ are phase shifts, and the strength and broadening of this signal is given by amplitudes $a_j$ and linewidths $w_j \approx 2$ kHz. We use the mean frequency $\bar{\nu}_j$ instead of precisely modeling the lineshape of each of the $\nu_j^{(1)}$ and $\nu_j^{(2)}$ to avoid overfitting. During the $\sigma^+$

SPaR fitting, $\mathcal{B}_{\sigma^+}^{(\alpha,\beta)}$ is the only free parameter, where $\mathcal{B}_{\sigma^-}^{(\alpha,\beta)}$ and $\mathcal{B}_{\pi}^{(\alpha,\beta)}$ are held at their initial estimates. Correspondingly, $\mathcal{B}_{\sigma^-}^{(\alpha,\beta)}$ and $\mathcal{B}_{\pi}^{(\alpha,\beta)}$ are the only free parameters during SPaR fitting of the $\sigma^-$ and $\pi$ transitions respectively.

The accuracy of the SPaR Rabi fits is within a few hundred Hz [see Fig. 5.5c] due to uncertainty in the relative amplitudes of the unresolved frequency components that make up $\nu_{\text{low}}$ and $\nu_{\text{hi}}$. Despite this, over a 17-minute period, we observe changes in Rabi rates using SPaR that align with those measured from Rabi oscillations as illustrated in Fig. 5.5(c). These observations occur at a magnetic field orientation $(\alpha, \beta) = (135°, 57°)$, which is intermediary to the Rabi and SPaR deadzones.

### 5.3.1 Linearization of eigenvalues

Fitting SPaR spectra by constantly reevaluating the eigenvalues $\lambda$ of $H$ is computationally intensive and slow. To circumvent this, we linearize the eigenvalues about spherical microwave component estimates ($\overline{\mathcal{B}}_{\sigma^+}$, $\overline{\mathcal{B}}_{\pi}$, $\overline{\mathcal{B}}_{\sigma^-}$) with 100 nT accuracy using a peak-finding algorithm of the $\sigma^{\pm}$ SPaR spectra and the calibrated microwave amplitude $|\vec{\mathcal{B}}|$ discussed in Sec. 5.3. For notational simplicity in this section, we leave out the $(\alpha, \beta)$ in the usual $\mathcal{B}_k^{(\alpha,\beta)}$ notation. This eigenvalue linearization is utilized for fitting the SPaR spectra of all $\sigma^{\pm}$ and $\pi$ hyperfine transitions. Throughout SPaR fitting we approximate all spherical microwave components and Rabi rates to be real and positive. All Rabi rates are determined from the spherical microwave components using Eq. (5.1).

The linearization of any given eigenvalue $\lambda_j$ takes the form

$$\lambda_j\Big|_{\mathcal{B}_{\sigma^+},\mathcal{B}_{\pi},\mathcal{B}_{\sigma^-}} = \lambda_j\Big|_{\overline{\mathcal{B}}_{+},\overline{\mathcal{B}}_{\pi},\overline{\mathcal{B}}_{+}} + \gamma_+(\mathcal{B}_{\sigma^+} - \overline{\mathcal{B}}_{\sigma^+}) + \gamma_\pi(\mathcal{B}_\pi - \overline{\mathcal{B}}_\pi) + \gamma_-(\mathcal{B}_{\sigma^-} - \overline{\mathcal{B}}_{\sigma^-}) \tag{5.15}$$

where

$$\gamma_+ = \frac{1}{\delta}\Big(\lambda_j\Big|_{\overline{\mathcal{B}}_{\sigma^+}+\delta,\overline{\mathcal{B}}_{\pi},\overline{\mathcal{B}}_{\sigma^-}} - \lambda_j\Big|_{\overline{\mathcal{B}}_{\sigma^+},\overline{\mathcal{B}}_{\pi},\overline{\mathcal{B}}_{\sigma^-}}\Big) \tag{5.16}$$

with similar formulas for $\gamma_\pi$ and $\gamma_-$. We use $\delta = 100$ nT for calculating $\gamma_\pm$ and $\gamma_\pi$. Systematic errors in the eigenvalue linearization are on the order of $h{\cdot}(100$ Hz) for 100 nT errors in initial spherical microwave component estimates that are dominated by neglecting second order cross-terms (e.g.

terms $\propto (\mathcal{B}_\pi - \overline{\mathcal{B}}_\pi) \times (\mathcal{B}_{\sigma^+} - \overline{\mathcal{B}}_{\sigma^+})$). These errors could be further compensated by generalizing the linearizaton to second-order about the initial spherical microwave component estimates.

### 5.3.2 Remove Larmor resonances

Prior to fitting Rabi rates $\Omega_m^{m'}$ from the $\nu_{\text{low/hi}}$ SPaR peaks, we first remove the broadened central Larmor $\nu_L$ peak that consists of multiple frequency components. These $\nu_L$ frequency components (dashed vertical lines in Fig. 5.6(b)) are each calculated from eigenvalue pairs of the atom-microwave Hamiltonian $H$ defined in Sec. 3.2. If the microwave field is turned off ($\Omega_m^{m'} = 0$), then the $\nu_L$ components reduce to the six frequency components $\nu_{\text{FID}}^{(j)}$ corresponding to nonlinear Zeeman (NLZ) shifts originating from the $F = 1, 2$ hyperfine manifolds (light blue vertical lines in Fig. 5.6(b)). In contrast, in the presence of microwave coupling at a microwave frequency $\nu_{\mu\text{w}}$ tuned near-resonance to the $\sigma^\pm$ and $\pi$ hyperfine transitions, as implemented in this work, there are always four $\nu_L^{(j)}$ components [see Fig. 5.6(b)].

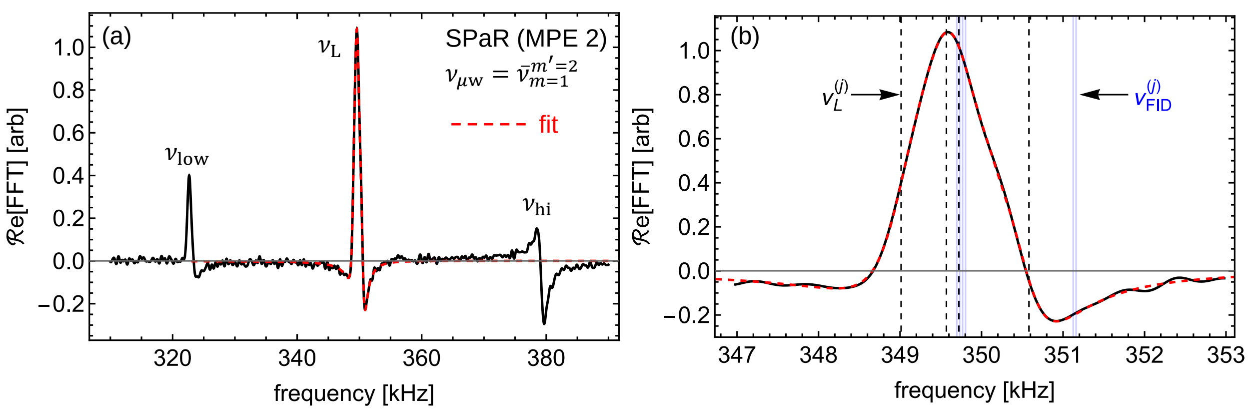


Figure 5.6: Fitting to $\nu_L$ frequency components within SPaR spectra. (a) MPE 2 $\sigma^+$ SPaR spectra with the $\nu_L$ fit overlayed. (b) a close-up of the $\nu_L$ feature with fit (red dashed) overlayed that consists of four frequency components $\nu_L^{(j)}$ (black dashed) calculated from the eigenvalues of $H$ using initial Rabi estimates. We also plot the unperturbed frequency components of the Larmor FID signal (light blue).

Initial estimates of the magnetic field strength $B$ and the buffer gas pressure shift $\nu_{\text{bg}}$ are known from FID and microwave spectroscopy measurements [94]. The Rabi rates $|\Omega_m^{m'}| \approx \nu_{\text{hi}} - \nu_{\text{low}}$ are estimated from the $\nu_{\text{low/hi}}$ peaks in the fast Fourier transform (FFT) of the $\sigma^\pm$ SPaR spectra [see Fig. 5.6(a)] with an accuracy of 1 kHz. These Rabi rates are approximated to be real and positive and can be used to calculate the spherical microwave components through Eq. (5.1). The 1 kHz accuracy in these initial Rabi rates affects the accuracy of the $\nu_L$ frequency components at the 10 Hz scale. We fix the $\nu_L^{(j)}$ frequency component estimates within the following model for the $\mathcal{R}e$[FFT] of the SPaR spectra

$$\mathcal{R}e[\text{FFT}] = \sum_{j=1}^{4} a_j \frac{\cos[\phi_j] - \sin[\phi_j](f - \nu_L^{(j)})}{(f - \nu_L^{(j)})^2 + w_j^2/4} \tag{5.17}$$

where the free fitting parameters $a_j$, $w_j$, and $\phi_j$ correspond to Lorentzian amplitudes, widths, and phases. We fit this model to the $\mathcal{R}e$[FFT] data over $\nu_{\text{FID}} \pm 3$ kHz, where $\nu_{\text{FID}} \approx 350$ kHz is the unperturbed FID frequency, and subtract this fit from the SPaR spectra as shown for the $\pi$ $|11\rangle - |21\rangle$ transition in Fig. 5.7(b) and the $\sigma^+$ $|11\rangle - |22\rangle$ transition in Fig. 5.5(d).

### 5.3.3 SPaR for $\pi$ transitions

In Fig. 5.7 we show the SPaR spectrum for the $|1,1\rangle - |2,1\rangle$ $\pi$ transition. A similar spectrum appears for the other $|1,-1\rangle - |2,-1\rangle$ $\pi$ transition. This spectrum contains more complexity than the $\sigma^{\pm}$ cases due to the fact that these $\pi$ hyperfine transitions are not end-resonances involving sublevels with maximum or minimum atomic spin projection. We can qualitatively identify the frequency components of the $\nu_{\text{low/hi}}$ sidebands in the level diagram of Fig. 5.7(a). The fitting model used for $\pi$ SPaR spectra is given by

$$\begin{aligned}\mathcal{R}e[\text{FFT}] = &\sum_{j=1}^{3} a_{j,\text{low}} \frac{\cos[\phi_{j,\text{low}}] - \sin[\phi_{j,\text{low}}](f - \nu_{\text{low}}^{(j)})}{(f - \nu_{\text{low}}^{(j)})^2 + w_{j,\text{low}}^2/4} \\ &+ \sum_{j=1}^{3} a_{j,\text{hi}} \frac{\cos[\phi_{j,\text{hi}}] - \sin[\phi_{j,\text{hi}}](f - \nu_{\text{hi}}^{(j)})}{(f - \nu_{\text{hi}}^{(j)})^2 + w_{j,\text{hi}}^2/4}\end{aligned} \tag{5.18}$$

where $a_{j,\text{low(hi)}}$, $w_{j,\text{low(hi)}}$, and $\phi_{j,\text{low(hi)}}$ are free Lorentzian amplitude, widths, and phases for the three $\nu_{\text{low(hi)}}$ frequency components. Only $\mathcal{B}_\pi$ spherical microwave component is left as a free variable to evaluate the $\nu_{\text{low(hi)}}$ frequency components (given in terms of the eigenvalues of $H$), while the $\mathcal{B}_{\sigma^\pm}$ components are held at their initial estimates $\overline{\mathcal{B}}_{\sigma^+}$ and $\overline{\mathcal{B}}_{\sigma^-}$. Due to the number of free parameters in Eq. (5.18) the $\pi$ SPaR fitting algorithm is more susceptible to systematic errors from overfitting than the $\sigma^{\pm}$ SPaR model discussed in Sec. 5.3.

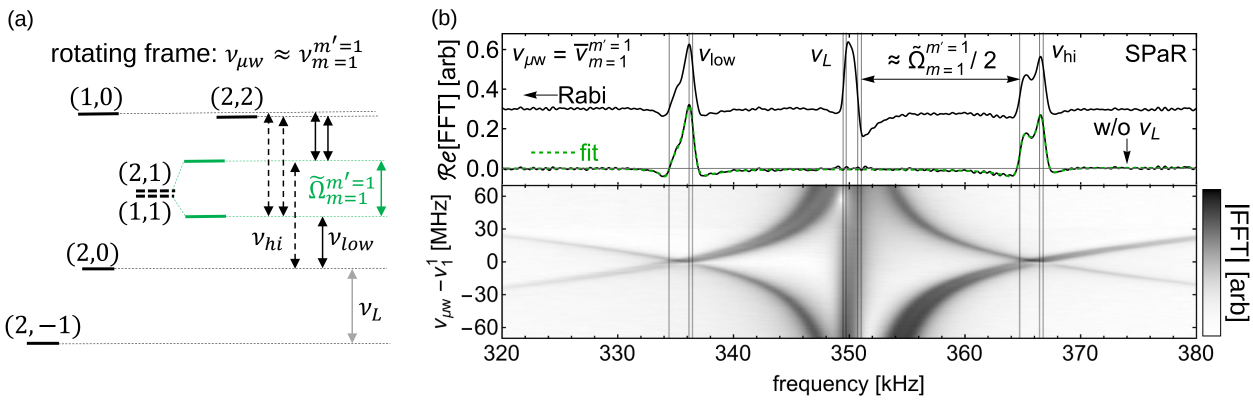


Figure 5.7: SPaR for $|11\rangle - |21\rangle$ $\pi$ transition. (a) Level diagram in a rotating frame near the $\pi$ hyperfine transition resonance $\nu_{m=1}^{m'=1}$. The anti-crossing (green) gives rise to several SPaR peaks above $\nu_{\text{hi}}$ (dashed arrows) and below $\nu_{\text{low}}$ (solid arrows) the central Larmor frequency peak $\nu_L$ The Larmor frequency peak $\nu_L$ is arise from the Zeeman splitting between sublevels weakly coupled by the microwave field. (b) The SPaR spectrum evaluated at $\overline{\nu}_{m=1}^{m'=1} = 6835.4701$ MHz. Solid vertical lines indicate eigenvalue pairs that correspond to arrows in (a). The bottom density plot shows the microwave detuning dependence of the SPaR spectrum.

## 5.4 Vector Magnetometry

After calibration of the microwave parameters in each $(\vec{\mathcal{B}}_m^{m'})_s$, which now serve as an accurate vector reference, we conduct vector magnetometry independently with the Rabi oscillation and SPaR measurements. For the Rabi oscillation data, we solve for the DC magnetic field direction $(\alpha, \beta)$ by fitting the generalized Rabi frequency $(\tilde{\Omega}_m^{m'})_s$ to the eigenvalue model $\delta\lambda_m^{m'}$ with the cost function

$$r_{\text{rabi}}^{(\alpha,\beta)} = \sum_{s=1}^{3} \sum_{m,m'} (\tilde{w}_m^{m'})_s \Big( \delta\lambda_m^{m'}((\vec{\mathcal{B}}_m^{m'})_s, \alpha, \beta) - (\tilde{\Omega}_m^{m'})_s \Big)^2. \tag{5.19}$$

For the SPaR data, we solve for $(\alpha, \beta)$ by fitting the measured Rabi rate $(\Omega_m^{m'})_s$ to the spherical microwave component (Eq. 3.9) with the cost function

$$\begin{aligned} r_{\text{spar}}^{(\alpha,\beta)} = \sum_{s=1}^{3} \sum_{m,m'} (w_m^{m'})_s \times \\ \Big( \Big| R_y(-\beta) R_z(-\alpha) \frac{\mu_m^{m'} (\vec{\mathcal{B}}_m^{m'})_s}{h} \cdot \epsilon_k \Big| - (\Omega_m^{m'})_s \Big)^2. \end{aligned} \tag{5.20}$$

The absolute value in Eq. (5.20) emphasizes the approximation, only during SPaR fitting, that the spherical microwave components and Rabi rates are positive numbers. For both, Eq. (5.19) and Eq. (5.20), the pairs of magnetic sublevels $m, m'$ are only summed over the four hyperfine transitions in Fig. 5.1(a). The weights $(\tilde{w}_m^{m'})_s = (\delta(\tilde{\Omega}_m^{m'})_s)^{-2}((r_m^{m'})_s)^{-1}$ in Eq. (5.19) are given by the fitting errors $\delta(\tilde{\Omega}_m^{m'})_s$ of the generalized Rabi frequencies and further weighted by the MPE squared residual error $\overline{r}_m^{m'} = ((r_m^{m'})_{s,1} + (r_m^{m'})_{s,2})/2$, defined in terms of $(r_m^{m'})_{s,1}$ and $(r_m^{m'})_{s,2}$ introduced in Section 5.2. The weights $(w_m^{m'})_s$ in Eq. (5.20) are similarly defined.

### 5.4.1 Vector sensitivity and accuracy evaluation

The evaluation of the accuracy and sensitivity of the vector measurements, conducted over 300 random $\vec{B}_{\mathrm{DC}}$ orientation, are depicted in Fig. 5.8. In the case of Rabi oscillation data, we exclude field directions that have polar angles within 90°, whereas for SPaR, the evaluation is specifically focused on polar angles that fall within $90° \pm 10°$. Despite the periodicity of $\mathcal{B}_k$ with respect to DC magnetic field direction $(\alpha, \beta)$ [see Fig. 5.1(c)], the Rabi measurements in Eq. (5.19) and Eq. (5.20), using three MPEs, find unique solutions for $(\alpha, \beta)$ [Sec. 5.7].

Accuracy evaluations were conducted by mathematically rotating the DC magnetic field $\vec{B}_m$, detected with either Rabi oscillation or SPaR measurements, onto the z-axis of the lab frame $\mathcal{L}$ through

$$(\delta B_x, \delta B_y, B_z) = R_y(-\beta) R_z(-\alpha) \vec{B}_m. \tag{5.21}$$

The rotation in Eq. (5.21) utilizes the field direction $(\alpha, \beta)$ predicted by a coil system calibration with 50 $\mu$rad accuracy [Sec. 2.4.1]. Up to the accuracy of the coil system calibration, residual transverse components $\delta B_x$ and $\delta B_y$ are d3ue to vector inaccuracies. These transverse components are converted into an angular inaccuracy through

$$\delta\theta = \tan^{-1}\Big(\frac{1}{B}\sqrt{\delta B_x^2 + \delta B_y^2}\Big), \tag{5.22}$$

where $B = |\vec{B}_m|$. These angular inaccuracies are represented by the shaded circular arcs in Fig. 5.8(a,b).

The mean angular accuracies of the Rabi oscillation and SPaR vector data are 0.46 mrad and 4.3 mrad respectively. These accuracies are consistent with the measured MPE calibration residuals from Rabi oscillation measurements at the 10 Hz scale [see Fig. 5.3(c)] and the 100 Hz scale systematics in the SPaR measurements [see Fig. 5.5(d)]. Rabi frequency systematic errors at the 10 Hz scale may partially be due to imperfect microwave drift compensation, but can also be due to a variety of sources stemming from microwave phase noise, magnetic field gradients, and microwave inhomogeneity discussed further in Sec. 5.6.

The sensitivity $S_{B_i} = \sigma_{B_i}\sqrt{t_m}$ of each vector component $B_i$, where $i = x, y, z$, is calculated from the standard error $\sigma_{B_i}$, using 10 repeated measurements of $\vec{B}_m$ over a total measurement time $t_m$. For Rabi oscillation data, this measurement duration was $t_m = 150$ ms, while for SPaR measurements the duration was $t_m = 270$ ms. Included in each $t_m$ is the FID measurement time lasting 30 ms. Angular sensitivities are similarly evaluated using Eq. (5.21) and Eq. (5.22). Rabi oscillation vector measurements reach a mean angular sensitivity of 35 $\mu$rad/$\sqrt{\text{Hz}}$ (1.7 nT/$\sqrt{\text{Hz}}$) evaluated over random field directions [see Fig. 5.8(c)]. The best measurements reach near the optical shot noise limit of 9 $\mu$rad/$\sqrt{\text{Hz}}$ (0.45 nT/$\sqrt{\text{Hz}}$) arising in the Faraday rotation detection [Sec. 5.4.2]. Suboptimal performance below this shot noise limit in most of the vector data is likely due to shot-to-shot amplitude fluctuations of the microwave field. For comparison, these vector component sensitivities are at the same 1 nT/$\sqrt{\text{Hz}}$ level reported in the Helium SWARM mission [66]. While this is not a direct comparison due to a variety of apparatus differences such as the smaller cell volume employed in this work, it demonstrates comparable vector sensitivity to high accuracy OPM implementations. In future work, the implementation of complete 3D control over the microwave field, rather than using planar MPEs, would permit the strategic selection of MPEs to achieve optimal vector sensitivity at all field directions.

### 5.4.2 Estimated vector sensitivity from detection noise

To estimate the contribution to the vector sensitivity arising from the optical detector noise in the Faraday rotation signals, we first compute the average Rabi signal amplitude $\overline{A}_{\text{rabi}}$ across the

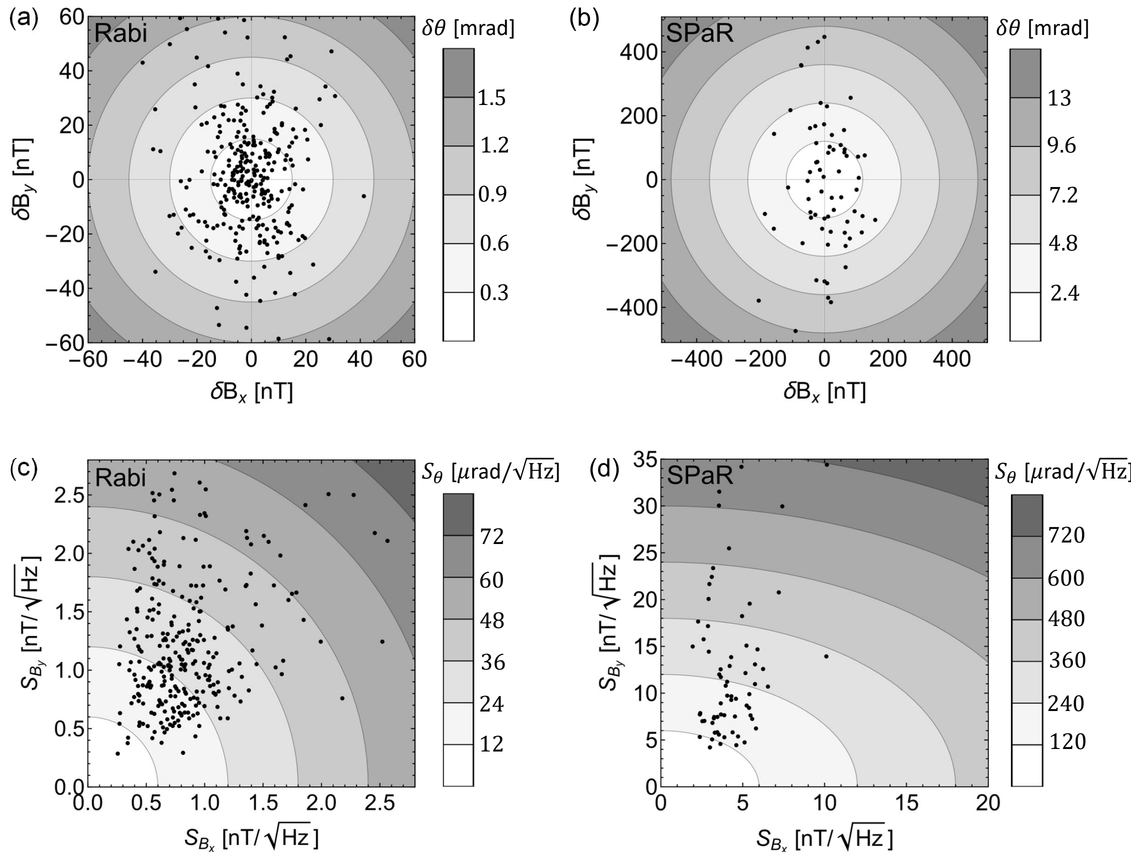


Figure 5.8: Comparative analysis of vector accuracy and sensitivity between Rabi oscillation and SPaR. (a) and (b) show the vector accuracy, and (c) and (d) show the vector sensitivity for Rabi and SPaR techniques evaluated over 300 and 80 random field directions respectively.

four hyperfine transitions for each polar angle $\beta$ [see Fig. 5.9(a)]. The Rabi amplitude is defined as the fitted sinusoidal amplitude of the measured Rabi oscillation. We find that the average Rabi signal amplitude across all $\beta$ is $\langle \overline{A}_{\mathrm{rabi}} \rangle = 0.061°$. Our detector noise is characterized by a standard deviation $\sigma_{\mathrm{det}} = 0.0043°$ measured over the duration of a typical Rabi oscillation [see Fig. 2.6]. As discussed in Sec. 2.3.2, this detector noise is near the shot-noise limit $\sigma_{\mathrm{shot}} = 0.0046°$.

With this noise and mean Rabi signal amplitude, we generate 1000 fake Rabi signals of the form

$$G(0°, \sigma_{\mathrm{det}}) + a_0 + a_1 e^{-t/t_1} + a_2 e^{-t/t_2} \cos(2\pi f t + \phi) \tag{5.23}$$

where $a_0 = 0$, $a_1 = 0.05°$, $a_2 = 0.061°$, $t_1 = 1$ ms, $t_2 = 0.27$ ms, $f = 50$ kHz, $\phi = 0$, and $G(0°, \sigma_{\mathrm{det}})$

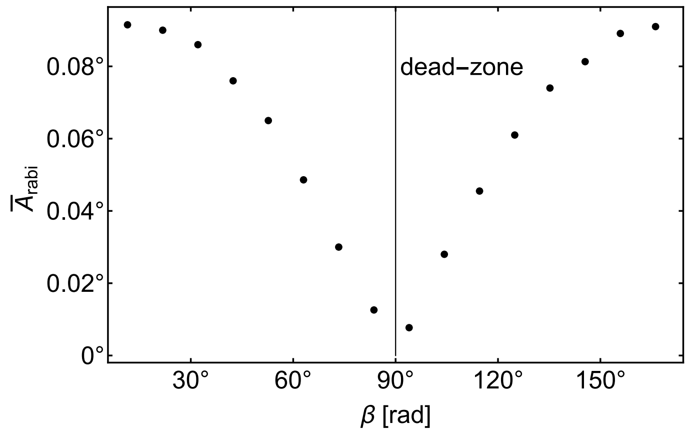


Figure 5.9: The mean Rabi amplitude averaged across all four hyperfine transitions for different polar angles $\beta$.

represents Gaussian noise with zero mean and standard deviation $\sigma_{\rm det}$. We fit these fake signals using the sinusoidal exponential decay model in Eq. (5.23) and found that the standard deviation of the corresponding Rabi frequency noise to be $\sigma_f = 3.4$ Hz.

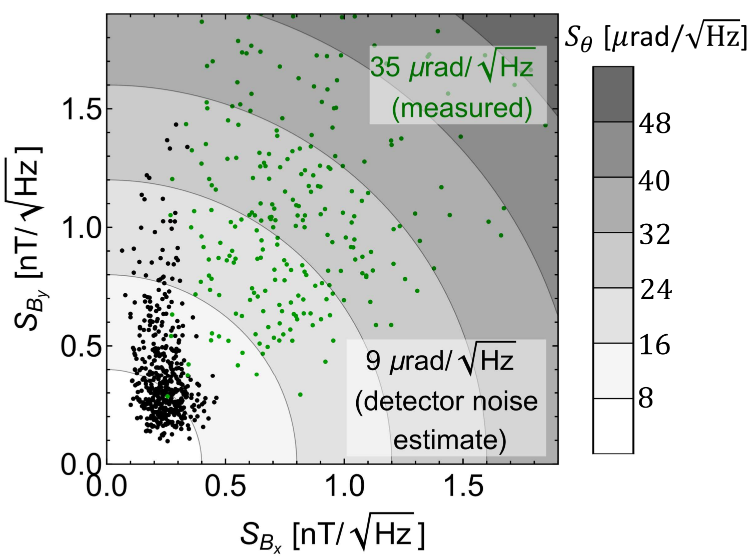


Figure 5.10: Sensitivities of magnetic vector components estimated from detector noise (black) compared to measured vector component sensitivity (green) over the same magnetic field orientations. The text labels denote the average directional sensitivities.

Next, we proceed by approximating all Rabi measurements as having $\sigma_f$ noise because this number was extracted from the mean Rabi amplitude and dephasing rate across all transitions and polar angles. We use the calibrated MPE parameters shown Table 5.2 to calculate all Rabi rates $\Omega_m^{m'}$ with random noise $\sigma_f$ from each of the four hyperfine transitions using

$$(\Omega_m^{m'}) = G\Big(\mu_m^{m'}|\mathcal{B}_k^{(\alpha,\beta)}|/h, (\sigma_f)^2\Big). \tag{5.24}$$

From these estimates of noisy Rabi rates, we solve the system of equations using $\mu_m^{m'}|\mathcal{B}_k^{(\alpha,\beta)}|/h$ as the model to solve for $(\alpha, \beta)$. We repeat this procedure 10 times for each magnetic field orientation to find the corresponding fluctuations in $(\alpha, \beta)$. From the corresponding measurement times $t_m = 150$ ms (including the FID measurement time), we convert these $(\alpha, \beta)$ fluctuations into sensitivities by scaling with $1/\sqrt{t_m}$. The corresponding vector component sensitivities are plotted in Fig. 5.10 along with the measured vector sensitivities corresponding to the same magnetic field orientations. We find that the mean vector sensitivities estimated from detector noise is about 4 times lower than the mean vector sensitivities likely due to technical microwave noise.

Table 5.2: Initial calibrated MPEs used to estimate vector sensitivity from detector noise.

| MPE | $\mathcal{B}_x$ $[\mu T]$ | $\mathcal{B}_y$ $[\mu T]$ | $\mathcal{B}_z$ $[\mu T]$ | $\phi_x$ [rad] | $\phi_y$ [rad] |
|---|---|---|---|---|---|
| 1 | 2.3222 | 3.9520 | 0.0601 | 2.6210 | 4.010 |
| 2 | 3.5027 | 2.3923 | 0.0560 | 3.0864 | 1.7690 |
| 3 | 5.5730 | 1.6342 | 0.0994 | 2.7799 | 4.7449 |

## 5.5 MPE drift detection without recalibration

Uncompensated drift of the calibrated MPE parameters in Eq. (5.19) and Eq. (5.20) will cause vector magnetometry errors. In this work, microwave field drifts due to instability of the microwave cavity temperaure are handled by employing running MPE calibrations described in Sec. 5.2. Although stable microwave fields would enable vector magnetometry without the need for constant MPE recalibration, any type of vector OPM will inevitably experience drift in its mechanical reference, like a coil system, over an extended period. Furthermore, current vector OPM techniques have limited information from atomic measurements to detect sensor drift. For example, vector OPMs using coil modulations can only compare consistency between the norm of the measured vector components $(B_x, B_y, B_z)$ with the scalar value $B$ to detect drift in parameters like coil non-orthogonality and coil factors. As a result many high accuracy vector OPMs employ blind recalibration, which can result in sensor downtime.

In contrast, Rabi measurements across multiple transitions and MPEs contain much more independent information to detect drift in the MPE reference. In this work, there are nine independent Rabi measurements corresponding to the three spherical microwave components of MPE 1, MPE 2, and MPE 3. In contrast, if we neglect the frequency dependence of the microwave cavity modes, the total number of unknowns that characterize our sensor are 15 unknown MPE parameters and the two unknown DC magnetic field directions. In theory, the MPE parameters can be reduced further because the microwave field of MPE 3 is the result of summing the microwave fields of MPE 1 and MPE 2. In this case, the number of unknown microwave parameters can be reduced from 15 to 11. This situation is expressed as

$$\begin{aligned}\vec{\mathcal{B}}_3 =& \vec{\mathcal{B}}_1 + \vec{\mathcal{B}}_2 = \{\mathcal{B}_{x,1}e^{-i\phi_{x,1}}, \mathcal{B}_{y,1}e^{-i\phi_{y,1}}, \mathcal{B}_{z,1}\}+ \\ & \{\mathcal{B}_{x,2}e^{-i(\phi_{x,2}+\phi_r)}, \mathcal{B}_{y,2}e^{-i(\phi_{y,2}+\phi_r)}, \mathcal{B}_{z,2}e^{-i\phi_r}\},\end{aligned} \tag{5.25}$$

where the additional parameter $\phi_r$ accounts for the relative phase between the microwave fields of MPE 1 and MPE 2. While we calibrate all three MPEs independently, the MPE 3 parameters are well approximated in terms of the 10 microwave parameters of MPE 1 and MPE 2 and a relative phase of $\phi_r = 1.058$ rad, as shown in Sec. 5.2.1. Thus, without frequency dependence of the cavity modes, the nine independent Rabi measurements are close to the total number of unknowns that characterize our vector sensor.

As a proof of concept, we show in Fig. 5.11 how the RMS error $\delta_{\text{detect}} = (r_{\text{rabi}}^{(\alpha,\beta)})^{-1/2}$, computed from Eq. (5.19) after solving for $(\alpha, \beta)$ and setting the weights $(\tilde{w}_m^{m'})_s \to 1$, provides a drift-detection measure. Establishing a specific threshold for $\delta_{\text{detect}}$ allows it to act as a cue to recalibrate, and thus eliminating the necessity for constant recalibration. Exploring how to further utilize MPE drift measures like $\delta_{\text{drift}}$ to mitigate MPE recalibration is the subject of future work.

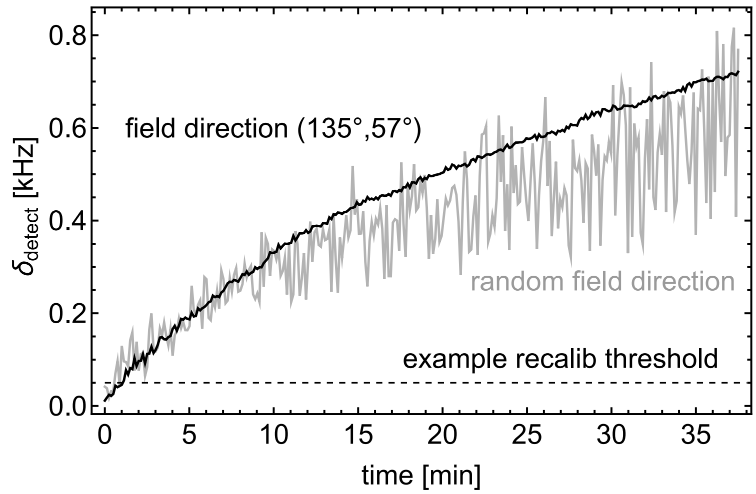


Figure 5.11: The drift parameter $\delta_{\text{detect}}$ evaluated over 37.5 minutes demonstrating drift detection without full MPE recalibration.

## 5.6 Potential systematics

Some systematic errors in the vector magnetometry data are expected due to the uncertianty in the microwave parameters from the finite MPE calibration length investigated in Sec. 5.2.3. From the analysis in Sec. 5.2.3, residuals between generalized Rabi frequency measurements and the eigenvalue model $\delta\lambda_m^{m'}$ are predicted to have a standard deviation of $\sigma = 5$ Hz, which is lower than the measured fluctuations of $\sigma = 13$ Hz reported in Fig. 5.3(c). Furthermore, these $\sigma = 13$ Hz residuals are fairly consistent with the mean vector magnetometry accuracy of 0.46 mrad reported in Sec. 5.4.1, which roughly correlates to 50 kHz $\cdot$ 0.00046 $\approx$ 23 Hz systematic errors for a 50 kHz Rabi frequency measurement. In the subsections below we highlight potential sources of systematic errors in the Rabi oscillation measurements. We tabulate approximate sizes of these various sources in Table 5.3. The estimated total contribution from all of these systematic errors are in agreement with the back-of-the-envelope 23 Hz error.

### 5.6.1 Microwave Phase Noise

Noise in our microwave drive is characterized by amplitude and phase noise. In a two level system this noise affects the Hamiltonian describing Rabi oscillations with Rabi rate $\Omega$ and detuning

Table 5.3: A list of potential systematic error sources and their estimated magnitudes for a 50 kHz Rabi frequency. Details behind these estimates are found in the cited subsections.

| Source | Systematic error [Hz] |
|---|---|
| Finite MPE calibration length (Sec. 5.2.3) | 3.4 |
| Microwave phase noise (Sec. 5.6.1) | 3 |
| DC magnetic field inhomogeneity (Sec. 5.6.2) | 10 |
| Microwave spatial inhomogeneity (Sec. 5.6.3) | 5 |
| Rabi frequency fitting errors (Sec. 4.6.3) | 2 |
| Beyond rotating wave effects (Sec. 75.6.4) | 0.1 |
| **Total** | $\approx 23$ |

$\Delta$ by

$$H = \frac{h}{2}(\Omega + \delta\Omega(t))\sigma_x + \frac{h}{2}(\Delta + \delta\Delta(t))\sigma_z \tag{5.26}$$

where $\sigma_i$ are the Pauli spin matrices. The effect of amplitude noise leads to Rabi frequency fluctuations $\delta\Omega(t)$ and phase noise leads to detuning fluctuations $\delta\Delta(t)$. The corresponding generalized Rabi frequency is given by

$$\tilde{\Omega}(t) = \sqrt{(\Omega + \delta\Omega(t))^2 + (\Delta + \delta\Delta(t))^2}. \tag{5.27}$$

For $\Omega \gg \delta\Omega(t)$ we have $\langle(\Omega + \langle\delta\Omega(t))^2\rangle = \Omega^2$ such that on-resonance ($\Delta = 0$) we have $\tilde{\Omega} = \sqrt{\Omega^2 + \langle\delta\Delta(t)^2\rangle}$. Therefore we expect a systematic shift in the on-resonance generalized Rabi frequency due to phase noise of the microwave drive. This effect will become negligible for $\Delta \gg \delta\Delta(t)$ such that $\langle(\Delta + \delta\Delta(t))^2\rangle = \Delta^2$.

For our microwave source (WindFreak SynthHD Pro + Mini-Circuits ZVE-8G+), these noise sources are characterized by the single-sideband (SSB) phase $\mathcal{L}_\phi$ and amplitude $\mathcal{L}_a$ noise displayed in Fig. 2.18 measured with a Rohde & Schwarz FSWP26 phase noise analyzer at 6835.82 MHz. As shown in [18], the SSB phase noise is related to the unilateral power spectral density (PSD) of the corresponding detuning fluctuations $\delta\Delta(t)$ by $S_\Delta(\omega) = \frac{\omega^2}{2}10^{\frac{\mathcal{L}_\phi(\omega)}{10}}$. This PSD can be converted into a time-series by reflecting $S_\Delta(\Omega)$ to the negative $-\omega$ frequencies, creating a complex noise spectral density $N(\omega) = e^{i\phi_r}\sqrt{S_\Delta(\omega)/2}$, where $\phi_r \in [0, 2\pi]$ is a random phase evaluated at each $\omega$. These random phases are chosen such that $N(\omega) = N(-\omega)^*$. By taking the absolute value of the

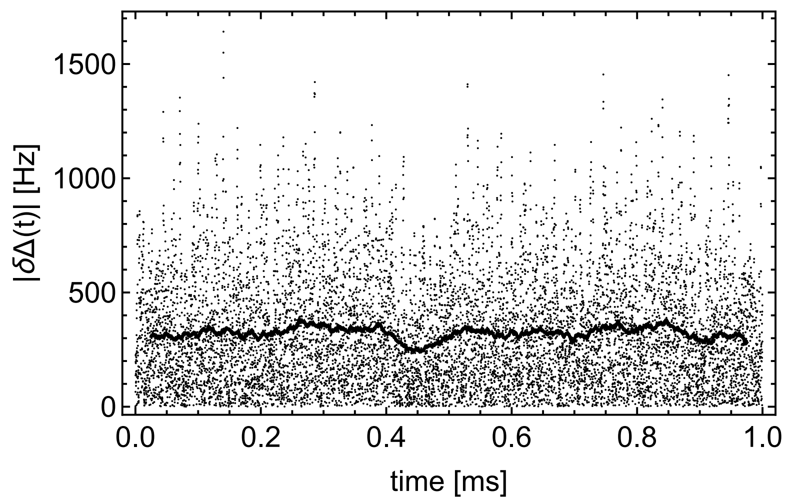


Figure 5.12: Microwave detuning fluctuations sampled at 10 MHz that are deduced from the measured phase phase in Fig. 2.18. The black line a moving average of 500 points.

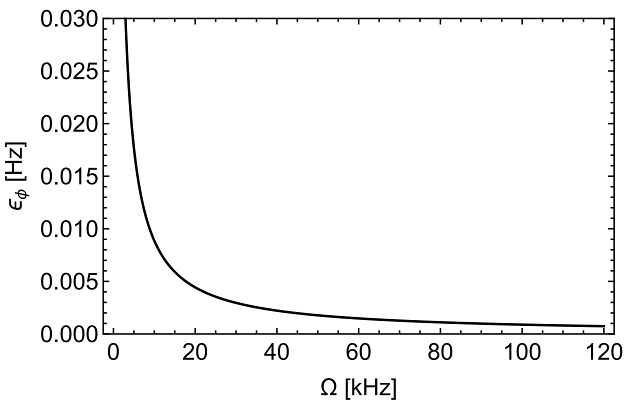


Figure 5.13: A plot of the estimated shift of a generalized Rabi frequency driven on-resonance given by $\epsilon_\phi = \langle(\delta\Delta(t))^2\rangle/2\Omega$.

inverse Fourier transform of $N(\omega)$ we obtain a time-series for $|\delta\Delta(t)|$ [Fig 5.12]. With this process we calculate $\langle(\delta\Delta(t))^2\rangle = 420$ Hz for our microwave drive. The corresponding systematic shift $\epsilon_\phi$ in the on-resonance generalized Rabi frequency is given by $\epsilon_\phi = \langle(\delta\Delta(t))^2\rangle/2\Omega$ plotted in Fig. 5.13.

### 5.6.2 Magnetic field gradients

Magnetic field gradients generate a similar error as that arising from microwave phase noise. Namely, the distribution of magnetic fields correspond to a spatial distribution of microwave detunings $\Delta(x, y, z)$. Averaging over these different microwave detunings will result in a positive systematic shift near the transition resonance. Taking the field variation in Table 2.1 of 51 nT across the 2 mm cell length as a would result in (51 nT) $\times$ (7 kHz/nT) $\times$ 3 $\approx$ 1 KHz detuning variations of the $|1,1\rangle - |2,2\rangle$ transition assuming $\vec{B}_{\mathrm{DC}} \parallel \hat{z}$. For a 50 kHz Rabi frequency this would cause an approximate systematic shift of $50 - \sqrt{50^2 + 1^2} = 0.01$ kHz assuming the two-level Rabi formula [Eq. (1.5)].

### 5.6.3 Microwave inhomogeneity

While the Rabi rate defined in Eq. 5.1 is complex, the Rabi oscillation frequencies measured from the Faraday signal are real numbers. This is akin to measuring $|\Omega_m^{m'}|$. For two complex numbers $c_1$ and $c_2$, it is generally true that $|c_1| + |c_2| \neq |c_1 + c_2|$. Similarly if there is microwave inhomogeneity, this results in a spatially varying Rabi frequency $\Omega_m^{m'}(x, y, z)$, such that the $|\Omega_m^{m'}|$ that we measure, neglecting the probe beam profile, is

$$|\Omega_m^{m'}| = \frac{1}{V}\int_V |\Omega_m^{m'}(x, y, z)| dV \neq \frac{1}{V}\Big|\int_V \Omega_m^{m'}(x, y, z) dV\Big|. \tag{5.28}$$

Thus, there is no single $\vec{\mathcal{B}}$ that accurately models the directional dependence of $|\Omega_m^{m'}|$ when there is microwave inhomogeneity.

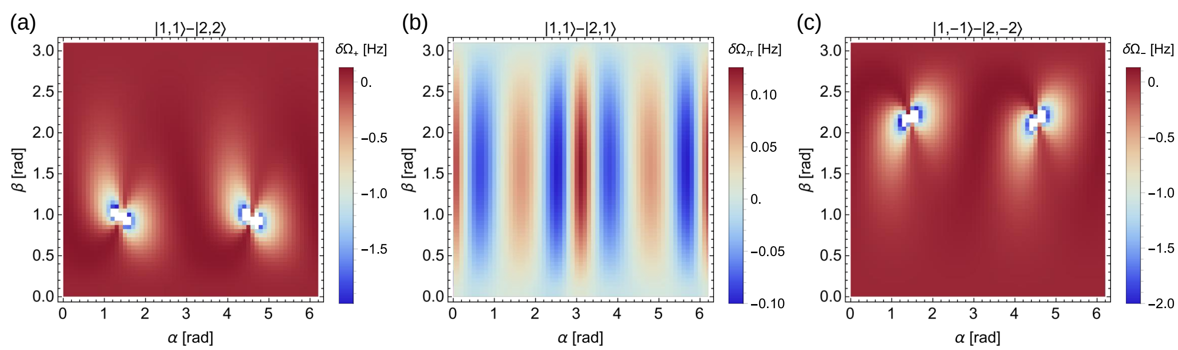


Figure 5.14: Predicted systematics of the Rabi frequencies assuming microwave amplitude ($\mathcal{B}_x$,$\mathcal{B}_y$,$\mathcal{B}_z$) inhomogeneities for the (a) $\sigma^+$, (b) $\pi$, and (c) $\sigma^-$ hyperfine transitions.

We test this by generating a spatially dependent MPE 1 parameters from Table 5.2 assuming that the spatial variation is only in the z-coordinate for simplicity. These variations are expressed

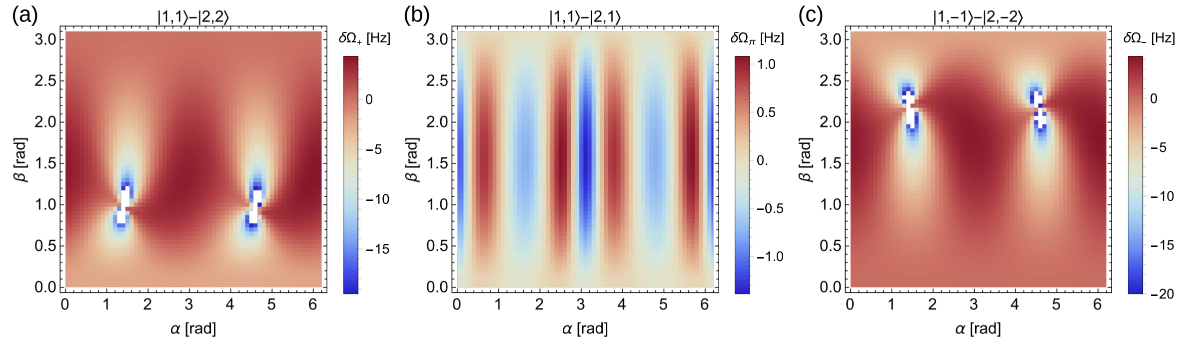


Figure 5.15: Predicted systematics of the Rabi frequencies assuming microwave phase ($\phi_x$,$\phi_y$) inhomogeneities for the (a) $\sigma^+$, (b) $\pi$, and (c) $\sigma^-$ hyperfine transitions.

to second-order

$$B_i(x) = B_{i,0}(1 + a_1 z + a_2 z^2) \tag{5.29}$$

$$\phi_i(x) = \phi_{i,0}(1 + b_1 z + b_2 z^2) \tag{5.30}$$

where $i = x, y, z$ and $a_1 = 1$ nT/mm, $a_2 = 1$ nT/mm$^2$, $b_1 = 1$ mrad/mm, and $b_2 = 2$ mrad/mm$^2$. Then over all field directions $(\alpha, \beta)$ we calculate the averaged spherical microwave component $\overline{\mathcal{B}}_k$ over the 2 mm z-dimension of the MEMS cell

$$\overline{\mathcal{B}}_k = \frac{1}{2}\int_{-1}^{1} \mathcal{B}_k(z)dz \tag{5.31}$$

where $k = \sigma^{\pm}, \pi$. These averaged spherical microwave components are then converted to real Rabi rates through the absolute value of Eq. (5.1). Next, we fit MPE parameters for each $k$ to the resulting $\overline{\mathcal{B}}_k$ using the real Rabi rate $|\Omega_m^{m'}|$ predicted from Eq. (5.1). The discrepancy between the averaged $|\Omega_m^{m'}|$ calculated with Eq. (5.1), and that predicted with the MPE parameter fits of the spatially-averaged data is shown in Fig. 5.14 for only microwave amplitude variations ($b_{1,2} = 0$) and Fig. 5.15 for only phase variations ($a_{1,2} = 0$). With these parameters, we see the largest systematics with the phase variations at the 5-10 Hz scale. Not considered here is how much microwave inhomogeneity modifies the exponential decay of the Rabi oscillation, which could also introduce its own systematic shifts in the Rabi frequency fitting. While it is challenging for us to estimate the exact microwave inhomogeneity in our experiment, this study demonstrates its importance when trying to make vector measurements reaching below 100 $\mu$rad accuracy.

### 5.6.4 Beyond RWA systematics

Another potential systematic, though likely having a smaller effect than the above systematic list are beyond rotating wave effects. An rough estimate of the scale of shift from beyond RWA is given by the Bloch-Siegert shift

$$\frac{1}{4}\frac{(\Omega_m^{m'})^2}{\nu_m^{m'}} \approx 0.1 \text{ Hz} \tag{5.32}$$

assuming $\Omega_m^{m'} \approx 50$ kHz and $\nu_m^{m'} \approx 6.834$ GHz.

## 5.7 Unique determination of the magnetic field direction with MPEs

We evaluate the uniqueness of the $(\alpha, \beta)$ fitted from measurements by evaluating the following cost function

$$\sum_{s=1}^{3}\sum_{m,m'}\Big(\big|R_y(-\beta)R_z(-\alpha)(\vec{\mathcal{B}}_m^{m'})_s\cdot\epsilon_k\big| - \big|R_y(-\beta_1)R_z(-\alpha_1)(\vec{\mathcal{B}}_m^{m'})_s\cdot\epsilon_k\big|\Big)^2 \tag{5.33}$$

which compares the spherical microwave components, calculated from the MPE parameters in Table 5.2, at $(\alpha_1, \beta_1) = (1.3, 1.4)$ rad with all other field directions. Plot1ting this cost function in Figure 5.16(a) reveals a global solution at the correct $(\alpha_1, \beta_1)$. However there is also local minimum. Instead of using MPEs all in a plane, we found that by replacing MPE 3 in Table 5.2 with $(\mathcal{B}_x, \mathcal{B}_y, \mathcal{B}_z, \phi_x, \phi_y) = (1\ \mu\text{T}, 2\ \mu\text{T}, 3\ \mu\text{T}, 0\ \text{rad}, 0.5\ \text{rad})$ gives a more pronounced optimum solution [see Fig. 5.16(b)].

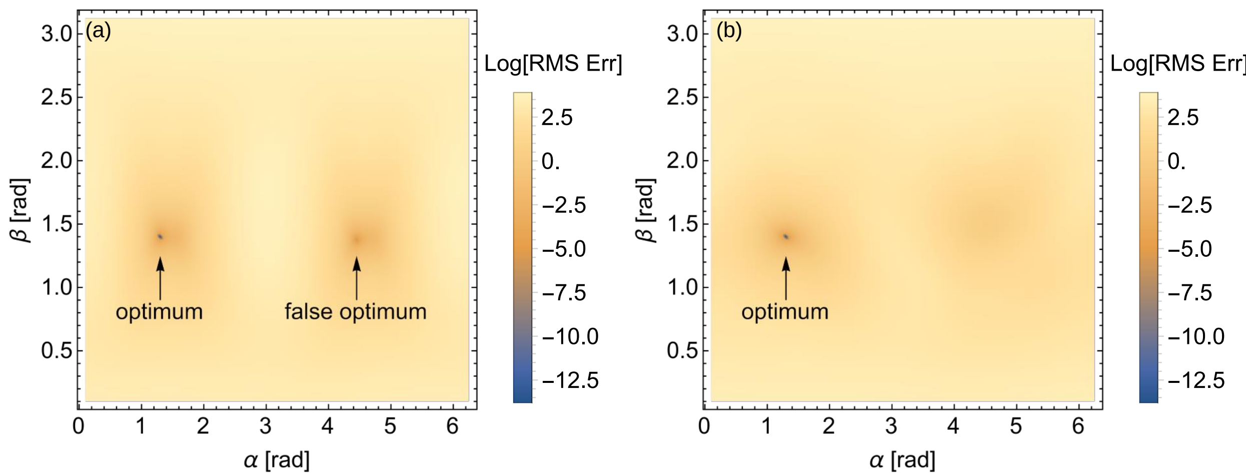


Figure 5.16: Unique vector detection with Rabi measurements. Evaluation of the cost function (5.33) for (a) the MPEs in Table 5.2 and (b) replacing MPE 3 parameter with an MPE that contains a significant $\mathcal{B}_z$ component. In both of these evaluations we observe a unique global minimum.

# Chapter 6

## Rabi Amplitude Nulling for measuring Beam Attitude (RANBA)

As with all vector magnetometers, our measurements in the previous chapter occur within an intrinsic magnetometer frame. In our case this intrinsic frame is determined by the coil system used during the calibration of the microwave polarization ellipses (MPEs). A common problem that can limit the absolute accuracy and consistency between multiple vector magnetometers is that the orientation of the intrinsic magnetometer frame is not well-defined. This is because calibration methods, that typically rely on scalar measurements, are unable to determine the overall orientation of the magnetometer frame [66, 122]. Consequently, vector measurements before and after recalibration may be taken in magnetometer frames that are not consistent with each other.

A viable approach to address these challenges would be to perform high accuracy laser beam attitude measurements that could monitor overall drifts in the intrinsic magnetometer frame. Beam attitude measurements of a laser passing through a vector gradiometer consisting of two atomic magnetometers could also calibrate the relative orientation of their magnetometer frames [see Fig. 6.1]. Conceivably, any all-optical vector OPM could be used to measure a laser beam attitude with respect to an intrinsic magnetometer frame. As discussed in Sec. 1.1.1, however, for many of these approaches achieving a directional accuracy better than $1°$ is a nontrivial task [87, 120, 121, 199].

In this chapter we discuss how to measure the attitude of a far-detuned probe beam with respect to an intrinsic magnetometer frame from the location of a Rabi oscillation signal's deadzones detected using Faraday rotation. This technique, namely Rabi Amplitude Nulling to measure Beam Attitude (RANBA), doesn't require precise modeling of the Rabi oscillation amplitude, which if done accurately, would have required knowing exact optical pumping and probe beam parameters. We apply this technique to the vector data discussed in Ch. 5, enabling us to pinpoint our probe beam's direction with a precision of 240 $\mu$rad at a 95% confidence level. This approach demonstrates consistent results using Rabi measurements across four hyperfine transitions and three different microwave driving fields. Furthermore, we project the theoretical accuracy of RANBA to be within 50 $\mu$rad for $\pi$ hyperfine transitions under realistic experimental conditions.

While beam attitude measurements are useful to monitor overall drifts of the magnetometer frame, full calibration to an external coordinate frame is limited by the axial symmetry of a single probe beam. Absolute calibration of a magnetometer frame is often done by referencing the magnetometer measurements to the location of distant objects using a nonmagnetic theodolite [76, 135] or star tracker [122]. In situations where making theodolite measurements is impractical, such as being inside an enclosed room, optical prisms firmly attached to a vector magnetometer are used instead [54, 152]. A drawback of optical prism techniques is the spatial distance between the magnetometer and prism, which, along with magnetic field gradients encountered during the calibration procedure, limit the overall accuracy. Instead of using an optical prism, the advantage of RANBA is that the laser beam attiude is referenced at the exact location of the magnetometer. At the end of this chapter we show a design concept, on how to reference the intrinsic magnetometer frame with RANBA to an external frame by measuring small angular deviations of the probe beam with a camera.

## 6.1 Theoretical framework

The two underlying mechanisms of RANBA are: firstly, Rabi oscillations induce spin dynamics exclusively in the direction $(\alpha, \beta)$ of the DC magnetic field $\vec{B}_{\mathrm{DC}}$, as specified within the intrinsic frame of the magnetometer; secondly, the Faraday rotation of the probe beam is sensitive solely to spin dynamics occurring along the probe beam. It follows from these two concepts that when the probe beam aligns exactly with the z-axis of the magnetometer frame, the amplitude of the Rabi oscillations will null in all $(\alpha, 90°)$ directions. This phenomenon manifests as a 'nulling'

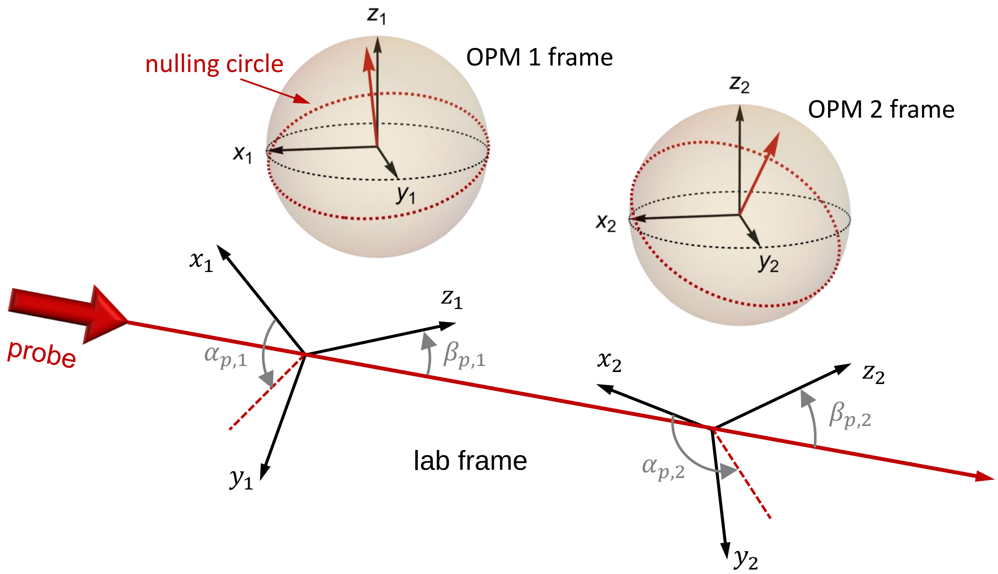


Figure 6.1: Schematic of two optically pumped magnetometer (OPM) frames referenced to the direction of a probe beam. Within the reference frames of OPM 1 and OPM 2 the probe points in directions $(\alpha_{p,1}, \beta_{p,1})$ and $(\alpha_{p,2}, \beta_{p,2})$ respectively. The orientations of the DC magnetic field, $\vec{B}_{\rm DC}$, that lead to the nulling of the Rabi oscillation amplitude, $A_m^{m'}$, between the hyperfine sublevels $|1, m\rangle$ and $|2, m'\rangle$, trace out a circle (red dashed) within a plane perpendicular to the direction of the probe beam.

circle on the equator of a unit sphere within the magnetometer frame [see Fig. 6.1]. If the probe beam is tilted by $(\alpha_p, \beta_p)$, the nulling circle will tilt, and the nulling polar angles will occur in the magnetometer frame at $\beta_0(\alpha, \alpha_p, \beta_p)$ expressed as

$$\beta_0(\alpha, \alpha_p, \beta_p) = \arctan\left(\frac{\sqrt{\cos^2(\alpha - \alpha_p)\cos^2(\beta_p) + \sin^2(\alpha - \alpha_p)}}{\cos(\alpha - \alpha_p)\sin(\beta_p)}\right) + (\beta_m^{m'}(\alpha) - \pi/2) + \beta_{\rm off}. \quad (6.1)$$

The arctan term in Eq. (6.1), hereby called the ‘tilt model’, is a geometrical term accounting for the tilt of the nulling circle, while $(\beta_m^{m'}(\alpha) - \pi/2)$ models small polar angle deviations arising from off-resonant microwave-driving to nearby hyperfine transitions. Also included in Eq. (6.1) is an overall offset $\beta_{\rm off}$ left as a fitting parameter.

To calculate the off-resonant driving term, $\beta_m^{m'}(\alpha)$, we first define the diagonalized atom-microwave Hamiltonian $H_d^{(\alpha,\beta)} = D^* H^{(\alpha,\beta)} D^T$ with $D$ consisting of the eigenvectors of the atom-microwave Hamiltonian $H^{(\alpha,\beta)}$ defined in Eq. (3.12). In the $\vec{F} = \vec{S} + \vec{I}$ basis, let $\rho_0$ be the density matrix characterizing the optically pumped atomic state prior to the Rabi oscillation and $S_{z,d}$ be the z-component of the electron spin operator with no off-diagonal elements. Then the amplitude $A_m^{m'}$ of the Rabi oscillation between hyperfine sublevels $|1,m\rangle$ and $|2,m'\rangle$ is expressed as

$$A_m^{m'} = |g(D^*\rho_0 D^T)_{ij}(D^* S_{z,d} D^T)_{ji}| \tag{6.2}$$

where the indices $i$ and $j$ correspond to the eigenvalues $\lambda_j$ and $\lambda_i$ of the diagonalized Hamiltonian $H_d^{(\alpha,\beta)}$ such that the generalized Rabi frequency is given by $\tilde{\Omega}_m^{m'} = (\lambda_j - \lambda_i)/h$. The exact value of the coupling constant $g$, which characterizes the Faraday rotation strength [Sec. 2.3], is not important in this experiment because we are only interested in the magnetic field directions that minimize $A_m^{m'}$. The Rabi oscillation amplitude $A_m^{m'}$ depends on the DC magnetic field direction $(\alpha,\beta)$ through the operator $D$ consisting of the eigenvectors of $H_d^{(\alpha,\beta)}$. We define $\beta_m^{m'}(\alpha)$ as the polar angle such that $A_m^{m'}$ is minimized. In general, the minimum $A_m^{m'}$ is zero, but off-resonant microwave driving can cause the minimum $A_m^{m'}$ to be small, but nonzero. The azimuthal angle dependence of $\beta_m^{m'}(\alpha)$ arises because the Rabi rates characterizing off-resonant driving depend on the DC magnetic field direction $(\alpha,\beta)$.

As an illustrative example, we calculate $\beta_m^{m'}(\alpha)$ using the MPE 1 parameters defined in Table 5.2 for the $\sigma^+$ and $\pi^+$ transitions driven at $\nu_{\mu\text{w}} = 6835.82$ MHz and $\nu_{\mu\text{w}} = 6835.57$ MHz respectively [see Fig. 6.2]. In both cases the pressure shift $\nu_{\text{bg}} = 88$ kHz and magnetic field strength $|\vec{B}_{\text{DC}}| = 50$ $\mu$T. As expected, when off-resonant microwave-driving is eliminated, by zeroing the corresponding spherical microwave components $\mathcal{B}_{\sigma^\pm,\pi}^{(\alpha,\beta)}$, $\beta_m^{m'}(\alpha)$ reduces to $\pi/2$ (90°) for all azimuthal angles $\alpha$. To illustrate the effects that state preparation can have on $\beta_m^{m'}(\alpha)$, we let $\rho_0 = \rho_1(p)$ be a spin temperature distribution with all the atomic population distributed only within $F=1$ manifold as shown in Fig. 6.2(a). Specifically, the population in $|1,m\rangle$ is proportional to $e^{b(p)m}$ defined by

$$b(p) = \ln\left(\frac{1+p}{1-p}\right). \tag{6.3}$$

We employ $\rho_1(p)$ primarily as a simplified model to explore how $\beta_m^{m'}(\alpha)$ responds to variations in atomic populations, rather than adopting a standard spin-temperature distribution that includes populations in $F=2$, where $\pi$ Rabi oscillations yield no signal because the populations in $|1,m\rangle$ and

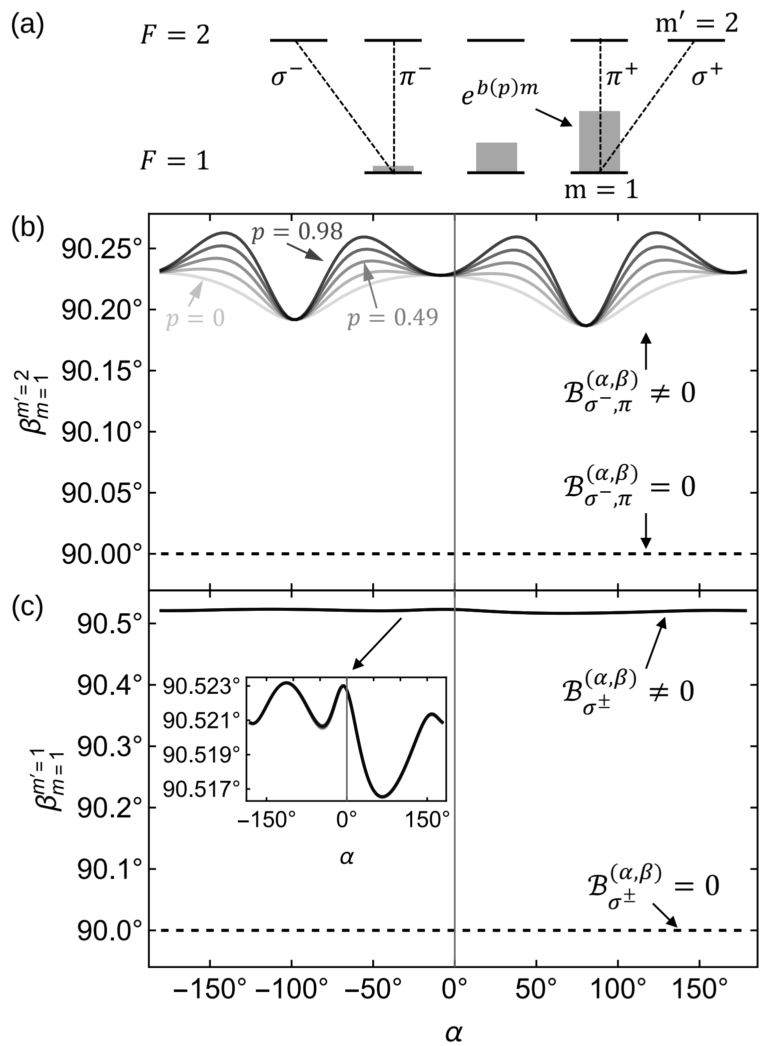


Figure 6.2: (a) Energy-level diagram representing $\rho_1(p)$ given by a modified spin-temperature distribution with all atomic population in the $F = 1$ manifold. (b,c) Nulling polar angles arising from off-resonant driving for the $\sigma^+$ (b) and $\pi^+$ (c) transitions evaluated at $\nu_{\mu\mathrm{w}} = 6835.82$ MHz and $\nu_{\mu\mathrm{w}} = 6835.47$ MHz respectively. Off-resonant driving from the spherical microwave components on adjacent hyperfine transitions causes $\beta_m^{m'}$ to deviate from 90° (dashed line). Calculation of $\beta_m^{m'}$ in both plots assumed MPE 1 parameters in Table 5.2, magnetic field strength $|\vec{B}_{\mathrm{DC}}| = 50\ \mu$T, and pressure shift $\nu_{\mathrm{bg}} = 88$ kHz. The different shades denote different values of $p$ in the initial atomic state $\rho_0 = \rho_1(p)$.

$|2, m\rangle$ are equal. Unlike the $\sigma^+$ transition depicted in Fig. 6.2(b), the $\pi^+$ transition demonstrates significant robustness to variations in $\rho_1(p)$ and shows a relatively uniform response to changes in $\alpha$ as illustrated in Fig. 6.2(c). A similar analysis indicates that both the $\sigma^-$ and $\pi^-$ transitions mirror the qualitative behaviors of their $\sigma^+$ and $\pi^+$ counterparts, respectively. The findings of this analysis emphasize the enhanced resilience of $\pi^{\pm}$ transitions against inaccuracies in the modeling of $\beta_m^{m'}(\alpha)$ due to uncertainties in the atomic state, as also confirmed by our experimental results in Sec. 6.2, in comparison to the $\sigma^{\pm}$ transitions.

## 6.2 Experimental implementation

To implement RANBA, we use the same Rabi oscillation measurements taken over random directions of $\vec{B}_{\rm DC}$ for the vector data in Ch.5. For this data set, each $A_m^{m'}$, corresponding to a random $\vec{B}_{\rm DC}$ direction, is calculated as the average of 10 separate measurements. The Rabi oscillation amplitudes are extracted from fitting parameters $a_3$ and $a_4$ in Eq. (3.30) through $A_m^{m'} = \sqrt{a_3^2 + a_4^2}$. To account for drift in the vapor temperature, which affects the Faraday rotation signal through the atomic density $n_{\rm Rb}$ in Eq. (2.32), we scale each $A_m^{m'}$ measurement according to the relative change of an interspersed Rabi oscillation amplitude evaluated at a consistent $\vec{B}_{\rm DC}$ direction. For this scaling we use the MPE 1 $A_{m=1}^{m'=2}$ measurement at the field direction $(0°, 57.3°)$. This interspersed measurement scaling effectively eliminates noise in the $A_m^{m'}$ data due to this temperature drift [see Fig. 6.3(c)].

Next, we map out the nulling circle by finding the nulling polar angles $\beta_0$ at different azimuthal angles $\alpha$. Todo this we enforce all Rabi oscillation amplitudes $A_m^{m'}$, evaluated at the $\vec{B}_{\rm DC}$ direction $(\alpha, \beta)$, to be negative if $\beta > \pi/2$. The nulling polar angle $\beta_0$ is measured by the zero crossing of $A_m^{m'}$ that is extrapolated from an interpolating polynomial $A_m^{m'} = f_{\rm pol,1}(\beta)$ at each fixed $\alpha$ measurement [see Fig. 6.3(d)]. We call this type of method to measure $\beta_0$ as negative-flipping (NF) detection. A challenge that occured with this analysis is that despite programming a rectangular grid of $(\alpha, \beta)$ field directions for our Rabi measurements, the 'fixed' $\alpha$ values varied slightly for different polar angles due to small corrections from the scalar calibration of our coil system. To account for this, we used another interpolating polynomial to constrain $\alpha = f_{\rm pol,2}(\beta)$, such that the zero-crossing in $A_m^{m'}$ also finds the correct azimuthal angle at the zero-crossing by evaluating $f_{\rm pol,2}(\beta_0)$.

The nulling angles $\beta_0$ obtained using NF detection with the MPE 1 $A_{m=1}^{m'=1}$ data are depicted in Fig. 6.3(a). These measurements are overlayed with a fit of Eq. (6.1) to determine the direction

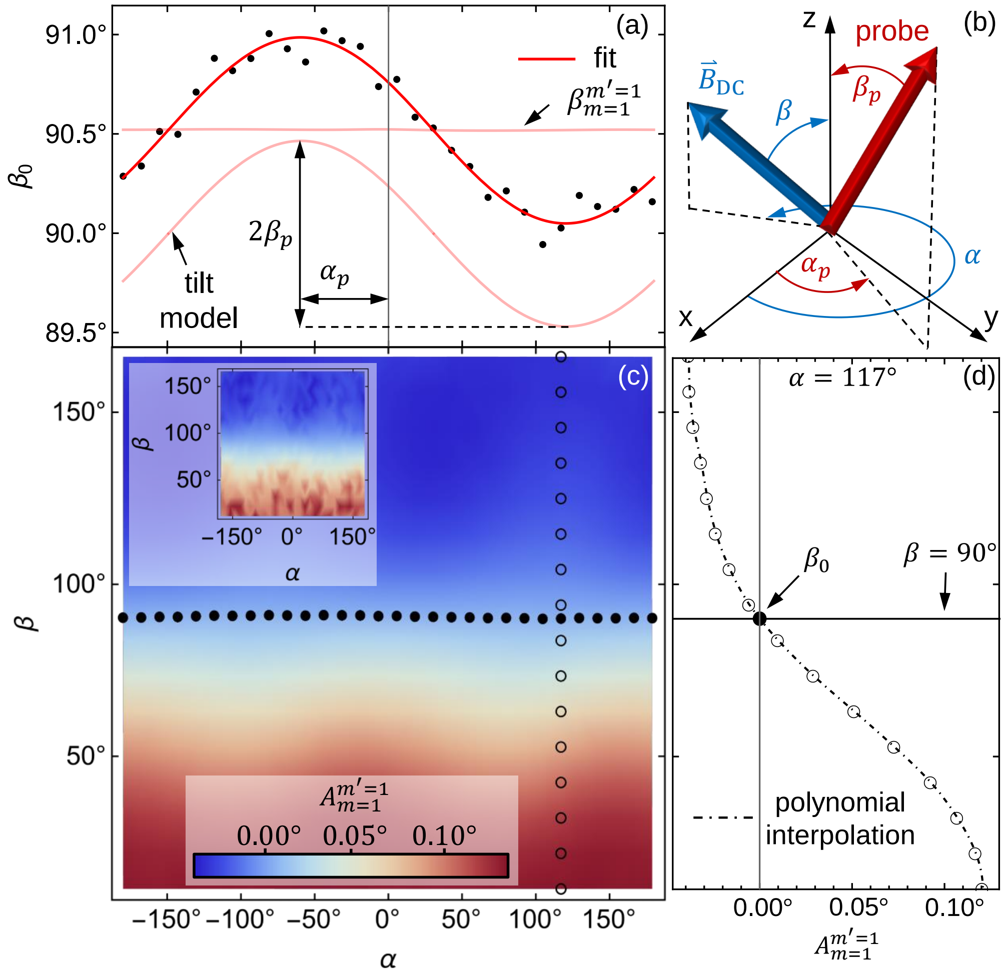


Figure 6.3: (a) The measured nulling polar angle $\beta_0$ at different azimuthal coordinates $\alpha$ in the intrinsic magnetometer frame. Transparent red lines show the tilt model and $\beta_m^{m'}(\alpha)$ components of fitting function given by Eq. (6.1) The direction $(\alpha_p, \beta_p)$ of the probe beam is contained in amplitude $(\beta_p)$ and azimuthal shift $(\alpha_p)$ of the tilt model. (b) Schematic of the magnetic field $\vec{B}_{\rm DC}$ and the probe beam in the intrinsic magnetometer frame. (c) Measured Rabi oscillation amplitude $A_m^{m'}$ of the $\pi^+$ transition. Inset shows the same Rabi amplitudes without rescaling to account for temperature drift of the atomic vapor. Filled black circles mark measured $\beta_0$ with NF detection. The empty black circles mark the data points used to measure $\beta_0$ at $\alpha = 117°$.

of the probe beam $(\alpha_p, \beta_p)$. In Fig. 6.3(a) we also plot the individual contributions of the tilt model and the $\beta_m^{m'}(\alpha)$ components of Eq. (6.1), where $(\alpha_p, \beta_p)$ are extracted from the amplitude and displacement of the sinusoidal shape of the tilt model. The perturbation from off-resonant driving $\beta_m^{m'}(\alpha)$ is calculated from the MPE 1 parameters in Table 5.2, $|\vec{B}_{\rm DC}| = 50\ \mu$T, $\nu_{\rm bg} = 88$ kHz, and $\rho_0 = \rho_1(p = 0)$. Despite there likely being some $F = 2$ population in the true atomic state $\rho_0$, we choose $\rho_0 = \rho_1(p = 0)$ as a rough approximation that appears to match our data well. The small fitted polar angle offset $\beta_{\text{off}} = 0.0025°$ attests to the accuracy of $\beta_m^{m'}(\alpha)$ despite uncertainty in the initial atomic state $\rho_0$.

The measured nulling polar angles $\beta_0$ for the $A_m^{m'}$ data across all three MPEs and all four hyperfine transitions, along with the corresponding fits of Eq. (6.1) are displayed in Fig. 6.4. For these fits, we use the same parameters to model $\beta_m^{m'}(\alpha)$ as stated for the $\pi^+$ case in Fig. 6.3(a), but use the correct MPE parameters in Table 5.2 according to how the Rabi oscillations were driven. Qualitatively, the offsets predicted by $\beta_m^{m'}$, shown as dashed lines in Fig. 6.4, agree will with the $\beta_0$ measurements. Compared to the $\pi^\pm$ transitions, the fitting residuals for the $\sigma^\pm$ data is worse likely from a combination in the uncertainty in $\rho_0$ as well as errors in NF detection discussed in Sec. 6.4. This result is consistent with the sensitvity of the $\sigma^\pm$ transitions to the atomic state observed in the theoretical analysis in Fig. 6.2.

Furthermore unaccounted drift in the MPE parameters and pressure shift throughout the Rabi measurements, as detailed in Ch. 5, adds some additional noise in $\beta_0$ measurements through drifts in $\beta_m^{m'}(\alpha)$. Drift in the MPE parameters is difficult to account for because the Rabi measurements at different $(\alpha, \beta)$ were ordered randomly in time. Thus, the exact MPE parameters and pressure shift $\nu_{\text{bg}}$ at the zero-crossing in Fig. 6.3(d) are not well-defined. Even so the residuals of the measured $\beta_0$ with Eq. (6.1) are close to the shot-noise limit. The standard deviation of $A_m^{m'}$ measurements for a Rabi oscillation lasting 0.85 ms due to detector noise characterized by $\sigma_\theta = 0.0043°$ [Sec. 2.3.2] is $\sigma_A = 0.00023°$ derived by fitting fake data generated from Eq. (3.30) with parameters $a_1 = 0°$, $a_1 = 0.01°$, $a_3 = a_4 = 0.05°$, $t_1 = 1$ ms, and $t_2 = 2$ ms. We estimate the corresponding standard deviation in $\beta_0$ measurements through

$$\sigma_{\beta_0} = \frac{\sigma_A}{\sqrt{10}} \left| \frac{\partial \beta}{\partial f_{\text{pol},1}(\alpha)} \right|^{-1} \Bigg|_{\beta=\pi/2} \tag{6.4}$$

where the $\sqrt{10}$ accounts for average 10 repeated Rabi measurements. For the MPE 1 $\pi^+$ transition data, the average slope of the interpolating polynomial at $\beta = \pi/2$, across different $\alpha$, is given by $\partial f_{\text{pol},1}(\beta)/\partial\beta = 0.0016$, from which Eq. (6.4) predicts $\sigma_{\beta_0} = 0.045°$. This is slightly lower compared

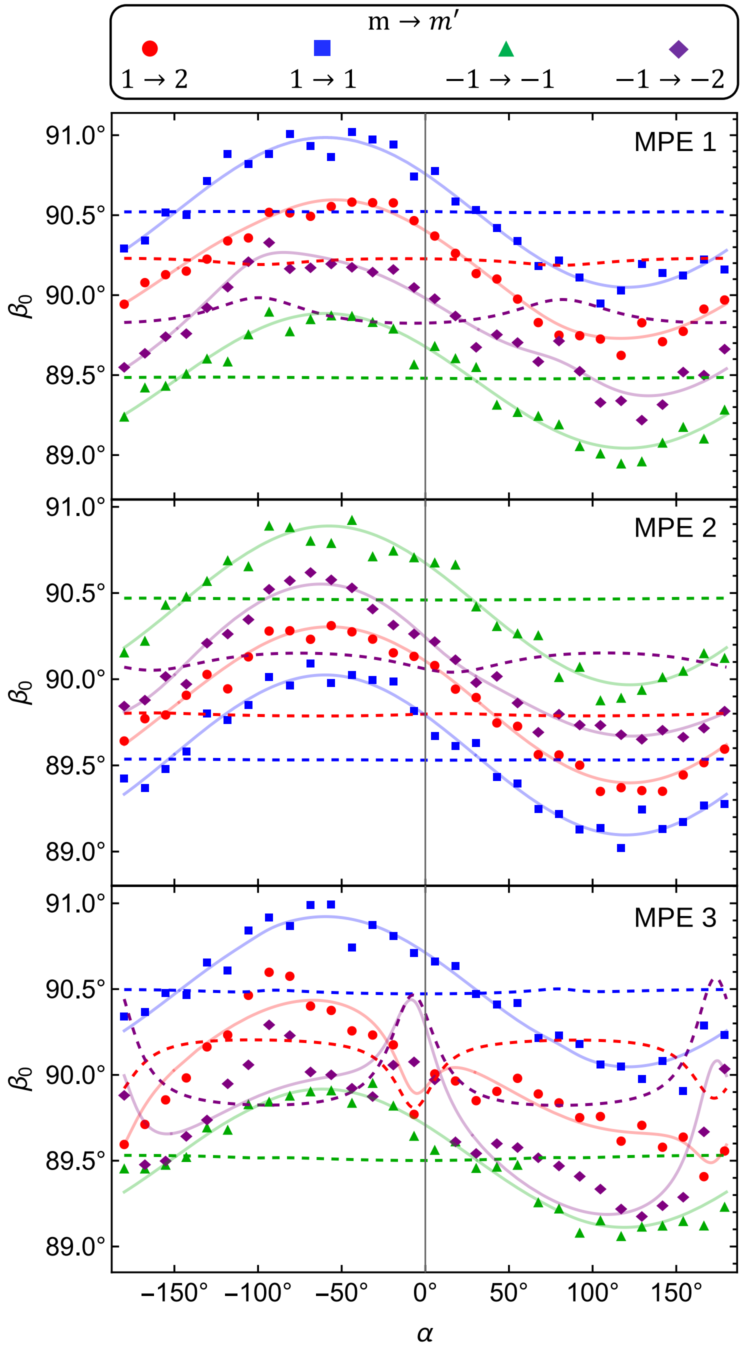


Figure 6.4: Measured $\beta_0$ across different hyperfine transitions for each MPE 1, MPE 2, and MPE 3. The $\beta_m^{m'}(\alpha)$ (dashed lines), calculated apriori using Eq. (6.2), matches well with the different offsets of each transition from 90°. Transparent solid lines are fits of Eq. (6.1).The larger disagreement of the $\sigma^{\pm}$ data in MPE 3 with Eq. (6.1) is predicted to be due to errors in the NF detection of $\beta_0$ as shown in Fig. 6.6.

to the measured $\sigma_{\beta_0} = 0.064°$.

## 6.3 RANBA measurement results

The probe beam attitude predicted by the MPE 1 $\pi^+$ alone, as a specific example, is $(\alpha_p \pm \sigma_{\alpha_p}, \beta_p \pm \sigma_{\beta_p}) = (-59° \pm 4°, -0.47° \pm 0.04°)$ and by the weighted mean of all the Rabi data in Fig. 6.4 is found to be $(\alpha_p \pm \sigma_{\alpha_p}, \beta_p \pm \sigma_{\beta_p}) = (-58.5° \pm 1.2°, -0.440° \pm 0.010°)$ [see Fig. 6.5] with $\sigma_{\alpha_p}$ and $\sigma_{\beta_p}$ denoting 95% confidence error bars. Because $\alpha_p \to \infty$ as $\beta_p \to 0$, $(\alpha_p, \beta_p)$ are not good coordinates for characterizing the overall directional precision. To calculate the overall precision, we follow the same approach used for Rabi vector magnetometry in Sec. 5.4.1. We define

$$\beta'_p = G(\beta_p, \sigma_{\beta_p}) \tag{6.5}$$

$$\alpha'_p = G(\alpha_p, \sigma_{\alpha_p}) \tag{6.6}$$

to be random Gaussian variables of the form $G(\mu, \sigma)$ with mean $\mu$ and standard deviation $\sigma$. We define the rotated probe vector as

$$(p_x, p_y, p_z) = R_y(-\beta_p)R_z(-\alpha_p)(\cos(\alpha'_p)\sin(\beta'_p), \sin(\alpha'_p)\sin(\beta'_p), \cos(\beta'_p)) \tag{6.7}$$

with component standard deviations denoted as $\sigma_{p_j}$ for $j = x, y, z$. Then, the overall angular precision $\delta\psi$ is given by

$$\delta\psi = \arctan\left(\sqrt{\sigma_{p_x}^2 + \sigma_{p_y}^2}\right) = 0.85 \text{ mrad } (0.05°) \tag{6.8}$$

from the MPE 1 $\pi^+$ data alone, and

$$\delta\psi = \arctan\left(\sqrt{\sigma_{p_x}^2 + \sigma_{p_y}^2}\right) = 240\ \mu\text{rad } (0.014°) \tag{6.9}$$

from all of the Rabi data.

## 6.4 Accuracy analysis

Two primary limitations to overall accuracy include: (1) the precision with which $\beta_0$ can be determined, and (2) the accuracy of predicting $\beta_m^{m'}(\alpha)$ given uncertainty in the MPE, the pressure shift $\nu_{\text{bg}}$, the strength of the magnetic field $|\vec{B}_{\text{DC}}|$, and the atomic state $\rho_0$. In this section, we analyze these two types of errors in RANBA for realistic experimental parameters.

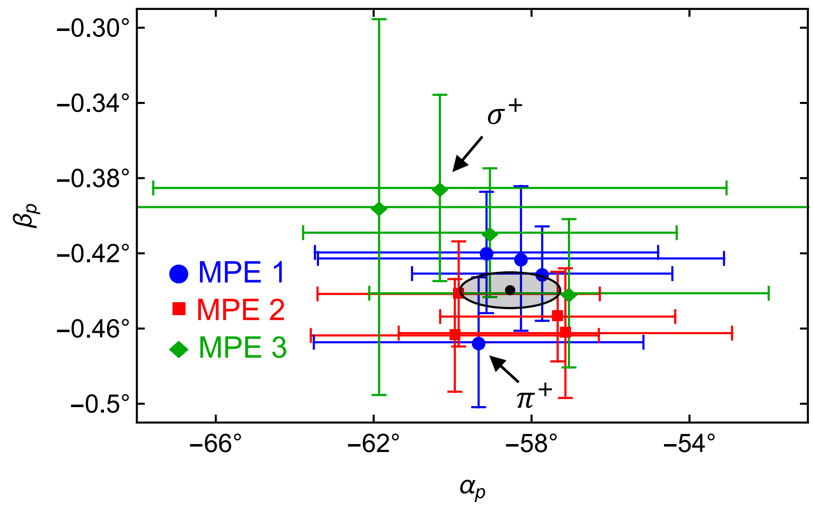


Figure 6.5: Measured probe direction $(\alpha_p, \beta_p)$ across all four hyperfine transitions and three MPEs. The shaded region denotes the weighted mean of all the measurements with 95% confidence. Systematic errors are not included in the confidence intervals.

The primary limitation to how accurately $\beta_0$ can be measured with NF detection, described in Sec. 6.2, is due to the fact that the minimum value of $A_m^{m'}$ is not always zero. A nonzero minimum $A_m^{m'}$ violates the zero-crossing assumption of NF fitting and causes a systematic error. This is exemplified in Fig. 6.6(a) for the $\pi^+$ transition calculated with MPE 1 parameters and the $\sigma^+$ transition calculated with MPE 3 parameters using Eq. (6.2). These calculations assumed the same pressure shift and magnetic field parameters as used in Fig. 6.2 with $\rho_0 = \rho_1(p = 0)$. We also scaled the calculated amplitudes $A_m^{m'} \to A_m^{m'} e^{-\beta/2}$ to give a similar assymetry in the Rabi amplitude for different polar angles as measured in Fig. 6.3(d). Errors in $\beta_0$, i.e. deviations of the zero crossing using NF detection [inset of Fig. 6.6(a)] with the actual location of the minimum value of $A_m^{m'}$ are shown in Fig. 6.6(b). This analysis predicts $\sigma^\pm$ transitions with MPE 3 parameters to have the highest $\beta_0$ errors, which explains the greater discrepancy with the model fits in Fig. 6.4. For $\pi^\pm$ transitons, as exemplified by the $\pi^+$ MPE 1 calculated error in Fig. 6.6(b), shows small $\beta_0$ errors on the order of 100 $\mu$rad (0.006°) due to the fact that the minimum $A_m^{m'}$ always approaches close to zero.

Next, to estimate errors in $\beta_m^{m'}(\alpha)$, we assume MPE parameter errors randomly sampled

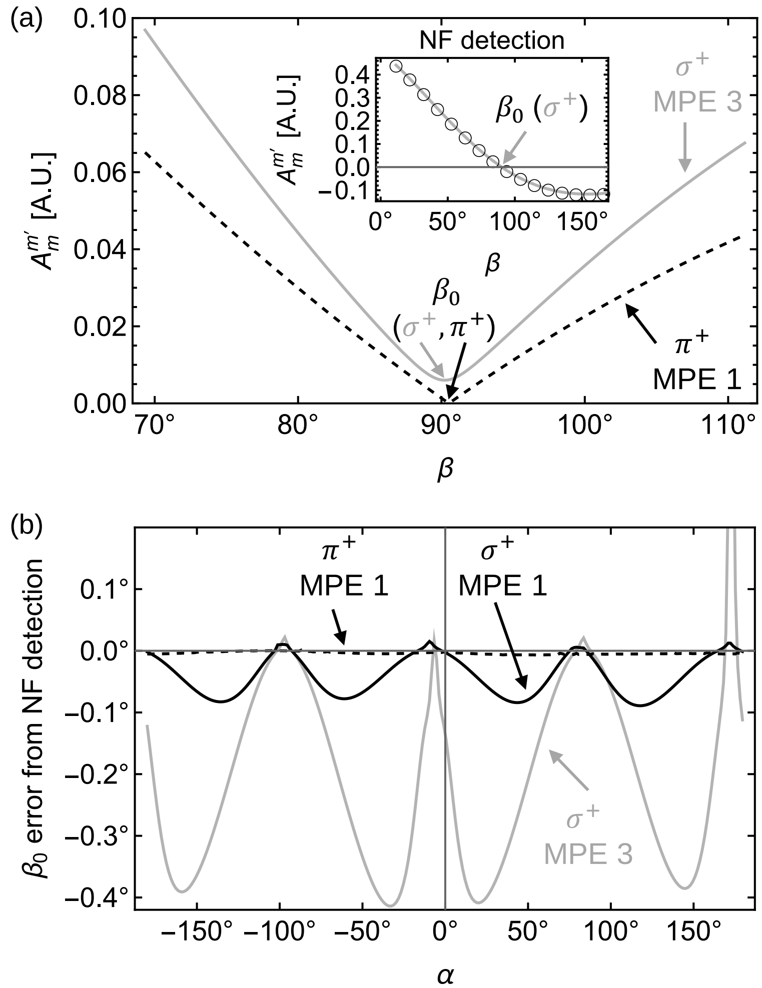


Figure 6.6: Errors in $\beta_0$ measurements using negative-flipping (NF) detection. (a) Calculated Rabi oscillation amplitudes $A_m^{m'}$ as a function of the polar angle $\beta$ for $\sigma^+$ and $\pi^+$ transitions using microwave parameters of MPE 3 and MPE 1 respectively. Due to stronger off-resonant driving for $\sigma^+$ MPE 3, the minimum $A_m^{m'}$ never approaches zero and causes a systematic error in $\beta_0$ using NF detection shown in the inset. (b) Estimated systematic errors of $\beta_0$ from NF detection. We superpose these errors on fake data generated by the tilt model to estimate their effects on $(\alpha_p, \beta_p)$.

within $\mathcal{B}_j \pm 2$ nT and $\phi_j \pm 2$ mrad. These are realistic and conservative error bounds compared to the systematic errors estimated from measured MPE calibration residuals in Sec. 5.2. We also randomly sample pressure shift errors within $\nu_{\text{bg}} = 88$ kHz $\pm 100$ Hz and magnetic field strength errors within $|\vec{B}_{\text{DC}}| = 50\ \mu$T $\pm 10$ nT, which are also realistic given the accuracies reported in Ch. 4. Finally we also randomly sample atomic states within $\rho_0 = \rho_1(p)$ with $p \in (0, 1)$.

To estimate systematic errors in the probe attitude $(\alpha_p, \beta_p)$ we superimpose the simulated $\beta_0$

errors [see Fig. 6.6(b)] and the simulated $\beta_m^{m'}(\alpha)$ errors onto fake data generated by the tilt model in Eq. (6.1) with $\alpha = 74.5°$, $\beta_p = 0.46°$ and $\beta_{\text{off}} = 0$. Errors fitting Eq. (6.1) to this fake data with superimposed errors for the case of $\pi^+$ with MPE 1 parameters and $\sigma^+$ with MPE 3 are reported in Table 6.1. From this analysis we observe that $\beta_0$ errors are the largest systematic, but can be constrained to within 50 $\mu$rad for $\pi^\pm$ Rabi amplitude measurements. These $\beta_0$ errors could in principle be reduced by detecting the actual minimum of $A_m^{m'}$ instead of using NF detection. Direct detection of the minimum of $A_m^{m'}$, however, would require very fine sampling of the Rabi amplitude at different polar angles $\beta$ that could be time intensive. This analysis did not directly take into account errors in $\rho_0$ that depend on the magnetic field direction $(\alpha, \beta)$, however, as shown for the $\pi^+$ transition in Fig. 6.2(b,c), this is expected to have a minimal effect on the $\pi^\pm$ measurements, but not on the $\sigma^\pm$ measuremetns.

Table 6.1: A table of systematic errors arising from NF detection of $\beta_0$ and modeling $\beta_m^{m'}(\alpha)$ for $\pi^+$ MPE 1 and $\sigma^+$ MPE 3 measurements. Errors in NF detection arise from the fact that $A_m^{m'}$ does not quite go to zero from off-resonant microwave driving, and the interpolation polynomial is not accurate to extrapolate $\beta_0$ enough due to a finite number of Rabi amplitude measurements at different $\beta$. Modeling errors in $\beta_m^{m'}(\alpha)$ occur due to errors in the parameters that go into Eq. 6.2.

| Source | $\pi^+$ MPE 1 error [$\mu$rad] | $\sigma^+$ MPE 3 error [$\mu$rad] |
|---|---|---|
| $\beta_0$ NF detection | 40 | 475 |
| $\beta_m^{m'}(\alpha)$ modeling | 4 | 113 |
| **Total** | 44 | 588 |

## 6.5 Design concept to reference to an external coordinate system

To end this chapter, we briefly discuss a design concept using the RANBA technique to reference an intrinsic magnetometer frame to an external lab frame [see Fig. 6.7]. The idea is to make small angular deviations $\delta\theta_p$ of the probe beam that can be measured in both the magnetometer frame and on a camera normally incident to the probe beam. Before the probe reaches the camera, an NPBS splits the probe beam into two orthogonal paths. We let the unperturbed probe beam direction define the x-direction of the lab frame ($x_{\text{lab}}$), and the probe path split by the NPBS define the y-direction of the lab frame ($y_{\mathrm{lab}}$). These two paths uniquely define the lab reference frame. Importantly, the probe angular deviations must be aligned to lie in the plane defined by $x_{\mathrm{lab}}$ and $y_{\mathrm{lab}}$. The camera is then oriented such that one of its two-axis is aligned with $y_{\mathrm{lab}}$. With this design, angular deviations of the probe beam in the intrinsic magnetometer frame ($x_{\mathrm{mag}}$,$y_{\mathrm{mag}}$,$z_{\mathrm{mag}}$), as measured by RANBA, can be translated to the lab frame through the camera measurements. The accuracy of this procedure relies on how well the NBS that splits the probe path and the probe angular deviations are both aligned to be in the same plane.

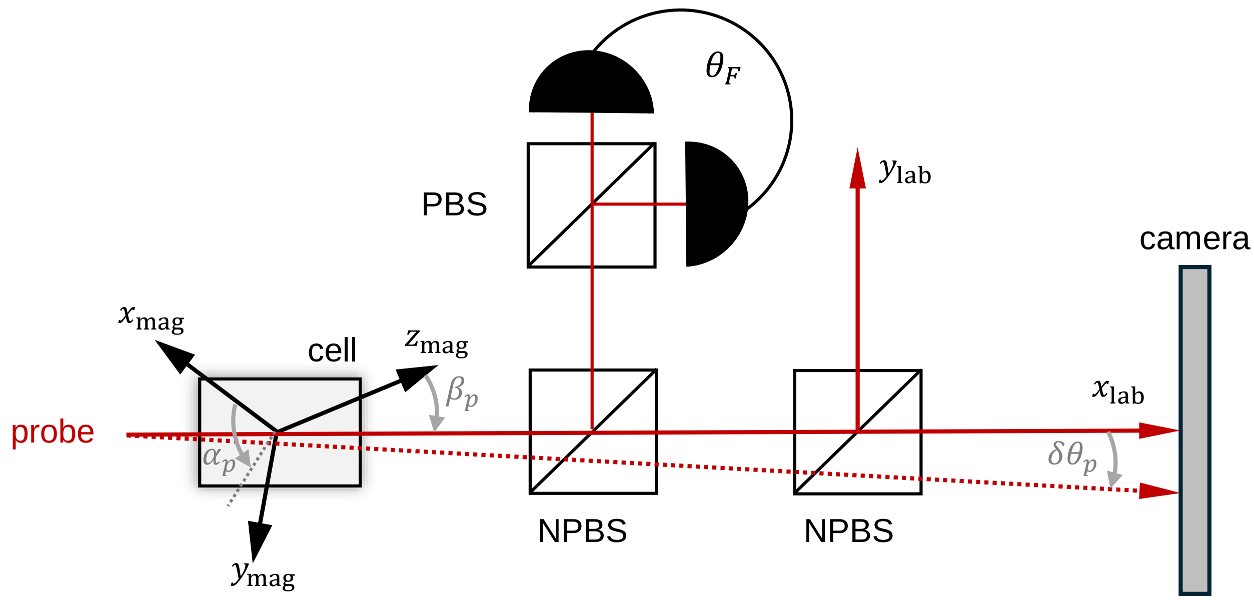


Figure 6.7: A design concept for calibrating to an external reference frame, defined by two laser beams along $x_{\mathrm{lab}}$ and $y_{\mathrm{lab}}$, using RANBA. Here angular deviations $\delta\theta_p$ of the probe beam, within the plane defined by $x_{\mathrm{lab}}$ and $y_{\mathrm{lab}}$, are detected on a camera. The camera screen is aligned to be orthogonal to $x_{\mathrm{lab}}$ but parallel to $y_{\mathrm{lab}}$.

# Chapter 7

# Conclusion

This thesis presented experimental results that push the boundary for accurate Rabi measurements in vapor cell platforms, and demonstrated their application towards accurate scalar and vector atomic magnetometry. An essential step towards this pursuit was proper modeling of Rabi oscillation frequencies in Ch. 3 that accounts for off-resonant microwave driving not fully accounted for in previous Rabi vapor cell experiments. Additionally, Ch. 3 delved into modeling the coherence and atomic population dynamics in hyperfine Rabi oscillations due to spin-exchange collisions in the strong-driving limit, which was important for our understanding of Rabi oscillation coherence. Using our model, we were able to link observed Rabi coherence and population dynamics across multiple hyperfine transitions with vapor parameters such as temperature, buffer gas pressure, and optically pumped spin polarization that aligned well with independent characterizations.

To validate the accuracy of our Rabi measurements, in Ch. 4 we conducted a comparative analysis between a standard OPM free induction decay (FID) measurement and magnetic field strength measurements using Rabi and Ramsey frequency spectroscopy. The agreement among Rabi measurements with multiple MPEs and Ramsey measurements, supported by simulation results, indicated that scalar magnetometry with Rabi measurements achieved an accuracy of 0.6 nT. This represents an almost tenfold increase in accuracy compared to the 5 nT accuracy of FID measurements.

In Ch. 5, we applied Rabi oscillations measurements towards vector magnetometry demonstrating sub-mrad accuracy in 50 $\mu$T fields and sensitivities reaching down to 10 $\mu\mathrm{rad}/\sqrt{\mathrm{Hz}}$. In this approach, extracting the $\vec{B}_{\text{DC}}$-direction $(\alpha, \beta)$ necessitates at least two generalized Rabi frequency measurements $\tilde{\Omega}_m^{m'}$ corresponding to two independent spherical microwave components $\mathcal{B}_k^{(\alpha,\beta)}$. Yet, the field direction derived from just two Rabi measurements can lack uniqueness and may not be as responsive to the magnetic field's orientation at certain DC field directions. To address these issues, we conducted Rabi rate measurements across four hyperfine transitions using three distinct MPEs. Among these four hyperfine transitions, two were $\pi$ transitions, selected for their symmetry within the $^{87}$Rb hyperfine structure, despite both measuring the same $\mathcal{B}_\pi^{(\alpha,\beta)}$. These additional measurements enhanced our vector sensitivity across all DC magnetic field orientations and allowed for the precise determination of a unique $(\alpha, \beta)$. Furthermore, we were able to detect drifts in MPE parameters as well as in the vector magnetic field through these Rabi rates that were consistent with drift identified in running MPE calibrations. We also demonstrated how to mitigate the Rabi probing deadzone associated with our single optical axis by extracting Rabi frequencies from the resonances occurring during simultaneous spin precession and Rabi driving (SPaR).

Several potential systematic errors were identified, whose sizes were consistent with our vector accuracy, and could be improved upon in future implementations. While the accuracy of these measurements are currently not near the 10 $\mu$rad level of modern high accuracy atomic magnetometers based on coil modulations [66], they achieved better performance compared to several other vector OPM techniques, and may reach this high accuracy level with improvement of the systematic sources identified in Ch. 5. The ultimate accuracy of the MPE calibrations is set by the calibration process itself, in which a coil system served as the reference. The ability to program magnetic field orientations with an accuracy of 50 $\mu$rad defines the highest level of accuracy achievable in these calibrations.

Finally, in Ch. 6 we demonstrated the RANBA technique to measure the attitude of our probe beam with respect to the intrinsic magnetometer frame defined by our coil system. As shown in Fig. 6.1, this technique could be useful for calibrating a vector gradiometer or monitoring the overall drift in the intrinsic magnetometer frame. By finding the 'nulling circles' where the Rabi oscillation signals disappear, using same Rabi measurements discussed in Ch. 5, we measured the probe attitude to be $(\alpha_p, \beta_p) = (-58.5°, -0.440°)$ with an overall precision of 0.014° (95 % confidence). From a theoretical analysis of the errors associated with finding the nulling polar angles $\beta_0$ and the variability of the RANBA signals to deviations in the microwave field, magnetic field strength, pressure shift, and the atomic state, we estimated that the accuracy of RANBA is within 50 $\mu$rad (0.003°) using $\pi$ hyperfine transitions under realistic experimental conditions. With small angular deviations of the probe beam and careful optical alignment of a camera, RANBA could be used to calibrate the intrinsic magnetometer frame to an external lab frame [see Fig. 6.7].

In this final chapter, I review some of the future work and extensions of the Rabi measurement techniques discussed in the previous chapters. Much of this is geared towards extending the 2D polarization ellipse control to full 3D control. This extension would enable enhanced vector sensitivity, increased robustness with identifying a unique magnetic field vector, and enable the possibility to recalibrate drifts in the microwave parameters without rotating a DC bias field. We first discuss the possibility of miniaturizing the microwave source using a dielectric resonator for a more practical implementation Rabi magnetometry. Next, we discuss generalizing the microwave drive to a radio frequency drive to measure Rabi oscillations between Zeeman transitions. We also discuss ideas to use RF field excitations to achieve vector recalibration without sensor rotations and DC field rotations. Finally we discuss the possibility to compare microwave calibrations to Rydberg EIT measurements to extract the full electromagnetic field.

## 7.1 Rabi magnetometry using a microwave dielectric resonator

In our experiment, a notable constraint is the calibration speed of our microwave fields, which is significantly limited by the dead time needed for Eddy currents to dissipate after altering the magnetic field direction, and the time required for electrical heaters attached to the cavity to maintain a vapor cell temperature around 100°C. Furthermore, the considerable size and weight of our cavity restrict its utility in creating a compact sensor. A potential solution to these issues could be the adoption of a microwave dielectric resonator (DR). Dielectric resonators have widely been used for microwave delivery in spin resonance experiments for enhancement of the microwave excitation field and to explore spin-cavity coupling dynamics [14]. Nitrogen vacancy (NV) center experiments have employed microwave DRs for fast control of spin qubits as well as the availability of low loss dielectric materials compatible with cryogenic temperatures [174]. In microfabricated vapor cell platforms, compact microwave delivery has been explored in the design of atomic clocks that have utilized non-resonant strip lines and micro coupling loops [34], as well as a microloop-gap resonator [178]. Typically, these resonators are engineered to efficiently generate either linear or circularly polarized microwave fields.

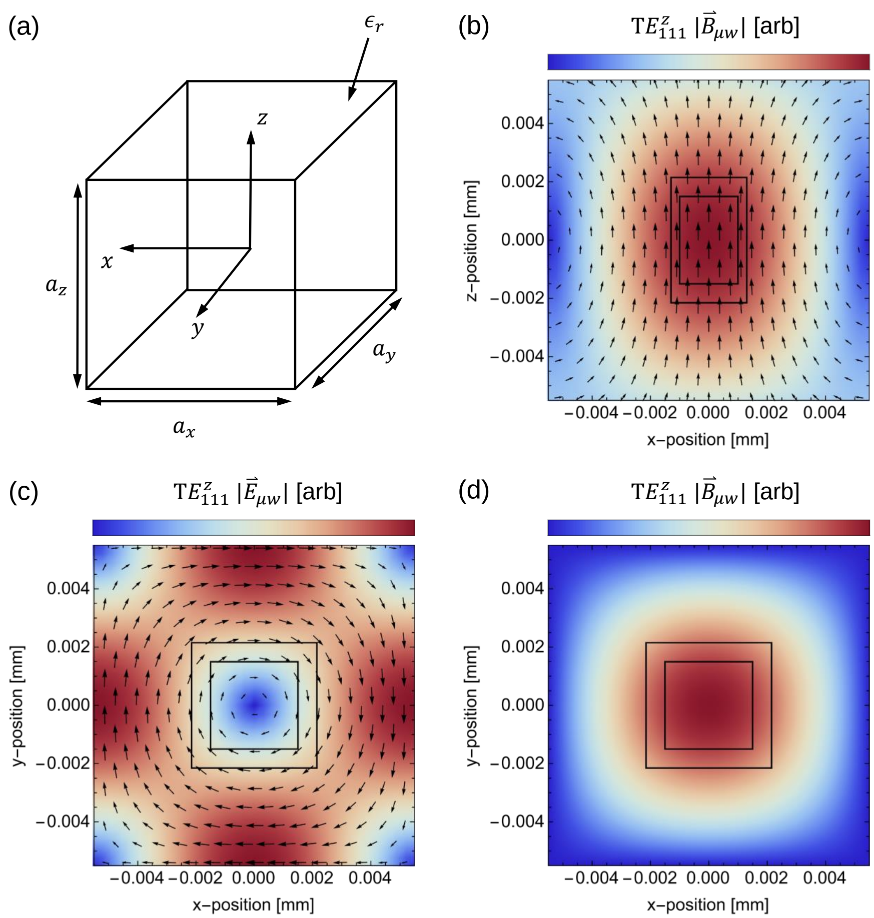


Figure 7.1: (a) Rectangular dielectric resonator schematic with dimensions $a_x$, $a_y$, and $a_z$. (b) The magnetic component of the $\text{TE}^z_{1,1,1}$ mode in the xz-plane positioned at $y = 0$. (c,d) The electric and magnetic field distributions in a xy-plane positioned at $z = 0$.

In contrast to previous resonator implementations that were designed for the efficient production of either linear or circular polarized microwave polarization, in Rabi magnetometry it is beneficial to have full 3D control of the microwave polarization ellipse [Sec. 5.7]. To create a DR with 3D control of the microwave polarization, we have started exploring a symmetric dielectric resonator cube design [see Fig. 7.1(a)]. The modes of a rectangular DR can be derived as the same modes of an infinite dielectric waveguide with the same traverse geometry as the dielectric resonator [128]. Within the resonator, the field patterns in the transverse x and y-directions resemble standing waves, akin to cavity modes, whereas the fields outside the resonator decay (evanescently) along these transverse directions. Truncation along the z-direction also gives rise to similar standing waveguide modes that also evanescently decay outside the resonator. Like waveguide and cavity modes, dielectric resonator modes can be classified as transverse magnetic (TM) or transverse electric (TE). The lowest order modes of a rectangular dielectric resonator are the $\mathrm{TE}^{j}_{1,1,1}$ modes with $j = x, y, z$. Here $j$ is the propagation direction of a phenomenological infinite waveguide with transverse directions the same as the dielectric resonator. For the case of $\mathrm{TE}^{z}_{1,1,1}$ these modes are characterized by [127]

$$Ex = k_y A\cos(k_x x)\sin(k_y y)\cos(k_z z) \tag{7.1}$$

$$E_y = -k_x A\sin(k_x x)\cos(k_y y)\cos(k_z z) \tag{7.2}$$

$$E_z = 0 \tag{7.3}$$

$$B_x = \frac{k_x k_z}{j\omega} A\sin(k_x x)\cos(k_y y)\sin(k_z z) \tag{7.4}$$

$$B_y = \frac{k_y k_z}{j\omega} A\cos(k_x x)\sin(k_y y)\sin(k_z z) \tag{7.5}$$

$$B_z = \frac{k_x^2 + k_y^2}{j\omega} A\cos(k_x x)\cos(k_y y)\cos(k_z z) \tag{7.6}$$

where $A$ is an arbitrary constant and $k_x = \pi/a_x$ and $k_y = \pi/a_y$ by enforcing the $\vec{E} \cdot \hat{n}$ at the transverse surfaces of the resonator. The z-wave number $k_z$ is given by the transcendental equation

$$k_z \tan(k_z a_z/2) = \sqrt{(\epsilon_r - 1)k_0^2 - k_z^2} \tag{7.7}$$

and

$$k_x^2 + k_y^2 + k_z^2 = \epsilon_r k_0^2. \tag{7.8}$$

The mm-scale of microfabricated vapor cells, that would sit inside the DR, constrains how large the dielectric constant $\epsilon_r$ can be while maintaining the resonant frequencies of the DR modes near the microwave transitions of $^{87}$Rb (6.8 GHz). Currently we are testing an alumina resonator with $\epsilon_r = 9.8$. The modes for the $\mathrm{TE}^z_{1,1,1}$ of an alumina resonator with dimensions $a_x = a_y = a_z = 1.1$ cm is shown in Fig. 7.1(b-d). The resonant frequency of these modes are calculated from Eq. (7.7) and Eq. (7.8) to be $f_0 = ck_0/2\pi = 6.8548$ GHz.

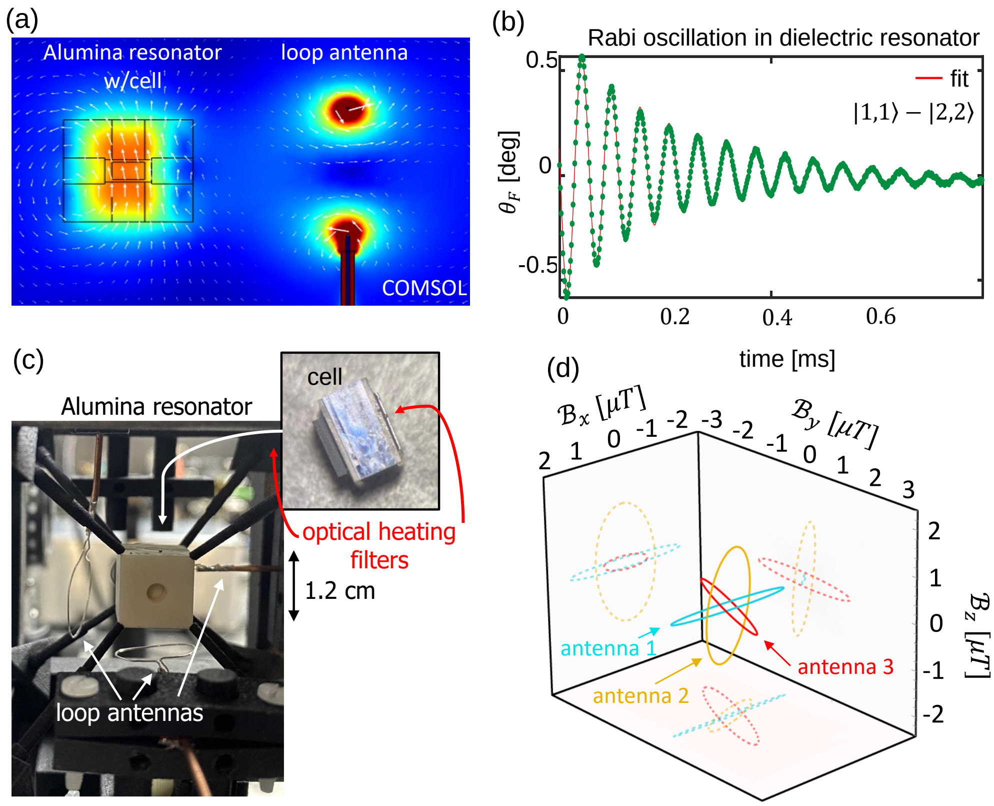


Figure 7.2: Design and implementation of an alumina dielectric resonator. (a) COMSOL simulation of exciting the $\mathrm{TE}^j_{1,1,1}$ modes. The arrow (white) and color scale show the orientation and strength of the magnetic components of the microwave field. Despite the cell and holes drilled into the resonator, uniform microwave excitation is still observed. (b) A $\sigma^+$ Rabi oscillation measured with the alumina resonator shown in (c). (c) Physical implementation of the alumina resonator with three orthogonally oriented loop antennas to excite the resonator modes. (d) MPE calibrations of the microwave fields produced by individual excitations of the three orthogonal loop antennas.

From COMSOL simulations we found that a loop antenna is the most efficient way to couple microwaves into these resonator modes [see Fig. 7.2(a)]. To optically access a cell contained inside requires holes drilled intot he resonator. We consider 3 mm holes drilled on all faces to maintain symmetry in the resonator modes. A COMSOL simulation featuring an alumina resonator encompassing the MEMS cell, optical access holes, and dimensions of 1.2 cm demonstrates efficient coupling to resonator modes, which are slightly perturbed by the presence of the cell and holes [see Fig. 7.2(a)]. We have further verified with COMSOL simulations that all 3 orthogonally oriented loop antennas can be used to individually excite these $\mathrm{TE}^{j}_{1,1,1}$ modes for 3D control of the microwave field.

In [see Fig. 7.2(c)], we show a physical implementation of the alumina resonator-loop antenna design. This setup was assembled and characterized by Thanmay Menon, who took the Rabi and MPE measurements in [see Fig. 7.2(b,d)]. To heat the cell, RG9 neutral density filters are positioned on both the front and back sides of the cell. These filters are specifically designed to uniformly heat the cell by absorbing a 1550 nm laser, yet remain transparent to the 780 nm and 795 nm wavelengths. The thicknesses of the front and back filters, selected to ensure equal optical power absorption by both, are 1 mm and 0.2 mm, respectively. In initial implementations, we found the heating uniformity to be very important for maintaining a uniform buffer gas pressure shift $\nu_{\mathrm{bg}}$ across the vapor cell. An example of a typical $\sigma^+$ ($|1,1\rangle - |2,2\rangle$) Rabi oscillation driven with the alumina resonator is displayed Fig. 7.2(b). The Rabi $T_2$ times were approximately twice as poor compared to those of Rabi oscillations induced within the microwave cavity for frequencies above 50 kHz. This decrease in performance was attributed to microwave inhomogeneity, which resulted from the smaller mode size and the imperfect design and positioning of the loop antennas. By performing MPE calibrations from $\sigma^+$ Rabi oscillations we have been able to verify excitation of microwave field with polarization ellipses spanning in 3D [see Fig. 7.2(d)]. These preliminary findings highlight the potential of using a dielectric resonator as a compact and lightweight microwave source for Rabi magnetometry This approach offers complete 3D microwave control without the limitations of Eddy current and the heating wait times associated with metal cavities.

## 7.2 Generalizing Rabi magnetometry to other types of driving fields and atomic transitions

Adapting the Rabi magnetometry techniques from microwave-driven hyperfine transitions to alternate driving fields and atomic configurations may provide substantial benefits. In this section we first discuss the potential advantages and work underway to implement Rabi magnetometry with a radio-frequency (RF) field to couple Zeeman transitions within each hyperfine manifold of $^{87}$Rb. We also discuss the possibility for an all-optical Rabi magnetometer utilizing two-photon Raman transitions.

### 7.2.1 Rabi magnetometry with radio-frequency (RF) fields

For geomagnetic fields ($B \approx 50$ $\mu$T) radio-frequency fields with frequency $\nu_{\rm rf} \approx 350$ kHz can drive either $\sigma^+$ ($F = 2$) and $\sigma^-$ ($F = 1$) Rabi oscillations between the Zeeman transitions within a hyperfine manifold [see Fig. 7.3(a)]. In this scheme, precise calibration of a 3D RF coil system, which can generate arbitrary RF polarization ellipses, acts as a vector reference to measure the response of Rabi frequencies to the orientation of a DC magnetic field. Physical implementation of a 3D RF coil system employing the same dielectric resonator described in Sec. 7.1 to house the vapor cell is depicted in Fig. 7.4. This arrangement allows for the convenience of a single setup to study Rabi measurements using either a microwave DR or an RF field. The diameters of the x, y, and z coil pairs are $D_x = 102.5$ mm, $D_y = 69.5$ mm, and $D_z = 83.5$ mm, each comprising around 40 wire turns. The design of the coils ensures they are non-resonant at the RF frequency $\nu_{\rm rf} \approx 350$ kHz. Assembly and characterization of Rabi oscillations, displayed in Fig. 7.3(b), in this RF coil system were done by Thanmay Menon.

Although this method uses a coil system as a vector reference, it offers a distinct advantage over conventional vector OPMs that utilize coil modulations. The key benefit is that RF Rabi oscillation involves resonant interaction, making the magnetic field sensitivity independent of the DC magnetic field's strength. This also allows for the rotation of RF fields, similar to scalar cali-

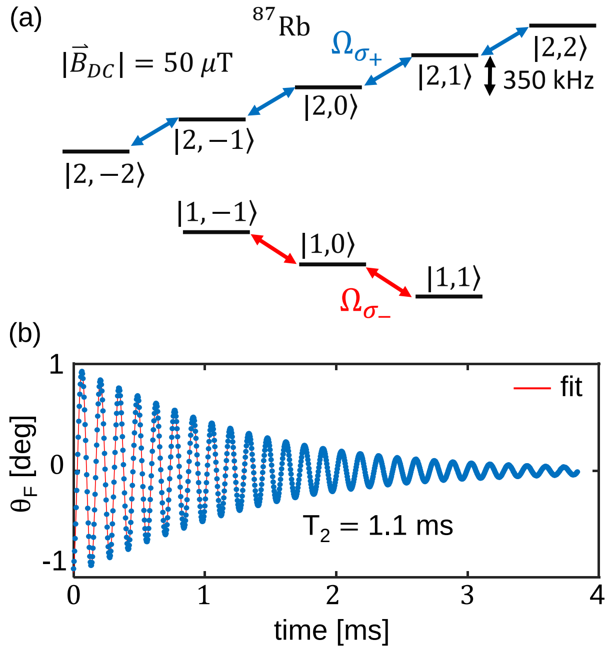


Figure 7.3: RF Rabi oscillation. (a) $^{87}$Rb energy level diagram highlighting the Zeeman transitions (double-sided arrow) that are driven by a radio-frequency magnetic field. Only $\sigma^+$ and $\sigma^-$ single photon transitions are allowed. (b) A RF Rabi oscillation measured in the apparatus shown in Fig. 7.4. We observe coherence times $T_2 \approx 1$ ms.

bration [ 2.4.1], for calibrating coil parameters. In Sec. 7.3, we discuss a method of algorithmically recalibrating coil system parameters not by rotating the DC magnetic field, but through RF coil excitations. In contrast, coil modulations with frequencies within a few kHz and minimal modulation depths are unable to recalibrate coil system parameters without increasing sensor complexity by rotating either the sensor or the DC magnetic field. We reiterate from Ch. 5 that in many cases weak modulation fields in vector OPMs are necessary due to power requirements, prevention of coupling to external objects, and slew-rate limitations of coil feedback electronics [198]. By employing RF coil excitations for rapid recalibration of coil parameters Sec. 7.3, it's conceivable to compensate for coil system drifts on a 50 ms timescale, thereby reducing the stability time-scale requirements for the coil system.

RF Rabi magnetometry, as opposed to the microwave Rabi magnetometry explored in this thesis, offers several benefits, which are enumerated here:

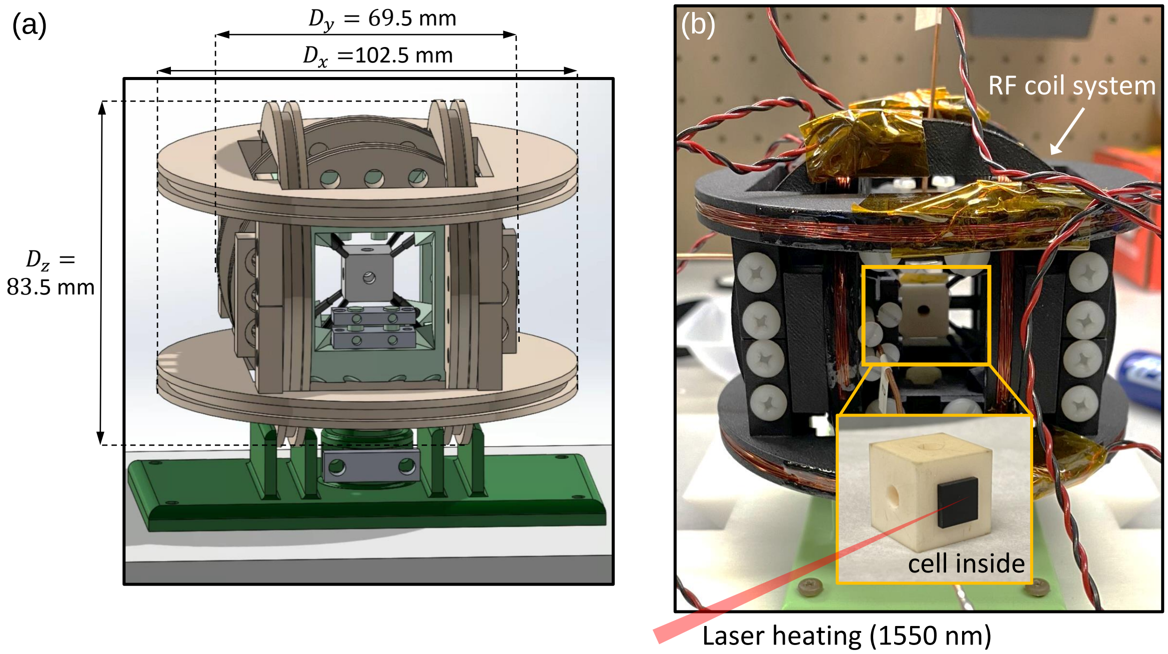


Figure 7.4: 3D RF coil system used for 3D control of RF fields. The microfabricated vapor cell is housed in a laser heated dielectric resonator. This is partially for convenience, but also enables us to explore dual microwave+RF interrogation.

- Radio-frequency fields, such as at $\nu_{\mathrm{rf}} = 350$ kHz for magnetic fields around 50 $\mu$T, are already employed in numerous OPM configurations. Consequently, integrating Rabi magnetometry using RF fields would align more seamlessly with existing commercial OPM design practices.

- RF Rabi oscillations have superior dephasing properties from spin-exchange collisions than Rabi oscillations driven between hyperfine transitions 7.3(b). This is because RF Rabi oscillations are Larmor preccesion in a rotating-frame picture. As discussed in Ch. 3, Larmor precession is more robust against dephasing from spin-exchange collisions than microwave-driven Rabi oscillations.

- RF fields generated by coil systems are expected to have better spatial homogeneity across the vapor cell due to the larger effective wavelength, and the fact that there are no standing waves involved.

- An RF coil system is likely a more stable reference since it is decoupled from the heating of the vapor cell.
- Since RF coil pairs individually generate linearly polarized fields, the RF polarization ellipses are easier to interpret. This may be beneficial for utilizing Rabi oscillation to compensate drifts with recalibration with DC field rotations. Conversely, the frequency dependence of microwave cavity modes and disturbances from the coupling pins pose challenges for implementing vector recalibration algorithms, such as that detailed in Sec. 7.3.

There are a few challenges to accurately modeling RF Rabi oscillations. One challenge is that RF Rabi oscillations suffer from the same nonlinear Zeeman (NLZ) shifts that cause systematic errors in scalar OPMs discussed in Ch. 4. The NLZ shifts give each Zeeman transition in Fig. 7.3(a) a different splitting. For example, at $B_{\mathrm{DC}} = 50\ \mu\mathrm{T}$ the Zeeman transition $|2,2\rangle - |2,1\rangle$ differs from the transition resonance $|2,1\rangle - |2,0\rangle$ by about 37 Hz as calculated from the Breit-Rabi formula [Eq. (3.11)]. As discussed in Ch. 4, the Zeeman transitions between the $F = 1, 2$ manifolds differ by 1.4 kHz at 50 $\mu$T. By tailoring RF polarization ellipses it should be possible to have $\Omega_{\sigma^+} \neq \Omega_{\sigma^-}$ such that you can differentiate driving between these two manifolds. Without precise knowledge of the initial atomic state, it is uncertain which frequency component from these Zeeman transitions contribute to the RF Rabi signal. Incorporating microwave interrogation may help with these challenges. For example, it has been demonstrated that microwave and RF excitation together can be used to map out the full atomic ground state [166].

Another challenge concerns the inaccuracy of the rotating-wave approximation (RWA) for RF Rabi oscillations. One metric that characterizes this is the Bloch-Siegert shift calculated in Sec. 5.6.4 to be about 0.1 Hz for a microwave-driven Rabi frequency of $\Omega = 50$ kHz. This estimated Bloch-Siegert shift for an RF Rabi oscillation is much larger at 1.8 kHz for a 50 kHz Rabi frequency and $B_{\mathrm{DC}} = 50\ \mu\mathrm{T}$ Zeeman splitting. Exact spin dynamics beyond the RWA, however, can be simulated fairly easily for an RF driving field compared to a microwave driving field. Reference to such a model could be useful for compensating beyond RWA effects. Furthermore, there are several perturbative methods to correct model time-dependent Hamiltonians beyond the RWA [63, 163, 195]. Exploration of how to mitigate these challenges is currently under investigation.

Two-photon Rabi oscillations within an RF system would also be interesting to explore [63, 112]. Such measurements have been demonstrated for induction imaging [118]. These could be used to measure the $\mathcal{B}_\pi$ component of the RF microwave field to gain additional information for vector sensing. Furthermore, if spin dynamics in the $F = 1$ manifold can be isolated, two-photon Rabi oscillations could be used to probe the magnetic resonance of that manifold without heading error from NLZ shifts. Such coherent control from both RF and microwave field could also be used to create and detect higher order atomic polarization moments not easily seen in high buffer gas pressure cells [191].

### 7.2.2 Potential for an all-optical Rabi magnetometer

Another interesting configuration to explore for Rabi magnetometry are Rabi oscillations from optical two-photon Raman transitions that could drive either hyperfine or Zeeman transitions [64, 114]. To our knowledge, there is little work on driving Rabi oscillations of such transitions in a vapor cell platform [85]. Exploring this case in future research is promising, given the appeal of all-optical detection. Its potential for integration into a compact sensor package, along with its inability to cause cross-talk with nearby sensors or instruments, makes it particularly attractive. Furthermore, laser beams are more easily referenced to other sensors, e.g. star trackers, than magnetic coils. Hence, the magnetometer reference frame, defined with respect to the Raman beams, would be more easily referenced to other sensors and mechanical objects. A possible complication of this approach is the difficulty in modeling the optical polarization ellipse of the Raman beams due to Faraday rotation and absorption effects.

## 7.3 Vector recalibration using RF Rabi magnetometry without $\vec{B}_{\text{DC}}$ field rotations

An intriguing possibility to explore that is motivated by the drift observable derived from microwave-driven Rabi oscillations in Ch. 5, is to recalibrate polarization ellipse parameters without requiring manual rotations of the DC magnetic field or of the sensor itself. Sensor rotations for calibration are not ideal due to mechanical complexity, limited rotation speeds, and likely have accuracy limits related to mechanical repeatability. Calibration of coil parameters through DC magnetic field rotations, with field strengths on the scale of 100 $\mu$T, are not ideal for geomagnetic applications that require low power consumption. Furthermore, weak magnetic field modulations are often required to prevent coupling to external objects, and slew-rate limitations of coil feedback electronics [198]. A new approach would be to use resonant interactions, such as Rabi oscillations. In this scenario coil system parameters are calibrated from Rabi rates that measure an electromagnetic field component, produced by AC coil excitations. This strategy avoids the necessity of using large coil fields to neutralize background DC magnetic fields, leading to lower power usage and coupling to external objects. Furthermore such calibrations, being electronically controlled, could be done quickly to minimize downtime of vector measurements.

In this section, we detail an algorithmic approach for calibrating a 3D RF coil system exclusively using Rabi measurements. The RF coil system is characterized by three pairs of coils that are nearly orthogonal, generating RF fields in directions $(\vec{x}_c, \vec{y}_c, \vec{z}_c)$ with coil currents expressed as

$$I_x(t) = I_x \cos(\omega_{RF} t + \phi_x), \tag{7.9}$$

$$I_y(t) = I_y \cos(\omega_{RF} t + \phi_y), \tag{7.10}$$

$$I_z(t) = I_z \cos(\omega_{RF} t), \tag{7.11}$$

where, we set $\phi_z = 0$ without loss of generality. In a rotating-frame, where fast-rotating terms oscillating at $2\omega_{RF}$ are dropped, the RF currents are expressed as

$$\tilde{I}_x = I_x e^{-i\phi_x} \tag{7.12}$$

$$\tilde{I}_y = I_y e^{-i\phi_y} \tag{7.13}$$

$$\tilde{I}_z = I_z. \tag{7.14}$$

In terms of coil coefficients $(a_x, a_y, a_z)$, the corresponding RF magnetic field components $\vec{\mathcal{B}}_{k,c}$ along each coil pair are given by

$$\vec{\mathcal{B}}_{x,c} = \tilde{I}_x a_x \vec{x}_c \tag{7.15}$$

$$\vec{\mathcal{B}}_{y,c} = \tilde{I}_y a_y \vec{y}_c \tag{7.16}$$

$$\vec{\mathcal{B}}_{z,c} = \tilde{I}_z a_z \vec{z}_c. \tag{7.17}$$

We express the non-orthogonal coil frame within an orthogonal lab frame $\mathcal{L} = (x, y, z)$ by the transformation

$$\vec{x}_c = R_y(\pi/2 + \delta\theta_x)\hat{z} = \{\cos[\delta\theta_x], 0, -\sin[\delta\theta_x]\} \tag{7.18}$$

$$\vec{y}_c = R_z(\pi/2 + \delta\phi_y)R_y(\pi/2 + \delta\theta_y)\hat{z} = \{-\cos[\delta\theta_y]\sin[\delta\phi_y], \cos[\delta\theta_y]\cos[\phi_y], -\sin[\delta\theta_y]\} \tag{7.19}$$

$$\vec{z}_c = \hat{z} = \{0, 0, 1\} \tag{7.20}$$

where $(\delta\theta_x, \delta\theta_y\delta\phi_y)$ are non-orthogonality angles. The total RF field expressed in the orthogonal coordinate system $(\vec{\mathcal{B}}_x, \vec{\mathcal{B}}_y, \vec{\mathcal{B}}_z)$ is given by

$$\vec{\mathcal{B}} = \Big\{ \sum_{k=x,y,z} \vec{B}_{k,c} \cdot \hat{x}, \sum_{k=x,y,z} \vec{B}_{k,c} \cdot \hat{y}, \sum_{k=x,y,z} \vec{B}_{k,c} \cdot \hat{z} \Big\} \tag{7.21}$$

Let $\vec{B}_{\mathrm{DC}}$ be a DC magnetic field that points in the $(\alpha, \beta)$ direction in the $\mathcal{L}$ orthogonal coordinate frame. We define an atom-frame $\mathcal{A} = (x_a, y_a, z_a)$ such that the $z_a$-direction is aligned with the $\vec{B}_{\mathrm{DC}}$ direction $(\alpha, \beta)$ in the lab frame $\mathcal{L}$. The RF phasor $\vec{\mathcal{B}}$ is defined in $\mathcal{A}$ as

$$\vec{\mathcal{B}}^{(\alpha,\beta)} = R_y(-\beta)R_z(-\alpha)\vec{\mathcal{B}} \tag{7.22}$$

where $R_y$ and $R_z$ are rotation matrices about the $\hat{y}$ and $\hat{z}$ directions respectively defined in the lab frame $\mathcal{L}$. We define complex spherical basis vectors in the $\mathcal{A}$ frame as

$$\hat{e_{\sigma^\pm}} = \{1, \mp i, 0\}/\sqrt{2} \tag{7.23}$$

$$\hat{e_\pi} = \{0, 0, 1\}. \tag{7.24}$$

The $\sigma^\pm$ Rabi rates driven by the RF field in the $F = 2$ and $F = 1$ hyperfine manifolds are given by

$$\Omega_{\sigma^+} \approx \mu_B g_{F=2} |\vec{\mathcal{B}}^{\alpha,\beta} \cdot \hat{e}_{\sigma^+}| \tag{7.25}$$

$$\Omega_{\sigma^-} \approx \mu_B g_{F=1} |\vec{\mathcal{B}}^{\alpha,\beta} \cdot \hat{e}_{\sigma^-}| \tag{7.26}$$

where $\mu_B$ is the Bohr magneton and $g_F$ is the hyperfine Landé g-factor. These formulas are approximations as they overlook the nonlinear Zeeman contributions and effects beyond the rotating wave approximation (RWA). While these influences can be precisely modeled, as elaborated in Sec. 7.2.1, they are not discussed in detail in this section.

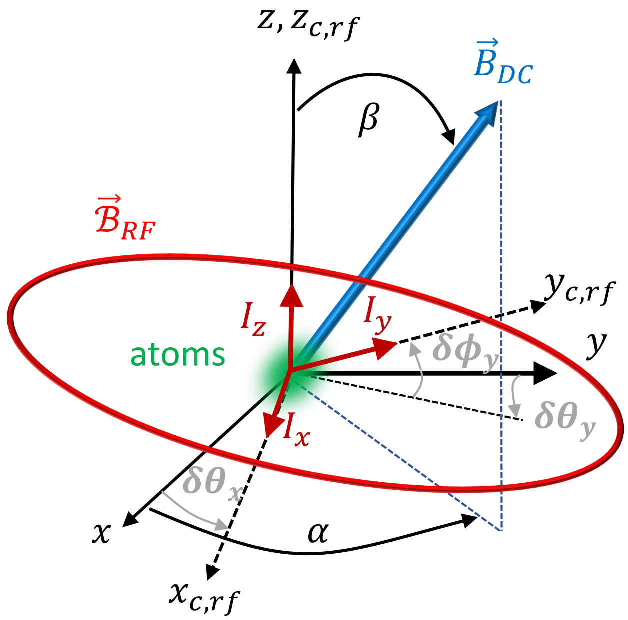


Figure 7.5: Schematic of system variables relevant for recalibration of the RF polarization ellipse (red).

Within this model for RF Rabi rates $\Omega_{\sigma\pm}$ there are 10 unknown parameters, namely namely 3 coil coefficients $(a_x, a_y, a_z)$, 3 non-orthogonality angles $(\delta\theta_x, \delta\theta_y, \delta\phi_y)$, 2 relative phases $(\phi_x, \phi_y)$, and the DC magnetic field direction $(\alpha, \beta)$. Using fake RF Rabi data generated from Using RF Rabi measurements combined with low-frequency coil modulations of the RF coil system we can extract nearly all of these parameters We examine a few cases to identify the specific measurements necessary for extracting different subsets of these 10 parameters from Rabi data generated by random RF coil excitations. This approach was informed by fitting the 10 model parameters to simulated RF Rabi data sets generated using Eq. (7.25) and Eq. (7.26).

**Case 1**: Extract either $(\alpha, \beta, \delta\theta_x, \delta\theta_y, \delta\phi_y)$ or $(\alpha, \beta, a_x, a_y, a_z)$:

Need to measure at least 6 RF Rabi rates (either $\Omega_{\sigma^+}$ or $\Omega_{\sigma^-}$, but both is not necessary) for random known RF currents $(I_x, I_y, I_z)$.

**Case 2**: Extract $(\alpha, \beta, \delta\theta_x, \delta\theta_y, \delta\phi_y, \phi_x, \phi_y)$ or $(\alpha, \beta, a_x, a_y, a_z, \phi_x, \phi_y)$:
Need to measure at least 6 RF Rabi rates of each $\Omega_{\sigma^+}$ and $\Omega_{\sigma^-}$ for random known RF currents $(I_x, I_y, I_z)$.

**Case 3**: Extract all parameters $(\alpha, \beta, \delta\theta_x, \delta\theta_y, \delta\phi_y, \phi_x, \phi_y, a_x, a_y, a_z)$:
This is not possible with only $\Omega_{\sigma^\pm}$ Rabi data. If one can also detect $\Omega_\pi$, for example through two-photon transitions discussed in Sec. 7.2.1, then extraction of all 10 parameters is possible by measuring at least 5 RF Rabi measurements for each $\Omega_{\sigma^+}$, $\Omega_\pi$, and $\Omega_{\sigma^-}$.

These cases are distinguished because it is not always necessary to recalibrate all RF coil system parameters (**Case 3**). For instance, during a year of recalibration data from the ESA SWARM mission, which employed a $^4$He optically pumped magnetometer (OPM) with coil modulations for vector detection, the non-orthogonality angles of the coil system drifted negligibly, by less than 1 millidegree (17 $\mu$rad). In contrast, the modulation coil factors experienced a notable drift of approximately 0.05% [109]. Thus, it could be that partial recalibration of some of the coil system parameters in **Case 1** and **Case 2** are enough to maintain sufficient vector accuracy. Investigation of these recalibration protocols with the RF coil system described in Sec. 7.2.1 is currently underway.

## 7.4 Summary and relation to other types of microwave sensors

The Rabi measurements presented in this thesis correct for a wide range of systematic inaccuracies previously overlooked in vapor cell Rabi oscillation experiments. Therefore, the calibrations of the microwave polarization ellipse detailed in Ch. 5, based on these Rabi measurements, could serve as a high-accuracy benchmark for assessing other microwave measurement techniques. One such technique commonly employed in vapor cells is the atomic candle method [47, 96, 171], which is a Rabi rate measurement that involves detecting the atomic population dynamics in response to modulating the phase of the microwave field. The largest population dynamics occurs when the phase modulation frequency, $f_m$, is half the Rabi rate, $\Omega$. While there has been little work assessing the accuracy of the atomic candle method, especially with regard to systematic errors from off-resonant driving, a direct comparison of the Rabi oscillation measurements described in this thesis, by conducting both measurements within the same vapor cell, would offer a clear benchmark of the atomic candle method's accuracy.

Another interesting comparison could be with EIT Rydberg sensors that detect microwave electric field components from the Autler-Townes splitting (ATS) of multi-photon ladder transitions to Rydberg states [77, 126, 158]. These sensors are regarded as capable of measuring electric fields with SI-traceability, but are estimated to accrue systematic errors on the 1% scale for AT splittings comparable to the EIT linewidths [78]. It would be interesting to measure simultaneous magnetic and electric microwave components using the Rabi techniques in this thesis with Rydberg EIT measurements in the same vapor cell over different electromagnetic field strengths and polarization ellipses. The magnetic $\vec{\mathcal{B}}_{\mu\mathrm{w}}$ and electric $\vec{E}_{\mu\mathrm{w}}$ microwave components, measured independently, can be mapped to compare consistency with Maxwell's equations [see Fig. 7.6]. A challenge to measuring the electric and magnetic components of the same microwave field is that Rydberg EIT sensors measure microwave field strengths of 1 V/m (10 nT). At these weak microwave fields, the magnetic field components would correspond to Rabi oscillation frequencies around $\Omega \approx 200$ Hz. Without buffer gas, Doppler broadening, given by

$$\Delta f = \sqrt{\frac{8kT\ln(2)}{m_{\mathrm{Rb}}c^2}}\nu_{\mathrm{hfs}} \approx 10 \text{ kHz}, \tag{7.27}$$

will produce Rabi oscillation linewidths much larger than 200 Hz. For this reason, Z. Feng et al. [59] performed an experiment that utilized the atomic candle method to assess the magnetic components of the microwave field within the same vapor cell used for Rydberg EIT measurements of the electric field components, but was not able to measure both methods at the same microwave field strengths.

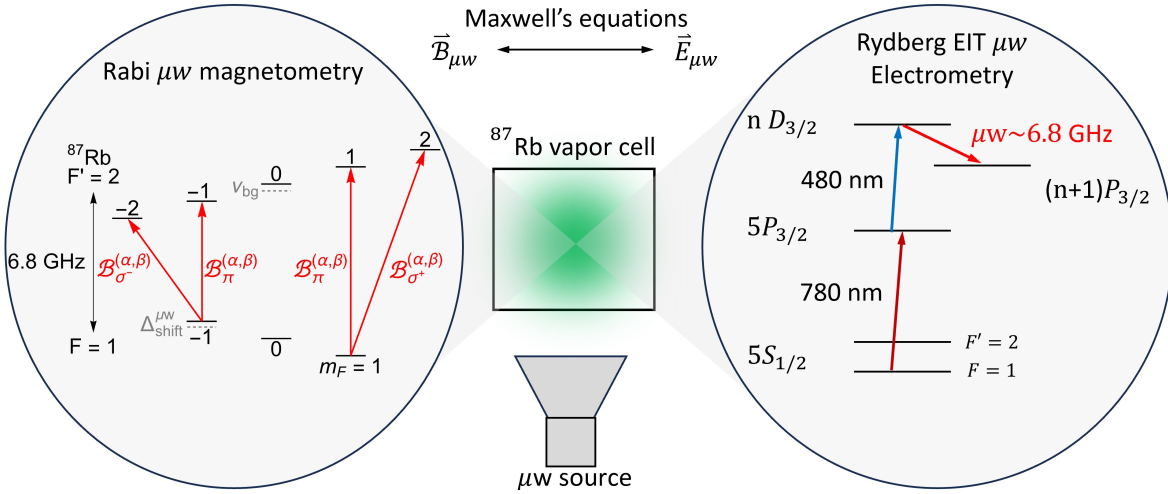


Figure 7.6: Measurement of magnetic and electric microwave components in the same vapor cell using Rabi oscillation and Rydberg EIT measurements. Maxwell's equations map the magnetic microwave components to the electric microwave components to compare the consistency between the two techniques.

One path around around this is to measure generalized Rabi frequencies off-resonance such that $\tilde{\Omega} \approx \sqrt{\Omega^2 + \Delta^2}$ is larger than the Dopper-broadened linewidth, and fit the Rabi rate $\Omega$ from the detuning dependence of $\tilde{\Omega}$. A limit to how large $\Delta/\Omega$ can be is constrained by the fact that the Rabi oscillation amplitude typically falls off as $1/\Delta^2$ (Eq. (3.32)). As discussed in Sec. 3.4.1, however, an initial $\pi/2$ pulse prior to driving the Rabi oscillation enables the Rabi oscillation amplitude to instead fall off as $1/\Delta$. The $\pi/2$ technique has the potential to produce Rabi oscillation signals with high signal-to-noise ratios (SNR) even when $\Delta/\Omega \gg 1$, facilitating the detection of microwave field strengths significantly below 0.5 $\mu$T, potentially reaching as low as 10 nT.

# Bibliography


[1] V. Acosta, M. Ledbetter, S. Rochester, D. Budker, D. J. Kimball, D. Hovde, W. Gawlik, S. Pustelny, J. Zachorowski, and V. Yashchuk, "Nonlinear magneto-optical rotation with frequency-modulated light in the geophysical field range", Phys. Rev. A **73**, 053404 (2006) (Cited on p. 84).

[2] V. Acosta, M. Auzinsh, W. Gawlik, P. Grisins, J. Higbie, D. J. Kimball, L. Krzemien, M. Ledbetter, S. Pustelny, S. Rochester, et al., "Production and detection of atomic hexadecapole at Earth's magnetic field", Opt. Express **16**, 11423 (2008) (Cited on p. 84).

[3] S. Afach, B. C. Buchler, D. Budker, C. Dailey, A. Derevianko, V. Dumont, N. L. Figueroa, I. Gerhardt, Z. D. Grujić, H. Guo, et al., "Search for topological defect dark matter with a global network of optical magnetometers", Nat. Phys. **17**, 1396 (2021) (Cited on p. 1).

[4] C. Affolderbach, G.-X. Du, T. Bandi, A. Horsley, P. Treutlein, and G. Mileti, "Imaging microwave and DC magnetic fields in a vapor-cell Rb atomic clock", IEEE Trans. Instrum. Meas. **64**, 3629 (2015) (Cited on p. 9).

[5] C. Affolderbach, W. Moreno, A. Ivanov, T. Debogovic, M. Pellaton, A. Skrivervik, E. De Rijk, and G. Mileti, "Study of additive manufactured microwave cavities for pulsed optically pumped atomic clock applications", Appl. Phys. Lett. **112** (2018) (Cited on pp. 10, 83).

[6] E. Aleksandrov, A. Vershovskiĭ, and A. Pazgalev, "Magnetometer based on a pair of symmetric transitions in the 87 Rb hyperfine structure", Tech. Phys. **51**, 919 (2006) (Cited on pp. 4, 83, 121).

[7] O. Alem, A. M. Benison, D. S. Barth, J. Kitching, and S. Knappe, "Magnetoencephalography of epilepsy with a microfabricated atomic magnetrode", J. Neurosci. **34**, 14324 (2014) (Cited on p. 4).

[8] E. Alexandrov, "Recent Progress in Optically Pumped Magnetometers", Phys. Scr. **2003**, 27 (2003) (Cited on pp. 4, 84).

[9] E. Alexandrov, M. Balabas, V. Kulyasov, A. Ivanov, A. Pazgalev, J. Rasson, A. Vershovski, and N. Yakobson, "Three-component variometer based on a scalar potassium sensor", Meas. Sci. Technol. **15**, 918 (2004) (Cited on p. 5).

[10] E. B. Alexandrov and V. A. Bonch-Bruevich, "Optically pumped atomic magnetometers after three decades", Opt. Eng. **31**, 711 (1992) (Cited on p. 2).

[11] L. Alldredge, "A proposed automatic standard magnetic observatory", J. Geophys. Res. **65**, 3777 (1960) (Cited on p. 5).

[12] J. Allred, R. Lyman, T. Kornack, and M. V. Romalis, "High-sensitivity atomic magnetometer unaffected by spin-exchange relaxation", Phys. Rev. Lett. **89**, 130801 (2002) (Cited on pp. 2, 10, 61).

[13] V. Andryushkov, D. Radnatarov, and S. Kobtsev, “Vector magnetometer based on the effect of coherent population trapping”, Appl. Opt. **61**, 3604 (2022) (Cited on p. 5).

[14] G. Annino, M. Cassettari, I. Longo, and M. Martinelli, “Dielectric Resonators in ESR: Overview, comments and perspectives”, Appl. Magn. Reson. **16**, 45 (1999) (Cited on p. 171).

[15] S. Appelt, A. B.-A. Baranga, C. Erickson, M. Romalis, A. Young, and W. Happer, “Theory of spin-exchange optical pumping of $^3$He and $^{129}$Xe”, Phys. Rev. A **58**, 1412 (1998) (Cited on pp. 61, 86, 103).

[16] H. Auster, K. Glassmeier, W. Magnes, O. Aydogar, W. Baumjohann, D. Constantinescu, D. Fischer, K. Fornacon, E. Georgescu, P. Harvey, et al., “The THEMIS fluxgate magnetometer”, Space Sci. Rev. **141**, 235 (2008) (Cited on p. 5).

[17] N. J. Ayres, G. Ban, L. Bienstman, G. Bison, K. Bodek, V. Bondar, T. Bouillaud, E. Chanel, J. Chen, P.-J. Chiu, et al., “The design of the n2EDM experiment: nEDM Collaboration”, Eur. Phys. J. C **81**, 512 (2021) (Cited on p. 1).

[18] H. Ball, W. Oliver, and M. Biercuk, “The role of master clock stability in quantum information processing”, Npj Quantum Inf. (2016) (Cited on p. 148).

[19] T. Baluktsian, C. Urban, T. Bublat, H. Giessen, R. Löw, and T. Pfau, “Fabrication method for microscopic vapor cells for alkali atoms”, Opt. Lett. **35**, 1950 (2010) (Cited on p. 4).

[20] G. Bao, D. Kanta, D. Antypas, S. Rochester, K. Jensen, W. Zhang, A. Wickenbrock, and D. Budker, “All-Optical Spin Locking in Alkali-Metal-Vapor Magnetometers”, Phys. Rev. A **105**, 043109 (2022) (Cited on p. 84).

[21] G. Bao, A. Wickenbrock, S. Rochester, W. Zhang, and D. Budker, “Suppression of the Nonlinear Zeeman Effect and Heading Error in Earth-Field-Range Alkali-Vapor Magnetometers”, Phys. Rev. Lett. **120**, 033202 (2018) (Cited on p. 84).

[22] A. B.-A. Baranga, S. Appelt, M. Romalis, C. Erickson, A. Young, G. Cates, and W. Happer, “Polarization of $^3$He by spin exchange with optically pumped Rb and K vapors”, Phys. Rev. Lett. **80**, 2801 (1998) (Cited on p. 65).

[23] E. Batori, C. Affolderbach, M. Pellaton, F. Gruet, M. Violetti, Y. Su, A. K. Skrivervik, and G. Mileti, “$\mu$POP Clock: A Microcell Atomic Clock Based on a Double-Resonance Ramsey Scheme”, Phys. Rev. Appl. **18**, 054039 (2022) (Cited on pp. 10, 83).

[24] W. E. Bell and A. L. Bloom, “Optical Detection of Magnetic Resonance in Alkali Metal Vapor”, Phys. Rev. **107**, 1559 (1957) (Cited on p. 1).

[25] W. E. Bell and A. L. Bloom, “Optically Driven Spin Precession”, Phys. Rev. Lett. **6**, 280 (1961) (Cited on pp. 1, 2).

[26] A. Ben-Kish and M. Romalis, “Dead-Zone-Free Atomic Magnetometry with Simultaneous Excitation of Orientation and Alignment Resonances”, Phys. Rev. Lett. **105**, 193601 (2010) (Cited on p. 5).

[27] J. S. Bennett, B. E. Vyhnalek, H. Greenall, E. M. Bridge, F. Gotardo, S. Forstner, G. I. Harris, F. A. Miranda, and W. P. Bowen, “Precision Magnetometers for Aerospace Applications: A Review”, Sensors **21**, 5568 (2021) (Cited on pp. 4, 5, 84).

[28] S. D. Billings, “Discrimination and classification of buried unexploded ordnance using magnetometry”, IEEE Trans Geosci Remote Sens. **42**, 1241 (2004) (Cited on pp. 4, 84).

[29] G. Bison, V. Bondar, P. Schmidt-Wellenburg, A. Schnabel, and J. Voigt, "Sensitive and stable vector magnetometer for operation in zero and finite fields", Opt. Express **26**, 17350 (2018) (Cited on p. 5).

[30] G. Bison, R. Wynands, and A. Weis, "A laser-pumped magnetometer for the mapping of human cardiomagnetic fields", Appl. Phys. B **76**, 325 (2003) (Cited on pp. 1, 4).

[31] A. L. Bloom, "Principles of Operation of the Rubidium Vapor Magnetometer", Appl. Opt. **1**, 61 (1962) (Cited on pp. 2, 125).

[32] P. Böhi and P. Treutlein, "Simple microwave field imaging technique using hot atomic vapor cells", Appl. Phys. Lett. **101** (2012) (Cited on p. 9).

[33] F. Bonetto, E. Anoardo, and M. Polello, "Saddle coils for uniform static magnetic field generation in NMR experiments", Concepts in Magnetic Resonance Part B: Magnetic Resonance Engineering: An Educational Journal **29**, 9 (2006) (Cited on p. 33).

[34] A. Braun, T. Davis, M. Kwakernaak, J. Michalchuk, A. Ulmer, W. Chan, J. Abeles, Z. Shellenbarger, Y. Jau, W. Happer, et al., "RF-Interrogated End-State Chip-Scale Atomic Clock", in Proceedings of the 39th annual precise time and time interval meeting (2007), pp. 233–248 (Cited on p. 171).

[35] P. J. Broser, S. Knappe, D.-S. Kajal, N. Noury, O. Alem, V. Shah, and C. Braun, "Optically Pumped Magnetometers for Magneto-Myography to Study the Innervation of the Hand", IEEE Trans. Neural Syst. Rehabil. Eng. **26**, 2226 (2018) (Cited on p. 1).

[36] J. Brossel, A. Kastler, and J. Winter, "Gréation optique d'une inégalité de population entre les sous-niveaux Zeeman de l'état fondamental des atomes", J. Phys. Radium **13**, 668 (1952) (Cited on p. 1).

[37] M. Brown, T. Thiele, C. Kiehl, T.-W. Hsu, and C. Regal, "Gray-molasses Optical-Tweezer Loading: Controlling Collisions for Scaling Atom-Array Assembly", Phys. Rev. X **9**, 011057 (2019) (Cited on p. 17).

[38] D. Budker, D. Kimball, S. Rochester, V. Yashchuk, and M. Zolotorev, "Sensitive magnetometry based on nonlinear magneto-optical rotation", Phys. Rev. A **62**, 043403 (2000) (Cited on p. 2).

[39] D. Budker, W. Gawlik, D. Kimball, S. Rochester, V. Yashchuk, and A. Weis, "Resonant nonlinear magneto-optical effects in atoms", Rev. Mod. Phys. **74**, 1153 (2002) (Cited on p. 2).

[40] D. Budker and D. F. J. Kimball, **Optical magnetometry** (Cambridge University Press, Oxford, 2013) (Cited on pp. 1, 61).

[41] D. Budker and M. Romalis, "Optical magnetometry", Nat. Phys. **3**, 227 (2007) (Cited on pp. 1, 2, 50).

[42] A. Canciani and J. Raquet, "Absolute Positioning Using the Earth's Magnetic Anomaly Field", Navig. J. Inst. Navig. **63**, 111 (2016) (Cited on pp. 4–6, 84).

[43] A. Canciani and J. Raquet, "Airborne Magnetic Anomaly Navigation", IEEE Trans. Aerosp. Electron. Syst. **53**, 67 (2017) (Cited on pp. 4, 6).

[44] B. Chéron, H. Gilles, and J. Hamel, "Spatial frequency isotropy of an optically pumped $^4$He magnetometer", EPJ Appl. Phys. **13**, 143 (2001) (Cited on p. 4).

[45] B. Chéron, H. Gilles, J. Hamel, O. Moreau, and E. Noël, "Improvement of the Spatial Amplitude Isotropy of a $^4$He Magnetometer Using a Modulated Pumping Beam", J. Phys. III **7**, 1735 (1997) (Cited on p. 4).

[46] J. Clarke, "Principles and applications of SQUIDs", Proc. IEEE **77**, 1208 (1989) (Cited on p. 5).

[47] J. Coffer and J. Camparo, "Atomic stabilization of field intensity using Rabi resonances", Phys. Rev. A **62**, 013812 (2000) (Cited on p. 183).

[48] L. Cutler, C. Flory, R. Giffard, and A. De Marchi, "Frequency pulling by hyperfine $\sigma$ transitions in cesium beam atomic frequency standards", J. Appl. Phys. **69**, 2780 (1991) (Cited on pp. 10, 83).

[49] T. F. Cutler, W. J. Hamlyn, J. Renger, K. A. Whittaker, D. Pizzey, I. G. Hughes, V. Sandoghdar, and C. S. Adams, "Nanostructured Alkali-Metal Vapor Cells", Phys. Rev. Appl. **14**, 034054 (2020) (Cited on p. 4).

[50] H. Dang, A. C. Maloof, and M. V. Romalis, "Ultrahigh sensitivity magnetic field and magnetization measurements with an atomic magnetometer", Appl. Phys. Lett. **97** (2010) (Cited on p. 1).

[51] E. Dantsker, D. Koelle, A. Miklich, D. Nemeth, F. Ludwig, J. Clarke, J. Longo, and V. Vinetskiy, "High-T c three-axis dc SQUID magnetometer for geophysical applications", Rev. Sci. Instrum. **65**, 3809 (1994) (Cited on p. 5).

[52] H. Dehmelt, "Modulation of a light beam by precessing absorbing atoms", Phys. Rev. **105**, 1924 (1957) (Cited on p. 1).

[53] R. Dicke, "The Effect of Collisions Upon the Doppler Width of Spectral Lines", Phys. Rev. **89**, 472 (1953) (Cited on pp. 23, 62).

[54] M. Dietrich, K. Bailey, and T. O'Connor, "Alignment of a vector magnetometer to an optical prism", Rev. Sci. Instrum. **88** (2017) (Cited on p. 155).

[55] M. Dougherty, S. Kellock, D. Southwood, A. Balogh, E. Smith, B. Tsurutani, B. Gerlach, K.-H. Glassmeier, F. Gleim, C. Russell, et al., "The Cassini Magnetic Field Investigation", Space Sci. Rev., 331 (2004) (Cited on pp. 4, 5, 8, 84).

[56] E. T. Dressler, A. E. Laux, and R. I. Billmers, "Theory and experiment for the anomalous Faraday effect in potassium", JOSA B **13**, 1849 (1996) (Cited on p. 30).

[57] A. Fabricant, I. Novikova, and G. Bison, "How to build a magnetometer with thermal atomic vapor: a tutorial", New J. Phys. (2023) (Cited on p. 2).

[58] A. Fairweather and M. Usher, "A vector rubidium magnetometer", J. Sci. Instrum. **5**, 986 (1972) (Cited on p. 5).

[59] Z. Feng, X. Liu, Y. Zhang, W. Ruan, Z. Song, and J. Qu, "Atom-based sensing technique of microwave electric and magnetic fields via a single rubidium vapor cell", Opt. Express **31**, 1692 (2023) (Cited on p. 184).

[60] W. Franzen, "Spin Relaxation of Optically Aligned Rubidium Vapor", Phys. Rev. **115**, 850 (1959) (Cited on p. 62).

[61] E. Friis-Christensen, H. Lühr, and G. Hulot, "Swarm: A constellation to study the Earth's magnetic field", Earth Planets Space **58**, 351 (2006) (Cited on pp. 4, 84).

[62] C. Gemmel, W. Heil, S. Karpuk, K. Lenz, C. Ludwig, Y. Sobolev, K. Tullney, M. Burghoff, W. Kilian, S. Knappe-Grüneberg, et al., "Ultra-sensitive magnetometry based on free precession of nuclear spins", Eur. Phys. J. D **57**, 303 (2010) (Cited on p. 105).

[63] X.-x. Geng, G. Yang, P.-l. Qi, W. Tang, S. Liang, G.-x. Li, and G.-m. Huang, "Laser-detected magnetic resonance induced by radio-frequency two-photon processes", Phys. Rev. A **103**, 053112 (2021) (Cited on p. 179).

[64] T. R. Gentile, B. J. Hughey, D. Kleppner, and T. W. Ducas, "Experimental study of one-and two-photon Rabi oscillations", Phys. Rev. A **40**, 5103 (1989) (Cited on p. 179).

[65] H. M. Gibbs and R. J. Hull, "Spin-exchange Cross Sections for Rb 87-Rb 87 and Rb 87-Cs 133 Collisions", Phys. Rev. **153**, 132 (1967) (Cited on pp. 62, 113, 132).

[66] O. Gravrand, A. Khokhlov, L. M. JL, and L. JM, "On the calibration of a vectorial $^4$He pumped magnetometer", Earth Planets Space **53**, 949 (2001) (Cited on pp. 5, 6, 15, 142, 154, 169).

[67] S. Groeger, G. Bison, J.-L. Schenker, R. Wynands, and A. Weis, "A high-sensitivity laser-pumped Mx magnetometer", Eur. Phys. J. **38**, 239 (2006) (Cited on p. 2).

[68] Z. D. Grujić, P. A. Koss, G. Bison, and A. Weis, "A sensitive and accurate atomic magnetometer based on free spin precession", Eur. Phys. J. D **69**, 1 (2015) (Cited on pp. 105, 107).

[69] C. Guttin, J. Leger, and F. Stoeckel, "An isotropic earth field scalar magnetometer using optically pumped helium 4", J. Phys. IV **4**, 655 (1994) (Cited on p. 4).

[70] Q. Hao, W. Xue, F. Xu, K. Wang, P. Yun, and S. Zhang, "Efforts towards a low-temperature-sensitive physics package for vapor cell atomic clocks", Satell. Navig. **1**, 1 (2020) (Cited on p. 81).

[71] W. Happer and A. Tam, "Effect of rapid spin exchange on the magnetic-resonance spectrum of alkali vapors", Phys. Rev. A **16**, 1877 (1977) (Cited on p. 2).

[72] W. Happer and H. Tang, "Spin-exchange shift and narrowing of magnetic resonance lines in optically pumped alkali vapors", Phys. Rev. Lett. **31**, 273 (1973) (Cited on pp. 2, 50).

[73] W. Happer, "Optical pumping", Rev. Mod. Phys. **44**, 169 (1972) (Cited on p. 50).

[74] W. Happer, Y.-Y. Jau, and T. Walker, **Optically Pumped Atoms** (John Wiley & Sons, 2010) (Cited on pp. 21, 26, 109, 113).

[75] W. Hawkins and R. Dicke, "The Polarization of Sodium Atoms", Phys. Rev. **91**, 1008 (1953) (Cited on p. 1).

[76] A. Hemshorn, H. Auster, and M. Fredow, "DI-flux measurement of the geomagnetic field using a three-axial fluxgate sensor", Meas. Sci. Technol. **20**, 027004 (2009) (Cited on p. 155).

[77] C. L. Holloway, J. A. Gordon, S. Jefferts, A. Schwarzkopf, D. A. Anderson, S. A. Miller, N. Thaicharoen, and G. Raithel, "Broadband Rydberg atom-based electric-field probe for SI-traceable, self-calibrated measurements", IEEE Trans. Antennas Propag. **62**, 6169 (2014) (Cited on p. 184).

[78] C. L. Holloway, M. T. Simons, J. A. Gordon, A. Dienstfrey, D. A. Anderson, and G. Raithel, "Electric field metrology for SI traceability: Systematic measurement uncertainties in electromagnetically induced transparency in atomic vapor", J. Appl. Phys. **121** (2017) (Cited on p. 184).

[79] Y. Horowicz, O. Katz, O. Raz, and O. Firstenberg, "Critical dynamics and phase transition of a strongly interacting warm spin gas", Proc. Natl. Acad. Sci. **118**, e2106400118 (2021) (Cited on pp. 50, 109).

[80] A. Horsley, G.-X. Du, M. Pellaton, C. Affolderbach, G. Mileti, and P. Treutlein, "Imaging of relaxation times and microwave field strength in a microfabricated vapor cell", Phys. Rev. A **88**, 063407 (2013) (Cited on pp. 9, 83, 124).

[81] A. Horsley, G.-X. Du, and P. Treutlein, "Widefield microwave imaging in alkali vapor cells with sub-100 $\mu$m resolution", New J. Phys. **17**, 112002 (2015) (Cited on p. 9).

[82] D. Hoult and N. Ginsberg, "The quantum origins of the free induction decay signal and spin noise", J. Magn. Reson. **148**, 182 (2001) (Cited on p. 2).

[83] E. Hrycyshyn and L. Krause, "Inelastic Collisions Between Excited Alkali Atoms and Molecules. VII. Sensitized Fluorescence and Quenching in Mixtures of Rubidium With $H_2$, HD, $D_2$, $N_2$, $CH_4$, $CD_4$, $C_2H_4$, and $C_2H_6$", Can. J. Phys. **48**, 2761 (1970) (Cited on p. 113).

[84] Y. Huang, L. Wu, and D. Li, "Theoretical Research on Full Attitude Determination Using Geomagnetic Gradient Tensor", J. Navig. **68**, 951 (2015) (Cited on p. 7).

[85] B. Huber, T. Baluktsian, M. Schlagmüller, A. Kölle, H. Kübler, R. Löw, and T. Pfau, "GHz Rabi flopping to Rydberg states in hot atomic vapor cells", Phys. Rev. Lett. **107**, 243001 (2011) (Cited on p. 179).

[86] D. Hunter, S. Piccolomo, J. D. Pritchard, N. L. Brockie, T. E. Dyer, and E. Riis, "Free-Induction-Decay Magnetometer Based on a Microfabricated Cs Vapor Cell", Phys. Rev. Appl. **10**, 014002 (2018) (Cited on pp. 2, 107).

[87] S. J. Ingleby, C. O'Dwyer, P. F. Griffin, A. S. Arnold, and E. Riis, "Vector Magnetometry Exploiting Phase-Geometry Effects in a Double-Resonance Alignment Magnetometer", Phys. Rev. Appl. **10**, 034035 (2018) (Cited on pp. 5, 14, 154).

[88] Y.-Y. Jau, A. Post, N. Kuzma, A. Braun, M. Romalis, and W. Happer, "Intense, narrow atomic-clock resonances", Phys. Rev. Lett. **92**, 110801 (2004) (Cited on pp. 50, 64, 65).

[89] Y.-Y. Jau, "New studies of optical pumping, spin resonances, and spin exchange in mixtures of inert gases and alkali-metal vapors", PhD thesis (Princeton University, 2005) (Cited on pp. 61, 62).

[90] K. Jensen, V. Acosta, J. Higbie, M. Ledbetter, S. Rochester, and D. Budker, "Cancellation of nonlinear Zeeman shifts with light shifts", Phys. Rev. A **79**, 023406 (2009) (Cited on p. 84).

[91] A. Karsenty, "A Comprehensive Review of Integrated Hall Effects in Macro-, Micro-, Nanoscales, and Quantum Devices", Sensors **20**, 4163 (2020) (Cited on p. 5).

[92] A. Kastler, "Quelques suggestions concernant la production optique et la détection optique d'une inégalité de population des niveaux de quantifigation spatiale des atomes. Application à l'expérience de Stern et Gerlach et à la résonance magnétique", J. Phys. Radium **11**, 255 (1950) (Cited on p. 1).

[93] K. Khurana, M. Kivelson, D. Stevenson, G. Schubert, C. Russell, R. Walker, and C. Polanskey, "Induced magnetic fields as evidence for subsurface oceans in Europa and Callisto", Nature **395**, 777 (1998) (Cited on p. 8).

[94] C. Kiehl, T. S. Menon, S. Knappe, T. Thiele, and C. A. Regal, "Correcting heading errors in optically pumped magnetometers through microwave interrogation", arXiv:2310.11017 (2023) (Cited on pp. 36, 123, 125, 138).

[95] C. Kiehl, D. Wagner, T.-W. Hsu, S. Knappe, C. A. Regal, and T. Thiele, “Coherence of Rabi oscillations with spin exchange”, Phys. Rev. Res. **5**, L012002 (2023) (Cited on pp. 68, 83, 113, 124).

[96] M. Kinoshita, K. Shimaoka, and K. Komiyama, “Atomic Microwave Power Standard Based on the Rabi Frequency”, IEEE Trans. Instrum. Meas. **60**, 2696 (2010) (Cited on p. 183).

[97] M. Kivelson, K. Khurana, J. Means, C. Russell, and R. Snare, “The Galileo magnetic field investigation”, Space Sci. Rev. **60**, 357 (1992) (Cited on p. 8).

[98] S. Knappe, K. J. Hughes, and O. Alem, “Microfabricated optically-pumped magnetometers for imaging applications”, in Quantum sensing, imaging, and precision metrology, Vol. 12447 (SPIE, 2023), pp. 45–51 (Cited on p. 4).

[99] R. Koch and J. Rozen, “Low-noise flux-gate magnetic-field sensors using ring-and rod-core geometries”, Appl. Phys. Lett. **78**, 1897 (2001) (Cited on p. 5).

[100] J. Koepsell, T. Thiele, J. Deiglmayr, A. Wallraff, and F. Merkt, “Measuring the polarization of electromagnetic fields using Rabi-rate measurements with spatial resolution: Experiment and theory”, Phys. Rev. A **95**, 053860 (2017) (Cited on pp. 12, 124).

[101] I. Kominis, T. Kornack, J. Allred, and M. V. Romalis, “A subfemtotesla multichannel atomic magnetometer”, Nature **422**, 596 (2003) (Cited on pp. 1, 2).

[102] J. Kong, R. Jiménez-Martínez, C. Troullinou, V. G. Lucivero, G. Tóth, and M. W. Mitchell, “Measurement-induced, spatially-extended entanglement in a hot, strongly-interacting atomic system”, Nat. Commun. **11**, 2415 (2020) (Cited on pp. 31, 50).

[103] H. Korth, K. Strohbehn, F. Tejada, A. G. Andreou, J. Kitching, S. Knappe, S. J. Lehtonen, S. M. London, and M. Kafel, “Miniature atomic scalar magnetometer for space based on the rubidium isotope $^{87}$Rb”, J. Geophys. Res. Space Phys. **121**, 7870 (2016) (Cited on pp. 4, 5, 84).

[104] A. Kuzmich, K. Mølmer, and E. Polzik, “Spin Squeezing in an Ensemble of Atoms Illuminated With Squeezed Light”, Phys. Rev. Lett. **79**, 4782 (1997) (Cited on p. 3).

[105] M. Ledbetter, I. Savukov, D. Budker, V. Shah, S. Knappe, J. Kitching, D. Michalak, S. Xu, and A. Pines, “Zero-field remote detection of NMR with a microfabricated atomic magnetometer”, Proc. Natl. Acad. Sci. **105**, 2286 (2008) (Cited on p. 4).

[106] K.-M. Lee, M. Li, and C.-Y. Lin, “Magnetic Tensor Sensor and Way-Finding Method Based on Geomagnetic Field Effects With Applications for Visually Impaired Users”, IEEE/ASME Trans. Mechatron. **21**, 2694 (2016) (Cited on p. 7).

[107] W. Lee, V. Lucivero, M. Romalis, M. Limes, E. Foley, and T. Kornack, “Heading errors in all-optical alkali-metal-vapor magnetometers in geomagnetic fields”, Phys. Rev. A **103**, 063103 (2021) (Cited on pp. 4, 84).

[108] J.-M. Leger, F. Bertrand, T. Jager, M. Le Prado, I. Fratter, and J.-C. Lalaurie, “Swarm Absolute Scalar and Vector Magnetometer Based on Helium 4 Optical Pumping”, Procedia Chem. **1**, 634 (2009) (Cited on p. 5).

[109] J.-M. Léger, T. Jager, F. Bertrand, G. Hulot, L. Brocco, P. Vigneron, X. Lalanne, A. Chulliat, and I. Fratter, “In-flight performance of the Absolute Scalar Magnetometer vector mode on board the Swarm satellites”, Earth Planets Space **67**, 1 (2015) (Cited on pp. 6, 125, 183).

[110] S. Li, P. Vachaspati, D. Sheng, N. Dural, and M. V. Romalis, “Optical rotation in excess of 100 rad generated by Rb vapor in a multipass cell”, Phys. Rev. A **84**, 061403 (2011) (Cited on p. 10).

[111] S.-Q. Liang, G.-Q. Yang, Y.-F. Xu, Q. Lin, Z.-H. Liu, and Z.-X. Chen, “Simultaneously improving the sensitivity and absolute accuracy of CPT magnetometer”, Opt. Express **22**, 6837 (2014) (Cited on p. 84).

[112] Z. Liang, X.-x. Geng, G.-q. Yang, K. Jin, S.-q. Liang, S.-p. Wu, G.-m. Huang, and G.-x. Li, “Atomic mixer based on phase control without ac Zeeman shift”, Phys. Rev. A **107**, 013115 (2023) (Cited on p. 179).

[113] L.-A. Liew, S. Knappe, J. Moreland, H. Robinson, L. Hollberg, and J. Kitching, “Microfabricated alkali atom vapor cells”, Appl. Phys. Lett. **84**, 2694 (2004) (Cited on p. 3).

[114] A. Linskens, I. Holleman, N. Dam, and J. Reuss, “Two-photon Rabi oscillations”, Phys. Rev. A **54**, 4854 (1996) (Cited on p. 179).

[115] G. Liu, O. Be’Er, Y. Margalit, M. Givon, D. Groswasser, Y. Japha, and R. Folman, “Survival of the fittest in the coherent evolution of quantum ensembles”, Phys. Rev. A **98**, 013856 (2018) (Cited on p. 9).

[116] V. G. Lucivero, A. Zanoni, G. Corrielli, R. Osellame, and M. W. Mitchell, “Laser-written vapor cells for chip-scale atomic sensing and spectroscopy”, Opt. Express **30**, 27149 (2022) (Cited on p. 4).

[117] V. G. Lucivero, P. Anielski, W. Gawlik, and M. W. Mitchell, “Shot-noise-limited magnetometer with sub-picotesla sensitivity at room temperature”, Rev. Sci. Instrum. **85** (2014) (Cited on p. 32).

[118] B. Maddox and F. Renzoni, “Two-photon electromagnetic induction imaging with an atomic magnetometer”, Appl. Phys. Lett. **122** (2023) (Cited on p. 179).

[119] V. Malinovsky and J. Krause, “General theory of population transfer by adiabatic rapid passage with intense, chirped laser pulses”, Eur. Phys. J. D **14**, 147 (2001) (Cited on p. 69).

[120] J. McKelvy, M. Maldonado, I. Novikova, E. Mikhailov, and A. Matsko, “Technical limits of sensitivity for EIT magnetometry”, Appl. Opt. **62**, 6518 (2023) (Cited on pp. 5, 14, 154).

[121] X. Meng, Y. Zhang, X. Zhang, S. Jin, T. Wang, L. Jiang, L. Xiao, S. Jia, and Y. Xiao, “Machine learning assisted vector atomic magnetometry”, Nat. Commun. **14**, 6105 (2023) (Cited on pp. 5, 154).

[122] J. Merayo, P. Brauer, F. Primdahl, and J. Petersen, “Absolute magnetic calibration and alignment of vector magnetometers in the Earth’s magnetic field”, Worshop on Calibration of Space-Borne Magnetometers in Ground and In-Flight Space Magnetometer Calibration Techniques (1999) (Cited on pp. 154, 155).

[123] R. Mhaskar, S. Knappe, and J. Kitching, “A low-power, high-sensitivity micromachined optical magnetometer”, Appl. Phys. Lett. **101** (2012) (Cited on p. 130).

[124] S. Micalizio, A. Godone, F. Levi, and J. Vanier, “Spin-exchange frequency shift in alkali-metal-vapor cell frequency standards”, Phys. Rev. A **73**, 033414 (2006) (Cited on pp. 61, 62, 65, 86, 103).

[125] G. Missout and J. Vanier, “Pressure and Temperature Coefficients of the More Commonly Used Buffer Gases in Rubidium Vapor Frequency Standards”, IEEE Trans. Instrum. Meas. **24**, 180 (1975) (Cited on pp. 22, 24).

[126] A. Mohapatra, T. Jackson, and C. Adams, “Coherent Optical Detection of Highly Excited Rydberg States Using Electromagnetically Induced Transparency”, Phys. Rev. Lett. **98**, 113003 (2007) (Cited on p. 184).

[127] R. K. Mongia and A. Ittipiboon, “Theoretical and experimental investigations on rectangular dielectric resonator antennas”, IEEE Trans. Antennas Propag. **45**, 1348 (1997) (Cited on p. 172).

[128] R. Mongia, “Theoretical and experimental resonant frequencies of rectangular dielectric resonators”, in Iee proceedings h (microwaves, antennas and propagation), Vol. 139, 1 (IET, 1992), pp. 98–104 (Cited on p. 172).

[129] L. A. Mount, “Navigation using Vector and Tensor Measurements of the Earth’s Magnetic Anomaly Field”, PhD thesis (Air Force Institute of Technology, 2018) (Cited on pp. 6, 7).

[130] A. Nagel, L. Graf, A. Naumov, E. Mariotti, V. Biancalana, D. Meschede, and R. Wynands, “Experimental realization of coherent dark-state magnetometers”, Europhys. Lett. **44**, 31 (1998) (Cited on p. 2).

[131] H. Nhalil, T. Givon, P. T. Das, N. Hasidim, V. Mor, M. Schultz, S. Amrusi, L. Klein, and A. Grosz, “Planar Hall Effect Magnetometer With 5 pT Resolution”, IEEE Sens. Lett. **3**, 1 (2019) (Cited on p. 5).

[132] G. Oelsner, V. Schultze, R. IJsselsteijn, F. Wittkämper, and R. Stolz, “Sources of heading errors in optically pumped magnetometers operated in the Earth’s magnetic field”, Phys. Rev. A **99**, 013420 (2019) (Cited on p. 84).

[133] Y. Okada and Y. Tokumaru, “Precise determination of lattice parameter and thermal expansion coefficient of silicon between 300 and 1500 K”, J. Appl. Phys. **56**, 314 (1984) (Cited on p. 25).

[134] N. Olsen, L. T. Clausen, T. J. Sabaka, P. Brauer, J. M. Merayo, J. L. Jørgensen, J.-M. Léger, O. V. Nielsen, F. Primdahl, and T. Risbo, “Calibration of the Ørsted vector magnetometer”, Earth Planets Space **55**, 11 (2003) (Cited on p. 125).

[135] K. Pajunpää, E. Klimovich, V. Korepanov, P. Posio, H. Nevanlinna, W. Schmidt, M. Genzer, A. Harri, and A. Lourenço, “Accredited vector magnetometer calibration facility”, Geophysica **43**, 59 (2007) (Cited on p. 155).

[136] L. Parsons and Z. Wiatr, “Rubidium vapour magnetometer”, J. Sci. Instrum. **39**, 292 (1962) (Cited on p. 1).

[137] B. Patton, E. Zhivun, D. Hovde, and D. Budker, “All-Optical Vector Atomic Magnetometer”, Phys. Rev. Letters **113**, 013001 (2014) (Cited on p. 5).

[138] J. M. Pendlebury, K. Smith, R. Golub, J. Byrne, T. McComb, T. Sumner, S. Burnett, A. Taylor, B. Heckel, N. Ramsey, et al., “Search for a neutron electric dipole moment”, Phys. Lett. B **136**, 327 (1984) (Cited on p. 1).

[139] T. Peyrot, C. Beurthe, S. Coumar, M. Roulliay, K. Perronet, P. Bonnay, C. Adams, A. Browaeys, and Y. R. Sortais, “Fabrication and characterization of super-polished wedged borosilicate nano-cells”, Opt. Lett. **44**, 1940 (2019) (Cited on p. 4).

[140] A. Pollinger, R. Lammegger, W. Magnes, C. Hagen, M. Ellmeier, I. Jernej, M. Leichtfried, C. Kürbisch, R. Maierhofer, R. Wallner, et al., “Coupled dark state magnetometer for the China Seismo-Electromagnetic Satellite”, Meas. Sci. Technol. **29**, 095103 (2018) (Cited on pp. 5, 84).

[141] M. Pospelov, S. Pustelny, M. Ledbetter, D. J. Kimball, W. Gawlik, and D. Budker, "Detecting Domain Walls of Axionlike Models Using Terrestrial Experiments", Phys. Rev. Lett. **110**, 021803 (2013) (Cited on p. 1).

[142] A. Pouliot, G. Carlse, H. Beica, T. Vacheresse, A. Kumarakrishnan, U. Shim, S. Cahn, A. Turlapov, and T. Sleator, "Accurate determination of an alkali-vapor–inert-gas diffusion coefficient using coherent transient emission from a density grating", Phys. Rev. A **103**, 023112 (2021) (Cited on pp. 62, 113).

[143] D. M. Pozar, **Microwave Engineering** (John wiley & sons, 2011) (Cited on p. 43).

[144] M. Prouty, **Real-Time Hand-Held Magnetometer Array**, tech. rep. (Geometrics, 2016) (Cited on pp. 4, 5, 84).

[145] M. L. Psiaki, L. Huang, and S. Fox, "Ground tests of magnetometer-based autonomous navigation (MAGNAV) for low-earth-orbiting spacecraft", J. Guid. Control Dyn. **16**, 206 (1993) (Cited on p. 5).

[146] M. L. Psiaki, L. Huang, and S. M. Fox, "Ground tests of magnetometer-based autonomous navigation (magnav) for low-earth-orbiting spacecraft", J. Guid. Control Dyn. **16**, 206 (1993) (Cited on pp. 4, 84).

[147] S. Pustelny, W. Gawlik, S. Rochester, D. J. Kimball, V. Yashchuk, and D. Budker, "Nonlinear magneto-optical rotation with modulated light in tilted magnetic fields", Phys. Rev. A **74**, 063420 (2006) (Cited on p. 5).

[148] T. Pyragius, H. M. Florez, and T. Fernholz, "Voigt-effect-based three-dimensional vector magnetometer", Phys. Rev. A **100**, 023416 (2019) (Cited on p. 5).

[149] M. Romalis, E. Miron, and G. Cates, "Pressure broadening of Rb $D_1$ and $D_2$ lines by $^3$He, $^4$He, $N_2$, and Xe: Line cores and near wings", Phys. Rev. A (1997) (Cited on pp. 22, 23).

[150] Y. Rosenzweig, D. Tokar, I. Shcerback, M. Givon, and R. Folman, "Heading Error Compensation in a Portable Optical Magnetometer Using a Double-Pass Single Beam Configuration", arXiv:2307.13982 (2023) (Cited on p. 84).

[151] M. D. Rotondaro and G. P. Perram, "Collisional broadening and shift of the rubidium $D_1$ and $D_2$ lines ($5^2S_{12}\rightarrow 5^2P_{12}$, $5^2P_{32}$) by rare gases, $H_2$, $D_2$, $N_2$, $CH_4$ and $CF_4$", J. Quant. Spectrosc. Radiat. Transf. **57**, 497 (1997) (Cited on pp. 22, 24).

[152] N. Rott, T. Middelmann, C. Hahn, and M. Albrecht, "Orientation of a Vector Magnetometer Optically Referenced to an External Coordinate System", IEEE Trans. Magn. **56**, 1 (2020) (Cited on p. 155).

[153] L. Rushton, L. Elson, A. Meraki, and K. Jensen, "Alignment-Based Optically Pumped Magnetometer Using a Buffer-Gas Cell", Phys. Rev. Appl. **19**, 064047 (2023) (Cited on p. 84).

[154] J. Rutkowski, W. Fourcault, F. Bertrand, U. Rossini, S. Gétin, S. Le Calvez, T. Jager, E. Herth, C. Gorecki, M. Le Prado, et al., "Towards a miniature atomic scalar magnetometer using a liquid crystal polarization rotator", Sens. Actuators A: Phys. **216**, 386 (2014) (Cited on p. 4).

[155] M. Salleras, E. Eklund, I. Prikhodko, and A. Shkel, "Predictive thermal model for indirect temperature measurement inside atomic cell of nuclear magnetic resonance gyroscope", in Transducers 2009-2009 international solid-state sensors, actuators and microsystems conference (IEEE, 2009), pp. 304–307 (Cited on p. 81).

[156] I. Savukov and M. Romalis, “Effects of spin-exchange collisions in a high-density alkali-metal vapor in low magnetic fields”, Phys. Rev. A **71**, 023405 (2005) (Cited on p. 50).

[157] V. Schultze, B. Schillig, R. IJsselsteijn, T. Scholtes, S. Woetzel, and R. Stolz, “An optically pumped magnetometer working in the light-shift dispersed Mz mode”, Sensors **17**, 561 (2017) (Cited on p. 2).

[158] J. A. Sedlacek, A. Schwettmann, H. Kübler, R. Löw, T. Pfau, and J. P. Shaffer, “Microwave electrometry with Rydberg atoms in a vapour cell using bright atomic resonances”, Nat. Phys. **8**, 819 (2012) (Cited on p. 184).

[159] S. J. Seltzer, “Developments in alkali-metal atomic magnetometry”, PhD thesis (Princeton University, 2008) (Cited on pp. 26–28, 30, 113).

[160] S. Seltzer, P. Meares, and M. Romalis, “Synchronous optical pumping of quantum revival beats for atomic magnetometry”, Phys. Rev. A **75**, 051407 (2007) (Cited on p. 84).

[161] R. J. Sewell, M. Koschorreck, M. Napolitano, B. Dubost, N. Behbood, and M. W. Mitchell, “Magnetic Sensitivity Beyond the Projection Noise Limit by Spin Squeezing”, Phys. Rev. Lett. **109**, 253605 (2012) (Cited on p. 3).

[162] V. Shah, G. Vasilakis, and M. Romalis, “High bandwidth atomic magnetometery with continuous quantum nondemolition measurements”, Phys. Rev. Lett. **104**, 013601 (2010) (Cited on pp. 10, 31).

[163] W. Shao, C. Wu, and X.-L. Feng, “Generalized James’ effective Hamiltonian method”, Phys. Rev. A **95**, 032124 (2017) (Cited on p. 179).

[164] D. Sheng, S. Li, N. Dural, and M. V. Romalis, “Subfemtotesla Scalar Atomic Magnetometry Using Multipass Cells”, Phys. Rev. Lett. **110**, 160802 (2013) (Cited on p. 1).

[165] T. Skillman and P. Bender, “Measurement of the Earth’s magnetic field with a rubidium vapor magnetometer”, J. Geophys. Res. **63**, 513 (1958) (Cited on p. 1).

[166] A. Smith, B. E. Anderson, H. Sosa-Martinez, C. A. Riofrio, I. H. Deutsch, and P. S. Jessen, “Quantum Control in the Cs $6S_{1/2}$ Ground Manifold using Radio-Frequency and Microwave Magnetic Fields”, Phys. Rev. Lett. **111**, 170502 (2013) (Cited on p. 178).

[167] M. Stähler, S. Knappe, C. Affolderbach, W. Kemp, and R. Wynands, “Picotesla magnetometry with coherent dark states”, Europhys. Lett. **54**, 323 (2001) (Cited on p. 2).

[168] D. A. Steck, “Rubidium 87 D Line Data”, (2001) (Cited on pp. 21, 31, 112).

[169] C. Stolle, N. Olsen, B. Anderson, E. Doornbos, and A. Kuvshinov, “Special issue “Characterization of the geomagnetic field and its dynamic environment using data from space-based magnetometers””, Earth Planets Space **73**, 1 (2021) (Cited on pp. 4, 84).

[170] T. Thiele, Y. Lin, M. O. Brown, and C. A. Regal, “Self-calibrating vector atomic magnetometry through microwave polarization reconstruction”, Phys. Rev. Lett. **121**, 153202 (2018) (Cited on pp. 11, 83, 85, 124).

[171] A. Tretiakov and L. LeBlanc, “Microwave Rabi resonances beyond the small-signal regime”, Phys. Rev. A **99**, 043402 (2019) (Cited on p. 183).

[172] C. Troullinou, R. Jiménez-Martínez, J. Kong, V. Lucivero, and M. Mitchell, “Squeezed-Light Enhancement and Backaction Evasion in a High Sensitivity Optically Pumped Magnetometer”, Phys. Rev. Lett. **127**, 193601 (2021) (Cited on p. 3).

[173] C. Troullinou, V. G. Lucivero, and M. W. Mitchell, "Quantum-Enhanced Magnetometry at Optimal Number Density", Phys. Rev. Lett. **131**, 133602 (2023) (Cited on p. 3).

[174] H. H. Vallabhapurapu, J. P. Slack-Smith, V. K. Sewani, C. Adambukulam, A. Morello, J. J. Pla, and A. Laucht, "Fast Coherent Control of a Nitrogen-Vacancy-Center Spin Ensemble Using a KTaO3 Dielectric Resonator at Cryogenic Temperatures", Phys. Rev. Appl. **16**, 044051 (2021) (Cited on p. 171).

[175] J. Vanier, "Relaxation in rubidium-87 and the rubidium maser", Phys. Rev. **168**, 129 (1968) (Cited on p. 50).

[176] J. Vanier and C. Audoin, **The Quantum Physics of Atomic Frequency Standards** (CRC Press, 1989) (Cited on pp. 12, 21, 23, 24, 50, 61–64, 132).

[177] J. Vanier, J.-F. Simard, and J.-S. Boulanger, "Relaxation and frequency shifts in the ground state of Rb 85", Phys. Rev. A **9**, 1031 (1974) (Cited on p. 50).

[178] M. Violetti, M. Pellaton, C. Affolderbach, F. Merli, J.-F. Zürcher, G. Mileti, and A. K. Skrivervik, "The Microloop-Gap Resonator: A Novel Miniaturized Microwave Cavity for Double-Resonance Rubidium Atomic Clocks", IEEE Sens. J. **14**, 3193 (2014) (Cited on p. 171).

[179] M. Wagshul and T. Chupp, "Optical pumping of high-density Rb with a broadband dye laser and GaAlAs diode laser arrays: Application to $^3$He polarization", Phys. Rev. A **40**, 4447 (1989) (Cited on p. 113).

[180] M. Wagshul and T. Chupp, "Laser optical pumping of high-density Rb in polarized $^3$He targets", Phys. Rev. A **49**, 3854 (1994) (Cited on p. 62).

[181] D. Walter, W. Griffith, and W. Happer, "Magnetic slowing down of spin relaxation due to binary collisions of alkali-metal atoms with buffer-gas atoms", Phys. Rev. Lett. **88**, 093004 (2002) (Cited on pp. 62, 113).

[182] H. Wang, T. Wu, W. Xiao, H. Wang, X. Peng, and H. Guo, "Dual-Mode Dead-Zone-Free Double-Resonance Alignment-Based Magnetometer", Phys. Rev. Appl. **15**, 024033 (2021) (Cited on p. 5).

[183] J. Wang, S. She, and S. Zhang, "An improved helmholtz coil and analysis of its magnetic field homogeneity", Rev. Sci. Instrum. **73**, 2175 (2002) (Cited on p. 33).

[184] T. Wang, W. Lee, M. Romalis, M. Limes, T. Kornack, and E. Foley, "Pulsed $^{87}$Rb vector magnetometer using a fast rotating field", arXiv:2304.00214 (2023) (Cited on p. 6).

[185] X. Wang, M. Ye, F. Lu, Y. Mao, H. Tian, and J. Li, "Recent Progress on Micro-Fabricated Alkali Metal Vapor Cells", Biosensors **12**, 165 (2022) (Cited on p. 3).

[186] W. Wasilewski, K. Jensen, H. Krauter, J. J. Renema, M. Balabas, and E. S. Polzik, "Quantum Noise Limited and Entanglement-Assisted Magnetometry", Phys. Rev. Lett. **104**, 133601 (2010) (Cited on p. 3).

[187] A. Weis, G. Bison, and A. S. Pazgalev, "Theory of double resonance magnetometers based on atomic alignment", Phys. Rev. A **74**, 033401 (2006) (Cited on p. 5).

[188] N. P. Wells, T. U. Driskell, and J. C. Camparo, "Stabilizing vapor-cell temperature: the isoclinic-point" atomic thermometer"", in 2014 european frequency and time forum (eftf) (IEEE, 2014), pp. 548–553 (Cited on p. 81).

[189] W. Wu, B. Zhou, G. Liu, L. Chen, J. Wang, and J. Fang, "Novel nested saddle coils used in miniature atomic sensors", AIP Adv. **8** (2018) (Cited on p. 33).

[190] H. Xia, A. Ben-Amar Baranga, D. Hoffman, and M. Romalis, "Magnetoencephalography with an atomic magnetometer", Appl. Phys. Lett. **89** (2006) (Cited on p. 1).

[191] V. Yashchuk, D. Budker, W. Gawlik, D. Kimball, Y. P. Malakyan, and S. Rochester, "Selective Addressing of High-Rank Atomic Polarization Moments", Phys. Rev. Lett. **90**, 253001 (2003) (Cited on pp. 84, 179).

[192] L. Li-Yeh, S.-B. Jiang, T.-L. Yeh, H.-C. Yeh, J.-Y. Liu, Y.-H. Hsu, and P. Ji-Yi, "The Magneto-Resistive Magnetometer of BCU on the Tatiana-2 Satellite", Terr. Atmos. Ocean. Sci. **23**, 317 (2012) (Cited on p. 5).

[193] V. Yudin, A. Taichenachev, Y. Dudin, V. Velichansky, A. Zibrov, and S. Zibrov, "Vector magnetometry based on electromagnetically induced transparency in linearly polarized light", Phys. Rev. A **82**, 033807 (2010) (Cited on p. 5).

[194] V. Yudin, A. Taichenachev, C. Oates, Z. Barber, N. D. Lemke, A. D. Ludlow, U. Sterr, C. Lisdat, and F. Riehle, "Hyper-Ramsey spectroscopy of optical clock transitions", Phys. Rev. A **82**, 011804 (2010) (Cited on pp. 85, 88).

[195] D. Zeuch, F. Hassler, J. J. Slim, and D. P. DiVincenzo, "Exact rotating wave approximation", Ann. Phys. **423**, 168327 (2020) (Cited on p. 179).

[196] J. Zhang, Y. Wang, C. Wang, Z. Zhou, and W. Li, "$^4$He Optically Pumped Magnetometer With RF Field Modulation and Light Stabilization in Deep Well for Earthquake Monitoring", IEEE Trans. Instrum. Meas. **71**, 1 (2022) (Cited on p. 5).

[197] R. Zhang, D. Kanta, A. Wickenbrock, H. Guo, and D. Budker, "Heading-Error-Free Optical Atomic Magnetometry in the Earth-Field Range", Phys. Rev. Lett. **130**, 153601 (2023) (Cited on p. 84).

[198] R. Zhang and R. Mhaskar, **Advanced Magnetometer System: Task II**, tech. rep. (Geometrics, 2019) (Cited on pp. 6, 176, 180).

[199] R. Zhang, R. Mhaskar, K. Smith, E. Balasubramaniam, and M. Prouty, "Vector measurements using all optical scalar atomic magnetometers", J. Appl. Phys. **129** (2021) (Cited on pp. 5, 14, 154).

# Appendix A

## Spin matrices

In this appendix we list the electron and nuclear spin matrices for $^{87}$Rb. These spin matrices can be evaluated in the $|S, I, m_s, m_I\rangle$ eigenbasis (Table A.1 and Table A.3), defined by

$$S_z |S, m_s\rangle = m_s |S, m_s\rangle \tag{A.1}$$

$$S_\pm |S, m_s\rangle = (S_x \pm iS_y) |S, m_s\rangle = \sqrt{S(S+1) - m_s(m_s \pm 1)}\, |S, m_s \pm 1\rangle \tag{A.2}$$

with the same corresponding definitions for $I_z$ and $I_\pm$. To work in the total atomic spin basis $|F, m_F\rangle$, which diagonalizes $\mathbf{I} \cdot \mathbf{S}$, requires a basis transformation by using the Clebsch-Gordan coefficients $c_{\{F,m_F,m_s,m_I\}}$ defined by $|F, m_F\rangle = \sum c_{\{F,m_F,m_s,m_I\}} |m_s, m_I\rangle$. We achieve this basis transformation with the transformation matrix $\mathcal{G}$, defined in Table A.5, through $\mathbf{S} \rightarrow \mathcal{G}^\dagger \mathbf{S} \mathcal{G}$. The explicit values of electron and nuclear spin operators in the $|F, m_F\rangle$ basis are listed in Table A.2 and Table A.4.

Table A.1: Electron spin matrices in the $|m_s, m_I\rangle$ basis for $^{87}$Rb.

| Spin | $\vert m_s, m_I\rangle$ | | | | | | | |
|---|---|---|---|---|---|---|---|---|
| Operator | $\vert -\frac{1}{2}, \frac{1}{2}\rangle$ | $\vert -\frac{1}{2}, -\frac{1}{2}\rangle$ | $\vert -\frac{1}{2}, -\frac{3}{2}\rangle$ | $\vert \frac{1}{2}, \frac{3}{2}\rangle$ | $\vert \frac{1}{2}, \frac{1}{2}\rangle$ | $\vert \frac{1}{2}, -\frac{1}{2}\rangle$ | $\vert \frac{1}{2}, -\frac{3}{2}\rangle$ | $\vert -\frac{1}{2}, \frac{3}{2}\rangle$ |

$$S_x = \begin{bmatrix} 0 & 0 & 0 & 0 & \frac{1}{2} & 0 & 0 & 0 \\ 0 & 0 & 0 & 0 & 0 & \frac{1}{2} & 0 & 0 \\ 0 & 0 & 0 & 0 & 0 & 0 & \frac{1}{2} & 0 \\ 0 & 0 & 0 & 0 & 0 & 0 & 0 & \frac{1}{2} \\ \frac{1}{2} & 0 & 0 & 0 & 0 & 0 & 0 & 0 \\ 0 & \frac{1}{2} & 0 & 0 & 0 & 0 & 0 & 0 \\ 0 & 0 & \frac{1}{2} & 0 & 0 & 0 & 0 & 0 \\ 0 & 0 & 0 & \frac{1}{2} & 0 & 0 & 0 & 0 \end{bmatrix}$$

$$S_y = \begin{bmatrix} 0 & 0 & 0 & 0 & \frac{i}{2} & 0 & 0 & 0 \\ 0 & 0 & 0 & 0 & 0 & \frac{i}{2} & 0 & 0 \\ 0 & 0 & 0 & 0 & 0 & 0 & \frac{i}{2} & 0 \\ 0 & 0 & 0 & 0 & 0 & 0 & 0 & -\frac{i}{2} \\ -\frac{i}{2} & 0 & 0 & 0 & 0 & 0 & 0 & 0 \\ 0 & -\frac{i}{2} & 0 & 0 & 0 & 0 & 0 & 0 \\ 0 & 0 & -\frac{i}{2} & 0 & 0 & 0 & 0 & 0 \\ 0 & 0 & 0 & \frac{i}{2} & 0 & 0 & 0 & 0 \end{bmatrix}$$

$$S_z = \begin{bmatrix} -\frac{1}{2} & 0 & 0 & 0 & 0 & 0 & 0 & 0 \\ 0 & -\frac{1}{2} & 0 & 0 & 0 & 0 & 0 & 0 \\ 0 & 0 & -\frac{1}{2} & 0 & 0 & 0 & 0 & 0 \\ 0 & 0 & 0 & \frac{1}{2} & & 0 & 0 & 0 \\ 0 & 0 & 0 & 0 & \frac{1}{2} & 0 & 0 & 0 \\ 0 & 0 & 0 & 0 & 0 & \frac{1}{2} & 0 & 0 \\ 0 & 0 & 0 & 0 & 0 & 0 & \frac{1}{2} & 0 \\ 0 & 0 & 0 & 0 & 0 & 0 & 0 & -\frac{1}{2} \end{bmatrix}$$

Table A.2: Electron spin matrices in the $|F, m_F\rangle$ basis for $^{87}$Rb.

$$
\begin{array}{c|cccccccc}
\text{Spin} & \multicolumn{8}{c}{|m_s, m_I\rangle} \\
\text{Operator} & |1,1\rangle & |1,0\rangle & |1,-1\rangle & |2,2\rangle & |2,1\rangle & |2,0\rangle & |2,-1\rangle & |2,-2\rangle
\end{array}
$$

$$
S_x = \begin{bmatrix}
0 & -\frac{1}{4\sqrt{2}} & 0 & -\frac{\sqrt{3}}{4} & 0 & \frac{1}{4\sqrt{2}} & 0 & 0 \\
-\frac{1}{4\sqrt{2}} & 0 & -\frac{1}{4\sqrt{2}} & 0 & -\frac{\sqrt{\frac{3}{2}}}{4} & 0 & \frac{\sqrt{\frac{3}{2}}}{4} & 0 \\
0 & -\frac{1}{4\sqrt{2}} & 0 & 0 & 0 & -\frac{1}{4\sqrt{2}} & 0 & \frac{\sqrt{3}}{4} \\
-\frac{\sqrt{3}}{4} & 0 & 0 & 0 & \frac{1}{4} & 0 & 0 & 0 \\
0 & -\frac{\sqrt{\frac{3}{2}}}{4} & 0 & \frac{1}{4} & 0 & \frac{\sqrt{\frac{3}{2}}}{4} & 0 & 0 \\
\frac{1}{4\sqrt{2}} & 0 & -\frac{1}{4\sqrt{2}} & 0 & \frac{\sqrt{\frac{3}{2}}}{4} & 0 & \frac{\sqrt{\frac{3}{2}}}{4} & 0 \\
0 & \frac{\sqrt{\frac{3}{2}}}{4} & 0 & 0 & 0 & \frac{\sqrt{\frac{3}{2}}}{4} & 0 & \frac{1}{4} \\
0 & 0 & \frac{\sqrt{3}}{4} & 0 & 0 & 0 & \frac{1}{4} & 0
\end{bmatrix}
$$

$$
S_y = \begin{bmatrix}
0 & \frac{i}{4\sqrt{2}} & 0 & -\frac{i\sqrt{3}}{4} & 0 & -\frac{i}{4\sqrt{2}} & 0 & 0 \\
-\frac{i}{4\sqrt{2}} & 0 & \frac{i}{4\sqrt{2}} & 0 & -\frac{i\sqrt{\frac{3}{2}}}{4} & 0 & -\frac{i\sqrt{\frac{3}{2}}}{4} & 0 \\
0 & -\frac{i}{4\sqrt{2}} & 0 & 0 & 0 & -\frac{i}{4\sqrt{2}} & 0 & -\frac{i\sqrt{3}}{4} \\
\frac{i\sqrt{3}}{4} & 0 & 0 & 0 & -\frac{i}{4} & 0 & 0 & 0 \\
0 & \frac{i\sqrt{\frac{3}{2}}}{4} & 0 & \frac{i}{4} & 0 & -\frac{i\sqrt{\frac{3}{2}}}{4} & 0 & 0 \\
\frac{i}{4\sqrt{2}} & 0 & \frac{i}{4\sqrt{2}} & 0 & \frac{i\sqrt{\frac{3}{2}}}{4} & 0 & -\frac{i\sqrt{\frac{3}{2}}}{4} & 0 \\
0 & \frac{i\sqrt{\frac{3}{2}}}{4} & 0 & 0 & 0 & \frac{i\sqrt{\frac{3}{2}}}{4} & 0 & -\frac{i}{4} \\
0 & 0 & \frac{i\sqrt{3}}{4} & 0 & 0 & 0 & \frac{i}{4} & 0
\end{bmatrix}
$$

$$
S_z = \begin{bmatrix}
-\frac{1}{4} & 0 & 0 & 0 & \frac{\sqrt{3}}{4} & 0 & 0 & 0 \\
0 & 0 & 0 & 0 & 0 & \frac{1}{2} & 0 & 0 \\
0 & 0 & \frac{1}{4} & 0 & 0 & 0 & \frac{\sqrt{3}}{4} & 0 \\
0 & 0 & 0 & \frac{1}{2} & 0 & 0 & 0 & 0 \\
\frac{\sqrt{3}}{4} & 0 & 0 & 0 & \frac{1}{4} & 0 & 0 & 0 \\
0 & \frac{1}{2} & 0 & 0 & 0 & 0 & 0 & 0 \\
0 & 0 & \frac{\sqrt{3}}{4} & 0 & 0 & 0 & -\frac{1}{4} & 0 \\
0 & 0 & 0 & 0 & 0 & 0 & 0 & -\frac{1}{2}
\end{bmatrix}
$$

Table A.3: Nuclear spin matrices in the $|m_s, m_I\rangle$ basis for $^{87}$Rb.

| Spin Operator | $\vert m_s, m_I\rangle$: $\vert -\frac{1}{2}, \frac{1}{2}\rangle$ $\vert -\frac{1}{2}, -\frac{1}{2}\rangle$ $\vert -\frac{1}{2}, -\frac{3}{2}\rangle$ $\vert \frac{1}{2}, \frac{3}{2}\rangle$ $\vert \frac{1}{2}, \frac{1}{2}\rangle$ $\vert \frac{1}{2}, -\frac{1}{2}\rangle$ $\vert \frac{1}{2}, -\frac{3}{2}\rangle$ $\vert -\frac{1}{2}, \frac{3}{2}\rangle$ |
|---|---|
| $I_x =$ | $\begin{bmatrix} 0 & 1 & 0 & 0 & 0 & 0 & 0 & \frac{\sqrt{3}}{2} \\ 1 & 0 & \frac{\sqrt{3}}{2} & 0 & 0 & 0 & 0 & 0 \\ 0 & \frac{\sqrt{3}}{2} & 0 & 0 & 0 & 0 & 0 & 0 \\ 0 & 0 & 0 & 0 & \frac{\sqrt{3}}{2} & 0 & 0 & 0 \\ 0 & 0 & 0 & \frac{\sqrt{3}}{2} & 0 & 1 & 0 & 0 \\ 0 & 0 & 0 & 0 & 1 & 0 & \frac{\sqrt{3}}{2} & 0 \\ 0 & 0 & 0 & 0 & 0 & \frac{\sqrt{3}}{2} & 0 & 0 \\ \frac{\sqrt{3}}{2} & 0 & 0 & 0 & 0 & 0 & 1 & 0 \end{bmatrix}$ |
| $I_y =$ | $\begin{bmatrix} 0 & -i & 0 & 0 & 0 & 0 & 0 & \frac{i\sqrt{3}}{2} \\ i & 0 & -\frac{i\sqrt{3}}{2} & 0 & 0 & 0 & 0 & 0 \\ 0 & \frac{i\sqrt{3}}{2} & 0 & 0 & 0 & 0 & 0 & 0 \\ 0 & 0 & 0 & 0 & -\frac{i\sqrt{3}}{2} & 0 & 0 & 0 \\ 0 & 0 & 0 & \frac{i\sqrt{3}}{2} & 0 & -i & 0 & 0 \\ 0 & 0 & 0 & 0 & i & 0 & -\frac{i\sqrt{3}}{2} & 0 \\ 0 & 0 & 0 & 0 & 0 & \frac{i\sqrt{3}}{2} & 0 & 0 \\ -\frac{i\sqrt{3}}{2} & 0 & 0 & 0 & 0 & 0 & 0 & 0 \end{bmatrix}$ |
| $I_z =$ | $\begin{bmatrix} \frac{1}{2} & 0 & 0 & 0 & 0 & 0 & 0 & 0 \\ 0 & -\frac{1}{2} & 0 & 0 & 0 & 0 & 0 & 0 \\ 0 & 0 & -\frac{3}{2} & & 0 & 0 & 0 & 0 \\ 0 & 0 & 0 & \frac{3}{2} & 0 & 0 & 0 & 0 \\ 0 & 0 & 0 & 0 & \frac{1}{2} & 0 & 0 & 0 \\ 0 & 0 & 0 & 0 & 0 & -\frac{1}{2} & 0 & 0 \\ 0 & 0 & 0 & 0 & 0 & 0 & -\frac{3}{2} & 0 \\ 0 & 0 & 0 & 0 & 0 & 0 & 0 & \frac{3}{2} \end{bmatrix}$ |

Table A.4: Nuclear spin matrices in the $|F, m_F\rangle$ basis for $^{87}$Rb.

| Spin Operator | $\|m_s, m_I\rangle$ | | | | | | | |
|---|---|---|---|---|---|---|---|---|
| | $\|1,1\rangle$ | $\|1,0\rangle$ | $\|1,-1\rangle$ | $\|2,2\rangle$ | $\|2,1\rangle$ | $\|2,0\rangle$ | $\|2,-1\rangle$ | $\|2,-2\rangle$ |

$$I_x = \begin{bmatrix} 0 & \frac{5}{4\sqrt{2}} & 0 & \frac{\sqrt{3}}{4} & 0 & -\frac{1}{4\sqrt{2}} & 0 & 0 \\ \frac{5}{4\sqrt{2}} & 0 & \frac{5}{4\sqrt{2}} & 0 & \frac{\sqrt{\frac{3}{2}}}{4} & 0 & -\frac{\sqrt{\frac{3}{2}}}{4} & 0 \\ 0 & \frac{5}{4\sqrt{2}} & 0 & 0 & 0 & \frac{1}{4\sqrt{2}} & 0 & -\frac{\sqrt{3}}{4} \\ \frac{\sqrt{3}}{4} & 0 & 0 & 0 & \frac{3}{4} & 0 & 0 & 0 \\ 0 & \frac{\sqrt{\frac{3}{2}}}{4} & 0 & \frac{3}{4} & 0 & \frac{3\sqrt{\frac{3}{2}}}{4} & 0 & 0 \\ -\frac{1}{4\sqrt{2}} & 0 & \frac{1}{4\sqrt{2}} & 0 & \frac{3\sqrt{\frac{3}{2}}}{4} & 0 & \frac{3\sqrt{\frac{3}{2}}}{4} & 0 \\ 0 & -\frac{\sqrt{\frac{3}{2}}}{4} & 0 & 0 & 0 & \frac{3\sqrt{\frac{3}{2}}}{4} & 0 & \frac{3}{4} \\ 0 & 0 & -\frac{\sqrt{3}}{4} & 0 & 0 & 0 & \frac{3}{4} & 0 \end{bmatrix}$$

$$I_y = \begin{bmatrix} 0 & -\frac{i5}{4\sqrt{2}} & 0 & \frac{i\sqrt{3}}{4} & 0 & -\frac{i}{4\sqrt{2}} & 0 & 0 \\ \frac{i5}{4\sqrt{2}} & 0 & -\frac{i5}{4\sqrt{2}} & 0 & \frac{i\sqrt{\frac{3}{2}}}{4} & 0 & \frac{i\sqrt{\frac{3}{2}}}{4} & 0 \\ 0 & \frac{i5}{4\sqrt{2}} & 0 & 0 & 0 & \frac{i}{4\sqrt{2}} & 0 & \frac{i\sqrt{3}}{4} \\ -\frac{i\sqrt{3}}{4} & 0 & 0 & 0 & -\frac{i3}{4} & 0 & 0 & 0 \\ 0 & -\frac{i\sqrt{\frac{3}{2}}}{4} & 0 & \frac{i3}{4} & 0 & -\frac{i3\sqrt{\frac{3}{2}}}{4} & 0 & 0 \\ -\frac{i}{4\sqrt{2}} & 0 & -\frac{i}{4\sqrt{2}} & 0 & \frac{i3\sqrt{\frac{3}{2}}}{4} & 0 & -\frac{i3\sqrt{\frac{3}{2}}}{4} & 0 \\ 0 & -\frac{i\sqrt{\frac{3}{2}}}{4} & 0 & 0 & 0 & \frac{i3\sqrt{\frac{3}{2}}}{4} & 0 & -\frac{i3}{4} \\ 0 & 0 & -\frac{i\sqrt{3}}{4} & 0 & 0 & 0 & \frac{i3}{4} & 0 \end{bmatrix}$$

$$I_z = \begin{bmatrix} \frac{5}{4} & 0 & 0 & 0 & -\frac{\sqrt{3}}{4} & 0 & 0 & 0 \\ 0 & 0 & 0 & 0 & 0 & -\frac{1}{2} & 0 & 0 \\ 0 & 0 & -\frac{5}{4} & 0 & 0 & 0 & -\frac{\sqrt{3}}{4} & 0 \\ 0 & 0 & 0 & \frac{3}{2} & 0 & 0 & 0 & 0 \\ -\frac{\sqrt{3}}{4} & 0 & 0 & 0 & \frac{3}{4} & 0 & 0 & 0 \\ 0 & -\frac{1}{2} & 0 & 0 & 0 & 0 & 0 & 0 \\ 0 & 0 & -\frac{\sqrt{3}}{4} & 0 & 0 & 0 & -\frac{3}{4} & 0 \\ 0 & 0 & 0 & 0 & 0 & 0 & 0 & -\frac{3}{2} \end{bmatrix}$$

Table A.5: Transformation matrix $\mathcal{G}$ for making the basis transformation $|m_s, m_I\rangle \to |F, m_F\rangle$ of the $F = 1$ and $F = 2$ ground states for $^{87}$Rb.

| | $\|1,1\rangle$ | $\|1,0\rangle$ | $\|1,-1\rangle$ | $\|2,2\rangle$ | $\|2,1\rangle$ | $\|2,0\rangle$ | $\|2,-1\rangle$ | $\|2,-2\rangle$ |
|---|---|---|---|---|---|---|---|---|
| $\langle -\frac{1}{2}, \frac{1}{2}\|$ | 0 | $-\frac{1}{\sqrt{2}}$ | 0 | 0 | 0 | $\frac{1}{\sqrt{2}}$ | 0 | 0 |
| $\langle -\frac{1}{2}, -\frac{1}{2}\|$ | 0 | 0 | $-\frac{1}{\sqrt{2}}$ | 0 | 0 | 0 | $\sqrt{\frac{3}{2}}$ | 0 |
| $\langle -\frac{1}{2}, -\frac{3}{2}\|$ | 0 | 0 | 0 | 0 | 0 | 0 | 0 | 1 |
| $\langle \frac{1}{2}, \frac{3}{2}\|$ | 0 | 0 | 0 | 1 | 0 | 0 | 0 | 0 |
| $\langle \frac{1}{2}, \frac{1}{2}\|$ | $\frac{1}{2}$ | 0 | 0 | 0 | $\frac{\sqrt{3}}{2}$ | 0 | 0 | 0 |
| $\langle \frac{1}{2}, -\frac{1}{2}\|$ | 0 | $\frac{1}{\sqrt{2}}$ | 0 | 0 | 0 | $\frac{1}{\sqrt{2}}$ | 0 | 0 |
| $\langle \frac{1}{2}, -\frac{3}{2}\|$ | 0 | 0 | $\frac{\sqrt{3}}{2}$ | 0 | 0 | 0 | $\frac{1}{2}$ | 0 |
| $\langle -\frac{1}{2}, \frac{3}{2}\|$ | $-\frac{\sqrt{3}}{2}$ | 0 | 0 | 0 | $\frac{1}{2}$ | 0 | 0 | 0 |